# Analysis of Deformation of Gas Diffusion Layers and the Impact on Performance of PEM Fuel Cells

Wang, Jiatang

2017

*Document Version:*
Publisher's PDF, also known as Version of record

# Analysis of Deformation of Gas Diffusion Layers and the Impact on Performance of PEM Fuel Cells

Jiatang Wang


LUND
UNIVERSITY

DOCTORAL DISSERTATION
by due permission of the Faculty of Engineering at Lund University, will be publicly defenced on Friday 20 October 2017, at 10:15 a.m. in Lecture Hall E in the M-building, Ole Römers väg 1, Lund, Sweden.

*Faculty opponent*
Professor Ned Djilali
University of Victoria
Victoria, BC, Canada

| Organization<br>LUND UNIVERSITY | Document name<br>DOCTORAL DISSERTATION |
|---|---|
| | Date of issue<br>August 15, 2017 |
| Author(s)<br>Jiatang Wang | Sponsoring organization<br>China Scholarship Council (CSC) |

Title and subtitle

Analysis of Deformation of Gas Diffusion Layers and the Impact on Performance of PEM Fuel Cells


Abstract

Proton exchange membrane (PEM) fuel cells have been promoted due to significant breakthroughs in various aspects and increasing public interests. The porous features of the gas diffusion layer (GDL) and the necessary assembly processes generate localized pressure forces on the channel/shoulder structure of the bi-polar plates (BPP). As a consequence, the assembly pressure acting on a single cell and a fuel cell stack has important influence on the geometric deformation of the GDL resulting in a change in porosity, permeability, and the resistance for heat and charge transfer in PEM fuel cells. It is expected that the cell performance is also affected by these physical parameters. To optimize the cell performance, it is necessary to consider the assembly effects, which is conducted by a numerical method in this work.

The effect of the GDL porosity change caused by various compression ratios is investigated by a three-dimensional (3D) PEM fuel cell model based on the finite volume method (FVM). The model was validated and further applied to predict the transport phenomena including heat, mass and charges, as well as the effects on the cell performance. The simulation results show that a high compression ratio on the GDL leads to lower porosity, which is favorable for the heat removal from the cell. However, the compression has contradictory effects on the mass transfer and finally deteriorates the cell performance.

To predict the GDL deformation and associated effects on the geometric parameters as well as porosity, mass transport properties and the cell performance, both the finite element method (FEM) and the FVM are applied, respectively. A non-homogeneous deformation, porosity, oxygen diffusion coefficient and the electric resistance of the GDL have been observed across the fuel cell in the in-plane direction. The obtained non-homogeneous physical parameters of the deformed GDL are applied for further computational fluid dynamics (CFD) analysis. The CFD results reveal that a higher assembly pressure decreases the porosity, GDL thickness, gas flow channel cross-sectional areas, oxygen diffusion coefficient, oxygen concentration and cell performance. It is found that, the reduction of the GDL porosity is a dominating factor that decreases the cell performance compared with the decreased gas channel flow area and GDL thickness in the assembly condition. A sufficient GDL thickness is required to ensure transfer of the fresh gas to the reaction sites far away from the channel.

As the entire electric resistance is considered, the optimized cell performance is obtained if the cell is operating below 1 MPa assembly pressure. It is found from a newly developed electric resistance model that both through-plane resistance of a cell and the interfacial resistance between the GDL and BPP for electrons decrease with higher assembly pressures. Comparing with a zero-compressed cell, the cell operating at an assembly pressure above 2 MPa creates a new contact area between the GDL and BPP at the vertical interface. Therefore, the corner of a BPP close to the channel becomes the dominating zones for electron transfer. Finally, it is suggested that the assembly pressure should be considered properly in designing and manufacturing of PEM fuel cells.



Key words:

PEM fuel cell, compression ratio, assembly pressure, porosity, deformed GDL, electric resistance, transport phenomena, model, performance, analysis, OpenFOAM.

Classification system and/or index terms (if any)

| Supplementary bibliographical information | | Language<br>English |
|---|---|---|
| ISSN and key title<br>ISSN 0282-1990<br>ISRN LUTMDN/TMHP-17/1134-SE | | ISBN<br>978-91-7753-395-5 (print)<br>978-91-7753-396-2 (pdf) |
| Recipient's notes | Number of pages 176 | Price |
| | Security classification | |




Signature Jiatang Wang Date August 15, 2017

# Analysis of Deformation of Gas Diffusion Layers and the Impact on Performance of PEM Fuel Cells

Jiatang Wang


LUND
UNIVERSITY

Thesis for the degree of Doctor of Philosophy in Engineering.

Coverphoto by Jiatang Wang



Division of Heat Transfer
Department of Energy Sciences
Faculty of Engineering (LTH)
Lund University
Box 118
SE-221 00 LUND
SWEDEN

ISBN 978-91-7753-395-5 (print)
ISBN 978-91-7753-396-2 (pdf)
ISRN LUTMDN/TMHP-17/1134-SE
ISSN 0282-1990

Printed in Sweden by Media-Tryck, Lund University.
Lund 2017

# Abstract

Proton exchange membrane (PEM) fuel cells have been promoted due to significant breakthroughs in various aspects and increasing public interests. The porous features of the gas diffusion layer (GDL) and the necessary assembly processes generate localized pressure forces on the channel/shoulder structure of the bi-polar plates (BPP). As a consequence, the assembly pressure acting on a single cell and a fuel cell stack has important influence on the geometric deformation of the GDL resulting in a change in porosity, permeability, and the resistance for heat and charge transfer in PEM fuel cells. It is expected that the cell performance is also affected by these physical parameters. To optimize the cell performance, it is necessary to consider the assembly effects, which is conducted by a numerical method in this work.

The effect of the GDL porosity change caused by various compression ratios is investigated by a three-dimensional (3D) PEM fuel cell model based on the finite volume method (FVM). The model was validated and further applied to predict the transport phenomena including heat, mass and charges, as well as the effects on the cell performance. The simulation results show that a high compression ratio on the GDL leads to lower porosity, which is favorable for the heat removal from the cell. However, the compression has contradictory effects on the mass transfer and finally deteriorates the cell performance.

To predict the GDL deformation and associated effects on the geometric parameters as well as porosity, mass transport properties and the cell performance, both the finite element method (FEM) and the FVM are applied, respectively. A non-homogeneous deformation, porosity, oxygen diffusion coefficient and the electric resistance of the GDL have been observed across the fuel cell in the in-plane direction. The obtained non-homogeneous physical parameters of the deformed GDL are applied for further computational fluid dynamics (CFD) analysis. The CFD results reveal that a higher assembly pressure decreases the porosity, GDL thickness, gas flow channel cross-sectional areas, oxygen diffusion coefficient, oxygen concentration and cell performance. It is found that, the reduction of the GDL porosity is a dominating factor that decreases the cell performance compared with the decreased gas channel flow area and GDL thickness in the assembly condition. A sufficient GDL thickness is required to ensure transfer of the fresh gas to the reaction sites far away from the channel.

As the entire electric resistance is considered, the optimized cell performance is obtained if the cell is operating below 1 MPa assembly pressure. It is found from a newly developed electric resistance model that both through-plane resistance of a cell and the interfacial resistance between the GDL and BPP for electrons decrease with higher assembly pressures. Comparing with a zero-compressed cell, the cell operating at an assembly pressure above 2 MPa creates a new contact area between the GDL and BPP at the vertical interface. Therefore, the corner of a BPP close to the channel

becomes the dominating zones for electron transfer. Finally, it is suggested that the assembly pressure should be considered properly in designing and manufacturing of PEM fuel cells.

**Keywords:** PEM fuel cell, compression ratio, assembly pressure, porosity, deformed GDL, electric resistance, transport phenomena, model, performance, analysis, OpenFOAM.

# Popular science summary

Proton exchange membrane (PEM) fuel cell is one of the promising fuel cells in conversion of chemical energy to electric energy with a relative high efficiency. It is widely known that the PEM fuel cell has nearly-zero pollutants if it is fueled by hydrogen. People can use the sustainable electric power without any noise in home usage, transportation and commutation facilities and so on. The current interest of this device is to replace combustion engines to release the environmental problems like $CO_2$ emissions.

A PEM fuel cell involves several technologies. Many achievements have been reached in the past decades. However, the cost and stability are two main limitations preventing wide use of PEM fuel cells. In various research and development fields, such as materials, design and manufacturing, some breakthroughs have been made in improving the cell performance. Even though large efforts have been paid in experiments, the closed-space and small-scale of the cell device make it hard to investigate. Therefore, numerical methods have become very popular and presented efficient ways to investigate the transport phenomena and optimizing the cell performance.

The assembly process of a single cell or a cell stack is a necessary step to prevent gas leakage and decrease the contact resistance between the various layers. The porous carbon fibers in the gas diffusion layer (GDL) are touching the channel/shoulder structure of the bi-polar plates (BPP). As a consequence, the physical properties of the GDL, such as dimensions, porosity, mass transfer resistance, and interfacial resistances for heat and electrons will be changed. These factors may result in unexpected or decreased cell performance.

In this work, the commercial software ANSYS and the newly developed open source code OpenFOAM ("Open Source Field Operation and Manipulation") are applied to study the important assembly processes. The model in ANSYS predicts the GDL deformation behavior. Then the deformed GDL and the corresponding yield properties are implemented in the PEM fuel cell model to study the effects of the assembly pressure on the transport phenomena and cell performance. To optimize the cell performance, the electric resistance in the deformed bulk of a cell and the interfacial resistance between the GDL and BPP are considered. All the parameters are expressed as a function of the assembly pressure.

To investigate the porosity effects independently, different porosities of the GDL caused by various assumed compression ratios are applied as initial conditions for the PEM fuel cell model. In the study of porosity effects, the GDL deformation and the electric resistance variations are neglected. Then the model is further extended to include real deformation of the GDL and the electron transfer effects, respectively. By evaluating several topics, the cell performance is optimized in terms of assembly

pressures or compression ratios. Guidelines for design and manufacturing of PEM fuel cells can be set up based on this thesis.

# Acknowledgments

This research work was carried out at the Division of Heat Transfer, Department of Energy Sciences at Lund University, Lund, Sweden. Financial support by the China Scholarship Council (CSC) of Chinese government as a scholarship to the author is highly appreciated. Additional research costs were covered by the Department of Energy Sciences.

First, I would like to express my greatest appreciation to my supervisors, Professor Jinliang Yuan and Professor Bengt Sundén, for providing me the opportunity to perform my doctoral study at the Department of Energy Sciences at Lund University. Their academic guidance, encouragement and all the support that I have received from them helped me enormously during the past four years. It is my honor to be supervised by them.

I would like to express my thanks to the kind help from my colleagues Jian Liu in model meshing and Cheng Gong in OpenFOAM (for "Open Source Field Operation and Manipulation") tips. I am very thankful to the OpenFOAM expert Hrvoje Jasak at University of Zagreb in Croatia to give me a chance to join a summer school and give me many suggestions about OpenFOAM modeling.

Many thanks go to all my fellow PhD students, especially for lots of help and happiness from Yiheng Tong, and the Department Administrators Catarina Lindén, Elna Andersson, Gity Yahoo and Jenny Oldbring at the Department of Energy Sciences for creating a harmonic study environment. Many thanks to the software supports from computer engineer Robert-Zoltan Szasz. In addition, I would like to thank all friends in Lund.

Finally, a special thanks to my parents, ZeBin Wang and Minzhi Zeng, my brothers Jiasen Wang and Jiaman Wang, and my sister Li Wang for all their support. Last but not least, sweetest thanks to my wife, Zheng Si. Greatest thanks for her stepping into my life and giving significant support during my PhD degree studies.

# List of publications

**I.** **Jiatang Wang**, Jinliang Yuan and Bengt Sundén. Coupled simulation approaches for PEM fuel cells by OpenFOAM. *9th OpenFOAM® Workshop*, June 23-26, 2014, Zagreb, Croatia. doi: http://lup.lub.lu.se/record/4588026.

**II.** **Jiatang Wang**, Jinliang Yuan and Bengt Sundén. Modeling of inhomogeneous compression effects of porous GDL on transport phenomena and performance in PEM fuel cells. *International Journal of Energy Research*. 2016; **41**(7): 985-1003. doi: 10.1002/er.3687.

**III.** **Jiatang Wang**, Jinliang Yuan , Jong-Sung Yu and Bengt Sundén. Investigation of effects of non-homogenous deformation of gas diffusion layer in a PEM fuel cell. *International Journal of Energy Research*. In press, 2017. doi: 10.1002/er.3774.

**IV.** **Jiatang Wang**, Jinliang Yuan and Bengt Sundén. On electric resistance effects of non-homogeneous GDL deformation in a PEM Fuel Cell. Submitted for journal publication.

**V.** **Jiatang Wang**, Jinliang Yuan and Bengt Sundén. Electric transport process for the bulk of a PEM fuel cell. *European Fuel Cell Technology & Applications Conference*, December 12-15, 2017, Naples, Italy.

# Nomenclature

Latin Characters

| | |
|---|---|
| $a_n$ | coefficient for dynamic viscosity, [-] |
| $A$ | cross-sectional area of conductor, [$m^2$] |
| $d_{pore}$ | mean pore diameter of electrode, [m] |
| $C_p$ | specific heat at constant pressure, [J $kg^{-1}$ $K^{-1}$] |
| $d_{pore}$ | mean pore diameter of porous medium, [m] |
| $D_i$ | diffusion coefficient of species *i*, [$m^2$ $s^{-1}$] |
| $D_n$ | viscous resistance, [$m^2$ $s^{-1}$] |
| $E_0$ | theoretical potential, [V] |
| $E_{act}$ | activation energy, [J $mol^{-1}$] |
| $E_{Nernst}$ | Nernst potential, [V] |
| $F$ | Faraday constant, 96487 [C $mol^{-1}$] |
| $F_n$ | viscous inertia, [$m^2$ $s^{-1}$] |
| $\Delta G_{rxn}$ | change in Gibbs free energy, [J $mol^{-1}$] |
| $h_i$ | thickness of component *i*, [m] |
| $\Delta H_e$ | enthalpy change per mole electron, [J $mol^{-1}e^{-1}$] |
| $\Delta H_{rxn}$ | enthalpy change, [J $mol^{-1}$] |
| $i$ | local current density, [A $cm^{-2}$] |
| $\bar{i}$ | average current density, [A $cm^{-2}$] |
| $i_{cell}$ | average current density of cell, [A $cm^{-2}$] |
| $i_0$ | local exchange current density, [A $cm^{-2}$] |
| $J_i$ | mass diffusion flux of species *i*, [kg $m^{-2}$ $s^{-1}$] |
| $k$ | effective thermal conductivity, [W $m^{-1}$ $K^{-1}$] |
| $l$ | length of conductor, [m] |
| $M_i$ | molecular-weight of species *i*, [kg $mol^{-1}$] |
| $n$ | number of electrons transferred, [-] |
| $P$ | gas pressure, [Pa] |

| | |
|---|---|
| $P_{Assembly}$ | assembly pressure of a cell, [MPa] |
| $P_{conatct}$ | contact pressure between GDL and BPP, [MPa] |
| $R$ | ideal gas constant, 8.3145 [J $mol^{-1}$ $K^{-1}$] |
| $R_{contact}$ | electric contact resistance, [m$\Omega$ $cm^2$] |
| $R_e$ | specific electric resistance of fuel cell, [m$\Omega$ $cm^2$] |
| $R_{GDL/BPP}$ | interfacial resistance between GDL and BPP, [m$\Omega$ $cm^2$] |
| $S_i$ | source terms, [kg $m^{-3}$ $s^{-1}$] or [J $m^{-3}$ $s^{-1}$] |
| $S_{ij}$ | deviatoric stress tensor, [-] |
| $\Delta S_{rxn}$ | entropy change, [J $mol^{-1}$ $K^{-1}$] |
| $T$ | temperature, [K] |
| $U$ | fluid velocity vector, [m $s^{-1}$] |
| $V$ | cell voltage, [V] |
| $V_i$ | diffusion volume of species *i*, [$m^{-3}$] |
| $X_i$ | mole fraction of species *i*, [-] |
| $Y_i$ | mass fraction of species *i*, [-] |

Greek symbols

| | |
|---|---|
| $\alpha_e$ | transfer coefficient, [-] |
| $\gamma_a$ | pre-constant at anode, [A $m^{-2}$] |
| $\gamma_c$ | pre-constant at cathode, [A $m^{-2}$] |
| $\delta_{ij}$ | Kronecker delta, [-] |
| $\varepsilon$ | porosity of porous medium, [-] |
| $\varepsilon_{com}$ | porosity of compressed GDL, [-] |
| $\varepsilon_{ij}^{EL}$ | elastic strain tensor, [-] |
| $\varepsilon_{ij}^{PL}$ | plastic strain tensor, [-] |
| $E$ | Young's modulus, [MPa] |
| $\eta$ | overpotential, [V] |
| $\eta_{acti,\ a}$ | anode activation overpotential, [V] |
| $\eta_{acti,\ c}$ | cathode activation overpotential, [V] |
| $\lambda$ | compression ratio, [-] |

| | |
|---|---|
| $\mu$ | dynamic viscosity, [kg $m^{-1}$ $s^{-1}$] |
| $v$ | Poisson's ratio, [-] |
| $\rho$ | gas mixture density, [kg $m^{-3}$] |
| $\rho_e$ | electric/protonic resistivity, [Ω m] |
| $\sigma$ | electric/protonic conductivity, [S $m^{-1}$] |
| $\sigma_{ij}$ | stress tensor, [-] |
| $\tau$ | tortuosity of porous medium, [-] |
| $\varphi$ | electric potential, [V] |
| $\omega$ | water content in membrane, [$H_2O/SO_3H$] |

Subscripts

| | |
|---|---|
| *0* | standard or ideal conditions |
| *a* | anode |
| *acti* | activation |
| *A* | gas species *A* |
| *AB* | binary species *A* and *B* |
| *Assembly* | assembly condition |
| *B* | gas species *B* |
| *c* | cathode |
| *cell* | PEM fuel cell |
| *com* | compressed |
| *contact* | contacted interface |
| *C* | gas species *C* |
| *e* | electron/electric |
| *GDL/BPP* | interface between GDL and BPP |
| *i* | gas species *i* |
| *initial* | initial condition |
| *Knudsen* | Knudsen diffusion |
| *m* | for source term in mass transfer equation |
| *max* | maximum value |

| | |
|---|---|
| *mem* | membrane |
| *min* | minimum value |
| *n* | for source term in momentum equation |
| *Nernst* | Nernst |
| *p* | constant pressure |
| *pore* | pores |
| *rxn* | reaction status |
| *solid* | solid matrix of porous medium |
| *Stefan-Maxwell* | Stefan-Maxwell diffusion |
| *T* | temperature |

Superscripts

| | |
|---|---|
| *a* | reaction order for oxygen |
| *b* | reaction order for water |
| *EL* | elastic |
| *m* | reaction order for hydrogen |
| *PL* | plastic |

Abbreviations

| | |
|---|---|
| 2D | two-dimensional |
| 3D | three-dimensional |
| CFD | computational fluid dynamics |
| BC | boundary condition |
| BPP | bi-polar plates |
| CL | catalyst layers |
| FEM | finite element method |
| FVM | finite volume method |
| GDL | gas diffusion layers |
| HOR | hydrogen oxidation reaction |
| I-V | current density vs. potential |

| | |
|---|---|
| LBM | Lattice Boltzmann Method |
| MEA | membrane electrode assembly |
| MPL | micro-porous layer |
| OpenFOAM | Open Source Field Operation and Manipulation |
| ORR | oxygen reduction reaction |
| PEM | proton exchange membrane |
| PISO | pressure-implicit split-operator |
| PTFE | polytetrafluoroethylene |
| TPB | triple-phase boundary |

# Content

# 1. Introduction

The fossil fuels, e.g., coal, oil, and natural gas, are the major energy sources, but are considered as dangerous for the survival of the environment. At the same time, the fear is often expressed that the rapid usage resulting in disappearance of fossil fuels will terminate the progress of increasing demands of more food, better housing and improved products in the fields of transportation and communication. With the increasing interest of clean and sustainable energy to overcome the fears, fuel cells are attracting more and more attention from research, industry and government. Investment in this technology is driven by this alternative energy conversion device with a potential of replacing fossil-fueled-engines.

One of the most promising fuel cells is the proton exchange membrane (PEM) fuel cell, owing to its advantages of efficient energy conversion, high power density and environmental friendliness. The first commercial use of a typical PEM fuel cell was in 1960's Gemini space program by NASA [1]. During the past two decades, the performance of PEM fuel cells has been improved significantly resulting from efforts in different aspects, e.g., implementation of innovative materials [2] and optimized design [3] based on experiments and simulations [4]. However, barriers for the widely use of PEM fuel cells are still present. Cost, durability and performance are supposed as the main challenges or bottlenecks in the development and commercialization of PEM fuel cells [5].

Assembling is one of the most important processes in manufacturing a single fuel cell into a stack to prevent leakage of reactants and reduce the contact resistances between the layers in PEM fuel cells. During the assembling process, the individual components of a fuel cell stack, namely the bi-polar plates (BPP), gas diffusion layers (GDL), catalyst layers (CL), membrane and gasket, must be clamped together using bolts. A proper torque, also called an assembly pressure, is provided on the bolts, as shown in Figure 1.1. However, the properties of the GDL and interface between GDL and BPP are strongly dependent on the assembly pressure due to the porous structure of GDL. The related parameters of the flow channels, performance of the cells will also be affected by this pressure. If the GDL is compressed too much, it will collapse and lose its mainly permeable function for gases [6]. Meanwhile, the cell performance may improve because of the reduced interfacial resistance. On the other hand, the polarization curve may exhibits severe mass transport limitations. Therefore,

investigation of the effect of assembly pressure on the GDL deformation, properties change and transport phenomenon is essential to provide appropriate strategies to improve the cell performance.

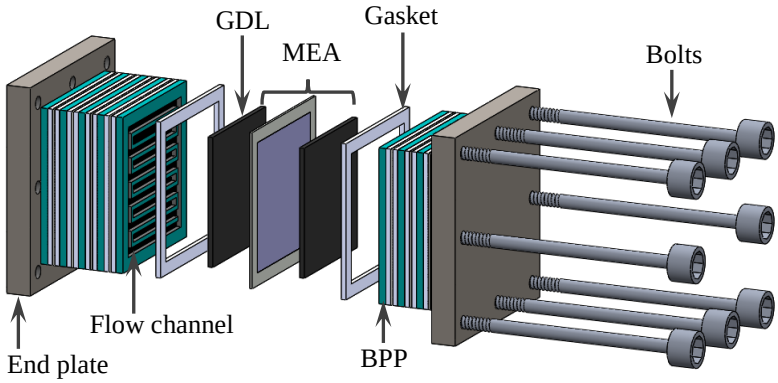


**Figure 1.1 Schematic of a PEM fuel cell stack.**

## 1.1 Research objectives

The main objective of this thesis is to study the effects of assembly pressure on the mechanical deformation of GDL and the transport phenomena of mass, electrons and the cell performance. More detailed objectives can be outlined as,

- To establish a mechanical model for predicting the GDL deformation and porous properties change when the cell operates under an assembly pressure.
- To develop electric model implemented in OpenFOAM ("Open Source Field Operation and Manipulation") for evaluating the electron transport phenomena within the deformed GDL.
- To simulate the electric contact resistance between GDL and BPP as a function of assembly pressure.
- To analyse mass transport phenomena considering the deformed GDL and physical properties using a PEM fuel cell model implemented in OpenFOAM.
- To optimize assembly pressure by cell performance based on the constant electric resistance and electron transfer dependent resistance, respectively.

## 1.2 Methodology

The mechanical simulations carried out in this work were performed in the commercial ANSYS software to predict the GDL deformation under various assembly pressures. The porous properties and the GDL thickness were obtained by the mechanical module and its related correlations. Subsequently the deformed GDLs with non-homogeneous thickness were implemented as input geometries to both the newly developed electron transfer model and PEM fuel cell model in the OpenFOAM software.

The electric resistance of a cell and the related electron transport phenomena were considered in the electron transfer model. The through-plane electric resistance of a cell under various assembly pressures was evaluated. The electric contact resistance (in the in-plane direction), which was one part of the overall electric resistances of a cell, was obtained by correlations relating GDL and BPP at different assembly pressure.

In addition to the deformed geometry of the GDL, a non-linear porosity was also implemented into the PEM fuel cell model to investigate the mass transport phenomena and cell performance. Both a constant electric resistance and the predicted electric resistances of a cell under various assembly pressures were applied to the PEM fuel cell model to optimize the cell performance and mass transport phenomena.

## 1.3 Thesis outline

The thesis is divided into seven chapters. The introduction is presented in Chapter 1 and includes the background, objectives, methodology and outline. Chapter 2 gives the basic knowledge about working principles of a PEM fuel cell, the porous properties of the GDL, and it reviews the up-to-date literatures in aspects of GDL deformation, mass transfer resistance, electric resistance in the bulk GDL, electric contact resistance and optimizing cell performance when a cell is operating under assembly pressure. Chapter 3 describes the equations, model domain, input parameters and validation details of the applied models. Chapter 4 summarizes the main results and provides a discussion considering the effects of porosity, GDL deformation and electric properties caused by assembly pressures. In addition, the validation results of the models are presented in this Chapter as well. Chapter 5 presents the main conclusions, followed by some ideas for future work in Chapter 6. Finally, the cited references are listed in Chapter 7.

# 2. Literature Review

The research focusing on PEM fuel cells has achieved considerable progress in the past two decades. The latest achievements have greatly to better understanding of the transport contributed phenomena and cell performance. The purpose of this chapter is to review the working principle of PEM fuel cells and present on up-to-date literature survey related to the specific topics studied in this thesis.

## 2.1 Working principle of PEM fuel cells

Typically a PEM fuel cell operates below 100 ºC (usually 80 ºC for low temperature PEM fuel cells and approximately 120 ºC for high temperature PEM fuel cells). A two-dimensional (2D) sketch of the cell including its reactions and transport processes is shown in Figure 2.1.

In a PEM fuel cell, hydrogen gas mixed with water stream is supplied at the anode side and air/water stream at the cathode side. The hydrogen is oxidized in the anode catalyst layer (CL) to release electrons and produce protons. Then electrons flow through the anode GDL, bi-polar plate (BPP), external circuit and further to the cathode CL (see Figure 2.1). The produced protons are transported through the solid electrolyte, i.e., membrane, to the cathode side. Oxygen is reduced in the cathode CLs, and then combined with the electrons and protons to produce water and heat. The reactions at the anode triple-phase boundary (TPB) and cathode TPB for a PEM fuel cell are, respectively, given by,

$$H_2 \rightarrow 2H^+ + 2e^- \tag{2.1}$$

$$\frac{1}{2}O_2 + 2H^+ + 2e^- \rightarrow H_2O \tag{2.2}$$

The electrochemical reactions in the cathode have always attracted more attention than the ones in the anode. The oxygen reduction reaction (ORR) in the cathode of a PEM fuel cell is regarded as the dominant limiting factor due to its several times slower reaction kinetics, compared to the hydrogen oxidation reaction (HOR) in the anode [7]. In addition, the formation and management of water at the cathode is another issue especially at high operating loads.

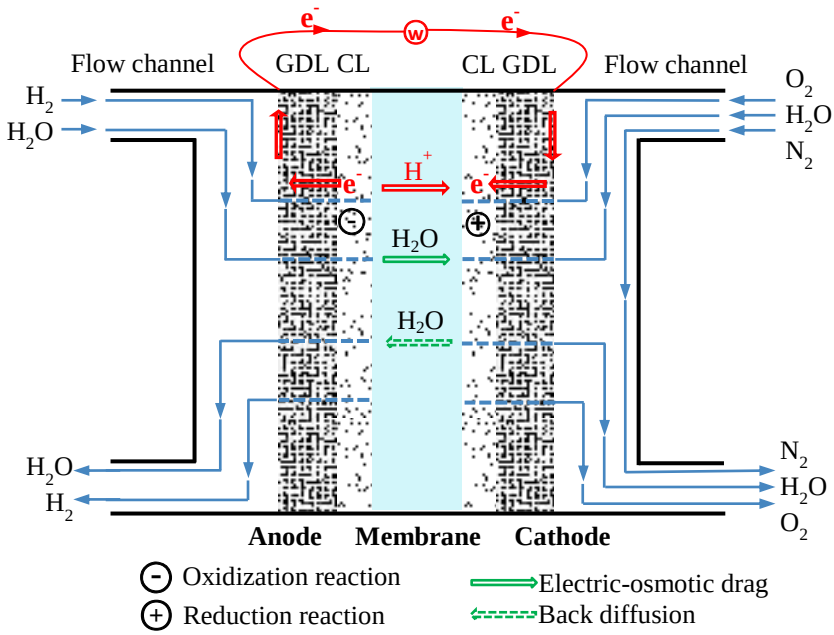


**Figure 2.1 Schematic reactions and transport processes in a PEM fuel cell.**

During the operating of a PEM fuel cell, the transport processes of water, heat, gases and charges (protons and electrons) occur simultaneously inside the porous media or the solid components. Taking the cathode of a PEM fuel cell as an example, the transport phenomena in the porous media are shown in Figure 2.2. The processes involve (a) transport of the reactants to the reaction sites; (b) transport of protons from membrane to the reaction sites; (c) conduction of electrons between the current collectors and the reaction sites; (d) transport of heat produced by the exothermic reaction; and (e) transport and probably phase change between water vapor and liquid water with condensation/evaporation [5].

The assembled component consisting of the two layers, GDL and CL, and a sandwiched membrane is named membrane electrode assembly (MEA). Some efforts have been already paid on the selection of functional materials to improve the MEA performance. For example, in order to avoid water flooding at high current densities, the GDLs are widely treated with polytetrafluoroethylene (PTFE) to impart hydrophobicity, which can force water droplets agglomerated at the surface of the

GDL close to the gas channel [4]. The interest of placing a micro-porous layer (MPL), approximately 30~40 μm, between the conventional GDL and CL is another strategy to improve the GDLs liquid water management capability, protect the membrane from punching fibers and also be beneficial in terms of electric and thermal contact of the CLs [8]. Novel nano-materials, such as nanotubes [9], ordered mesoporous carbon [10] and graphene [11], are applied in CLs to improve the ORR/HOR rates. Platinum is a noble and expensive metal, however, it shows the best ORR reaction rate. Nafion is regarded as the best element for the membrane so far [6]. However, the protonic conductivity of the Nafion membrane is a water content dependent parameter which is heavily affected by the temperature distribution.

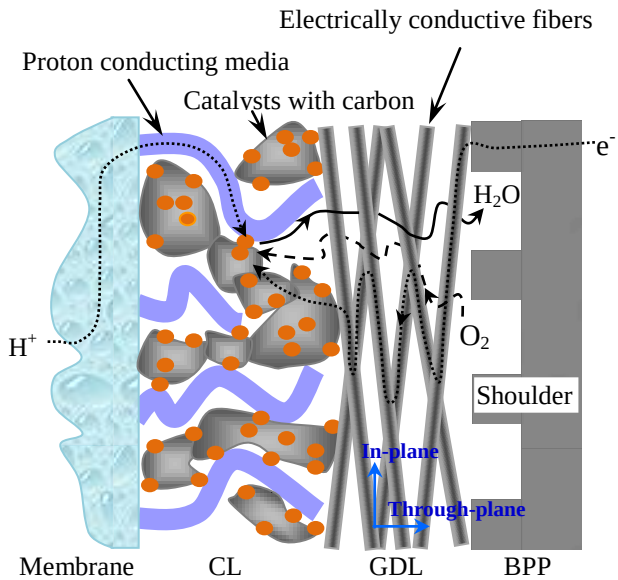


**Figure 2.2 Transport processes in PEM fuel cell cathode.**

## 2.2 Electrode porous features

Porous feature is one of the main typical properties in PEM fuel cell electrodes. The GDL, CL and membrane compose porous layers. The porous material of those layers consists of pores and a solid matrix. The void space of pores in PEM fuel cells ensures the transport of species (gases and possible liquid water) through the functional components. The solid matrix of the porous layers is for the transport of electrons/protons and also for heat removal.

Ideally, the GDL serves to provide a uniform distribution of the reactants to the CL for the electrochemical reaction, and to ensure proper and rapid transport of product electrons to the external circuit as well as removal of product water and excess heat from the CLs [12]. Despite its a function to transport media, a GDL acts mechanically support for the membrane and CL, further grouped into the membrane electrode assembly (MEA).

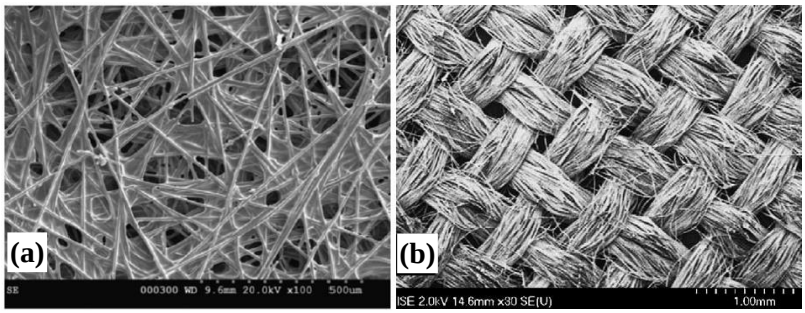


**Figure 2.3 TEM images of GDL treated with PTFE, (a) carbon fiber [13] and (b) carbon cloth [14].**

The GDL is made of either carbon fiber paper or non-woven (also namely carbon cloth), as shown, respectively, in Figure 2.3a and Figure 2.3b. Both the so types of GDLs have heterogeneous structure with pore sizes ranging from a few microns to tens of microns. Table 2.1 lists the physical properties of the GDL (for carbon fiber paper as an example) and CL applied in PEM fuel cells. Typically the fiber GDL is about 0.2~0.5 mm in thickness [14] with pores ranging from 20 to 50 μm [15] and the filament diameter of carbon fiber is around 5~15 μm [14]. The CLs, composed of platinum based carbon agglomerates, show much smaller pore size than the GDL. This apparent difference in pore size of the fiber GDL and CL is another reason of applying an MPL between these functional layers.

**Table 2.1 Physical properties of carbon fiber GDL and CL applied in PEM fuel cells.**

| Parameters | GDL | CL |
|---|---|---|
| Thickness (mm) | 0.2~0.5 [14] | ~ 0.01 [14] |
| Pore size (μm) | 20~50 [15] | 0.04~1.0 [16] |
| Fiber diameter (μm) | 5~15 [14] | --- |
| Porosity | 0.7~0.8 [15] | 0.4~0.6 [17] |

To avoid "flooding" within the GDLs at higher current densities, the standard GDLs produced today come with hydrophobic PTFE treatment to modify the wetting characteristics (see Figure 2.3a). PTFE treatment in the GDL aims to enhance gas transport and water transport when a PEM fuel cell operates under flooding conditions.

The use of PTFE, however, reduces the electric conductivity of the GDL [18]. Proper PTFE content helps effectively to remove the liquid water from the GDL to the flow channels [19]. An additional thin MPL of carbon black mixed with PTFE is usually applied to provide better electrical contact and mechanical compatibility between the GDL and CL, and to reduce the cathode GDL flooding as well [12].

## 2.3 Assembly effects on PEM fuel cells

### 2.3.1 GDL deformation

As mentioned in the first Chapter, and illustrated in Figure 1.1, the components of the BPP, GDL, CL, membrane and gasket are usually assembled using bolts to ensure the gas sealing security and reduce the contact resistance. However, the assembly pressure will lead to a deformation because the GDL fibers exhibit very high tensile and compressive strength [14]. Consequently, the GDL below the shoulders becomes thinner and intrudes into the channel center. This phenomenon before and after deformation was observed in an experiment, as shown in Figure 2.4 [20]. A similar phenomenon of the GDL deformation for different GDL materials was also observed by Kleemann et al. [8] and illustrated in [21, 22].

The non-homogeneous deformation of the GDL is caused by the channel/shoulder structure operation occurs under assembly pressure. The GDL below the shoulders becomes thinner because the compression effect is stronger in this area than at the areas below the channel. The decreased thickness of the GDL below the shoulders was regarded as a loss of porosity [23]. Meanwhile, the cross-sectional area of the gas flow channel is reduced due to the GDL intrusion in the channel center. With an assembly pressure, the local stress concentration near the shoulder edge was numerically observed, and this local stress concentration resulted in GDL deformation [24]. Increasing assembly pressure usually increases the deformation of a specific GDL. The GDL deformation depends not only on the magnitudes of the assembly pressure [20] but also the temperature [25], initial thickness [26] and the types of the GDL [8]. An experimental study performed by Nitta et al. [26], concluded that the GDL intrusion into the channel is dependent on the initial thickness of the GDL but not the width of the channel. The fiber GDL below the channel center mostly remains at its initial thickness (see Figure 2.4), however, the compressed thickness does not reach its initial thickness for the non-woven GDL [8].

The GDL deformation has been numerically predicted by Taymaz et al. [27] in ANSYS and by Bograchev et al. [28, 29] in ABAQUS with a two-dimensional (2D) model. The numerical modeling is regarded as an efficient method to study the phenomenon of the GDL deformation due to the rapidly development of commercial softwares in the past decade. A limited number of modeling studies were presented taking into account these deformation phenomena. In the study by Bograchev et al.

[28], the evolution of the residual deformation for various bolt torques was presented. However, the deformed GDL was not further implemented into a three-dimensional (3D) cell to evaluate mass transport and fuel cell performance.

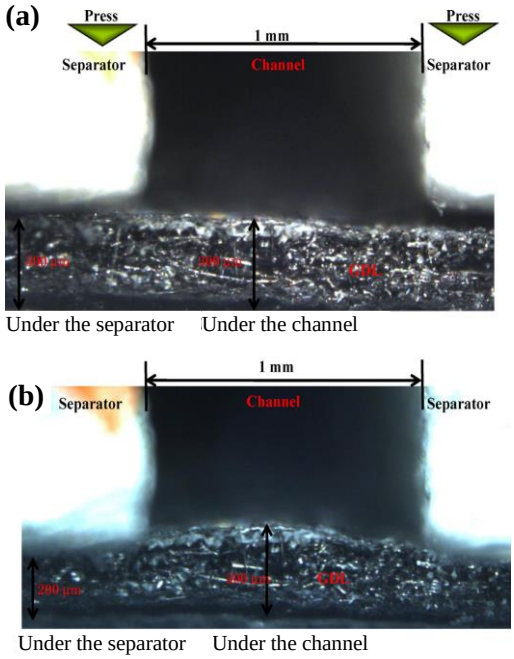


**Figure 2.4 Cross-sectional view of the GDL and flow field plate (a) before and (b) after deformation with an assembly pressure [20].**

## 2.3.2 Mass transfer resistance

Gas species transport in the porous material is by gas convection and diffusion in PEM fuel cells. An externally supplied pressure difference creates the convective flow. The diffusion is drived by concentration gradients of reactants consumed and products generated in the electrochemical reactions. During the diffusion transport process, the mass transfer resistance is an important physical parameter on limiting the access/removal of the reactant/product to/from the porous media of the GDL and CL in PEM fuel cells as operation occurs at an assembly pressure.

The importance of the effects of assembly pressure on the mass transport in GDLs has been identified by experimental studies. The physical compression of the GDL directly decreases its diffusion coefficient because the assembling pressure decreases the porosity of the GDL which leads to a higher mass transfer resistance [30]. Due to the non-homogeneous deformation of the GDL, a non-linear gas permeability of the GDL

in the in-plane direction was experimentally observed in the case of a uniform pressure maintained on the BPP [26]. It was suggested that the non-linear gas permeability is caused by the non-linear porosity distribution and the decreased pore diameters because of the compression. This indicates that the clamping force during the assembling process of the PEM fuel cell will cause a non-homogeneous porosity distribution in the in-plane direction of the GDL. This fact agrees fairly well with the conclusion obtained by Zhou et al. [31]. A more comprehensive experiment was designed to simultaneously measure the thickness, gas permeability, and porosity of a GDL under compression by Chang et al. [32]. These experiments observed that the assembly pressure magnitude has significant effects on the non-homogeneous deformation and also the mass transfer resistance in GDLs.

The non-linear porosity distribution in the GDL is another important feature due to the GDL deformation by an assembly pressure. Salaberri et al. [33] studied a non-linear porosity distribution along the in-plane direction with the influence of the shoulder width, GDL thickness and the fillet radius of the shoulder under various assembly pressures by a non-linear orthotropic model. In that study they demonstrated that a varying and non-linear porosity is an important parameter. A remarkable numerical work was presented by Shi et al. [34], who investigated water management under non-homogeneous compression coinciding with the calculated non-linear porosity. That study reported that the presence of liquid water could result in a non-uniform distribution of the porosity and permeability in the GDL.

Due to limitations of in-situ diagnostic methods for mass transfer in PEM fuel cells due to the small scale of the mass transport processes, computational methods are currently suggested as powerful tools to investigate such phenomena. The modeling of the mass transfer phenomena consists of predicting the distribution of reactants, products, and inert species. To numerically predict the GDL deformation under the assembly conditions and further the effects on mass transfer resistance, Zhou et al. [23, 31] and Taymaz et al. [27] developed similar models to study the GDL behavior for different assembly pressures. They believed that the deformed GDL caused by the assembly pressure reduces the diffusion path for the mass transport especially at high current densities.

A large number of publications in investigating the computational mass transport phenomena without assembling effects have appeared in the past decade [35-39]. Those numerical studies assumed for simplicity a uniformly distributed porosity and homogeneous material for the GDL [40, 41]. The real GDL compression distribution for different assembly pressures was not incorporated. However, the physical properties of the GDL caused by the assembly pressure are non-homogeneous in the cross-sectional view [26]. On the other hand, the assembly pressure has a significant effect on the fuel cell performance [31, 42]. Neglecting the assembly effects, however, cannot reflect the real condition of fuel cell stacks. It is currently believed that a more realistic model for PEM fuel cells is able to take into account both the non-homogeneous distribution of the properties of the GDL and the deformed GDL due to uneven compression during assembling processes [43].

The non-linear distribution of porosity is regarded as a direct reflection of the non-homogeneous deformation of the GDL. Only a couple of modeling studies has been presented accounting for the GDL deformation to investigate the cell performance, but did not consider the non-linear distribution of porosity in the GDL [23, 27, 44]. Some results were obtained under limited conditions, e.g., homogeneous compression and 2D modeling by the Lattice Boltzmann Method (LBM) [30], non-uniform porosity of the GDL without GDL deformation [43]. This thesis attempts to investigate the overall effects of the assembly pressure on GDLs on the non-linear porosity distribution and deformation during operation at assembling conditions.

### 2.3.3 Electric resistance in bulk GDLs

One of the most important properties of a PEM fuel cell is the electric resistance. The bulk resistance should be distinguished from the total resistance, the latter including the bulk and interfacial contact resistance between the layers [6].

In determining the performance, the cell potential at a certain current density is important, as it decreases from the equilibrium value because of the irreversible potential losses (the so-called overpotentials) caused by the activation, concentration and ohmic resistances. Numerical results have demonstrated that the overpotential values decrease in the order of $\eta_{act,c} > \eta_{ohm}^{pro} > \eta_{ohm}^{el} > \eta_{act,a} > \eta_{conc,c} > \eta_{conc,a}$ (where act, ohm and conc, el, pro, c and a denote activation loss, ohmic loss, concentration loss, electrons, protons, cathodic and anodic, respectively) [40]. Many studies have explored the reduction of concentration and activation losses by optimizing the design [45], manufacturing [46] and materials synthesis [47]. The ohmic resistance of the layers, however, seems still poorly studied except some investigations on the membrane [48].

The previous studies have concentrated on the investigation of the ohmic resistances, including the resistance for the electron transfer through electrodes (in both in-plane and through-plane directions) [49, 50] and the one for proton flow through the membrane (water content dependent parameter) [51], as illustrated in Figure 2.2. A comparison of the electric resistances below the shoulders and gas channels has shown that the total electric resistance below the channels is much higher than that below the shoulders due to the channel/shoulder structure [49, 50]. Because of these reasons, the fuel cell operation strategies become more complex and should be introduced adjustment when considering the assembly pressure because the ohmic loss is sensitive to the electric/ionic conductivity in the functional layers [6].

The ohmic resistance during the assembly conditions is another important property in choosing the assembly pressure and achieving acceptable cell performance. A consequence of the GDL compression due to the assembly pressure is the increase of electric conductivity (the reciprocal of its electric resistivity) of the GDL. It has been observed that a high compression increases the GDL conductivity [26]. Escribano et al. [21] studied the effects of the GDL deformation on the through-plane electric

resistance. A consequence of the assembly conditions is that the electric resistance of the GDL is dropped due to the loss of the pores below the shoulders [27]. In addition, a numerical and experimental study was conducted by Tanaka et al. [52] and a significant difference of the electric resistance in the through-plane direction was observed when the cell was operated with various assembly pressures. A relationship between electric resistance and GDL was experimentally formulated by Hamour et al. [53] when the cell was operated at assembly conditions. Taymaz et al. [27] suggested that 0.5 MPa and 1 MPa pressure values are optimum assembly pressures when a prescribed electric property of the fuel cell components is applied. Although nowadays knowledge exists on the electric resistance of the GDL, the behavior with an applied assembly pressure is poorly known. One of the aims of this thesis is to explore a prediction method for the electric resistance of the deformed GDL in the through-plane direction.

### 2.3.4 Electric contact resistance

The channel/shoulder structure of the BPP is connected with the fibrous materials [54, 55] of the GDL as shown in Figure 2.5a. The electric contact resistance between GDL and BPP is considered as an electric circuit in a parallel connection as illustrated in Figure 2.5b. According to this assumption, the entire electric resistance in both GDL and BPP is set up by the bulk resistance of $R_G$ and $R_B$ for GDL and BPP, respectively, and the interfacial contact resistance $R_{G/B}$ between the double layers.

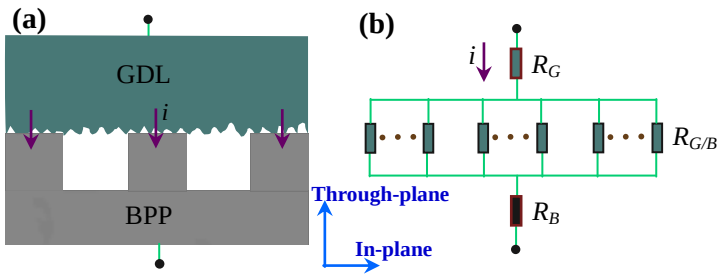


**Figure 2.5 Schematic of the contact electric circuit in a parallel connection for the contact interface between the GDL and BPP.**

The contact resistance for electrons occurring at the interface between the GDL and BPP contributes to a significant part of the ohmic resistance [56]. The electric contact resistance was regarded as a dominating factor causing a potential loss, as revealed in the study by Chang et al. [32]. This contact resistance is sometimes regarded as more important than the bulk resistance, especially at the assembly conditions. Therefore an effective prediction of the contact resistance between the GDL and BPP is fundamental to investigate the effects of the assembly process and to optimize the fuel cell performance [57].

Some theoretical models have been developed to predict the electric contact resistance between the GDL and BPP, such as the Greenwood-Williamson model [58], the Cooper-Mikic-Yovanovitch model [59] and the Majumdar-Tien fractal model [60]. A limitation of those models is their geometric dependent prediction for the electric contact resistance. The electric contact resistance generally depends not only on material properties of the contact layers [6], surface treatment [55] and operating conditions [56], but also on the assembly pressure [52]. An assembly pressure will accelerate the electron flows through the interface. It was found that a high compression decreases the contact resistances [26]. A relationship of the assembly pressure and the contact resistance between the GDL and BPP was formulated in the literature [56]. An optimal assembly pressure was obtained by employing this relationship for the contact resistance [23]. Nitta et al. [25] experimentally analyzed that the assembly pressure magnitude has significant effects on the cell performance.

### 2.3.5 Optimizing cell performance

Understanding the transport processes and phenomena is crucial for optimizing the design and performance of PEM fuel cells. Despite the efforts in materials synthetizing, numerical simulation employing a suitable model is becoming widely used in this kind of sustainable energy applications promoted by the rapid development of computer technology. However, the cell performance is related to many involved parameters associated with the materials, geometry and operation conditions. As demonstrated in the topics described above, the GDL deformation, mass transfer resistance, electric bulk resistance of GDL and electric contact resistance play important roles in determining the PEM fuel cell performance as assembly pressures are considered.

Several investigations have concentrated on the optimal PEM fuel cell performance considering the assembly pressure [31, 61, 62]. An optimum cell performance was obtained in the cell tested by Lee et al. [61] for a range of torques on the bolts in a single cell. The results showed that a higher torque results in a worse cell performance. Ge et al. [62] identified that an optimal compression ratio exists for which the cell performance is maximized, i.e., the I-V curve first increases with less compression, then declines with more compression after a certain point. A certain assembly pressure operated on a PEM fuel cell is necessary because gas leakage should be avoided as it might result in poor cell performance and dangerous situation. However, over-compression will decrease the mass transport abilities of the GDL and result in a reduced cell performance [63]. On the other hand, in the interest of obtaining high electric conductivity of the bulk material and the one between layers, a higher assembly pressure is favorable. However, the cell performance will decrease with increasing assembly pressure if the variation of the interfacial ohmic resistance is neglected, but there is an optimal pressure found in the work by Zhou et al. [64], if the interfacial ohmic resistance is considered. Therefore, a balance between the GDL

deformation, electric contact resistance, through-plane electric resistance and mass transfer is necessary for an optimal assembly pressure for a single cell or a stack.

An assembly pressure is favorable to obtain a better cell performance, but limited by the increasing mass transfer resistance. Generally speaking, increasing assembly pressure increases the deformation of the GDL resulting in lower porosity and higher mass transfer resistance. However, lower electric resistance at the interface and in the bulk materials for electrons transfer occur. The contact resistance for electrons at the interface between BPP and GDL is regarded as significant because it is obviously a strong function of the assembly pressure. High assembly pressure results in a tight connection between the two layers. From a practical point of view, in addition to the fundamental requirement of choosing low electric/ionic resistance for each component, the strategies of ensuring a lower electric resistance for a cell stack is another attractive topic.

# 3. Numerical Methodology

The rapid development of mathematical and computational methods provides efficient means to simulate the mechanical behavior, mass transport phenomena and PEM fuel cell performance. Before solving the specific problem, some fundamental governing equations, boundary conditions (BCs) and validations are required. In this Chapter, the equations, modeling domain, input parameters and validations applied in the mechanical model (in **Papers III** and **IV**), electric contact resistance model (only in **Paper IV**), electric resistance model (in **Papers IV** and **V**) and the PEM fuel cell model (in **Papers II**, **III** and **IV**) are presented in detail.

## 3.1 PEM fuel cell model

Multiscale transport processes are involved in the 3D PEM fuel cell model as it includes all components within a complex system. The governing equations to be solved consist of a series of equations for conservation of mass, momentum, species transport and energy with some necessary assumptions. The electrochemical reactions are coupled with the parameters in the partial differential equations. The physical parameters of the porous GDLs are obtained from the results under the assembly pressure in **Papers II**, **III** and **IV**.

### 3.1.1 Model assumptions

In order to properly solve the equations in the selected domain of the PEM fuel cell model, it is necessary to make a number of assumptions. The assumptions made in this thesis are as follows:

- The fuel cell operates at steady-state.
- The gas mixtures involved are regarded as incompressible and ideal.
- Reynolds number in the gas channel is less than 100, i.e., laminar flow prevails.

- The water is always in gaseous state without any phase change.
- Electrochemical reactions occur at the interface between the membrane and the CLs.
- Membrane is considered as impermeable to the gases.
- The GDL has no change in the geometry and pore sizes under various compression ratios (only in **Paper II**).
- The porosity does not change in the GDL below the channel but changes below the shoulders due to a specific compression ratio (only in **Paper II**).
- Transfer of electrons and protons is not considered (only in **Papers II** and **III**).

Most of these assumptions are similar to those in previous modeling studies [40, 65]. Under those assumptions presented above, the partial differential equations and electrochemical reactions are solved in the PEM fuel cell model and formulated as below.

### 3.1.2 Conservation of mass

The mass conservation for the gas mixture flow with a varying density can be expressed as [22],

$$\nabla \cdot (\rho U) = S_m \tag{3.1}$$

where $\rho$ is the gas mixture density, $U$ is the fluid velocity vector and the source term $S_m$ is related to the electrochemical reactions appearing at the reaction sites. The varying gas mixture density $\rho$ is expressed as,

$$\rho = \frac{P}{RT \sum_{i=1}^{N} (Y_i / M_i)} \tag{3.2}$$

where $Y_i$ and $M_i$ are the mass fraction and molar weight of species $i$, respectively, $T$ the temperature, $P$ the gas pressure, and $R$ the ideal gas constant (8.3145 J $mol^{-1}$ $K^{-1}$). A constant mixture density is applied at the cell inlet based on fully humidified conditions, however, in the other regions a variable density is considered by Eq. (3.2).

The source term $S_m$ for mass conservation in Eq. (3.1) can be expressed by Eq. (3.3) for the cathode and by Eq. (3.4) for the anode, respectively, based on the electrons released in the stoichiometric reactions of the fuel cell [66],

$$S_{m,c} = -\frac{i}{4F} M_{O_2} + \frac{i}{2F} M_{H_2O} \tag{3.3}$$

$$S_{m,a} = -\frac{i}{2F} M_{H_2} \tag{3.4}$$

where $i$ is the local current density, $M$ the molar weight of the involved gas species and $F$ the Faraday's constant (96485 C $mol^{-1}$). The plus sign (+) is applied for the product generation and the negative sign (-) for the reactant consumption.

### 3.1.3 Conservation of momentum

Navier-Stokes equations, known as the momentum equations, are the important equations in computational fluid dynamics (CFD). The velocity and pressure distributions in this model are solved by employing the pressure-implicit split-operator (PISO) algorithm, which is based on a higher degree of the approximate relation between the corrections for pressure and velocity. The PISO method has been widely used for solving pressure-velocity coupling because it can solve both steady state and transient problems [67].

The Navier-Stokes equations applied in the gas flow regions, i.e., gas flow channel, GDL and CL, can be expressed as [68],

$$\nabla \cdot (\rho UU) = -\nabla P + \nabla \cdot \mu \nabla U + S_n \tag{3.5}$$

where $U$ is the fluid velocity vector, $\mu$ is the dynamic viscosity of the fluid, and $S_n$ stands for the source term.

The dynamic viscosity of the fluid is treated as a weighted sum of all the involved gas species [69],

$$\mu = \sum_{i=1}^{N} \mu_i Y_i \tag{3.6}$$

where the localized dynamic viscosity of species $i$ for the specific gas, $\mu_i$, is a function of temperature $T$ and represented by a six-order polynomial [69],

$$\mu_i = \sum_{n=0}^{6} a_n \left( \frac{T}{1000} \right)^n \tag{3.7}$$

where the coefficients $a_n$ are unique for every species $i$ and can be found in the literature [69].

To consider the effect of the porous structures of the GDL and CL, extra pressure losses occur and the source term $S_n$ in Eq. (3.5) will be set non-zero in the porous layers. Equation (3.8) is applied in the gas flow channels, while Eq. (3.9) is used in the porous GDLs and CLs [70], respectively,

$$S_n = 0 \tag{3.8}$$

$$S_n = -\left( \mu D_n + 0.5 \rho |U| F_n \right) U \tag{3.9}$$

In Eq. (3.9), the non-linear term is not considered in this model, i.e., $F_n$ is set to zero. However, the pore diameter $d_{pore}$ and porosity $\varepsilon$ are involved in the first term of the right hand side in Eq. (3.9) for the fluid in the porous zones [71]:

$$D_n = \frac{150}{d_{pore}^2} \frac{(1-\varepsilon)^2}{\varepsilon^3} \tag{3.10}$$

where the porosity $\varepsilon$ is a physical parameter defined as the ratio between the void space and the bulk volume.

### 3.1.4 Conservation of species transport

The mass fraction is another important parameter to identify the gas composition in the mixture. The mass fraction of water, oxygen in the cathode and that of hydrogen in the anode are to be determined, respectively, by the species transport equation shown in Eq. (3.11) [72],

$$\nabla \cdot \left( \rho U Y_i \right) + \nabla \cdot J_i = 0 \tag{3.11}$$

where the mass diffusion flux $J_i$ is evaluated by the Fick's law [40], i.e.,

$$J_i = -\rho D_{i,gas} \nabla Y_i \tag{3.12}$$

where $D_{i,gas}$ is the mass diffusion coefficient of species $i$ in the gas mixture. It should be noted that the mass fractions of the inert species (nitrogen in the cathode and water in the anode) are not solved by Eq. (3.11) but they are determined from the total mass subtracted by the summation of the mass fractions of the other active species, respectively, for the anode and the cathode [73].

Due to the multi-component diffusion occurring in the cathode side, i.e., oxygen, water and nitrogen are involved, the Stefan-Maxwell model is used to evaluate the individual diffusion coefficients in the gas mixture, as shown in Eq. (3.13) [70].

$$D_{Stefan-Maxwell} = D_{A,gas} = \frac{1 - X_A}{X_B / D_{AB} + X_c / D_{AC} + \ldots} \tag{3.13}$$

where $D_{A,gas}$ is the diffusion coefficient of the species $A$ in the mixture, $X_i$ is the molar fraction of the specie $i$, $D_{i,j}$ is the diffusion coefficient based on the binary diffusion model of species $i$ and $j$. In the anode of the PEM fuel cells, only two species are present, and the diffusion coefficients of hydrogen and water are directly evaluated by the binary diffusion model. The binary diffusion coefficient and the Knudsen diffusion coefficient are described by Eq. (3.14) and Eq. (3.15), respectively [65],

$$D_{AB} = \frac{10^{-7} T^{1.75} \sqrt{1/M_A + 1/M_B}}{P_{tot}\left(V_A^{1/3} + V_B^{1/3}\right)^2} \tag{3.14}$$

$$D_{Knudsen} = \frac{d_{pore}}{3} \sqrt{\frac{8RT}{\pi M}} \tag{3.15}$$

where $V$ is the diffusion volume, $P_{tot}$ is the total pressure of gases $A$ and $B$, $d_{pore}$ the mean pore diameter of the porous medium. To account for the effects from both the small scale and porous features in the GDL and CL, the effective diffusion coefficient of the species $i$ for the gas mixture in the porous layers can be evaluated as in Eq. (3.16) [74],

$$D_{i,gas} = \frac{\varepsilon}{\tau^2 \left(1/D_{Stefan-Maxwell} + 1/D_{Knudsen}\right)} \tag{3.16}$$

where $\tau$ is the tortuosity, similar to porosity, describing the porous properties of the porous structure. The porosity and tortuosity will be evaluated in details in Section 3.1.7.

### 3.1.5 Conservation of energy

The temperature variation inside the PEM fuel cell has significant effects on the electrochemical reaction, inlet humidification conditions, protonic conductivity of the membrane and water management. The conservation of energy is evaluated in the entire PEM fuel cell domain by the thermal energy equation [70],

$$\nabla \cdot \left(\rho U C_p T\right) = \nabla \cdot k \nabla T + S_T \tag{3.17}$$

where $S_T$ is the volumetric heat source term, $C_p$ the specific heat at constant pressure and $k$ the effective thermal conductivity corrected by the porosities of local porous materials,

$$k = k_s\left(1-\varepsilon\right) + k_g \varepsilon \tag{3.18}$$

where the $k_s$ and $k_g$ are the thermal conductivity of solid materials and gases, in the porous regions, respectively.

The source term $S_T$ for the energy conservation equation is composed of the enthalpy change of the electrochemical reactions and the ohmic heating caused by the resistance of electron/proton transfer. Thus the heat source term in the model can be written as [65, 70],

$$S_T = \Delta H_e \frac{i_{cell}}{F h_{cell}} - \frac{i_{cell} V}{h_{cell}} + \frac{i_{cell}^2 R_e}{h_{cell}} \tag{3.19}$$

where $\Delta H_e$ is the enthalpy change, $i_{cell}$ is the average current density of the cell, $V$ is the cell operating voltage, $R_e$ is the total electric resistance of the fuel cell and $h_{cell}$ is the cell height.

### 3.1.6 Electrochemistry reactions

The electrochemical reaction is very important for the performance of fuel cells. The objective of this section is to establish the relationship between the localized mole fraction of the reactants and the cell voltage, and current density. The electrochemical

reactions are assumed to occur at the interfaces between the membrane and the CL. The fuel cell current density $i_{cell}$ is then calculated based on the Ohm's Law [75],

$$i_{cell} = \frac{E_{Nernst} - V - \eta}{R_e} \tag{3.20}$$

where $\eta$ is the activation overpotential of the fuel cell. The Nernst potential $E_{Nernst}$ in Eq. (25) can be described as [75],

$$E_{Nernst} = E_0 + \frac{RT}{nF} \ln \frac{X_{O_2}^{0.5} \cdot X_{H_2}}{X_{H_2O}} \tag{3.21}$$

where $n$ is the number of electrons transported, $E_0$ the theoretical potential [76] at the standard atmosphere condition (298 K, 1 bar), which is approximately 1.23 V,

$$E_0 = -\frac{\Delta G_{rxn}}{nF} = -\frac{\left(\Delta H_{rxn} - T\Delta S_{rxn}\right)}{nF} \tag{3.22}$$

where $\Delta G_{rxn}$ is the Gibbs free energy change, $\Delta H_{rxn}$ is the enthalpy change and $\Delta S_{rxn}$ the entropy change of the reaction. The superscript in Eq. (3.21) refers to the stoichiometric coefficient of the hydrogen fuel cell reaction in PEM fuel cells. The cell activation overpotential has anodic and cathodic contributions,

$$\eta = \eta_{acti,a} + \eta_{acti,c} \tag{3.23}$$

where the activation overpotential $\eta_{acti,a}$ is for the anode and $\eta_{acti,c}$ for the cathode, respectively. Values of $\eta$ at the electrodes are obtained using a root finder based on the Ridder's method after obtaining numerical solutions of the Butler-Volmer equation [41],

$$i = i_0 \left[\exp\left(A\eta_e\right) - \exp\left(B\eta_e\right)\right] \tag{3.24}$$

where

$$A = \frac{2\alpha_e F}{RT} \tag{3.25}$$

$$B = -\frac{2(1-\alpha_e)F}{RT} \tag{3.26}$$

here $\alpha_e$ is the transfer coefficient and $\eta_e$ is the activation overpotential for any electrode. The local exchange current densities are given by [75],

$$i_{0,a} = \gamma_a \left(\frac{P_{H_2}}{P_0}\right)^m \exp\left(-\frac{E_{act,a}}{RT}\right) \tag{3.27}$$

$$i_{0,c} = \gamma_c \left(\frac{P_{O_2}}{P_0}\right)^a \left(\frac{P_{H_2O}}{P_0}\right)^b \exp\left(-\frac{E_{act,c}}{RT}\right) \tag{3.28}$$

The reaction orders, $a$, $b$, $m$, the pre-constants $\gamma_a$ and $\gamma_c$, and the activation energies $E_{\text{act},a}$ and $E_{\text{act},c}$, together with the transfer coefficients $\alpha_e$, are listed in Table 3.3.

### 3.1.7 Porous properties of compressed GDL

The GDL used in PEM fuel cells is porous and flexible, and has physical properties being affected by the deformation caused by the compression on it. Here it is assumed that the porous GDLs consist of pores and a solid bulk, and only the pores under compression leads to a change of the GDL thickness in the through-plane direction, as illustrated in Figure 3.1.

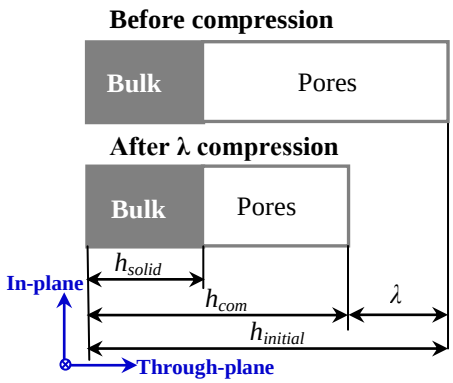


**Figure 3.1 Assumed model of porous GDL before and after deformation.**

To numerically describe the porosity, tortuosity and electric conductivity of the deformed GDL, the thickness of the compressed GDL, $h_{com}$, is expressed as,

$$h_{com} = (1-\lambda)h_{initial} \tag{3.29}$$

where $\lambda$ is the compression ratio and $h_{initial}$ is the initial thickness of the uncompressed GDL. The thickness of the solid material $h_{solid}$ is then evaluated as [22],

$$h_{solid} = h_{initial}(1-\varepsilon_0) \tag{3.30}$$

where $\varepsilon_0$ is the initial porosity of the uncompressed GDL. The model assumes that the change of the GDL thickness is only caused by the change in the volume of the pores but not of the solid part. Thus the porosity of the compressed GDL might be evaluated as a function of the GDL thickness [22],

$$\varepsilon_{com} = \varepsilon_0 \frac{h_{com} - h_{solid}}{h_{initial} - h_{solid}} \tag{3.31}$$

where $\varepsilon_{com}$ is the porosity of the compressed GDL. Another physical parameter describing the porous structures, tortuosity, is evaluated as [77],

$$\tau = 1 - 0.49\ln(\varepsilon) \tag{3.32}$$

The electric conductivity of the layers in the through-plane direction determines the electric performance in the electric resistance model. The electric conductivity $\sigma_{com}$ in the bulk of a GDL is related to the obtained thickness of the mechanical analysis by an expression given by [55],

$$\sigma_{com} = \frac{\sigma_{initial} \cdot h_{initial}}{h_{com}} \tag{3.33}$$

Then the electric conductivity of the compressed GDL can be evaluated by the compression ratio,

$$\sigma_{com} = \frac{\sigma_{initial}}{1-\lambda}, \ (\lambda \neq 1) \tag{3.34}$$

In **Paper II**, the porosity of the GDL varies with the assumed compression ratios along the in-plane direction (*y*-direction in the PEM fuel cell model). The

corresponding non-homogeneous porosity, tortuosity of the compressed GDL evaluated by equations (3.29) to (3.32) are shown in Table 3.1 as function of the assumed compression ratio. Then these porous properties of the GDL are implemented in the PEM fuel cell model for evaluation of transport coefficients.

However, in **Papers III** and **IV**, the initial thickness and compressed thickness of the deformed GDL were obtained from a mechanical analysis (in Chapter 3.2). Then the non-homogeneous porosity, tortuosity and compression ratio of the deformed GDL can be evaluated by equations (3.29) to (3.32). In addition, the electric conductivity of the deformed GDL is considered as well by equations (3.33) and (3.34) in **Paper IV**.

**Table 3.1 Compression cases and related porous properties of the GDL investigated. "$\lambda$" is the compression ratio, "$\varepsilon$" is the porosity and "$\tau$" is the tortuosity.**

| Cases | $\lambda$ (%) / $\varepsilon$(-) / $\tau$ | |
|---|---|---|
| | Shoulder areas | Channel area |
| Base | 0 / 0.8/1.109 | 0 / 0.8/1.109 |
| A1 | 10 / 0.7/1.175 | 0 / 0.8/1.109 |
| A2 | 20 / 0.6/1.250 | 0 / 0.8/1.109 |
| A3 | 30 / 0.5/1.340 | 0 / 0.8/1.109 |
| A4 | 40 / 0.4/1.449 | 0 / 0.8/1.109 |

### 3.1.8 Input parameters and validation

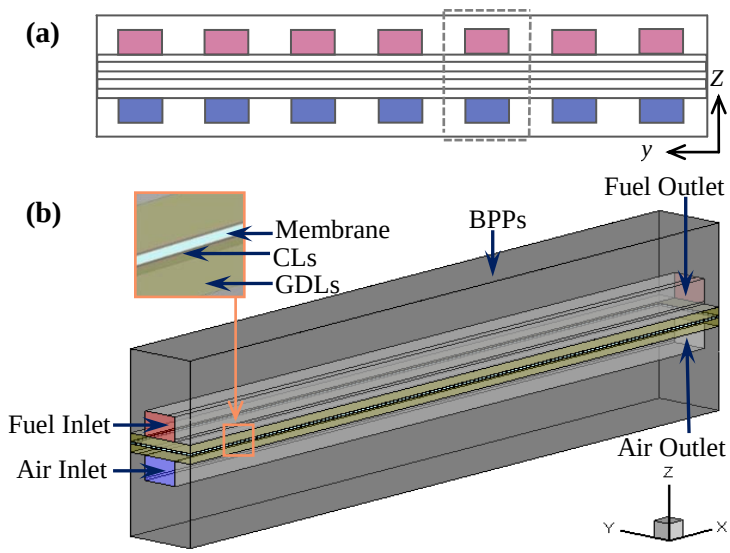


**Figure 3.2 Schematic illustration of a PEM fuel cell: (a) parallel channels in 2D and (b) computational domain in 3D.**

To decrease the computational efforts, a single channel domain was selected from the periodical channels as shown by the grey dashed zone in Figure 3.2a. This single channel domain illustrated in Figure 3.2b contains the entire components at a scale of several centimeters. As shown in Figure 3.2b, the anode (fuel side) and cathode (air side) are symmetric with respect to the membrane. Each side consists of a BPP, gas channel, GDL and CL. The initial geometry and physical parameters applied in the PEM fuel cell model are listed in Table 3.2. It must be noted that different initial dimensions were applied in **Papers II**, **III** and **IV**.

**Table 3.2 Initial geometry and physical parameters applied in PEM fuel cell model.**

| Parameters | **Paper II** | | **Papers III** and **IV** | |
|---|---|---|---|---|
| | Value and Unit | Reference | Value and Unit | Reference |
| Gas channel length | $4.0\times10^{-2}$ m | [1, 6, 14, 78, 79] | $5.0\times10^{-2}$ m | [80] |
| Gas channel width | $2.0\times10^{-3}$ m | | $1.0\times10^{-3}$ m | [80] |
| Gas channel height | $1.5\times10^{-3}$ m | | $1.0\times10^{-3}$ m | [80] |
| Land area width | $1.0\times10^{-3}$ m | | $0.5\times10^{-3}$ m | [80] |
| Thickness of BPP | $3.5\times10^{-3}$ m | | $0.3\times10^{-3}$ m | [80] |
| Thickness of GDL | $0.3\times10^{-3}$ m | | $0.3\times10^{-3}$ m | [80] |
| Thickness of CL | $2.0\times10^{-5}$ m | | $1.29\times10^{-5}$ m | [80] |
| Thickness of electrolyte | $1.0\times10^{-4}$ m | | $1.08\times10^{-4}$ m | [80] |

The PEM fuel cell was modeled at an initial temperature of 353 K, a pressure outlet condition of 3 bars and humidified gases at the inlets [80]. More details of the BCs of this model can be found in **Papers II** and **III**. A constant electric resistance was employed to predict the ohmic loss in **Papers II** and **III**. However, the electric resistance of the cell was predicted by new models (presented in Chapter 3.3 and 3.4) in **Paper IV**. The details in terms of other input properties of the related materials, kinetics and electrochemical reactions are listed in Table 3.3.

**Table 3.3 Numerical parameters and properties for PEM fuel cell model.**

| Parameters and Symbols | Value and Unit | Reference |
|---|---|---|
| Dynamic viscosity, $\mu$ | | |
| Air/water | $2.03715\times10^{-5}$ kg m$^{-1}$s$^{-1}$ | [69] |
| Hydrogen/water | $1.0502\times10^{-5}$ kg m$^{-1}$ s$^{-1}$ | [69] |
| Density, $\rho$ | | |
| Air/water | 0.98335 kg m$^{-3}$ | [81] |
| Hydrogen/water | 0.1732 kg m$^{-3}$ | [81] |
| Electrolyte | 1980 kg m$^{-3}$ | [82] |
| BPP | 2200 kg m$^{-3}$ | [6] |
| Specific heat, $C_p$ | | |
| Air/water | 1070 J kg$^{-1}$ K$^{-1}$ | [69] |

| | | |
|---|---|---|
| Hydrogen/water | 11956 J $kg^{-1}$ $K^{-1}$ | [69] |
| Electrolyte | 800 J $kg^{-1}$ $K^{-1}$ | [83] |
| GDL | 1000 J $kg^{-1}$ $K^{-1}$ | [83] |
| CL | 0.27 J $kg^{-1}$ $K^{-1}$ | [83] |
| BPP | 935 J $kg^{-1}$ $K^{-1}$ | [6] |
| Thermal conductivity, $k$ | | |
| Air/water | 0.0291965 W $m^{-1}$ $K^{-1}$ | [69] |
| Hydrogen/water | 0.173176 W $m^{-1}$ $K^{-1}$ | [69] |
| Electrolyte | 0.29 W $m^{-1}$ $K^{-1}$ | [84] |
| GDL | 1.7 W $m^{-1}$ $K^{-1}$ | [84] |
| CL | 0.27 W $m^{-1}$ $K^{-1}$ | [84] |
| BPP | 24 W $m^{-1}$ $K^{-1}$ | [6] |
| Porosity, $\varepsilon$ | | |
| CL | 0.6 | [45] |
| GDL | 0.8 | [15] |
| Pore size, $d$ | | |
| CL | $1\times10^{-6}$ m | [85] |
| GDL | $5\times10^{-5}$ m | [15] |
| Reaction order of $O_2$, $a$ | 0.5 | |
| Reaction order of $H_2O$, $b$ | -1 | |
| Reaction order of $H_2$, $m$ | 1 | |
| Pre-constant at cathode, $\gamma_c$ | $1\times10^{-5}$ A $m^{-2}$ | [86] |
| Pre-constant at anode, $\gamma_a$ | 10 A $m^{-2}$ | [6] |
| Cathode transfer coefficient, $\alpha_c$ | 0.5 | [73] |
| Anode transfer coefficient, $\alpha_a$ | 0.5 | [68] |
| Cathode activation energy, $E_{act,c}$ | $6.6\times10^{4}$ J $mol^{-1}$ | [6] |
| Anode activation energy, $E_{act,a}$ | $3.46\times10^{4}$ J $mol^{-1}$ | [6] |
| Electric resistance, $R_e$ | 150 mΩ $cm^2$ (in **Paper II**)<br>120 mΩ $cm^2$ (in **Papers III** and **IV**) | [6] |

In order to reveal the model performance and save computational resources, a grid independence study was performed. In **Paper II**, zero percent compression ratio of the PEM fuel cell without GDL deformation was applied for the grid independence study. The results listed in Table 3.4 indicate that the model with 68000 cells has the minimum grid number in terms of numerical accuracy and stability. Then the mesh size with 68000 cells and the parameters listed in Table 3.3 were selected for investigation of the effect of porosity.

However, as the GDL deformation under assembly pressures was considered in **Papers III** and **IV**, the grid number was optimized for the case with 3 MPa assembly pressure (the most difficult one to reach convergence). Here, the monitored average current densities vary with the grid number are listed in Table 3.5. The results indicate

that the case with 221493 meshes ($x \times y \times z$: 101×43×51) has the proper number of grids when considering convergence and stability. Therefore the mesh size No. 6 was selected for the further cases studies under various assembly pressures considered in **Papers III** and **IV**.

**Table 3.4 Results of mesh independence study (in Paper II).**

| No. | Total grid numbers | Average current density (A $cm^{-2}$) |
|---|---|---|
| 1 | 15600 | 0.53879 |
| 2 | 24000 | 0.53942 |
| 3 | 40800 | 0.54144 |
| 4 | 68000 | 0.54292 |
| 5 | 103200 | 0.54292 |
| 6 | 143100 | 0.54284 |

**Table 3.5 Grid independence study for the PEM fuel cell under 3 MPa assembly pressure and the monitored average current densities (in Papers III and IV).**

| No. | Grids ($x \times y \times z$) | Total grid numbers | Average current density (A $cm^{-2}$) |
|---|---|---|---|
| 1 | 51×20×26 | 26520 | 0.49033 |
| 2 | 61×26×32 | 50752 | 0.49807 |
| 3 | 71×29×37 | 76183 | 0.50109 |
| 4 | 81×33×42 | 112266 | 0.50575 |
| 5 | 91×38×46 | 159068 | 0.51101 |
| 6 | 101×43×51 | 221493 | 0.51327 |
| 7 | 111×46×57 | 291042 | 0.51326 |
| 8 | 121×50×63 | 381150 | 0.51327 |

## 3.2 Mechanical model

The mechanical model aims to study the mechanical properties versus stress or pressure. During the assembly process of PEM fuel cells in this thesis, GDLs consisting of fibers, namely TGP-H-120 carbon paper, are applied similar to [27, 57]. The GDL is composed of isotropic and compressible materials.

There are isotropic models [27] and anisotropic models [33] to predict the GDL deformation, and large variations were observed between these two models [26] in the literature. The variations appear because different magnitudes of Young's modulus ranging from MPa to GPa were applied in the in-plane direction and through-plane direction [28, 31, 33, 87]. In this thesis, the classical elastic-plastic model following the one described in [28, 29] was applied to predict the GDL deformation. The GDL

behavior is divided into an elastic region and a plastic region. The tensor of deformation is presented as the sum of these [28],

$$\varepsilon_{ij} = \varepsilon_{ij}^{EL} + \varepsilon_{ij}^{PL} \tag{3.35}$$

where $\varepsilon_{ij}^{EL}$ is the elastic strain tensor and $\varepsilon_{ij}^{PL}$ is the plastic strain tensor. The Hooke's law is employed in the elastic region, i.e., the first term of the right-hand side of Eq. (3.35) [29],

$$\sigma_{ij} = \frac{E}{(1+\nu)(1-2\nu)}\left(\nu\varepsilon_{ij}^{EL} + \sum_{k}(1-2\nu)\varepsilon_{kk}^{EL}\delta_{ij}\right) \tag{3.36}$$

where $\sigma_{ij}$ is the stress tensor, $\nu$ is the Poisson's ratio, $E$ is the Young's modulus, and $\delta_{ij}$ the Kronecker $\delta$-symbol. In the plastic region, the plastic behavior is evaluated by Prandtl-Reuss theory, and the von Mises yield function is expressed as [88],

$$f(\sigma_{ij}) = \sqrt{\frac{3}{2}S_{ij}S_{ji}} - \sigma_0 \tag{3.37}$$

where $\sigma_0$ is the yield strength and $S_{ij}$ is the component of the deviatoric stress tensor [29],

$$S_{ij} = \sigma_{ij} - \frac{1}{3}\sigma_{kk}\delta_{ij} \tag{3.38}$$

If $f(\sigma_{ij}) = 0$, the yield occurs in the GDL based on the von Mises yield criterion. For $f(\sigma_{ij}) < 0$, the material deforms elastically.

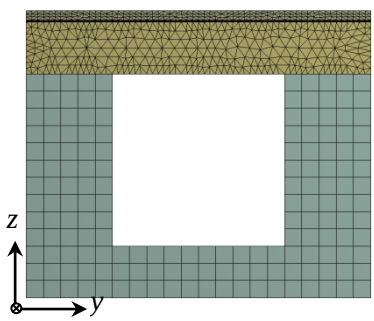


**Figure 3.3 A cross-section view of a mechanical model before deformation.**

In the mechanical model, the GDL deformation was predicted in the ANSYS software with a 3D domain of a half-cell. This domain was applied under the assumption of the same structure for the cathode and anode in a PEM fuel cell. Accordingly it is composed of a single channel with a BPP, GDL, CL and half-size of membrane as shown in Figure 3.3.

The dimensions of the mechanical model domain were extracted from a real PEM fuel cell used in the reference [80], and presented in Table 3.2. This was applied in **Papers III** and **IV**. It is noted that the length of the 3D cell, i.e., 0.005 m, was selected to reduce the computational cost specifically for this mechanical model. The deformations of the BPP, CLs and membrane were neglected because of their much larger Young's modulus compared with the GDL [27, 31]. The related mechanical properties of the GDL are listed in Table 3.6. The parameters of other components are not listed as there were treated as rigid materials.

**Table 3.6 Physical parameters of GDL (carbon paper) applied in the mechanical model.**

| Parameters and Symbols | Value and Unit | Reference |
|---|---|---|
| Density, $\rho$ | 400 kg $m^{-3}$ | [29] |
| Young's modulus, $E$ | 6.3 MPa | [57] |
| Poisson's ratio, $v$ | 0.09 | [57] |

In terms of BCs of the mechanical model, a uniform pressure was applied on the top surface of the BPP (in the through-plane direction in Figure 3.3) during the assembling evaluation. A fixed bottom (in the through-plane direction), horizontal moveable surrounding surfaces (in the in-plane direction) and a bonded interface without slip between the components were selected as BCs. In addition, as shown in Figure 3.3, an unstructured mesh refined by 0.02 mm (comparative size of the one used in [89]), with a total of 49538 elements and 97870 nodes were employed.

## 3.3 Electric contact resistance model

The electric contact resistance between the GDL and BPP is one of the contributions to the ohmic loss in PEM fuel cells. It is an important part of the entire electric resistance and a function of the material properties, surface treatment of the GDL and BPP, and the assembly pressure. In the present thesis, the variation of the electric contact resistance due to the assembly pressure has been taken into account. The electric contact resistance $R_{contact}$, in the unit of m$\Omega$ $cm^2$, has been formulated in [57] as,

$$R_{contact} = 2.2163 + \frac{3.5306}{p_{contact}} \tag{3.39}$$

where $p_{contact}$ is the contact pressure. Duo to the channel/shoulder structure of the flow field plate, i.e., BPP, the assembly area affected by assembly pressure is different from the contact area between the GDL and BPP. Thus in a real PEM fuel cell stack or a single cell, the contact pressure is evaluated by the assembly pressure, assembly area and the cell contact area [27],

$$p_{Assembly} \cdot A_{Assembly} = p_{contact} \cdot A_{contact} \tag{3.40}$$

where $p_{Assembly}$, $A_{Assembly}$ and $A_{contact}$ denote the assembly pressure, assembly area and contact area, respectively. The contact resistance between the GDL and BPP can then be calculated as,

$$R_{GDL/BPP} = 2.2163 + \frac{3.5306 A_{contact}}{p_{Assembly} \cdot A_{Assembly}} \tag{3.41}$$

In the present electric contact resistance model, the intrusion of the GDL into a gas channel was considered, i.e., the decreased thickness of the GDL is considered. The small increase of the contact area $A_{contact}$ between the GDL and the BPP caused by the intrusion at high assembly pressures was neglected.

## 3.4 Electric resistance model

The electric resistance model was developed to evaluate the electric resistance in the through-plane direction of the cell. This section aims to formulate the equations applied in the electric resistance model presented in **Papers IV** and **V**.

The governing equation for the electron transfer through GDL, CL and BPP and the protons through the membrane can be evaluated by a Laplacian equation [90],

$$\nabla \cdot (\sigma \nabla \varphi) = 0 \tag{3.42}$$

where φ is the electric potential. The electric/protonic conductivity σ for electrons or protons is the reciprocal of its electric/protonic resistivity $\rho_e$,

$$\sigma = \frac{1}{\rho_e} \tag{3.43}$$

The local current density $i$ appearing in the cell components is related to the conductivity σ based on Ohm's law [65], defined as,

$$i = -\sigma \nabla \varphi \tag{3.44}$$

The electric resistance of the domain is predicted by a function of the average current density based on Ohm's law [65],

$$R_e = \frac{\left|\varphi_{\max} - \varphi_{\min}\right|}{\bar{i}} \tag{3.45}$$

where $\bar{i}$ is the average current density, $\varphi_{max}$ and $\varphi_{min}$ are the maximum and minimum electric potential occurring in the domain, respectively.

It should be observed that not only the deformed geometry but also the electric/protonic properties as results of the GDL deformation were considered in this electric resistance model. The electric conductivity of the layers in the through-plane direction determines the flow of electrons in the electric resistance model. The electric conductivity in the bulk of the compressed GDL is presented in Section 3.1.7. The protonic conductivity in a membrane is depending on the local temperature and water content. The correlation between these parameters has been taken into account in this model [6],

$$\sigma_{mem} = (0.005139\omega - 0.00326)\exp\left[1268\left(\frac{1}{303} - \frac{1}{T}\right)\right] \tag{3.46}$$

where $\omega$ is the water content and $T$ is the local temperature. It has been suggested that there might exist several possible ways of the ionic transfer in Nafion like materials [6], i.e., hydronium ions move via a vehicle mechanism at low water content ($\omega$=2~4 $H_2O/SO_3H$), easier movement of hydronium ions at a partially hydrated membrane ($\omega$=5~14 $H_2O/SO_3H$). Finally, both water and ions move freely in a fully hydrated membrane ($\omega$>14 $H_2O/SO_3H$). In this model, the water content $\omega$ =10 $H_2O/SO_3H$ and $T$=353 K were selected to evaluate the protonic conductivity of a membrane as formulated by Eq. (3.46).

Because electrons/protons are released at the anode of a PEM fuel cell, a half-cell, i.e., anodic side is selected as the representative domain for the electric resistance

modeling, as shown in Figure 3.4. This domain includes anodic BPP, GDL, CL and a half-sized membrane but without the gas channel.

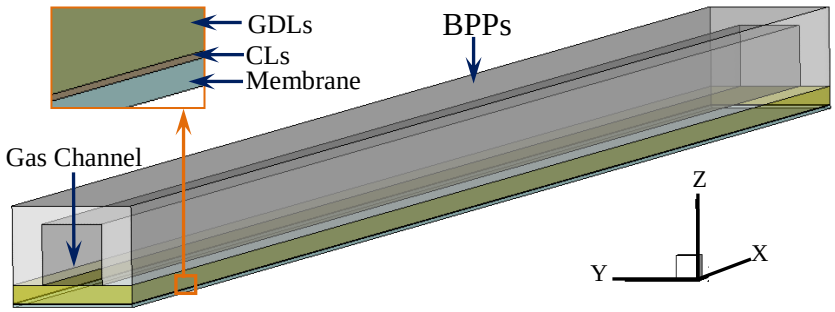


**Figure 3.4 Schematic illustrations of the electric resistance model.**

The dimensions for this model are the same as the one listed in Table 3.2 applied in **Papers III** and **IV**. The physical parameters implemented in the electric resistance model are presented in Table 3.7.

**Table 3.7 Physical parameters for electric resistance model.**

| Parameters | Value & Unit | Reference |
|---|---|---|
| GDL electric conductivity | 1250 S $m^{-1}$ | [27] |
| CL electric conductivity | 100 S $m^{-1}$ | [44] |
| BPP electric conductivity | $2.22\times10^{4}$ S $m^{-1}$ | [27] |
| Water content in membrane | 10 $H_2O/SO_3H$ | [6] |

As the BC, a constant current density $i_{cell}$ = 0.7 A $cm^{-2}$ was applied at the membrane as the current source, which occurs at the bottom surface (membrane or electrolyte). The variable potential BC the Laplacian equation (Eq. (3.42)) of the electric resistance model at the membrane is set as a gradient potential which is a function of the local conductivity [65],

$$\nabla\varphi = -\frac{i_{cell}}{\sigma} \tag{3.47}$$

For the BPP domain, a reference potential value of zero is arbitrarily set at the top surface of the anodic BPP [65]. The BCs for the other boundaries are set as symmetry conditions.

Validation of this newly developed electric resistance model is important to ensure the accuracy of the OpenFOAM code. Two different geometrical cuboids, Cuboid A with

1 cm×1 cm×2 cm and Cuboid B with 2 cm×2 cm×1 cm, were employed to validate the model,. Constant potential values (easier for theoretical calculation) of 0 V and 1 V were set as BCs at the top of the BPP and the bottom of the membrane, respectively, for both Cuboids. The remaining BCs are set as mentioned above. The theoretical prediction is based on both Pouillet's law and Ohm's law,

$$R_e = \frac{l}{\bar{\sigma} A} \tag{3.48}$$

$$i = \frac{\Delta \varphi}{R_e} \tag{3.49}$$

where $l$ and $A$ denote the length and cross-sectional area of the conductor, respectively, $\bar{\sigma}$ is the average electric conductivity. $\Delta\varphi$ is the maximum potential difference between the membrane and BPP (Here 1 V was applied for the theoretical prediction).

# 4. Main Results and Discussion

In this Chapter, a summary of the validated and main results in terms of the effects of assembly pressures obtained in **Papers II**, **III**, **IV** and **V** is presented.

## 4.1 Validation results

Before solving the cases, the PEM fuel cell model was validated and compared with numerical data [91] and experimental results [92] cited from references with the corresponding dimensions and operating conditions, respectively. The comparison is shown in Figure 4.1.

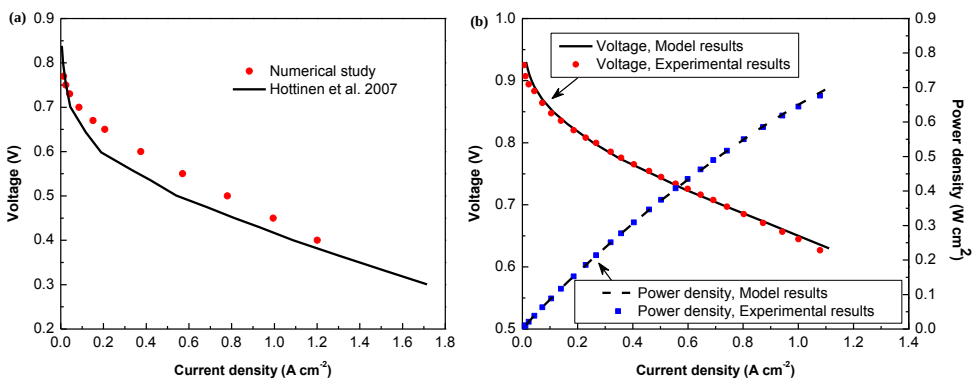


**Figure 4.1 Comparison of numerical predictions with (a) numerical results [91], and (b) experimental data [92].**

The operating voltage of the predicted results in Figure 4.1 shows some differences compared with the reference. With increasing current density, greater differences are observed between the present work and the reference. A constant binary diffusion coefficient was used in the investigation by Hottinen et al. [91] and it was a 2D model

ignoring the direction along the channel. These limitations might be the main reason for the discrepancies.

However, good agreement between the experimental [92] and the predicted results is obtained in Figure 4.1b, in terms of the current density and the power densities when cell operating voltages higher than 0.63 V. Both the calculated and measured voltages drop fast when the current density is small, which is mainly caused by the activation losses. The voltage then keeps a linear decrease to the voltage 0.63 V, where the Ohmic loss becomes dominating.

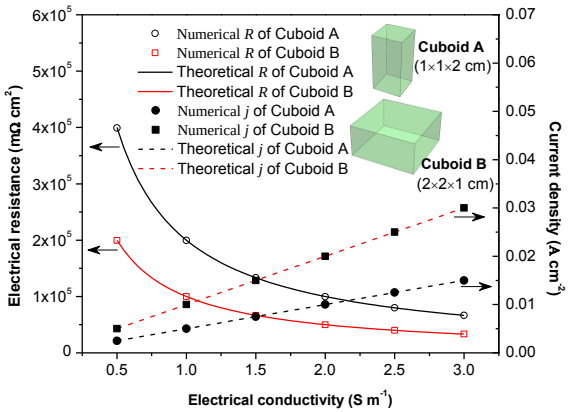


**Figure 4.2 Comparison of electric resistance and current density v.s. electric conductivity.**

The validation of the electric resistance model was conducted by comparing the theoretical predictions obtained by Eq. (3.48) and Eq. (3.49), and the numerical results, as shown in Figure 4.2. Relatively accurate electric conductivity and current density were obtained by the electric resistance model for the various bulk electric conductivities.

The electric contact resistance between the GDL and BPP for various assembly pressures was considered. A comparison of the electric contact resistance between the predictions using Eq. (3.39) to Eq. (3.41) and experimental results is presented in Figure 4.3. It is found that the contact resistance measured by Mishra et al. [55] can be fitted with a good accuracy. The assembly pressure decreases the contact resistance, which supports the fact that there is a better contact between the GDL and BPP as the assembly pressure increases. The contact resistance decreases sharply with increasing assembly pressure at pressures below 1 MPa. However, above 1.0 MPa there is still a slight decrease in the resistance for increasing pressure. But there is no significant change of the contact resistance at higher assembly pressures. This is so because the maximum contact between the GDL and BPP is reached at a certain pressure.

To implement the electric resistance, a contact resistance of 14.3 $m\Omega\ cm^2$ based on Figure 4.3 was applied for the case of zero assembly pressure (the same value of the constant resistance was also taken from references [55] and [23]).

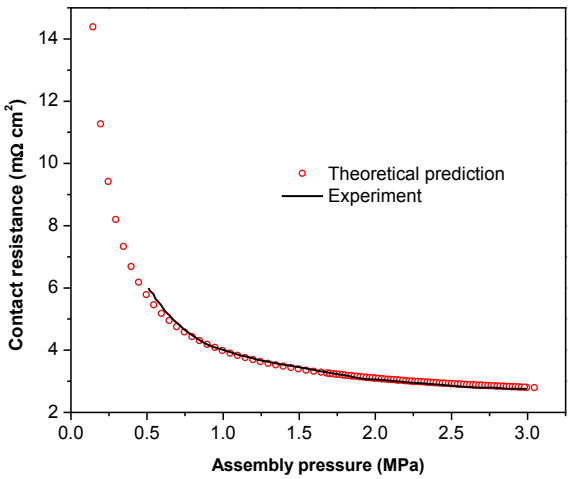


**Figure 4.3 Comparison of theoretical and experimental contact resistances [55] between GDL and BPP.**

# 4.2 Effect of porosity

The effect of porosity of the GDL is presented in this section. The main results presented are obtained from **Paper II**.

To study the effect of the porosity change caused by the assembly pressure, five cases with different compression ratios $\lambda$ of 0%, 10%, 20%, 30% and 40% of the GDL were employed. Then these porous properties of the GDL (listed in Table 3.1) were implemented into the PEM fuel cell model to evaluate the thermal conductivity and the species diffusion coefficient. The physical properties of the GDL below the channel areas are kept constant at the initial value (zero compression). The Base case with zero compression of the GDL was included to evaluate the difference of compressed and uncompressed GDLs.

## 4.2.1 Effects on temperature distribution

Thermal equilibrium is a key parameter during operation of a PEM fuel cell. The thermal conductivity of a GDL is usually treated as uniform in previous numerical studies. However, this parameter was observed to increase when a compression load was applied on the cell [93].

Figure 4.4 displays the profiles of the effective thermal conductivity of the GDL close to the CL for different compression cases. In Figure 4.4, the effective thermal conductivity below the channel region is lower than that below the shoulder regions as GDL compression prevails. Increasing compression ratio results in a higher effective thermal conductivity below the shoulders. This means that the porosity of the GDL is the main factor affecting the effective thermal conductivity. This agrees well with equation (3.18) that is dependent on local porosity. No change of porosity leads to a constant effective thermal conductivity, similar to the Base case along the cell direction and the GDL regions below the channel for other cases.

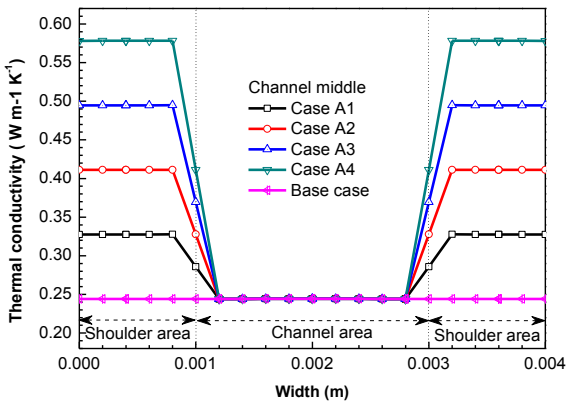


**Figure 4.4 Distributions of effective thermal conductivities at GDL interface close to CL at the middle channel for different compression cases.**

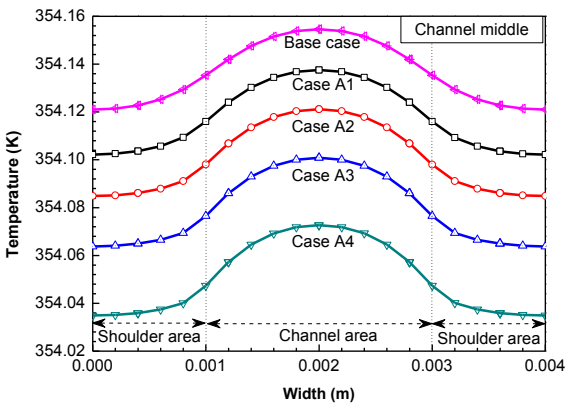


**Figure 4.5 Temperature profile of GDL interface close to CL at channel middle for different compression cases.**

The temperature profiles of the GDL close to the CL along the channel for different compression cases are shown in Figure 4.5. It is found that, the local temperature at the GDL interface across the cell width direction is decreasing with smaller porosity of

the GDL. This might be explained by the fact that the higher effective thermal conductivity caused by the higher compression ratio increases the heat transfer. At this point the assembling pressure on the GDL is favorable for the heat removal from the cell. However, the reaction effects on the temperature distribution can not be neglected and it will be analyzed below.

### 4.2.2 Effects on mass transfer

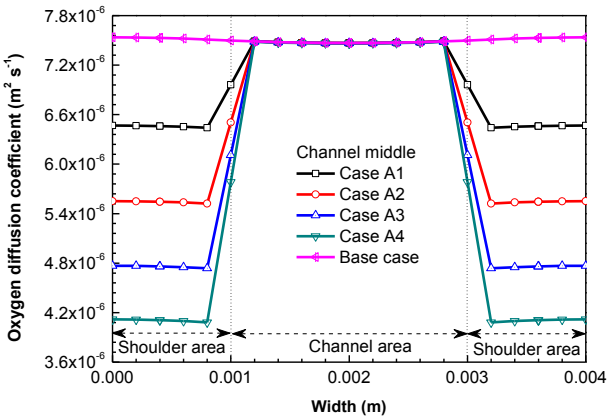


**Figure 4.6 Distribution of oxygen diffusion coefficients at the interface of GDL close to CL for different compression cases at middle of the cell.**

The diffusion coefficient determines the local reactant/product distribution. The diffusion coefficient of the compressed GDL is a function of the porosity and tortuosity, as formulated by Eqs. (3.13) to (3.16).

The profile of the effective oxygen diffusion coefficient at the interface of the GDL close to the CL in the middle part of the cell for different compression cases is shown in Figure 4.6. The distribution is similar to the one of effective thermal conductivities illustrated in Figure 4.4. The oxygen diffusion coefficient is almost constant for the uncompressed cases. However, lower porosity values with increasing compression ratios on the shoulders of the GDL result in a deteriorated oxygen diffusion coefficient. A related work performed by Nitta et al., [26] considering inhomogeneous compression of GDL indicated that the gas diffusion coefficient decreases as a result of the reduced pore size.

It is important to study the distribution of the reactants at the cathode reaction sites, because they determine the local current densities, according to Eq. (3.28). The distributions of the oxygen mole fraction at the reaction interface for Base case and Case A4 are shown in Fig. 9. No significant difference is observed at the reaction interface below the channel areas when various compression ratios are applied. However, a significant difference appears below the both shoulder areas.

A nearly zero oxygen mole fraction is observed in the shoulder area for Case A4 for the biggest compression. Based on this, a lower porosity caused by a higher compression ratio results in a more non-uniform oxygen concentration, especially far away from the channel areas.

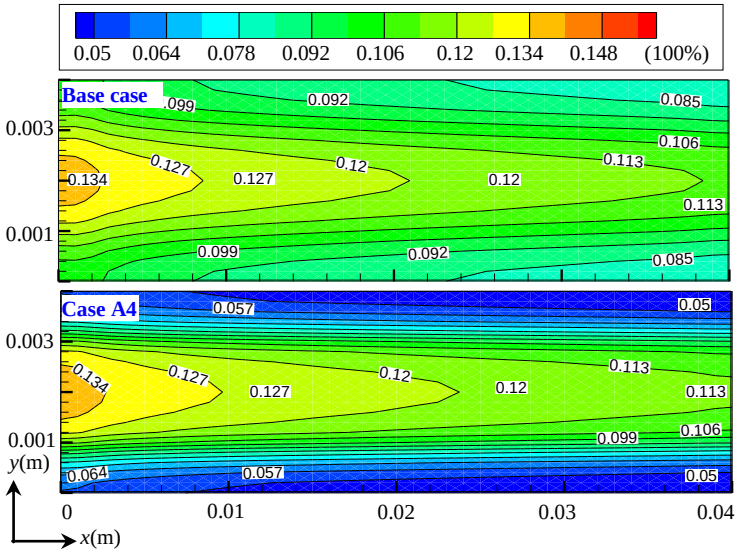


**Figure 4.7 Profile of oxygen mole fractions predicted at the reaction interface for Base case (above) and Case A4.**

## 4.2.3 Effects on cell performance

The average current density, which is the output of the cell during operation, is shown in Figure 4.8 when the cells operate at 0.55 V cell voltages. The plot shows the drop current density from the case with zero compression ratio (the Base case) to the case with 40% (the Case 4) of that in the GDL. The corresponding average current density decreases from 0.570 A $cm^{-2}$ to 0.536 A $cm^{-2}$.

Figure 4.8 indicates that the decreased porosity of the GDL limits the cell performance. Even though the effective thermal conductivity improves with lower porosity (see Figure 4.4), the degraded reactant diffusion term has a more important effect on the cell performance.

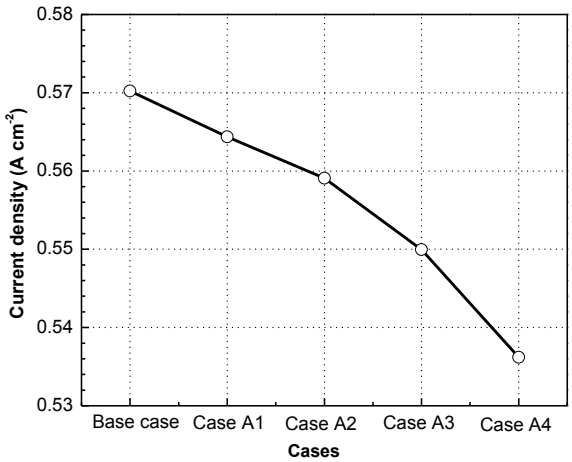


**Figure 4.8 Average current densities for different compression cases at 0.55 V operating cell voltages.**

# 4.3 Effect of GDL deformation

The GDL deformation under assembly pressures computed in the mechanical model and the yield corresponding porous properties variations are considered in this section. Four assembly conditions including 0 MPa, 1 MPa, 2 MPa and 3 MPa are applied and a summary of the main results from **Paper III** is presented.

## 4.3.1 Effects on GDL shape

During the PEM fuel cell assembly process, each component including the GDL is clamped by the bipolar plates. Figure 4.9 shows the shapes of a deformed GDL at 0 MPa, 1 MPa, 2 MPa and 3 MPa assembly pressure, respectively. The thickness of the GDL is kept constant along the cell width for the uncompressed case (0 MPa), but varies for the different assembly pressures. A thinner GDL above the shoulder areas and the GDL intrusion in the middle channel are observed as the assembly pressure is applied. This is so because the GDL above the shoulders is crushed and deformed due to its porous and flexible properties. A consequence of the intrusion is a reduction of the gas flow channel cross-section areas and a decreased gas diffusion area above the shoulders as clearly shown in Figure 4.9.

Another consequence of the GDL intrusion/deformation is a decreased porosity of the GDL above the shoulders, as shown in Figure 4.10 in a cross-section view for various assembly pressures. The predicted porosity shown in Figure 4.10 was calculated with

the assumptions for the porous materials illustrated in Figure 3.1 and the Eqs. (3.29) to (3.31).

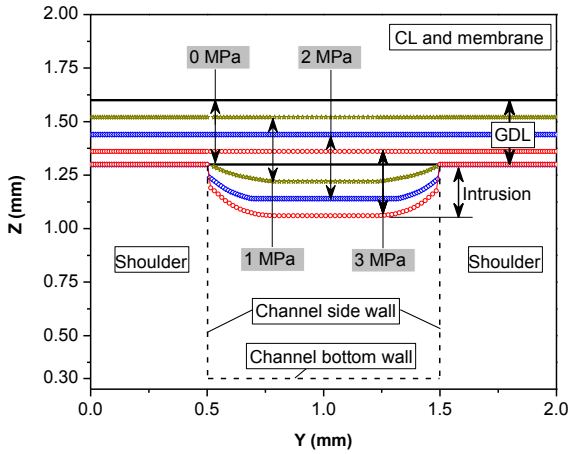


**Figure 4.9 Deformed shape of the GDL in a cross-section view for different assembly pressures.**

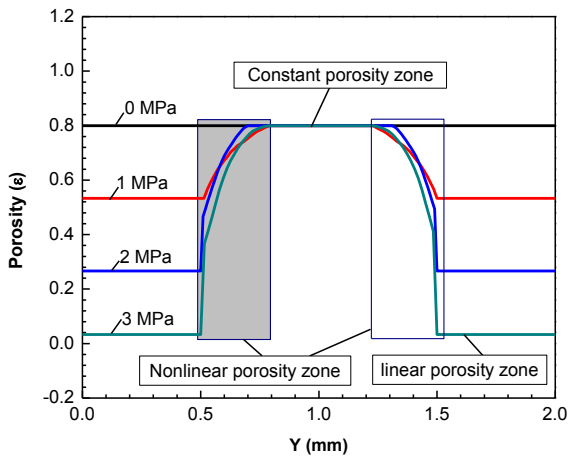


**Figure 4.10 Porosity distribution in the GDL in cross-section view for different assembly pressures.**

Figure 4.10 shows different porous features in different regions in the in-plane direction. There exists a transitional region, i.e., a nonlinear porosity distribution zone in the GDL region corresponding to the interface between the channel and the shoulders, a linear porosity distribution zone above the shoulders and a constant porosity distribution zone above the middle part of the channels for the cases when an assembly pressure is applied. The impact of such nonlinear porosity distributions in

the GDL has been identified in the GDL models, but unfortunately, a constant porosity distribution was widely assumed in the available literatures [23, 34].

It is noted that the porosity of the GDL in the constant porosity distribution zone is kept at the initial value even though the assembly pressure increases. This agrees with the GDL shape shown in Figure 4.9, in which the GDL keeps the initial thickness below the channel center.

### 4.3.2 Effects on mass transfer

After the prediction of the GDL deformation caused by the assembly pressure, the PEM fuel cell model takes advantage of the above mechanical results, including the deformed shape and the porous features of GDLs. For the settings presented in Chapter 3.1 and the validations in Chapter 4.1, the PEM fuel cell model was applied for various assembly pressure conditions (i.e., 0 MPa, 1 MPa, 2 MPa and 3 MPa).

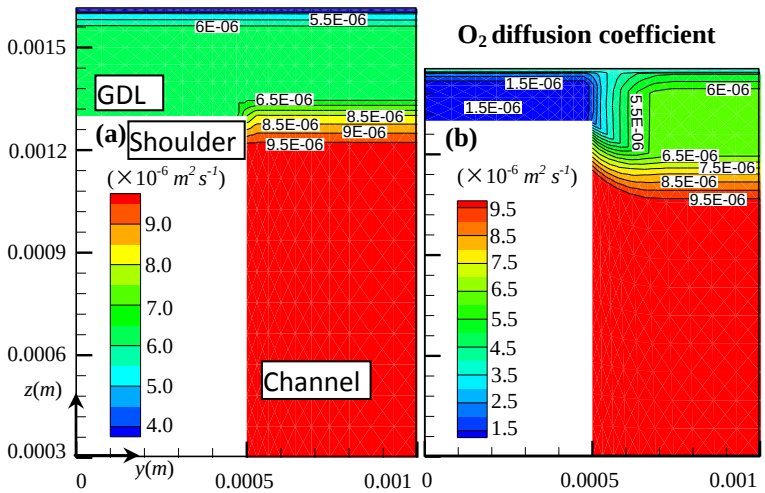


**Figure 4.11 Distribution of oxygen diffusion coefficient for the left-hand half domain along the in-plane direction in the cell middle ($x$=0.025 m) for: (a) uncompressed condition, (b) 2 MPa assembly pressure.**

The oxygen diffusion coefficient was studied with the implementation of the deformed GDL and the corresponding porous properties. The involved porous properties include the non-homogeneous porosity shown in Figure 4.10, pore size and tortuosity, etc. Due to the significant deformation of the GDL at 3 MPa assembly pressure (see Figure 4.9), the result shown below is from the case with 2 MPa assembly pressure instead of 3 MPa condition.

The oxygen diffusion coefficients of the left-hand half domain in the cell middle ($x$=0.025 m along the cell main flow direction) for the case of 2 MPa assembly pressure and uncompressed condition are presented in Figure 4.11. From Figure 4.11, a similar distribution of the oxygen diffusion coefficient is observed in the gas channels except of the gradients in GDLs. The coefficient gradient facing the channel is caused by viscous resistance of the GDL, however, another one appearing at shoulder corner in the in-plane direction is the result of the sharp-changing of the porosity (see Figure 4.10). Comparing the two cases, several times lower oxygen diffusion coefficient appears above the shoulders for the 2 MPa assembly pressure caused by the extremely low porosity.

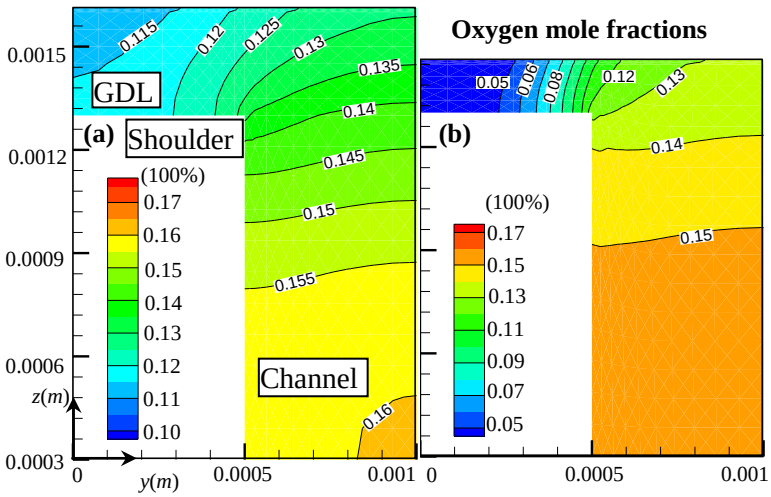


**Figure 4.12 Distribution of oxygen mole fraction for the left-hand half domain along the in-plane direction in the cell middle ($x$=0.025 m) for: (a) uncompressed condition, (b) 2 MPa assembly pressure.**

The oxygen mole fractions at the same position for the case of 2 MPa assembly pressure and uncompressed condition are shown in Figure 4.12. The results show a comparable variation for both cases. A more uniform distribution of the oxygen mole fraction is observed for the uncompressed case. However, the profile agrees with the distribution of the oxygen diffusion coefficient (see Figure 4.11), i.e., a maximum oxygen mole fraction occurs where the maximum porosity exists for the case of 2 MPa assembly pressure. This reflects again that the porosity distribution plays a significant role on the mass diffusion coefficients and the oxygen mole fractions in the GDLs.

### 4.3.3 Effects on cell performance

The cell performance was evaluated as well. As illustrated in Figure 4.13, the cell performance is not sensitive to the assembly pressure at high operating cell voltages

because a small amount of reactants is consumed. With increasing cell voltages, the current densities and power densities are declining but vary with higher assembly pressures above a specific voltage. A higher assembly pressure causes a worse cell performance. It is expected that a condition of 3 MPa assembly pressure may hardly ensure the gas transfer from the channel to the reaction sites via a deformed GDL as the result of reduced porosity and oxygen diffusion coefficient.

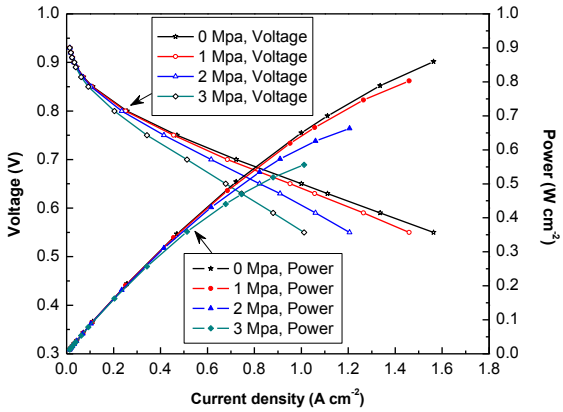


**Figure 4.13 Comparison of current densities and power densities for different assembly pressures.**

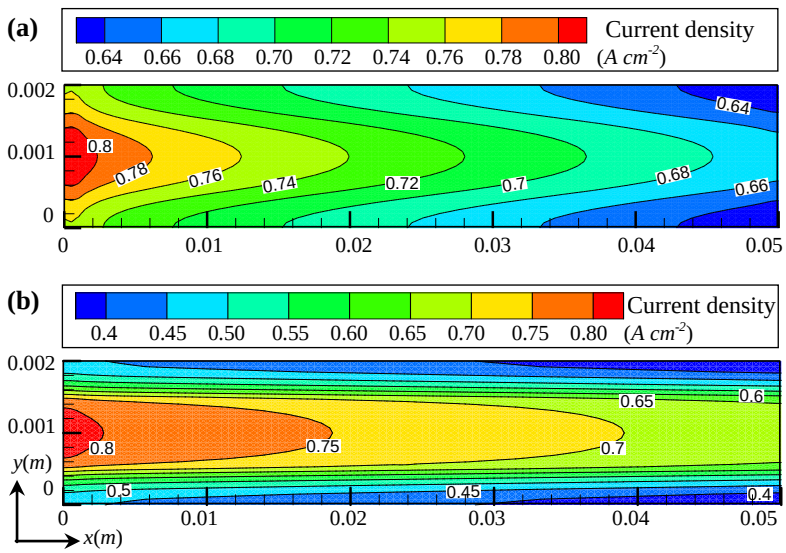


**Figure 4.14 Distribution of local current densities at the reaction interface for (a) uncompressed condition and (b) 2 MPa assembly pressure at cell operating voltage of 0.70 V.**

Figure 4.13 reflects that the mass transfer resistance is accumulated as the porosity decreases for increasing assembly pressure. However, in the published literature the reduced performance was claimed to be due to the combined effects of a reduction of the porosity, the narrowed gas flow channel cross-section areas and the reduction of the flow path from the gas channel to the reaction sites.

A significant difference in the cell performance was observed between the case with uncompressed condition and the one with 2 MPa assembly pressure. The performance deterioration could be observed in Figure 4.14. For both cases, the highest local current density occurs in the reaction region above the channel as the result of the presence of sufficient fresh reactants. However, the one for the case with 2 MPa assembly pressure is extremely low in the regions above the shoulders, especially the area at the cell outlet, which results in the reduction of the overall cell performance.

To figure out the dominating factor in deteriorating the cell performance when considering the reduction of porosity, gas flow channel cross-section areas and GDL thickness, the cases for different assembly pressures with various porosities are considered and shown in Figure 4.15. The results show that the current density decreases with an increase of the assembly pressure whatever porosity applied. The cell performance for the combination of the reduced GDL thickness and gas flow channel areas could decrease the current density by 8.9% at 3 MPa assembly pressure. However, a significant deterioration of the current density by 29.0% appears as a decrease of the GDL porosity is further applied. Thus, the current density is decreased approximately 20.0% purely by the reduction of porosity at an assembly pressure of 3 MPa compared and a non-deformed cell.

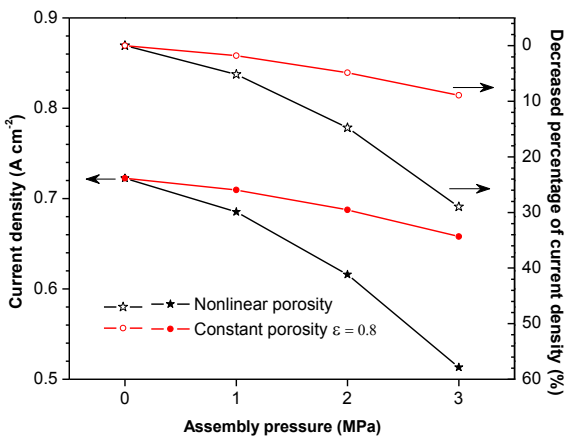


**Figure 4.15 Average current densities and decrease percentage versus assembly pressures and porosities at cell operating voltage 0.70 V.**

Another case study for the 2 MPa assembly pressure with an initial constant porosity 0.8 but ignoring the GDL intrusion into the channels was conducted (see **Paper III**). A decrease at the current density of 5.0% is observed compared to the uncompressed

case. Therefore, the decreased porosity is the dominating factor in reduction of the current density compared with effects of the reduced gas flow channel areas and GDL thickness.

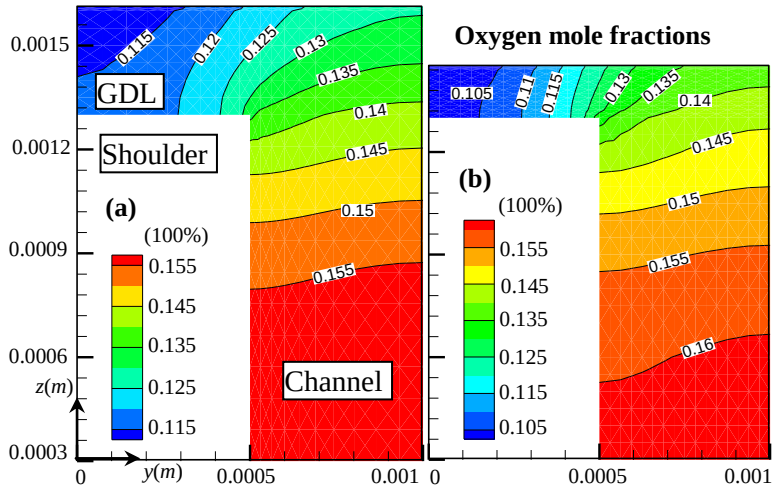


**Figure 4.16 Cathodic oxygen mole fraction for the left-hand half domain at the middle of the cell (*x*=0.025 m) for (a) uncompressed condition (b) 2 MPa assembly pressure, with constant porosity 0.8 and without the GDL intrusion into the channels.**

The effect of a reduced GDL thickness on the current density is shown in Figure 4.16. Figure 4.16a and Figure 4.16b are for the cases with uncompressed condition and 2 MPa assembly pressure but without GDL intrusion into the gas channel center, respectively. A constant porosity of 0.8 was applied for both cases. Figure 4.16 shows that a smaller oxygen mole fraction (10.5% in Figure 4.16b) occurs in the compressed case with the 2 MPa assembly pressure compared with the uncompressed case (11.5% in Figure 4.16a). This indicates that a reduction of the GDL thickness leads to an increased resistance from the channels to the CLs through the GDLs.

## 4.4 Effect of electric properties

The aim of this section covering **Papers IV** and **V** is to study the effects of electric resistance on the cell performance under assembly pressure condition. The electric resistance model, electric contact resistance model and PEM fuel cell model under various assembly conditions including 0 MPa, 1 MPa, 2 MPa and 3 MPa are analyzed in this section.

### 4.4.1 Effects on electric resistance

It is essential to examine the cell resistances as the bulk resistance (in the through-plane direction) and the contact resistance. The electric conductivity is one of the most important parameters characterizing the transport of electrons/protons in a PEM fuel cell. The result of the assembly pressure is the deformation of the GDL and then a reduction of the electric conductivity in the through-plane direction, as shown in Figure 4.17. It is found that the electric conductivity distributions exhibit non-homogeneous features, i.e., a nonlinear distribution zone in the GDL region corresponding to the corner between the channel and the shoulders (as shown in both the grey areas in Figure 4.17), a linear distribution zone below the shoulders and a constant distribution zone below the middle part of the channels for the cases when an assembly pressure is applied.

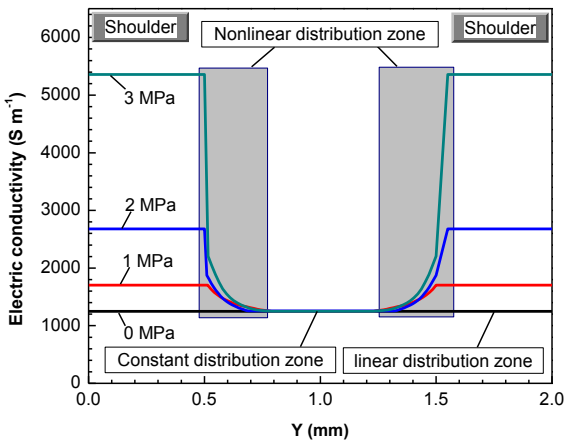


**Figure 4.17 Cross-sectional distribution of electric conductivity in the GDL for different assembly pressures.**

With the implementation of the nonlinear electric conductivity of the GDL and other parameters listed in Table 3.7, the bulk resistance (in the through-plane direction) of a cell was investigated in the electric resistance model. The bulk resistances (in the through-plane direction) of a cell as well as the contact resistances between the GDL and BPP are presented in Figure 4.18 as function of the assembly pressure. As shown in Figure 4.18, the bulk resistance decreases with increasing assembly pressure, as expected. A similar tendency is observed for both the contact resistance and the sum of both resistances which is denoted as the entire resistance of a cell.

However, the contact resistance between the GDL and BPP is quite small compared with the bulk resistance predicted by this model. The bulk resistance through the cell contributes as much as 76 percent of the total cell resistance at the assembly pressure of 0 MPa but 92.7 percent at the higher assembly pressure of 3 MPa. The results from Figure 4.18 show that the bulk resistance plays a dominating role in the cell electric

resistance for varying assembly pressure. On the other hand, the contact resistance between GDL and BPP should not be neglected when considering the assembly processes.

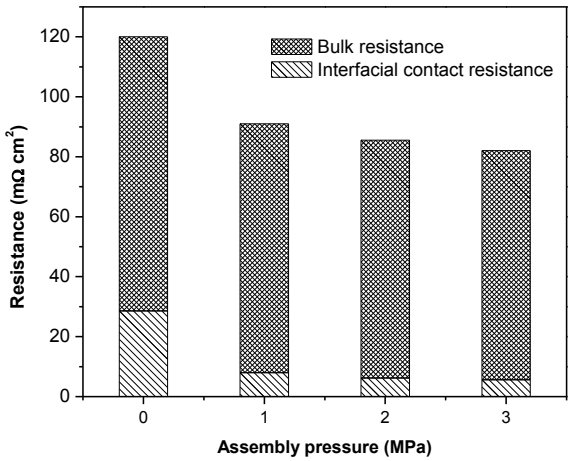


**Figure 4.18 Variation of the bulk resistance and total interfacial contact resistance between GDL and BPP for different assembly pressures.**

## 4.4.2 Effects on electric field

The electric field, also called the electrostatic field, is caused by the electric charges/current flow from the reaction sites to the external circuit. In general, this electric field does not change with time because charges/currents are stationary when a fuel cell is operating at steady-state.

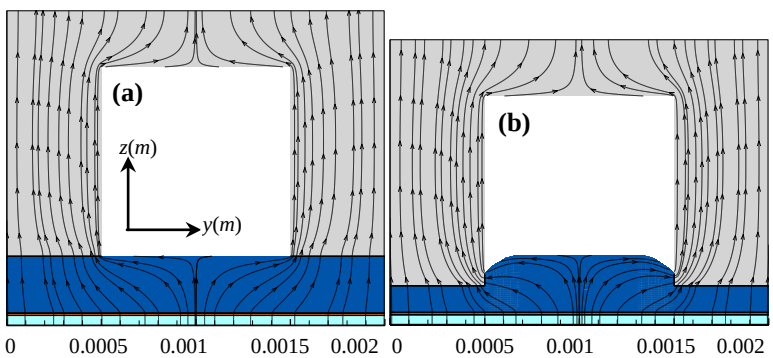


**Figure 4.19 Streamlines of electric field transfer through membrane and anodic cell at the middle of the cell (x=0.025 m) for (a) uncompressed condition (b) 2 MPa assembly pressure.**

In the electric resistance model, the corresponding streamlines are presented in Figure 4.19 for the electric field through the membrane and the anodic side at the middle of the cell (x=0.025 m along the cell main flow direction) for the case of 2 MPa assembly pressure, and another one for uncompressed condition. The lines and arrows illustrate the current flow direction which starts from the current source, i.e., the membrane interface, to the lower potential zone, i.e., the top surface of BPP.

As found, the current below the channel flows across with a longer distance from the middle of the GDL to the BPP's shoulders. In other words, the electric field is redistributed and becomes more uniform from the shoulders to the top of BPP. It is noted that the electric field at the BPP's corner close to the channel is significantly concentrated, especially for the case with 2 MPa assembly pressure. The reason is that the channel/shoulder structure makes a portion of the BPP to contact with the GDL, and the intrusion of the GDL into the channel generates a reduced contact area in the vertical interface of BPP. As a consequence, part of the additional electric current flows from the intrusion of the GDL below the channel back to BPP's shoulders along the cell width direction.

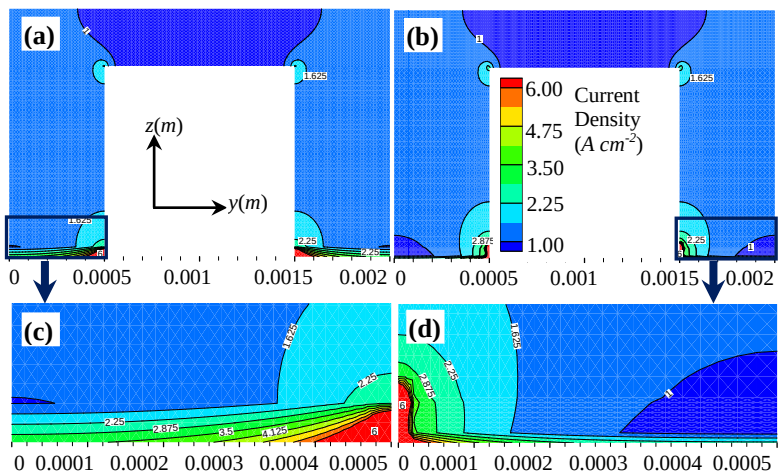


**Figure 4.20 Current density distribution in anodic BPP at the middle of the cell (x=0.025 m) for (a) uncompressed condition (b) 2 MPa assembly pressure, and (c) and (d) magnification of rectangular area highlighted in (a) and (b), respectively.**

The local current density for the BPP at the middle of the cell (x=0.025 m) for the case of 2 MPa assembly pressure and uncompressed condition, respectively, is presented in Figure 4.20. It is clear that the highest current density occurs in the corner of the BPP close to the channel. The maximum distributions are magnified in Figure 4.20c and Figure 4.20d. The profile of the maximum values varies for the different conditions. The maximum current density is distributed over longer distances from the BPP's corner to a position far away from the channel in the cell width direction for the case

with zero assembly pressure. This appears mainly along the vertical direction close to the interface for the other case. This is so because the electric current more easily flows upward from the GDL to the BBP's shoulder around the corner for the case with zero assembly pressure. However, more current favors to flow along the horizontal direction from the intrusion of the GDL below the channel center to the vertical interface between the GDL and BPP. This phenomenon is also observed in Figure 4.19. This means that this larger connecting area of the case at 2 MPa assembly pressure is favorable in passing through electrons in the horizontal directions.

### 4.4.3 Effects on cell performance

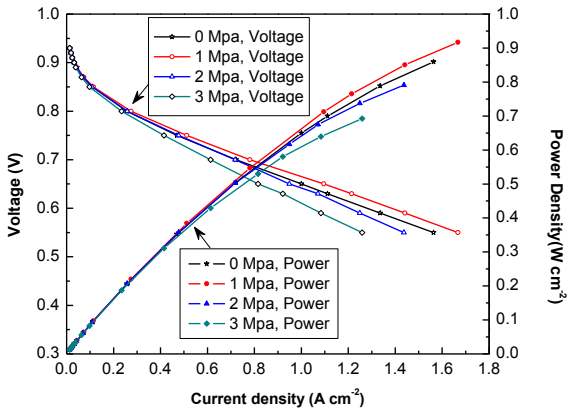


**Figure 4.21 Comparison of voltage and power densities v.s. current density for different assembly pressures.**

After obtaining the through-plane electric resistance of a cell and the contact resistance between GDL and BPP, the overall cell resistance including two main factors (see Figure 4.18) was analyzed. Simulation validation was carried out at the same condition as in **Papers III** and **IV**. For the cases studied, the overall cell resistance of the cell is regarded as assembly pressure dependent.

As illustrated in Figure 4.21, the cell performance is not sensitive to the assembly pressure and the overall electric resistances at high cell operating voltages. It is expected that a small amount of the reactants is consumed at the reaction sites at the higher cell voltages. However, the cell operating at 1 MPa assembly pressure shows the best cell performance compared with the other cases at lower cell voltages. Then the cell performance becomes worse with increasing assembly pressure. A similar phenomenon has been observed in the study [23], in which a constant cell resistance was applied and 0.3 MPa was identified as the optimized assembly pressure.

However, the results of Chapter 4.3 show that cells operating under a non-zero assembly pressure have a reduced cell performance, i.e., a higher assembly pressure causes a worse cell performance due to the reduced porosity of the deformed GDL,

reduction of the GDL thickness and the narrowed cross-sectional areas of the gas flow channel. This is because the mass transfer resistance is accumulated as the porosity decreases. In this sense, an improved electric conductivity may overcome the deterioration by the mass transfer resistance when the cell is operating at a proper assembly pressure.

# 5. Conclusions

The research presented in this thesis aims to investigate the GDL deformation caused by assembly pressures and its impact on the transport phenomena and performance of PEM fuel cells. Several models relating to the porosity, mechanical deformation and electric resistances have been developed to study the individual factors affected by the assembly processes. The obtained findings can be summarized as,

(1) GDL above the channels intrudes into the gas channels as an assembly pressure is applied, and accordingly non-homogeneous thickness and porosity along the cell in the in-plane direction appear. Three zones are identified by the mechanical model based on the porosity variations along the cell in the in-plane direction, i.e., a linear porosity distribution zone, a constant porosity distribution zone and a nonlinear porosity distribution zone. The thickness and porosity of the GDL are unchanged in the constant porosity distribution zone, but vary linearly or nonlinearly in the other two distribution regions.

(2) The lower porosity of the GDL below the shoulder areas caused by the higher compression ratios is a positive factor for the thermal conductivity and contributes to obtaining a more uniform temperature. However, a depletion phenomenon is observed for the oxygen diffusion coefficient and oxygen distribution and cell performance for the compression conditions.

(3) The results of the PEM fuel cell model show that a higher assembly pressure results in a reduction of the thickness and porosity of the GDL, gas flow channel area, oxygen diffusion coefficient in the porous medium and cell performance. It is found that the reduction of the GDL porosity plays a dominating role compared with the decreased gas channel flow area and GDL thickness. An extremely low oxygen diffusion coefficient, oxygen concentration and local current density appear in the GDL above the shoulders far away from the channels for the high assembly pressure. It is observed that a sufficiently thick GDL is favorable to ensure the gas transfer from the channel to the reaction sites in the PEM fuel cell.

(4) A non-homogeneous electric conductivity along the cell in-plane direction appeared. The simulated results suggest that a higher assembly pressure results in a decreased cell resistance. However, 1 MPa assembly pressure is an

optimized assembly condition when both the contact resistance between GDL and BPP, and the electric resistance in the through-plane of the cell are considered. It is found that the through-plane resistance plays a dominating role compared with the contact resistance in a cell. The BPP's corner close to the channel becomes a concentrated area for the electric field and the current, because the additional contact interface area is created by the intrusion of the GDL into the channel.

(5) To obtain the optimized cell performance, the assembly pressure should be considered properly to ensure the gas sealing security and lower electric resistance. On the other hand, an improved electric conductivity may overcome the deterioration by the mass transfer resistance when the cell is operating at a proper assembly pressure. The results from this investigation may provide guidance for the design development and manufacturing of PEM fuel cells.

# 6. Future Outlook

Despite the achieved results in this thesis, there still exist a lot of unknown or unclear questions in understanding the transport phenomena of PEM fuel cells. The assumptions of no phase-change, the reaction appearing at the membrane interface and the isotropic GDL deformation are the major limitations in the present thesis, which might be considered in future work. Apart from those limitations, the shortages of the larger scale of the CFD simulations cannot be neglected as well. Further work in following aspects might be considered in PEM fuel cells.

(1) More attention should be paid on the water phase change and water transport process in the porous media when an assembly pressure is acting on a cell.

(2) The GDL made of carbon fiber paper is nonhomogeneous in the in-plane direction and in the through-plane direction. A non-linear anisotropic Young's modulus and related anisotropic mass diffusion coefficients might be applied in future work.

(3) The real electrochemical reaction in CLs is a species concentration-weighted energy conversion but not at the membrane interface. To achieve this purpose, the reactions should be considered in 3D.

(4) The shortage of the CFD analysis is that the porous features of the GDL and CL are not captured in detail but these play an important role for the mass transfer of a cell. A potential solution is to use a multiscale modeling approach to couple the microscopic and macroscopic flow characters.

# 7. Bibliography


[1] Bhatt S, Gupta B, Sethi V, Pandey M. Polymer exchange membrane (PEM) fuel cell: a review. *International Journal of Current Engineering and Technology* 2012; **2**(1): 219-226. doi:http://inpressco.com/category/ijcet.

[2] Fang B, Kim JH, Kim M, Yu J-S. Ordered hierarchical nanostructured carbon as a highly efficient cathode catalyst support in proton exchange membrane fuel cell. *Chemistry of Materials* 2009; **21**(5): 789-796. doi:10.1021/cm801467y.

[3] Imbrioscia GM, Fasoli HJ. Simulation and study of proposed modifications over straight-parallel flow field design. *International Journal of Hydrogen Energy* 2014; **39**(16): 8861-8867. doi:10.1016/j.ijhydene.2013.11.079.

[4] Reifsnider K, Huang X, Ju G, Solasi R. Multi-scale modeling approaches for functional nano-composite materials. *Journal of Materials Science* 2006; **41**(20): 6751-6759. doi:10.1007/s10853-006-0214-5.

[5] Djilali N. Computational modelling of polymer electrolyte membrane (PEM) fuel cells: challenges and opportunities. *Energy* 2007; **32**(4): 269-280. doi:10.1016/j.energy.2006.08.007.

[6] Barbir F. PEM Fuel Cells: Theory and Practice. Elsevier (ed.). Published: Academic Press, Cambridge, 2013.

[7] Zhang L, Zhang J, Wilkinson DP, Wang H. Progress in preparation of non-noble electrocatalysts for PEM fuel cell reactions. *Journal of Power Sources* 2006; **156**(2): 171-182. doi:10.1016/j.jpowsour.2005.05.069.

[8] Kleemann J, Finsterwalder F, Tillmetz W. Characterisation of mechanical behaviour and coupled electrical properties of polymer electrolyte membrane fuel cell gas diffusion layers. *Journal of Power Sources* 2009; **190**(1): 92-102. doi:10.1016/j.jpowsour.2008.09.026.

[9] Titov A, Zapol P, Král P, Liu D-J, Iddir H, Baishya K, et al. Catalytic Fe-x N sites in carbon nanotubes. *The Journal of Physical Chemistry C* 2009; **113**(52): 21629-21634. doi:10.1021/jp810792d.

[10] Liu R, Wu D, Feng X, Müllen K. Nitrogen-doped ordered mesoporous graphitic arrays with high electrocatalytic activity for oxygen reduction. *Angewandte Chemie* 2010; **122**(14): 2619-2623. doi:10.1002/ange.200907289.

[11] Zhang L, Xia Z. Mechanisms of oxygen reduction reaction on nitrogen-doped graphene for fuel cells. *The Journal of Physical Chemistry C* 2011; **115**(22): 11170-11176. doi:10.1021/jp201991j.

[12] Ramasamy RP, Kumbur EC, Mench MM, Liu W, Moore D, Murthy M. Investigation of macro-and micro-porous layer interaction in polymer electrolyte fuel cells. *International Journal of Hydrogen Energy* 2008; **33**(13): 3351-3367. doi:10.1016/j.ijhydene.2008.03.053.

[13] Zamel N, Li X. Effective transport properties for polymer electrolyte membrane fuel cells–with a focus on the gas diffusion layer. *Progress in Energy and Combustion Science* 2013; **39**(1): 111-146. doi:10.1016/j.pecs.2012.07.002.

[14] Dicks AL. The role of carbon in fuel cells. *Journal of Power Sources* 2006; **156**(2): 128-141. doi:10.1016/j.jpowsour.2006.02.054.

[15] Chu HS, Yeh C, Chen F. Effects of porosity change of gas diffuser on performance of proton exchange membrane fuel cell. *Journal of Power Sources* 2003; **123**(1): 1-9. doi:10.1016/S0378-7753(02)00605-5.

[16] Uchida M, Aoyama Y, Eda N, Ohta A. Investigation of the Microstructure in the Catalyst Layer and Effects of Both Perfluorosulfonate Ionomer and PTFE-Loaded Carbon on the Catalyst Layer of Polymer Electrolyte Fuel Cells. *Journal of the Electrochemical Society* 1995; **142**(12): 4143-4149. doi:10.1149/1.2048477.

[17] Brandon N, Brett D. Engineering porous materials for fuel cell applications. *Philosophical Transactions of the Royal Society of London A: Mathematical, Physical and Engineering Sciences* 2006; **364**(1838): 147-159. doi:10.1098/rsta.2005.1684.

[18] Spernjak D, Prasad AK, Advani SG. Experimental investigation of liquid water formation and transport in a transparent single-serpentine PEM fuel cell. *Journal of Power Sources* 2007; **170**(2): 334-344. doi:10.1016/j.jpowsour.2007.04.020.

[19] Park S, Lee J-W, Popov BN. Effect of PTFE content in microporous layer on water management in PEM fuel cells. *Journal of Power Sources* 2008; **177**(2): 457-463. doi:10.1016/j.jpowsour.2007.11.055.

[20] Saha LK, Tabe Y, Oshima N. Effect of GDL deformation on the pressure drop of polymer electrolyte fuel cell separator channel. *Journal of Power Sources* 2012; **202**: 100-107. doi:10.1016/j.jpowsour.2011.11.038.

[21] Escribano S, Blachot JF, Etheve M, Morin A, Mosdale R. Characterization of PEMFCs gas diffusion layers properties. *Journal of Power Sources* 2006; **156**(1): 8-13. doi:10.1016/j.jpowsour.2005.08.013.

[22] Nitta I, Karvonen S, Himanen O, Mikkola M. Modelling the effect of inhomogeneous compression of GDL on local transport phenomena in a PEM fuel cell. *Fuel Cells* 2008; **8**(6): 410-421. doi:10.1002/fuce.200700058.

[23] Zhou Y, Lin G, Shih A, Hu S. Multiphysics modeling of assembly pressure effects on proton exchange membrane fuel cell performance. *Journal of Fuel Cell Science and Technology* 2009; **6**(4): 041005-041012. doi:10.1115/1.3081426.

[24] Kanda D, Watanabe H, Okazaki K. Effect of local stress concentration near the rib edge on water and electron transport phenomena in polymer electrolyte fuel cell. *International*

*Journal of Heat and Mass Transfer* 2013; **67**: 659-665. doi:10.1016/j.ijheatmasstransfer.2013.08.065.

[25] Nitta I, Himanen O, Mikkola M. Thermal conductivity and contact resistance of compressed gas diffusion layer of PEM fuel cell. *Fuel Cells* 2008; **8**(2): 111-119. doi:10.1002/fuce.200700054.

[26] Nitta I, Hottinen T, Himanen O, Mikkola M. Inhomogeneous compression of PEMFC gas diffusion layer: part I. Experimental. *Journal of Power Sources* 2007; **171**(1): 26-36. doi:10.1016/j.jpowsour.2006.11.018.

[27] Taymaz I, Benli M. Numerical study of assembly pressure effect on the performance of proton exchange membrane fuel cell. *Energy* 2010; **35**(5): 2134-2140. doi:10.1016/j.energy.2010.01.032.

[28] Bograchev D, Gueguen M, Grandidier JC, Martemianov S. Stress and plastic deformation of MEA in fuel cells: Stresses generated during cell assembly. *Journal of Power Sources* 2008; **180**(1): 393-401. doi:10.1016/j.jpowsour.2008.02.048.

[29] Bograchev D, Gueguen M, Grandidier JC, Martemianov S. Stress and plastic deformation of MEA in running fuel cell. *International Journal of Hydrogen Energy* 2008; **33**(20): 5703-5717. doi:10.1016/j.ijhydene.2008.06.066.

[30] Espinoza M, Andersson M, Yuan J, Sundén B. Compress effects on porosity, gas-phase tortuosity, and gas permeability in a simulated PEM gas diffusion layer. *International Journal of Energy Research* 2015; **39**(11): 1528-1536. doi:10.1002/er.3348.

[31] Zhou P, Wu C, Ma G. Influence of clamping force on the performance of PEMFCs. *Journal of Power Sources* 2007; **163**(2): 874-881. doi:10.1016/j.jpowsour.2006.09.068.

[32] Chang W, Hwang J, Weng F, Chan S. Effect of clamping pressure on the performance of a PEM fuel cell. *Journal of Power Sources* 2007; **166**(1): 149-154. doi:10.1016/j.jpowsour.2007.01.015.

[33] García-Salaberri PA, Vera M, Zaera R. Nonlinear orthotropic model of the inhomogeneous assembly compression of PEM fuel cell gas diffusion layers. *International Journal of Hydrogen Energy* 2011; **36**(18): 11856-11870. doi:10.1016/j.ijhydene.2011.05.152.

[34] Shi Z, Wang X, Guessous L. Effect of compression on the water management of a proton exchange membrane fuel cell with different gas diffusion layers. *Journal of Fuel Cell Science and Technology* 2010; **7**(2): 021012. doi:10.1115/1.3177451.

[35] Futerko P, Hsing I-M. Two-dimensional finite-element method study of the resistance of membranes in polymer electrolyte fuel cells. *Electrochimica Acta* 2000; **45**(11): 1741-1751. doi:10.1016/S0013-4686(99)00394-1.

[36] Solasi R, Zou Y, Huang X, Reifsnider K, Condit D. On mechanical behavior and in-plane modeling of constrained PEM fuel cell membranes subjected to hydration and temperature cycles. *Journal of Power Sources* 2007; **167**(2): 366-377. doi:10.1016/j.jpowsour.2007.02.025.

[37] Lee C, Mérida W. Gas diffusion layer durability under steady-state and freezing conditions. *Journal of Power Sources* 2007; **164**(1): 141-153. doi:10.1016/j.jpowsour.2006.09.092.

[38] Mohammadi M, Banks-Lee P, Ghadimi P. Air permeability of multilayer needle punched nonwoven fabrics: Theoretical method. *Journal of Industrial Textiles* 2002; **32**(1): 45-57. doi:10.1106/152808302031065.

[39] Mohammadi M, Banks-Lee P, Ghadimi P. Air permeability of multilayer needle punched nonwoven fabrics: Experimental method. *Journal of Industrial Textiles* 2002; **32**(2): 139-150. doi: 10.1106/152808302031161.

[40] Min CH. Performance of a proton exchange membrane fuel cell with a stepped flow field design. *Journal of Power Sources* 2009; **186**(2): 370-376. doi:10.1016/j.jpowsour.2008.10.048.

[41] Obayopo SO, Bello-Ochende T, Meyer JP. Three-dimensional optimisation of a fuel gas channel of a proton exchange membrane fuel cell for maximum current density. *International Journal of Energy Research* 2013; **37**(3): 228-241. doi:10.1002/er.1935.

[42] Xing XQ, Lum KW, Poh HJ, Wu YL. Optimization of assembly clamping pressure on performance of proton-exchange membrane fuel cells. *Journal of Power Sources* 2010; **195**(1): 62-68. doi:10.1016/j.jpowsour.2009.06.107.

[43] Chi PH, Chan SH, Weng FB, Su A, Sui PC, Djilali N. On the effects of non-uniform property distribution due to compression in the gas diffusion layer of a PEMFC. *International Journal of Hydrogen Energy* 2010; **35**(7): 2936-2948. doi:10.1016/j.ijhydene.2009.05.066.

[44] Zhou Y, Lin G, Shih A, Hu S. Assembly pressure and membrane swelling in PEM fuel cells. *Journal of Power Sources* 2009; **192**(2): 544-551. doi:10.1016/j.jpowsour.2009.01.085.

[45] Sinha PK, Wang CY, Beuscher U. Effect of flow field design on the performance of elevated-temperature polymer electrolyte fuel cells. *International Journal of Energy Research* 2007; **31**(4): 390-411. doi:10.1002/er.1257.

[46] Mehta V, Cooper JS. Review and analysis of PEM fuel cell design and manufacturing. *Journal of Power Sources* 2003; **114**(1): 32-53. doi:10.1016/S0378-7753(02)00542-6.

[47] Wang J, Li S, Zhu G, Zhao W, Chen R, Pan M. Novel non-noble metal electrocatalysts synthesized by heat-treatment of iron terpyridine complexes for the oxygen reduction reaction. *Journal of Power Sources* 2013; **240**: 381-389. doi:10.1016/j.jpowsour.2013.03.189.

[48] Cappadonia M, Erning JW, Niaki SMS, Stimming U. Conductance of Nafion 117 membranes as a function of temperature and water content. *Solid State Ionics* 1995; **77**: 65-69. doi:10.1016/0167-2738(94)00289-5.

[49] Higier A, Liu H. Effects of the difference in electrical resistance under the land and channel in a PEM fuel cell. *International Journal of Hydrogen Energy* 2011; **36**(2): 1664-1670. doi:10.1016/j.ijhydene.2010.11.007.

[50] Higier A, Liu H. Direct measurement of current density under the land and channel in a PEM fuel cell with serpentine flow fields. *Journal of Power Sources* 2009; **193**(2): 639-648. doi:10.1016/j.jpowsour.2009.03.059.

[51] Bautista-Rodríguez CM, Rosas-Paleta A, Rivera-Márquez JA, Solorza-Feria O. Study of electrical resistance on the surface of Nafion 115® membrane used as electrolyte in

PEMFC technology part ii: surface response methodology. *International Journal of Electrochemical Science* 2009; **4**: 60-76. doi:www.electrochemsci.org.

[52] Tanaka S, Bradfield WW, Legrand C, Malan AG. Numerical and experimental study of the effects of the electrical resistance and diffusivity under clamping pressure on the performance of a metallic gas-diffusion layer in polymer electrolyte fuel cells. *Journal of Power Sources* 2016; **330**: 273-284. doi:10.1016/j.jpowsour.2016.08.121.

[53] Hamour M, Grandidier J, Ouibrahim A, Martemianov S. Electrical conductivity of PEMFC under loading. *Journal of Power Sources* 2015; **289**: 160-167. doi:10.1016/j.jpowsour.2015.04.145.

[54] Wu Z, Zhou Y, Lin G, Wang S, Hu SJ. An improved model for predicting electrical contact resistance between bipolar plate and gas diffusion layer in proton exchange membrane fuel cells. *Journal of Power Sources* 2008; **182**(1): 265-269. doi:10.1016/j.jpowsour.2008.03.044.

[55] Mishra V, Yang F, Pitchumani R. Measurement and prediction of electrical contact resistance between gas diffusion layers and bipolar plate for applications to PEM fuel cells. *Journal of Fuel Cell Science and Technology (Transactions of the ASME)* 2004; **1**(1): 2-9. doi:10.1115/1.1782917.

[56] Zhou Y, Lin G, Shih A, Hu S. A micro-scale model for predicting contact resistance between bipolar plate and gas diffusion layer in PEM fuel cells. *Journal of Power Sources* 2007; **163**(2): 777-783. doi:10.1016/j.jpowsour.2006.09.019.

[57] Zhang L, Liu Y, Song H, Wang S, Zhou Y, Hu SJ. Estimation of contact resistance in proton exchange membrane fuel cells. *Journal of Power Sources* 2006; **162**(2): 1165-1171. doi:10.1016/j.jpowsour.2006.07.070.

[58] Greenwood J, Williamson JP. Contact of nominally flat surfaces. Proceedings of the Royal Society of London A: Mathematical, Physical and Engineering Sciences: The Royal Society; 1966. p. 300-319.

[59] Cooper M, Mikic B, Yovanovich M. Thermal contact conductance. *International Journal of Heat and Mass Transfer* 1969; **12**(3): 279-300. doi:10.1016/0017-9310(69)90011-8.

[60] Majumdar A, Tien C. Fractal characterization and simulation of rough surfaces. *Wear* 1990; **136**(2): 313-327. doi:10.1016/0043-1648(90)90154-3.

[61] Lee WK, Ho CH, Van Zee JW, Murthy M. The effects of compression and gas diffusion layers on the performance of a PEM fuel cell. *Journal of Power Sources* 1999; **84**(1): 45-51. doi:10.1016/S0378-7753(99)00298-0.

[62] Ge J, Higier A, Liu H. Effect of gas diffusion layer compression on PEM fuel cell performance. *Journal of Power Sources* 2006; **159**(2): 922-927. doi:10.1016/j.jpowsour.2005.11.069.

[63] Bazylak A, Sinton D, Liu Z-S, Djilali N. Effect of compression on liquid water transport and microstructure of PEMFC gas diffusion layers. *Journal of Power Sources* 2007; **163**(2): 784-792. doi:10.1016/j.jpowsour.2006.09.045.

[64] Zhou P, Wu C. Numerical study on the compression effect of gas diffusion layer on PEMFC performance. *Journal of Power Sources* 2007; **170**(1): 93-100. doi:10.1016/j.jpowsour.2007.03.073.

[65] Berning T, Lu D, Djilali N. Three-dimensional computational analysis of transport phenomena in a PEM fuel cell. *Journal of Power Sources* 2002; **106**(1): 284-294. doi:10.1016/S0378-7753(01)01057-6.

[66] Hussain M, Li X, Dincer I. Multi-component mathematical model of solid oxide fuel cell anode. *International Journal of Energy Research* 2005; **29**(12): 1083-1101. doi:10.1002/er.1141.

[67] Wu H, Berg P, Li X. Steady and unsteady 3D non-isothermal modeling of PEM fuel cells with the effect of non-equilibrium phase transfer. *Applied Energy* 2010; **87**(9): 2778-2784. doi:10.1016/j.apenergy.2009.06.024.

[68] Wang J, Yuan J, Sundén B. Modeling of inhomogeneous compression effects of porous GDL on transport phenomena and performance in PEM fuel cells. *International Journal of Energy Research* 2016; **41**(7): 985–1003. doi:10.1002/er.3687.

[69] Todd B, Young J. Thermodynamic and transport properties of gases for use in solid oxide fuel cell modelling. *Journal of Power Sources* 2002; **110**(1): 186-200. doi:10.1016/S0378-7753(02)00277-X.

[70] Yuan J, Huang Y, Sundén B, Wang WG. Analysis of parameter effects on chemical reaction coupled transport phenomena in SOFC anodes. *Heat and Mass Transfer* 2009; **45**(4): 471-484. doi:10.1007/s00231-008-0449-6.

[71] Di Stefano G. Modeling thermal energy storage systems with OpenFOAM. *Doctoral Dissertation* 2014: 1-94. doi:http://hdl.handle.net/10589/98281.

[72] Su A, Chiu Y, Weng F. The impact of flow field pattern on concentration and performance in PEMFC. *International Journal of Energy Research* 2005; **29**(5): 409-425. doi:10.1002/er.1059.

[73] Ferng YM, Su A, Lu SM. Experiment and simulation investigations for effects of flow channel patterns on the PEMFC performance. *International Journal of Energy Research* 2008; **32**(1): 12-23. doi:10.1002/er.1320.

[74] Yuan J, Sundén B. On mechanisms and models of multi-component gas diffusion in porous structures of fuel cell electrodes. *International Journal of Heat and Mass Transfer* 2014; **69**: 358-374. doi:10.1016/j.ijheatmasstransfer.2013.10.032.

[75] Akkaya AV. Electrochemical model for performance analysis of a tubular SOFC. *International Journal of Energy Research* 2007; **31**(1): 79-98. doi:10.1002/er.1238.

[76] Borup RL, Davey JR, Garzon FH, Wood DL, Inbody MA. PEM fuel cell electrocatalyst durability measurements. *Journal of Power Sources* 2006; **163**(1): 76-81. doi:10.1016/j.jpowsour.2006.03.009.

[77] Barrande M, Bouchet R, Denoyel R. Tortuosity of porous particles. *Analytical Chemistry* 2007; **79**(23): 9115-9121. doi:10.1021/ac071377r.

[78] Obayopo SO, Bello-Ochende T, Meyer JP. Three-dimensional optimisation of a fuel gas channel of a proton exchange membrane fuel cell for maximum current density. *International Journal of Energy Research* 2013; **37**(3): 228-241. doi:10.1002/er.1935.

[79] Miao Z, He Y-L, Zou J-Q. Modeling the effect of anisotropy of gas diffusion layer on transport phenomena in a direct methanol fuel cell. *Journal of Power Sources* 2010; **195**(11): 3693-3708. doi:10.1016/j.jpowsour.2009.12.048.

[80] Sivertsen B, Djilali N. CFD-based modelling of proton exchange membrane fuel cells. *Journal of Power Sources* 2005; **141**(1): 65-78. doi:10.1016/j.jpowsour.2004.08.054.

[81] Cengel YA, Boles MA. Thermodynamics: An Engineering Approach. Kanoğlu M (ed.). Published: McGraw-Hill Higher Education, New York (USA), 1994.

[82] Zhang Z, Jia L, Wang X, Ba L. Effects of inlet humidification on PEM fuel cell dynamic behaviors. *International Journal of Energy Research* 2011; **35**(5): 376-388. doi:10.1002/er.1692.

[83] He G, Yamazaki Y, Abudula A. A three-dimensional analysis of the effect of anisotropic gas diffusion layer (GDL) thermal conductivity on the heat transfer and two-phase behavior in a proton exchange membrane fuel cell (PEMFC). *Journal of Power Sources* 2010; **195**(6): 1551-1560. doi:10.1016/j.jpowsour.2009.09.059.

[84] Khandelwal M, Mench M. Direct measurement of through-plane thermal conductivity and contact resistance in fuel cell materials. *Journal of Power Sources* 2006; **161**(2): 1106-1115. doi:10.1016/j.jpowsour.2006.06.092.

[85] Uchida M, Aoyama Y, Eda N, Ohta A. Investigation of the Microstructure in the Catalyst Layer and Effects of Both Perfluorosulfonate Ionomer and PTFE-Loaded Carbon on the Catalyst Layer of Polymer Electrolyte Fuel Cells. *Journal of the Electrochemical Society* 1995; **142**(12): 4143-4149. doi:10.1149/1.2048477.

[86] Nguyen PT, Berning T, Djilali N. Computational model of a PEM fuel cell with serpentine gas flow channels. *Journal of Power Sources* 2004; **130**(1): 149-157. doi:10.1016/j.jpowsour.2003.12.027.

[87] Lai Y-H, Rapaport PA, Ji C, Kumar V. Channel intrusion of gas diffusion media and the effect on fuel cell performance. *Journal of Power Sources* 2008; **184**(1): 120-128. doi:10.1016/j.jpowsour.2007.12.065.

[88] Martemianov S, Gueguen M, Grandidier J, Bograchev D. Mechanical effects in PEM fuel cell: application to modeling of assembly procedure. *Journal of Applied Fluid Mechanics* 2009; **2**: 49-54. doi:www.jafmonline.net.

[89] Kandlikar S, Lu Z, Lin T, Cooke D, Daino M. Uneven gas diffusion layer intrusion in gas channel arrays of proton exchange membrane fuel cell and its effects on flow distribution. *Journal of Power Sources* 2009; **194**(1): 328-337. doi:10.1016/j.jpowsour.2009.05.019.

[90] Yang WJ, Kang SJ, Kim YB. Numerical investigation on the performance of proton exchange membrane fuel cells with channel position variation. *International Journal of Energy Research* 2012; **36**(10): 1051-1064. doi:10.1002/er.2904.

[91] Hottinen T, Himanen O, Karvonen S, Nitta I. Inhomogeneous compression of PEMFC gas diffusion layer: part II. Modeling the effect. *Journal of Power Sources* 2007; **171**(1): 113-121. doi:10.1016/j.jpowsour.2006.10.076.

[92] Wang L, Husar A, Zhou T, Liu H. A parametric study of PEM fuel cell performances. *International Journal of Energy Research* 2003; **28**(11): 1263-1272. doi:10.1016/S0360-3199(02)00284-7.

[93] Karimi G, Li X, Teertstra P. Measurement of through-plane effective thermal conductivity and contact resistance in PEM fuel cell diffusion media. *Electrochimica Acta* 2010; **55**(5): 1619-1625. doi:10.1016/j.electacta.2009.10.035.

# Appended publications

# Paper I

9th OpenFOAM® Workshop
23-26 June 2014 in Zagreb, Croatia

# Coupled simulation approaches for PEM fuel cells by OpenFOAM

**Jiatang Wang*[1], Jinliang Yuan[1] and Bengt Sundén[1]**

1 *Department of Energy Sciences, Lund University, Box 118, Lund 22100, Sweden*
* *E-mail: Jiatang.wang@energy.lth.se*

## ABSTRACT

Proton exchange membrane (PEM) fuel cells are known as environmental friendly energy conservation devices, and have the potential to be suitable alternative power sources. The cost and durability of a PEM fuel cell are strongly affected by the involved transport phenomena and reactions, which are two major challenges to be overcome before commercialization. Modeling and simulation are crucial for the cell design and operation. Various "add-on" fuel cell modules are available in commonly-used commercial CFD codes: FLUENT, STAR-CD and COMSOL Multiphysics. However, the length scale of PEM fuel cell's main components ranges from the micro over the meso to the macro level. The various transport processes at different scales sometimes cannot be captured simultaneously by these codes. On the other hand, physical properties of functional layers used in MEA (membrane electrolyte assembly, consisting of catalyst layers, gas diffusion layers and membrane) play an important role for the cell performance. Therefore coupling of the multi-scale structural and transport characteristics in the functional layers might be an effective way to understand the electrochemical reactions and transient transport phenomena in PEM fuel cells. OpenFOAM (Open Field Operation and Manipulation) is an open source finite volume code having an object-oriented design written in C++, which allows implementation of own models and numerical algorithms. Furthermore, it is possible to integrate other models, e.g., particle-based models, with the OpenFOAM CFD Toolbox. Thus OpenFOAM has the potential to meet the requirements faced in PEM fuel cell simulations as mentioned above. In this paper, various models and applications of OpenFOAM are outlined and reviewed, focusing on the multi-phase transport processes and reactions in PEM fuel cells. The potential methods and challenges coupling OpenFOAM with other modeling techniques are also discussed and highlighted.

**Key words:** PEM fuel cells, simulation, multi-scale, coupling, OpenFOAM, transport phenomena

## 1. INTRODUCTION

Proton exchange membrane (PEM) fuel cells fuelled by hydrogen are considered to be promising devices for the direct conversion of chemical energy into electrical energy. The first commercial use of a typical PEM fuel cell was in 1960's Gemini space program by NASA [1]. Owing to its advantages of efficient energy conversion, high power density and environmental friendliness, tremendous research programs worldwide promoted PEM fuel cells as power sources replacing internal combustion engines in sub- to mega-Watt applications in transportation, heating, manufacturing, and communication [2, 3]. The energy resources crisis all over the world also promotes the development of PEM fuel cells. After the first energy crisis happened in 1973, the new energy devices, e.g., PEM fuel cells, attracted more and more attentions [1].

Cost and durability are supposed as the main challenges or bottlenecks to the development and commercialization of PEM fuel cells [4]. During the past decades, the performance of PEM fuel cells

have been improved significantly resulting from research efforts on different aspects, e.g., implementation of innovative materials [5] and optimized design [6] based on experiments and modeling [7]. Even though many efforts have been taken into account for comprehensive improvement of the performance, barriers for the widely use of PEM fuel cells are still present.

### *1.1 Working principles of PEM Fuel Cell*

Typically a PEM fuel cell operates below 100 ºC (usually at 80 ºC). Hydrogen gas mixed with water is supplied to the anode side and air/water stream to the cathode side. Anodic hydrogen is oxidized in the anode catalyst layer (CL) to liberate electrons and produce protons. Then the electrons flow through the anode gas diffusion layer (GDL), bipolar plate, external circuit and further to the cathode CL. The produced protons are transported through the solid electrolyte membrane to the cathodic side. Oxygen is reduced within the cathodic CLs, and then combines with the electrons and protons to produce water and heat. A two-dimensional (2-D) sketch of the reactions and transport processes are shown in Fig. 1. The reactions at the anode and cathode for a PEM fuel cell are respectively given by,

$$H_2 \rightarrow 2H^+ + 2e^- \tag{1a}$$

$$\frac{1}{2}O_2 + 2H^+ + 2e^- \rightarrow H_2O \tag{1b}$$

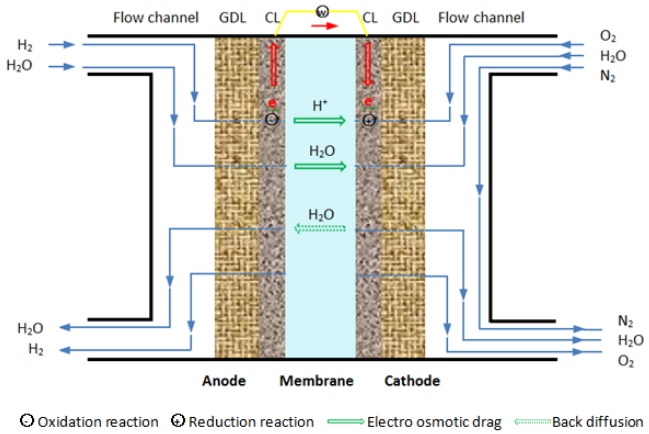


Fig. 1 Schematic of PEM fuel cell.

### *1.2 Transport Phenomena in PEM Fuel Cells*

Typically the transport processes of water, heat, gases and charges (protons and electrons) occur simultaneously inside the porous media of PEM fuel cells. These are (a) transport of the reactants to the reaction sites; (b) transport of protons between the reaction sites and membrane; (c) conduction of electrons between the current collectors and the reaction sites; (d) transport, primarily through the solid matrix, of heat produced by the exothermic reaction; and (e) transport of water vapor and liquid water with phase-change by condensation/evaporation [4]. It is believed that water management and the heat balance are extremely important for the operation of PEM fuel cells, because the performance of the membrane, with good proton conductivities if fully hydrated, highly depends on the water content and temperature [1].

Water content inside the fuel cell can be determined by the balance between water production and three water transport processes, which are electro-osmotic drag, back diffusion and diffusion of water

from/to the fuel/oxidant gas streams, as shown in Fig. 1. In order to ensure that the membrane is hydrated, water is introduced into the fuel cell with the reactants. But the temperature of the humidifying water also affects the performance of the membrane. In fact, membrane dehydration occurs if that temperature is too high as the water may completely evaporate, while flooding may take place at a lower temperature, particularly in the GDLs and CLs [8].

The transport of ions is another factor affecting the fuel cell efficiency. In the initial operating stage, a small amount of oxygen (or hydrogen) reaches to the catalyst surfaces of the CLs by diffusion due to the small gas concentration gradient. After some amount of oxygen (or hydrogen) consumed due to the electrochemical reactions, the gas mixture is then transported by combined convection and diffusion in the voids through the GDLs towards the CLs. The charge transport through the membrane and electrodes is driven by electrical and chemical potentials. There is a resistance for the transport of protons and electrons through the membrane and the electrode, respectively. Commonly the resistance depends on the corresponding structural properties and operating conditions.

It is believed that the catalyst layers, in which complex and coupled processes unfold in, are the toughest unknown components because all physicochemical processes occur there [3]. In operational PEM fuel cells, all components have to be designed well to optimize the complex interplaying transport phenomena and reactions. Due to the nano/micro scales and complex porous structures used in the membrane electrode assembly (MEA), the interactions between fluid and solid particles within the multi-scale and porous structures become strong and should be taken into account. It is clear that the oxygen reduction reaction (ORR) in the cathode of the PEM fuel cell is especially regarded as the dominant limiting factor because of its lower reaction kinetics on electrochemical reactions, compared to the hydrogen oxidized reaction (HOR) in the anode [9]. Therefore, reducing various polarizations and keeping a balance on the transport species inside the fuel cell are important in the operation of PEM fuel cells.

The understanding of the transport processes of different phenomena is crucial for optimizing the design and performance of PEM fuel cells. With the rapid development of computer technology, simulation of a desired model is becoming widely used in this kind of sustainable energy applications. In this paper, the problems remaining in the analysis of transport phenomena and simulations of PEM fuel cells are discussed. The modeling approaches of OpenFOAM for PEM fuel cells are briefly reviewed. Additionally, the opportunity of OpenFOAM to be used in multi-scale modeling in PEM fuel cells is discussed.

## 2. CHALLENGES FOR ANALYSIS OF TRANSPORT PROCESSES IN PEM FUEL CELLS

The technology development of PEM fuel cells currently cannot meet the requirement of commercialization. Large amount of experimental data have been established revealing the relationships between the different operating and design parameters, which are the initial and basic knowledge for understanding the mechanisms of PEM fuel cells. However, the interplaying transport processes inside the porous functional layers are not fully understood, especially for the CLs and membrane. Additionally, the limitations of experimental measurements are apparent for the interplaying transport processes appearing at the small scales and the complex structures.

### *2.1 Material applications and effects*

Synthesizing of functional materials is important for MEA performance. The distributions and structures of functional materials in GDLs and CLs are quite non-uniform, as shown in Fig. 2 and Fig. 3. The distributions of platinum on carbon particle carriers is also not constant in time, as the catalyst particles usually migrate with time due to their involvement in the unintended transport processes and side-reactions during operation [10].

Material treatment and applications in CLs, GDLs and membrane are always related to the optimized and important transport processes in PEM fuel cells. For example, in order to avoid water flooding at high current densities, the GDLs are treated with PTFE to impart hydrophobicity, which can force water droplets to agglomerate at the surface of the GDL [4].

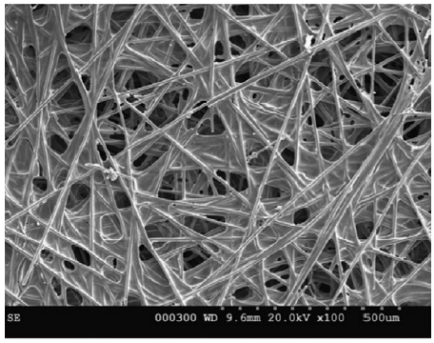


Fig. 2 SEM image of GDL carbon paper treated with PTEF [11].

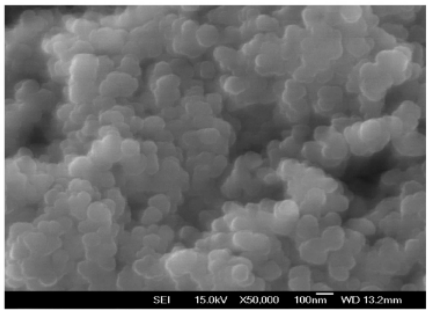


Fig. 3 SEM image of a CL [12].

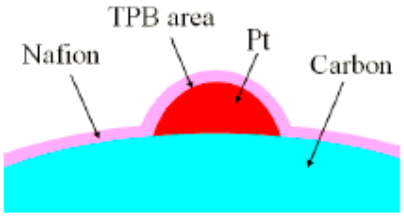


Fig. 4 A schematic drawing of the TPB [13].

The effect of the catalyst synthesizing is also important. A porous carbon support with excellent conductivities is commonly selected. Apparently, the porous carbon has a better ability for the transport of reactants and products in the fuel cells, and a good conductivity for the conduction of electrons, which can decrease the concentration polarization and ohmic polarization, respectively. Currently researchers are also interested in synthesizing ordered mesoporous and macroporous carbon used as the catalyst support [5]. It is believed that the gas, charges and water transport through this kind of ordered 3D porous media is more efficient. On the other hand, the Pt particles can be doped on the Pt/carbon more uniform, which is another advantage for the reacting species transport to active sites. Kim and co-workers [12] stated that large pores with significant volume fraction play a dominant role for enhancing transport of the gas phases in the CLs. Particularly, the pores between 20 and 200 nm are important. With microscopic structure of CLs, carbon (or other) particles with surface deposits of platinum (a preferred catalyst) may be bonded by the membrane (an ion-conducting ionomer), as shown in Fig. 4. It is believed that the triple-phase boundary (TPB) between the catalyst/support,

ionomer and pores is the place where the electrochemical reactions occur [13]. Moreover, a carbon layer with micropores is sandwiched between GDL and CL in recent years [14]. This innovative method may avoid flooding at high current densities. This inserted layer can be regarded as the bridge connecting between the CL and GDL. Pasaogullari and co-workers [15] confirmed, by simulations, that placing a micro-porous layer between the GDL and CL enhances the liquid-water removal and reduces the liquid saturation in the catalyst layer.

*2.2 Simulation and analysis methods.*

During the past decades, tremendous researches have been carried out on investigating the manufacturing, design and optimization. It is widely realized that modeling and simulation are crucial for the cell design and optimization. It can decrease the research cost and time. Moreover, simulation can solve the problems which cannot be captured in experiments, e.g., the water, heat, charge, and gases distributions inside the fuel cell, particularly in the functional layers.

Nowadays, modeling becomes an effective way to deeply understand the transport phenomena and the reactions of PEM fuel cells. This can give directions on the fuel cell manufacturing and improved performance. Various continuum approaches, e.g., computational fluid dynamics (CFD), have been developed to evaluate the water transport processes and the effects on the reactions and other transport phenomena [16]. Various "add-on" fuel cell modules are available in commonly-used commercial CFD codes, e.g., FLUENT, STAR-CD, and COMSOL Multiphysics.

A general classification of these modeling efforts can be identified as: from one-dimensional to multi-dimensional, from isothermal to non-isothermal, from single-phase to multi-phase, from single components to the unit cell, and from transient to steady state [17]. The dimensions of these modeling can be divided into several scales, i.e. large-scale [18], macro-scale [19], micro-scale and nano-scale [20, 21], based on the length scale of the computational domain. The processes in large-scale and macro-scales are commonly simulated by the computational fluid dynamics (CFD) method, while small-scale treated by Molecular Dynamics (MD) method [20] and Lattice Boltzmann Method (LBM) [21]. Every method has its own advantages and disadvantages in investigating the transport processes of PEM fuel cells. With the help of effective and commercial simulation codes, a large number of articles have been published. But sometimes the individual commercial CFD tool and MD method cannot meet the requirement of analyzing PEM fuel cells. This is due to the multiscale nature, coupled functional structure and physical properties, which cannot be captured by a single tool.

The basic parameters and cell performance, e.g., pore size and mean free path of gas molecules and Knudsen number of PEM fuel cell components, are listed in Table 1. It can be seen that the parameters of different layers in PEM fuel cells range from nanometers to centimeters, i.e., in a typical multi-scale scope. The Knudsen number, $K_n$ used in the CFD, is calculated by Equation (2),

$$K_n = \frac{\lambda}{L} \tag{2}$$

where $\lambda$ is the mean free path, $L$ a representative physical length scale. The pore size inside the porous materials is widely assumed as the physical length scale in PEM fuel cells [22]. The Knudsen number, $K_n$, based on the ratio of average distance between gas collisions and the pore size (~10 nm), is about 8.2 for the CLs [23]. For the GDLs, the Knudsen number becomes in the range of 0.01 to 10. It means that the continuum approach is not able to directly resolve the influence of the structural morphology on the water transport/state-change dynamics, particularly in the CLs.

The common assumptions in CFD are the continuum transport processes appearing in the homogeneous structures. However， the active sites, "triple point" locus shown in Fig. 4, should not be simply represented in a two-dimensional or homogeneous idealization. Pharoah and co-workers [26] reviewed the modeling development evaluating the current densities and effective transport

coefficients in porous PEMFC electrodes. It was concluded that a majority of the existing PEMFC models volume-averaging the effect of porous media by a function that assumes the electrode to be isotropic. But this ignorance of the fact of inherent anisotropic microstructure in the porous carbon-fiber electrode results in distinctly different effective mass diffusivity, electronic conductivity, thermal conductivity, and hydraulic permeability in the through-plane and the in-plane directions.

Table 1 Typical parameter in PEM fuel cells [3, 22, and 24, 25].

| Components | Thickness | Particle size | Pores size | Mean free path (gas) | $K_n$ |
|---|---|---|---|---|---|
| CLs | 10-20 μm | 5-10 nm (Carbon Particle)<br>30-100 nm (Agglomerates) | 1-10 nm<br>10-50 nm | 100 nm | 10-100<br>2-10 |
| GDLs | 100-300 μm | 5-10 μm | 10 nm-10 μm | 100 nm | 0.01-10 |
| Membrane | 50-300 μm | 5 nm | 1 nm | 100 nm | 100 |
| Channel | 10 cm (length) | — | 1 mm (height) | 100 nm | < 0.001 |

Thus the homogeneous assumption used in the continuum methods sometimes cannot successfully capture the transport phenomena inside the porous structure and clusters, e.g., carbon particles. The simulation on interplaying transport processes concerning the multi-scale, porous functional and anisotropic structural materials used in the PEM fuel cells requires a coupled modeling approach.

## 3. SIMULATION OF PEM FUEL CELLS BY OPENFOAM

### *3.1 Advantages of OpenFOAM*

A recently developed simulation code is OpenFOAM, which is a general purpose open-source CFD C++ code for fluid and continuum mechanics. It has a large number of active users working in many areas of engineering and science, in both industries and academic organizations. OpenFOAM uses an object oriented approach which makes it easy to extend. The package includes modules for a wide range of applications. The numerical solution of differential equations implemented in OpenFOAM uses the finite volume (FV) method on unstructured meshes, and provides many capabilities, including free-surface and multi-phase flow modeling, Lagrangian spray model and automatic mesh motion. OpenFOAM allows implementing own models and numerical algorithms. Accordingly it is possible to combine other models, e.g., particle-based models, with the OpenFOAM CFD Toolbox. Thus OpenFOAM has the potential to meet the requirements faced in PEM fuel cell simulations as mentioned above. There is almost no limitation according to the features of OpenFOAM.

### *3.2 Literature Survey of Fuel Cell Simulations by OpenFOAM*

Simulations of PEM fuel cells by OpenFOAM were conducted by several researchers in recent years, who were also involved in modeling of solid oxide fuel cells (SOFC). The development of the SOFC model by OpenFOAM was first described by Novaresio and co-workers [27] in 2011. The SOFC module library can only be used in the version OpenFOAM-1.6-ext, which is the initial version of OpenFOAM. Several multi-component mass-transport models were implemented in this code, e.g., Fick's, Stefan-Maxwell and the Dusty Gas diffusion model, which can simulate both porous media and porosity-free domains. Almost in the same year a special code for SOFC simulation called 'openfuelcell' was developed and financially supported by the Multi-Scale Integrated Fuel Cell (MuSIC) program, which can be used in the new version of OpenFOAM 2.1.1. The 'openfuelcell' model was designed for the comprehensive simulation of single channel or several parallel channels. It should be noted that both codes developed for SOFC can be freely downloaded from the website.

Moreover, several PEM fuel cell simulation papers using OpenFOAM can also be found. However, the number of published papers related to SOFC by OpenFOAM is substantially bigger than that for PEM fuel cells.

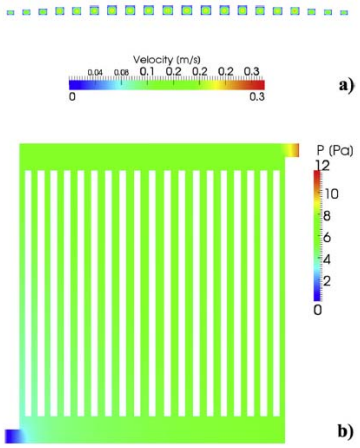


Fig. 5 Numerical simulation results of optimized sample for (a) cross reaction velocity field, (b) pressure field [6].

Regarding the usage of OpenFOAM for PEM fuel cells, about ten articles have been published in journals or conferences [6, 16, 28-31]. In the work of Mustata et al. [16], two kinds of gas inlet, i.e., "U" shape and "Z" shape were considered and the focus is on distribution of the air flow rate in a proton exchange membrane fuel cell stack. In all cases the flow pattern is adequate, although the Z configuration is preferable. Regarding the work by Lozano et al. [29], an experimental and numerical study was presented to analyze the gas flow across a GDL from different bipolar plates. The experimental results were compared with the predictions obtained from a numerical simulation. Additionally, a review made by Siegel [30] stated that large-scale problems can be solved using parallel computing and the MPI-protocol. OpenFOAM is well suited for fuel cell modeling besides the commercial CFD softwares. However, coding knowledge is required. It means that OpenFOAM has advantages for simulation at large scales. Imbrioscia and partner [6] used OpenFOAM for optimizing the bipolar plate geometry, e.g., width, depth and shape of the distributing channels (collectors) as well as over the main channels, in order to get a homogeneous flow distribution. The numerical simulation results of optimized samples were shown in Fig. 5 (a) for the cross section velocity field, (b) for the pressure field. Valino and co-workers [28] studied numerically the nonhomogeneous distribution of the reacting flows at the catalyst layers of a working bipolar plate of a PEMFC for pure hydrogen and oxygen. Moreover, they used OpenFOAM to model real single cell geometry, using a 3D finite volume discretization. The results are validated against experimental data. The model was implemented in a developed module attached to OpenFOAM general package [31].

## 4. DOWN-SCALE MODELING APPROACHES

The physical properties of the functional materials vary significantly and show high anisotropy in GDLs and CLs of PEM fuel cells. In the CLs of a PEM fuel cell, the void space is filled with the reactant and product species, hence, the protonic and electronic conductivity of the void space is zero. Especially the ionomer phases also act as electrical insulators [32]. Moreover, the basic fibers applied in GDLs cause anisotropic permeability and thermal conductivity. The interplaying transport phenomena in the functional microstructure inside the fuel cell need to be concerned.

Operating at a low temperature, which is the advantage of PEM fuel cells, turns into a complex problem compared with other kinds of fuel cells. The electrochemical reaction at the TPBs and multiphase flow (water vapor and liquid phases) occur inside the porous media and on the surface of

the solid particles. The CFD method used in a PEM fuel cell employs the effective values that can simulate the fluid flow and species transport distributions, velocity and pressure with proper boundary conditions. However, analytical techniques used to capture the liquid water distribution inside the diffusion media have revealed that many of the theories and assumptions used for liquid water transport mechanism are inappropriate under normal operating conditions [33, 34]. On the other hand, the fluids have a homogenous appearance on macroscopic scales, but are very disordered and heterogeneous over smaller scales due to thermal fluctuations and complex interactions inside the PEM fuel cell.

From the microscopic point of view, the molecular dynamics (MD) and discrete particle method, e.g., the dissipative particle dynamics (DPD) and smoothed particle hydrodynamics (SPH) are realistic approaches but suffer from the inability to explore suitable spatial and time scales outside the microscopic regime [35, 36]. MD is too expensive for large numbers of molecules. In the so-called pseudo particle methods, e.g., coarse-grained (CG) MD or DPD, a particle represents a small cluster of atoms and molecules, and it can be used at larger particle size [37]. The DPD is acceptable for the length and time scales ranging from 10-1000 nm and 1 ns-10 ms, respectively [38, 39]. The SPH is a fully Lagrangian scheme where a set of macroscopic governing equations are discretized by interpolating the flow properties over a discrete set of points, i.e., pseudo particles, which are distributed randomly within the domain of solution, without the need to define a spatial mesh [36].

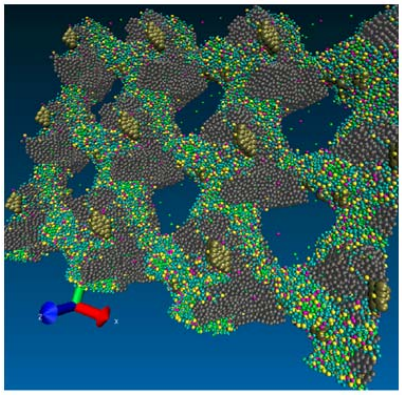

Fig. 6 Reconstruction of CLs by the CG method [2].

A specific example using CG-MD method was presented by Wescott and coworkers [41]. They divided the membrane system into three components, namely the backbone, side-chain and water, to analyze the water content. The interaction parameters for this model were generated using classical molecular dynamics. The CG-MD method was also applied in the study of CLs in a PEM fuel cell. A CL structure was reconstructed by Xiao et al. [2] as shown in Fig. 6. The simulation results were also compared with laboratory test data. In principle, the process-based CG method can provide various microscopic parameters from the reconstructed microstructure, which are related to the important structural and effective transport parameters used in the upper scale models, for comprehensive understanding of the multifunctional porous materials and the various transport processes coupled with the electrochemical reactions in the PEM fuel cell [40].

Additionally, the LBM has become an effective tool to simulate the water transport in GDL. LBM can give more realistic pore-scale dynamic simulations of water transport in GDL with accurate pore geometry taken into consideration. Niu et al. [21] presented an LBM model in which a water-gas flow in the GDL is simulated and the saturation-dependent transport properties under different conditions are investigated. Compared to the MD simulation, the LBM approach assumes that the fluid is made of large amounts of fluid “particles”, instead of individual molecules, which are still considerably smaller than the smallest length scale of the simulation domain [17].

## 5. COUPLED MODELING METHODS

A desired model should have a multiscale character to couple both microscopic and macroscopic flow characters [36]. Despite recent progress in developing multiscale modeling [42], enormous challenges still remain in bridging between atomistic simulation of realistic structures and continuum models which describe the overall performance for PEM fuel cell applications.

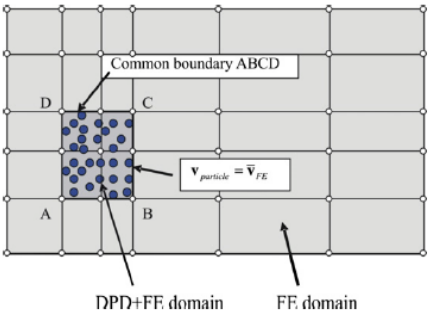


Fig. 7 Two domains within a flow field and boundary conditions at the common boundary (interface) between fine (meso) and coarse (FE) models [44].

The above-mentioned microscopic approaches are limited, in terms of investigated phenomena and the number of particles simulated even by the largest supercomputers. Also they are considered too difficult for resolving the micro- to macroscopic interactions that must be captured in the analysis of any real devices. The recognition of these issues has led to the development of several methods for the coupling of micro- and macroscopic descriptions in a single modeling and simulation framework. The major goal of these methods is to allow the use of a continuum-based technique, e.g., CFD in the parts of the domain where such a description is valid, while using a microscopic method for the subdomain where the continuum description breaks down, i.e., in the porous CLs or and GDLs of PEMFCs.

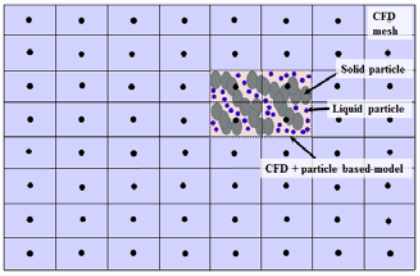


Fig. 8 Coupled methodology might be used in PEM fuel cells by OpenFOAM.

Some attempts have been made previously to couple and bridge the approaches. In 1997, Groot and partner [43] reviewed DPD as a mesoscopic simulation method and also made the link between various parameters in Flory-Huggins-type models. This is possible because the equation of state of the DPD fluid is essentially quadratic in density. This link opens the way to do large scale simulations, effectively describing millions of atoms. Kojic and co-workers [44] reviewed the possibility to couple equations of a multiscale procedure by considering a mesoscale discrete particle model and a macroscale continuum model for incompressible fluid flow. Also they supplied a simple example to confirm the possibility. The finite element (FE) method was applied for the Navier-Stokes and continuity equations. The DPD method was applied for the mesoscale discrete particle model, As shown in Fig. 7.

Although OpenFOAM uses the FV method on unstructured meshes, the progress made by Groot and Kojic and their partners mentioned above supplied a possible direction for coupling the pseudo particle method to the CFD in OpenFOAM. It is possible to insert a particle-based model to the open

source toolbox, as shown in Fig. 8. The entire simulation domain is divided into a local domain and a global domain. The transport processes and reactions in the local domain are modeled with both the particle based-model and CFD, while those in the global domain modeled by the CFD (FV method) only. Consequently, modeling for a PEM fuel cell with improved and optimized mathematical functions for the small-scaled processes may come through. Most importantly, the different components inside the PEM fuel cell with different Knudsen numbers might be simulated simultaneously in one model.

## 6. CONCLUSION

Multi-scale and -functional porous materials used in MEA of PEM fuel cells play an important role on the overall performance of the fuel cell. Owing to the improvement in computer technology, modeling of multiscale phenomena is an effective way to gain deeper understanding of the interplaying transport phenomena in PEM fuel cells. OpenFOAM is an open source C++ code and has the potential to be coupled with other models, e.g., particle-based models. Especially coupling of the dissipative particle method and the continuum method is envisaged. The coupling method using OpenFOAM might be a promising approach in deeper investigations to promote the understanding of PEM fuel cells. By this hybrid approach, it is feasible to capture the effects of property gradient related fluxes at the continuum scale and the particle inclusions/boundaries within the particle based-domain simultaneously, which is significant to evaluate the continuum transport processes and water transfer dynamics in PEM fuel cells.

## ACKNOWLEDGMENTS

The first author (J. Wang) is supported by a scholarship from China Scholarship Council (CSC) to carry out his PhD studies in Sweden. The National Swedish Research Council (VR) is also gratefully acknowledged for complementary financial support.

## REFERENCES

[1] Bhatt, S., Gupta, B., Sethi, V. K., & Pandey, M. (2012). Polymer Exchange Membrane (PEM) Fuel Cell: A Review. *International Journal of Current Engineering and Technology*, *2*(1), 219-226.

[2] Xiao, Y., Dou, M., Yuan, J., Hou, M., Song, W., & Sundén, B. (2012). Fabrication Process Simulation of a PEM Fuel Cell Catalyst Layer and Its Microscopic Structure Characteristics. *Journal of the Electrochemical Society*, *159*(3), B308-B314.

[3] Zhang, J. (Ed.). (2008). PEM Fuel Cell Electrocatalysts and Catalyst Layers: Fundamentals and Applications. Springer, UK.

[4] Djilali, N. (2007). Computational Modelling of Polymer Electrolyte Membrane (PEM) Fuel Cells: Challenges and Opportunities. *Energy*, *32*(4), 269-280.

[5] Fang, B., Kim, J. H., Kim, M., & Yu, J. S. (2009). Ordered Hierarchical Nanostructured Carbon as a Highly Efficient Cathode Catalyst Support in Proton Exchange Membrane Fuel Cell. *Chemistry of Materials*, *21*(5), 789-796.

[6] Imbrioscia, G. M., & Fasoli, H. J. (2014). Simulation and Study of Proposed Modifications over Straight-parallel Flow Field Design. *International Journal of Hydrogen Energy*, *39*(16), 8861-8867.

[7] Reifsnider, K., Huang, X., Ju, G., & Solasi, R. (2006). Multi-scale Modeling Approaches for Functional Nano-composite Materials. *Journal of Materials Science*, *41*(20), 6751-6759.

[8] Costamagna, P. (2001). Transport Phenomena in Polymeric Membrane Fuel Cells. *Chemical Engineering Science*, *56*(2), 323-332.

[9] Zhang, L., Zhang, J., Wilkinson, D. P., & Wang, H. (2006). Progress in Preparation of Non-noble Electrocatalysts for PEM Fuel Cell Reactions. *Journal of Power Sources*, *156*(2), 171-182.

[10] Wang, Y., Chen, K. S., Mishler, J., Cho, S. C., & Adroher, X. C. (2011). A Review of Polymer Electrolyte Membrane Fuel Cells: Technology, Applications, and Needs on Fundamental Research. *Applied Energy*, *88*(4), 981-1007.

[11] Zamel, N., & Li, X. (2013). Effective Transport Properties for Polymer Electrolyte Membrane Fuel Cells-With a Focus on the Gas Diffusion Layer. *Progress in Energy and Combustion Science, 39*(1), 111-146.

[12] Siddique, N. A., & Liu, F. (2010). Process Based Reconstruction and Simulation of a Three-dimensional Fuel Cell Catalyst Layer. *Electrochimica Acta*, *55*(19), 5357-5366.

[13] Khan, M., Xiao, Y., Sundén, B., & Yuan, J. "Analysis of Multiphase Transport Phenomena in PEMFCS by Incorporating Microscopic Model for Catalyst Layer Structures", Proc. 2011 ASME Int. Mech. Eng. Cong. and Exp., New York, IMECE2011-65142, pp. 903-912.

[14] Wang, X. L., Zhang, H. M., Zhang, J. L., Xu, H. F., Tian, Z. Q., Chen, J., ... & Yi, B. L. (2006). Micro-Porous Layer with Composite Carbon Black for PEM Fuel Cells. *Electrochimica Acta*, *51*(23), 4909-4915.

[15] Pasaogullari, U., & Wang, C. Y. (2004). Two-phase Transport and the Tole of Micro-porous Layer in Polymer Electrolyte Fuel Cells. *Electrochimica Acta*, *49*(25), 4359-4369.

[16] Mustata, R., Valiño, L., Barreras, F., Gil, M. I., & Lozano, A. (2009). Study of the Distribution of Air Flow in a Proton Exchange Membrane Fuel Cell Stack. *Journal of Power Sources*, *192*(1), 185-189.

[17] Wu, H. (2009). Mathematical Modeling of Transient Transport Phenomena in PEM Fuel Cells (Doctoral Dissertation, University of Waterloo).

[18] Chang, P. A., St-Pierre, J., Stumper, J., & Wetton, B. (2006). Flow Distribution in Proton Exchange Membrane Fuel Cell Stacks. *Journal of Power Sources*, *162*(1), 340-355.

[19] Mench, M. M. (2010). Advanced Modeling in Fuel Cell Systems: A Review of Modeling Approaches. Chapter 5 in: *Hydrogen and Fuel Cells: Fundamentals, Technologies and Applications*, ed.: Detlef, S., *John Wiley & Sons,* 89-118, UK.

[20] Jang, S. S., Molinero, V., Cagin, T., & Goddard, W. A. (2004). Nanophase-segregation and Transport in Nafion 117 from Molecular Dynamics Simulations: Effect of Monomeric Sequence. *The Journal of Physical Chemistry B*, *108*(10), 3149-3157.

[21] Niu, X. D., Munekata, T., Hyodo, S. A., & Suga, K. (2007). An Investigation of Water-gas Transport Processes in the Gas-diffusion-layer of a PEM Fuel Cell by a Multiphase Multiple-relaxation-time Lattice Boltzmann Model. *Journal of Power Sources*, *172*(2), 542-552.

[22] Becker, J., Wieser, C., Fell, S., & Steiner, K. (2011). A Multi-scale Approach to Material Modeling of Fuel Cell Diffusion Media. *International Journal of Heat and Mass Transfer*, *54*(7), 1360-1368.

[23] Djilali, N., & Lu, D. (2002). Influence of Heat Transfer on Gas and Water Transport in Fuel Cells. *International Journal of Thermal Sciences*, *41*(1), 29-40.

[24] Litster, S., & McLean, G. (2004). PEM Fuel Cell Electrodes. *Journal of Power Sources*, *130*(1), 61-76.

[25] Hsu, W. Y., & Gierke, T. D. (1983). Ion Transport and Tlustering in Nafion Perfluorinated Membranes. *Journal of Membrane Science, 13*(3), 307-326.

[26] Pharoah, J. G., Karan, K., & Sun, W. (2006). On Effective Transport Coefficients in PEM Fuel Cell Electrodes: Anisotropy of the Porous Transport Layers. *Journal of Power Sources*, *161*(1), 214-224.

[27] Novaresio, V., García-Camprubí, M., Izquierdo, S., Asinari, P., & Fueyo, N. (2012). An Open-source Library for the Numerical Modeling of Mass-transfer in Solid Oxide Fuel Cells. *Computer Physics Communications*, *183*(1), 125-146.

[28] Valiño, L., Mustata, R., Gil, M. I., & Martín, J. (2010). Effect of the Relative Position of Oxygen-hydrogen Plate Channels and Inlets on a PEMFC. *International Journal of Hydrogen Energy*, *35*(20), 11425-11436.

[29] Lozano, A., Valiño, L., Barreras, F., & Mustata, R. (2008). Fluid Dynamics Performance of Different Bipolar Plates: Part II. Flow Through the Diffusion Layer. *Journal of Power Sources*, *179*(2), 711-722.

[30] Siegel, C. (2008). Review of Computational Heat and Mass Transfer Modeling in Polymer-electrolyte-Membrane (PEM) Fuel Cells. *Energy*, *33*(9), 1331-1352.

[31] Valiño, L., Mustata, R., & Dueñas, L. (2013). Consistent Modeling of a Single PEM Fuel Cell Using Onsager's Principle. *International Journal of Hydrogen Energy, 39*(8), 4030-4036.

[32] Khan, M. (2011). Multiphysics Modelling of PEM Fuel Cells-with Reacting Transport Phenomena at Micro and Macroscales (Doctoral dissertation, Lund University).

[33] Hartnig, C., Manke, I., Kuhn, R., Kardjilov, N., Banhart, J., & Lehnert, W. (2008). Cross-sectional Insight in the Water Evolution and Transport in Polymer Electrolyte Fuel Cells. *Applied Physics Letters*, *92*(13), 134106.

[34] Turhan, A., Kim, S., Hatzell, M., & Mench, M. M. (2010). Impact of Channel Wall Hydrophobicity on Through-plane Water Distribution and Flooding Behavior in a Polymer Electrolyte Fuel Cell. *Electrochimica Acta*, *55*(8), 2734-2745.

[35] Español, P., Serrano, M., & Zuñiga, I. (1997). Coarse-Graining of a Fluid and Its Relation with Dissipative Particle Dynamics and Smoothed Particle Dynamic. *International Journal of Modern Physics C*, *8*(04), 899-908.

[36] Filipovic, N., Ivanovic, M., & Kojic, M. (2009). A Comparative Numerical Study between Dissipative Particle Dynamics and Smoothed Particle Hydrodynamics When Applied to Simple Unsteady Flows in Microfluidics. *Microfluidics and Nanofluidics*, *7*(2), 227-235.

[37] Kojic, M., Filipovic, N., & Tsuda, A. (2008). A Mesoscopic Bridging Scale Method for Fluids and Coupling Dissipative Particle Dynamics with Continuum Finite Element Method. *Computer Methods in Applied Mechanics and Engineering*, *197*(6), 821-833.

[38] Flekkøy, E. G., Wagner, G., & Feder, J. (2000). Hybrid Model for Combined Particle and Continuum Dynamics. *EPL (Europhysics Letters)*, *52*(3), 271-276.

[39] Espanol, P., & Warren, P. (1995). Statistical Mechanics of Dissipative Particle Dynamics. *EPL (Europhysics Letters)*, *30*(4), 191-196.

[40] Xiao, Y., Yuan, J., & Sundén, B. (2012). Process Based Large Scale Molecular Dynamic Simulation of a Fuel Cell Catalyst Layer. *Journal of the Electrochemical Society*, *159*(3), B251-B258.

[41] Wescott, J. T., Qi, Y., Subramanian, L., & Capehart, T. W. (2006). Mesoscale Simulation of Morphology in Hydrated Perfluorosulfonic Acid Membranes. *The Journal of Chemical Physics*, *124*(13), 134702-137016.

[42] Morrow, B. H., & Striolo, A. (2007). Morphology and Diffusion Mechanism of Platinum Nanoparticles on Carbon Nanotube Bundles. *The Journal of Physical Chemistry C*, *111*(48), 17905-17913.

[43] Groot, R. D., & Warren, P. B. (1997). Dissipative Particle Dynamics: Bridging the Gap between Atomistic and Mesoscopic Simulation. *The Journal of Chemical Physics*, *107*(11), 4423.

[44] Kojic, M., Filipovic, N., & Tsuda, A. (2008). A Mesoscopic Bridging Scale Method for Fluids and Coupling Dissipative Particle Dynamics with Continuum Finite Element Method. *Computer Methods in Applied Mechanics and Engineering*, *197*(6), 821-833.

# Paper II

INTERNATIONAL JOURNAL OF
ENERGY RESEARCH

INTERNATIONAL JOURNAL OF ENERGY RESEARCH
*Int. J. Energy Res.* 2017; **41**:985–1003
Published online 5 December 2016 in Wiley Online Library (wileyonlinelibrary.com). DOI: 10.1002/er.3687

# Modeling of inhomogeneous compression effects of porous GDL on transport phenomena and performance in PEM fuel cells

Jiatang Wang*,†, Jinliang Yuan and Bengt Sundén

Department of Energy Sciences, Lund University, PO Box 118, Lund, SE-221 00, Sweden

## SUMMARY

A comprehensive, three-dimensional model of a proton exchange membrane (PEM) fuel cell based on a steady state code has been developed. The model is validated and further be applied to investigate the effects of various porosity of the gas diffusion layer (GDL) below channel land areas, on thermal diffusivity, temperature distribution, oxygen diffusion coefficient, oxygen concentration, activation loss and local current density. The porosity variation of the GDL is caused by the clamping force during assembling, in terms of various compression ratios, that is, 0%, 10%, 20%, 30% and 40%.

The simulation results show that the higher compression ratio on the GDL leads to lower porosity, and this is helpful for the heat removal from the cell. The compression effects of the GDL below the land areas have a contrary impact on the oxygen diffusion coefficient, oxygen concentration, cathode activation loss, local current density and cell performance. Generally, a lower porosity leads to a smaller oxygen diffusion coefficient, a less uniform oxygen concentration, a higher activation loss, a smaller local current density and worse cell performance. In order to have a better cell performance, the clamping force on the cell should be as low as possible but ensure gas sealing. Copyright © 2016 John Wiley & Sons, Ltd.

**KEY WORDS**

PEM fuel cells; transport phenomena; compression ratio; porosity; GDL; OpenFOAM

Correspondence

*Jiatang Wang, Department of Energy Sciences, Lund University, PO Box 118, Lund SE-221 00, Sweden.

†E-mail: Jiatang.wang@energy.lth.se

Received 27 June 2016; Revised 19 October 2016; Accepted 23 October 2016

## 1. INTRODUCTION

Proton exchange membrane (PEM) fuel cells fueled by hydrogen are considered as clean power devices for the direct conversion of chemical energy into electrical energy. The first commercial use of a typical PEM fuel cell was in 1960s Gemini space program by NASA. Then, after the first energy crisis in 1973, PEM fuel cells attracted more and more attention [1]. Owing to its advantages of efficient energy conversion, high power density and environmental friendliness, tremendous research programs worldwide have promoted PEM fuel cells as power sources replacing internal combustion engines in sub- to mega-Watt applications for transportation, heating, manufacturing and communication [2]. During the past decades, the performance of PEM fuel cells has been improved significantly resulting from research efforts on different aspects, for example, implementation of innovative materials [3] and optimized design based on experiments [4] and simulations [5]. However, barriers for the wide use of PEM fuel cells are still present. Cost and durability are supposed as the main challenges or bottlenecks to the development and commercialization of PEM fuel cells [6]. More efforts have to be taken to further improve the performance and provide a deeper understanding of the coupled transport phenomena with reactions taking place in PEM fuel cells.

Generally, a gas diffusion layer (GDL) used in PEM fuel cells plays a very important role in the cell performance [7]. Ideally the GDL is a functional, soft and flexible carbon material in supporting the operation of PEM fuel cells, that is, providing of mechanical support for the membrane and catalyst layer, a passage for both reactants and products, conduction of heat and electrons. It is well known that the mass transport in the GDL plays an important role on the cell performance especially at high current densities [8]. During assembling of a single cell or a fuel cell stack, the components of the PEM fuel cell, including the GDL, the bipolar plates and other components, are usually bolted under a certain pressure to prevent gas leakages and reduce the contact electronic/thermal resistance, as shown in Figure 1 [9]. Gas leakage should be avoided as it might result in poor cell performance and dangerous

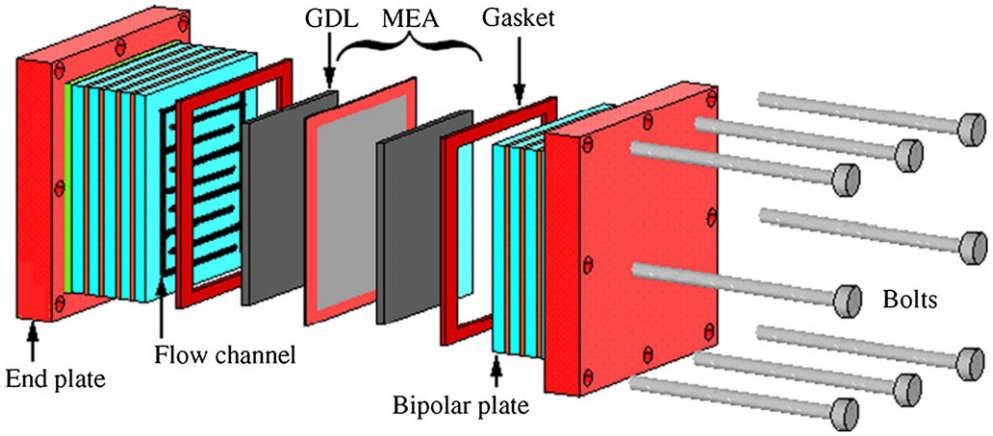


**Figure 1.** Schematic of a PEM fuel cell stack [9]. [Colour figure can be viewed at wileyonlinelibrary.com]

situation. However, over-compressing on the GDL will decrease the mass transport abilities and result in a reduced cell performance [10]. It has been found by experimental [11] and numerical studies [9] that the assembled pressure has much effect on the cell performance.

Some properties of the compressed GDL in a PEM fuel cell have been presented in the published PEM fuel cell works. High assembling pressure can decrease the porosity of the GDL which leads to higher mass transfer resistance, and it has been shown that physical compression of the GDL directly decreases its diffusion coefficient [12]. However, Ge et al. [11] experimentally revealed that there exists an optimal compression on the GDL, that is, the I–V curve first increases with less compression, then declines with increased compression beyond a certain value. The resulting effects of the GDL compression ratio on the interfacial ohmic resistance and the performance of a PEM fuel cell were investigated by Zhou et al. [13] using a numerical method. It was found that the cell performance will decrease with increasing compression if the change of the interfacial ohmic resistance is neglected, but there is one optimal compression if the interfacial ohmic resistance is considered. It is revealed that the GDL becomes solid under compression, which is good for the electron transport through the interface between GDL and CL. Regarding this aspect, the compression force on the cell assembling is good for obtaining a better cell performance. Cunningham et al. [14] reached almost the same conclusion by their experiment. However, Zhou et al. [9] revealed that the interfacial ohmic resistance will increase with increasing clamping force. Nitta et al. [15] evaluated the thermal properties of the GDL experientially and numerically as a function of compression. Their results revealed that the temperature distribution inside the PEM fuel cell was more uniform with the higher GDL deformation in the result of the thermal diffusion coefficient between the GDL and bipolar plates increased as the compression force increased. Generally speaking, increasing compression increases the deformation of the GDL resulting in lower porosity, higher mass transfer resistance and poorer cell performance, and lower resistance at the interface for heat and electron transfer.

The physical properties of the GDL will change during the fuel cell assembling in the reason of the porous properties of the GDL. However, the changes of the physical properties of the GDL caused by compression are not homogeneous. As shown in Figure 2 [16], the GDL below the ribs becomes thinner and intrudes into the channel. The compression effect is stronger below the ribs than at the parts below the channel because the rib/channel structure of the flow field. In practice, this structure creates a distribution of inhomogeneous compression, which results in spatial variations of GDL properties. An experimental study was performed by the research group of Nitta et al. [17]. The results from the measurements show that the GDL intrusion into the channel is depending on the initial thickness of GDL but not the width of channel. The GDL below the channel will remain at its initial thickness. Therefore, the decrease of thickness of the GDL below the ribs might be because of the loss of porosity. The in-plane permeability has been found in the experiments to be non-linear. The authors predicted that the pore size and its distribution changed because of the compression. This indicates that the clamping force during assembling of the PEM fuel cell will cause an inhomogeneous porosity distribution in the in-plane GDL. This fact agrees fairly well with the conclusion obtained by Zhou et al. [9].

The effect of the assembling process on the deformation of GDL in PEM fuel cells may not be neglected and has not been sufficiently studied yet. To the authors' knowledge, only a limited number of the published papers consider the inhomogeneous compression of the GDL and its effects in fuel cells [11,13,14,16]. Generally the physical properties of GDL, that is, thickness, porosity, heat/electric resistances and mass diffusion coefficients are assumed as constants in these models. However, this assumption might have significant difference between the numerical models and realistic situations. Furthermore, some of the results are obtained under the limited conditions, for example, by two-dimensional (2D) modeling


*Int. J. Energy Res.* 2017; **41**:985–1003 © 2016 John Wiley & Sons, Ltd.
DOI: 10.1002/er

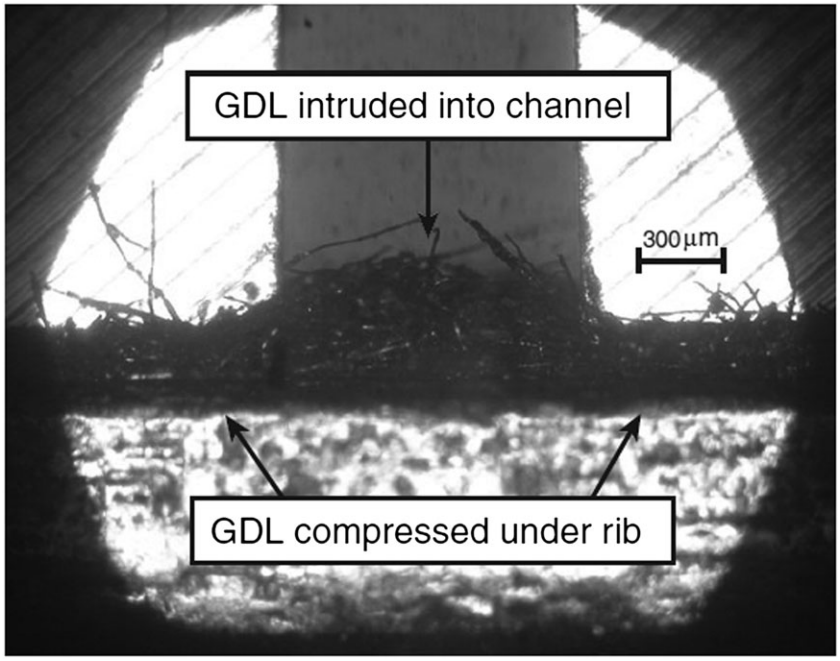


**Figure 2.** A sectional view of the deformed GDL after assembling process of a PEM fuel cell [16].

[16,17] or based on the carbon paper properties tested under clamping force in experiments [14,17]. However, the models that considered the effects of dimensional variations of GDL thickness, porosity, contact heat/electric resistances and mass diffusion coefficients have not been found. The aim of this work is to numerically study the physical parameters of the GDL (porosity, effective thermal conductivity and the mass diffusion coefficient) being affected by the inhomogeneous compression caused by the assembling condition. We report an effective and cheap numerical method to evaluate this deformation effect via characteristic parameters, and a comprehensive analysis is developed to obtain the optimal cell performance. In addition, one of the main results obtained from this study points out that the clamping force neglected in the past should be considered to obtain the best cell performance. The effects of inhomogeneous compression on the local transport processes and electrochemical performance are taken into account. Determination of the GDL thickness and electric resistance will be considered in future work. The models are performed using the finite volume method (FVM) based on computational fluid dynamics (CFD) method in Open Field Operation and Manipulation (OpenFOAM).

## 2. MODEL DESCRIPTION

### 2.1. Modeling domain

A single cell is a typical and minimum unit of a PEM fuel cell, and it contains all components corresponding to several centimeters. It is assumed that the fuel cell channel is periodically parallel as shown in Figure 3(a). A partial domain of the single cell is selected and investigated to decrease the computational efforts. The modeled domain is a 3D, single channel and multi-components of a unit cell, as shown by the grey dashed lines in Figure 3(a) and further details of the model in Figure 3(b). The anode (fuel side) and cathode (air side) were assembled symmetrically, and each side consists of a bipolar plate, gas channel, GDL and CL. Additionally, the electrolyte membrane was sandwiched between the CLs. The detailed dimensions of the single channel domain are listed in Table I.

The effects of inhomogeneous compression on the GDL are conducted by varying compression ratios. The GDL of the base case is compressed with a small and evenly distributed compression but without any deformation. The deformed GDL in other cases and the dependence of physical properties (i.e. porosity, effective thermal conductivity and mass diffusion coefficient) on the various local compression ratios will be described in the Section 2.2.

### 2.2. Model assumptions

A PEM fuel cell including all components is a complex system involving multiscale transport processes. In order to develop a numerical 3D model of the selected domain, it is necessary to make a number of assumptions. The assumptions made in this study are as follows:

1. The fuel cell operates in steady state.
2. Gas mixtures are regarded as incompressible ideal gases.
3. Reynolds number in the gas channel is less than 100, that is, laminar flow is assumed.

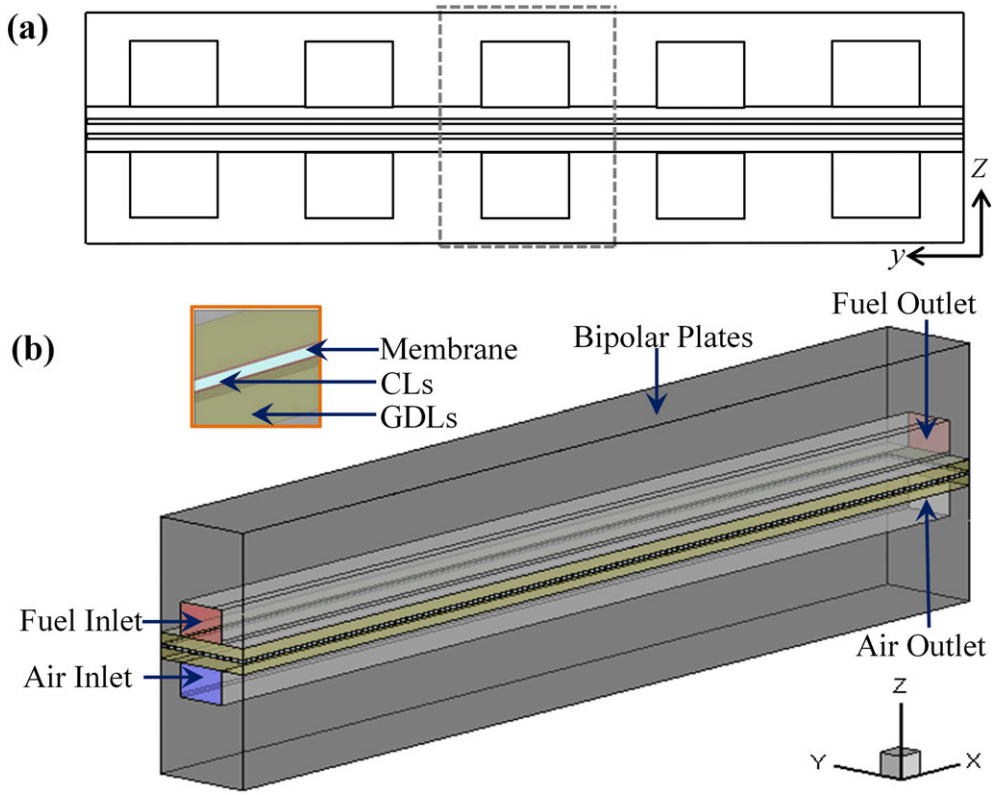


**Figure 3.** Schematic illustration of a PEM fuel cell: (a) parallel channels in 2D and (b) computational domain in 3D. [Colour figure can be viewed at wileyonlinelibrary.com]

4. The water is always in gaseous state without any phase change. At the inlet of the PEM fuel cell, the gas phase at the actual inlet temperature is humidified gas without any liquid water, as the mass fraction of the gaseous water at the inlets is lower than the point of maximum water content [18]. The influence from a possible small amount of liquid water in the cathodic channels is neglected.
5. Electrochemical reaction occurs at the interface between the membrane and the CLs.
6. Membrane is considered as impermeable to the gases.
7. Transfer of electrons and protons is not considered.
8. The porosity does not change in the GDL below the channel but changes below the ribs because of the compression.

Most of these assumptions are similar to previous modeling studies. However, the assumption of no phase-change is the major limitation in this study, which will be considered in the future work. In addition, the neglected transfer of electrons and protons might be another limitation to evaluate the compression effects of the GDL.

## 2.3. Model equations

The governing equations to be solved consist of a series of partial differential equations for the conservation of momentum, continuity, species transport and heat transfer. The electrochemical reactions are coupled with the parameters solved in the partial differential equations. The porous media in GDLs and CLs are considered for the gas species and heat transfer. Because of the compression force on the GDL, the properties are changed, but not the thickness.

### 2.3.1. Momentum equations

Navier–Stokes equations (known as the momentum equations) are the important equations in the computational fluid dynamics (CFD). The velocity and pressure coupling is handled by employing the PISO method. The Navier–Stokes equations are applied in the gas flow channel, GDL and CL, and can be expressed as [30],

$$\nabla\cdot(\rho UU) = -\nabla P + \nabla\cdot\mu\nabla U + S_n \quad (1)$$

where $\rho$ is the gas mixture density, $U$ is the fluid velocity vector, $P$ is the gas pressure, $\mu$ is the dynamic viscosity of the fluid and $S_n$ stands for the source term. Because of the porous structure effect of porous media in a PEM fuel cell, there exist pressure losses and the source term in Eq. [1] is needed to solve the pressure and velocity in the porous layers.

The source term $S_n$ should be different while the fluid passes from the open channel to the porous zones. Equation (2) will be applied in the gas flow channel, but Eq. (3) for the porous GDLs and CLs [30].


*Int. J. Energy Res.* 2017; **41**:985–1003 © 2016 John Wiley & Sons, Ltd.
DOI: 10.1002/er

**Table I.** Numerical parameters and properties.

| Parameters and symbols | Value | Reference |
|---|---|---|
| Gas channel length | $4 \times 10^{-2}$ m | |
| Gas channel width | $2 \times 10^{-3}$ m | |
| Gas channel height | $1.5 \times 10^{-3}$ m | |
| Land area width | $1 \times 10^{-3}$ m | |
| Thickness of bipolar plate | $3.5 \times 10^{-3}$ m | [1,6,16,18,19] |
| Thickness of GDL | $0.3 \times 10^{-3}$ m | |
| Thickness of CL | $2 \times 10^{-5}$ m | |
| Thickness of electrolyte | $1 \times 10^{-4}$ m | |
| Dynamic viscosity, $\mu$ | | |
| Air/water | $2.03715 \times 10^{-5}$ kg m$^{-1}$ s$^{-1}$ | [20] |
| Hydrogen/water | $1.0502 \times 10^{-5}$ kg m$^{-1}$ s$^{-1}$ | [20] |
| Density, $\rho$ | | |
| Air/water | 0.98335 kg m$^{-3}$ | [21] |
| Hydrogen/water | 0.1732 kg m$^{-3}$ | [21] |
| Electrolyte | 1980 kg m$^{-3}$ | [22] |
| Interconnect | 2200 kg m$^{-3}$ | [18] |
| Specific heat, $C_p$ | | |
| Air/water | 1070 J kg$^{-1}$ K$^{-1}$ | [20] |
| Hydrogen/water | 11956 J kg$^{-1}$ K$^{-1}$ | [20] |
| Electrolyte | 800 J kg$^{-1}$ K$^{-1}$ | [23] |
| GDL | 1000 J kg$^{-1}$ K$^{-1}$ | [23] |
| CL | 0.27 J kg$^{-1}$ K$^{-1}$ | [23] |
| Interconnect | 935 J kg$^{-1}$ K$^{-1}$ | [18] |
| Thermal conductivity, $k$ | | |
| Air/water | 0.0291965 W m$^{-1}$ K$^{-1}$ | [20] |
| Hydrogen/water | 0.173176 W m$^{-1}$ K$^{-1}$ | [20] |
| Electrolyte | 0.29 W m$^{-1}$ K$^{-1}$ | [24] |
| GDL | 1.7 W m$^{-1}$ K$^{-1}$ | [24] |
| CL | 0.27 W m$^{-1}$ K$^{-1}$ | [24] |
| Interconnect | 24 W m$^{-1}$ K$^{-1}$ | [18] |
| Porosity, $\varepsilon$ | | |
| CL | 0.6 | [25] |
| GDL | 0.8 | [26] |
| Pore size, $d$ | | |
| CL | $1 \times 10^{-6}$ m | [27] |
| GDL | $5 \times 10^{-5}$ m | [26] |
| Reaction order of $O_2$, $a$ | 0.5 | |
| Reaction order of $H_2O$, $b$ | $-1$ | |
| Reaction order of $H_2$, $m$ | 1 | |
| Pre-constant at cathode, $\gamma_c$ | $1 \times 10^{-5}$ A m$^{-2}$ | [28] |
| Pre-constant at anode, $\gamma_a$ | 10 A m$^{-2}$ | [18] |
| Cathode transfer coefficient, $\alpha_c$ | 0.5 | [29] |
| Anode transfer coefficient, $\alpha_a$ | 0.5 | [26] |
| Cathode activation energy, $E_{act,c}$ | $6.6 \times 10^4$ J mol$^{-1}$ | [18] |
| Anode activation energy, $E_{act,a}$ | $3.46 \times 10^4$ J mol$^{-1}$ | [18] |
| Electric resistance, $R_e$ | $1.5 \times 10^{-5}$ Ω m$^{-2}$ | [18] |

$$S_n = 0 \tag{2}$$

$$S_n = -(\mu D_n + 0.5\rho|U|F_n)U \tag{3}$$

where the values of $D_n$ and $F_n$ in Eq. (3) are related to the properties of the fluid and the porous structures. In particular, the pore diameter $d_{pore}$ and porosity $\varepsilon$ are involved [31]:

$$D_n = \frac{150}{d_{pore}^2}\frac{(1-\varepsilon)^2}{\varepsilon^3} \tag{4}$$

In this study, the non-linear term is not considered, that is, $F_n$ is set to zero. The conservation equation for gases with non-constant gas density can be expressed as [29],

$$\nabla\cdot(\rho U) = S_m \tag{5}$$

where the source term $S_m$ comes from the electrochemical reaction effects on the reaction sites, which can be expressed as Eq. (7) for the cathode and Eq. (8) for the anode [16], respectively.

$$S_{m,c} = -\frac{i}{4F}M_{O_2} + \frac{i}{2F}M_{H_2O} \tag{6}$$

$$S_{m,a} = -\frac{i}{2F}M_{H_2} \tag{7}$$

where $i$ is the local current density, $M$ the molar weight of the involved gas species and $F$ the Faraday's constant ($96\,485\,\mathrm{C\,mol^{-1}}$). The plus sign is used for the products and the negative sign for the reactants.

### 2.3.2. Mass transfer equations

The mass fraction is another important parameter in describing the gas compositions in the mixture. This is solved by the species transport equation shown in Eq. (8) [29]. The species to be solved by this equation are water, oxygen and hydrogen. The mass fraction of chemical inert species (nitrogen in the cathode and water in the anode) will be solved by considering that the sum of species is unity in the anode and cathode, respectively.

$$\nabla\cdot(\rho U Y_i) + \nabla\cdot j_i = S_{Y_i} \tag{8}$$

where the Fick's law is used for the mass diffusion flux [29], that is,

$$j_i = -\rho D_{i,gas}\nabla Y_i \tag{9}$$

where $D_{i,gas}$ is the mass diffusion coefficient of species $i$ in mixture, and $Y_i$ is the mass fractions of species $i$. Because of the multi-component diffusion occurring in fuel cells, the Stefan–Maxwell model is often used to evaluate the diffusion coefficient based on each species, as shown in Eq. (10) (30).

$$D_{Stefan-Maxwell} = D_{A,gas} = \frac{1 - X_A}{X_B/D_{AB} + X_c/D_{AC} + \ldots} \tag{10}$$

where $D_{i,gas}$ is the diffusion coefficient of species $i$ in the mixture, $X_i$ is the molar fraction of the specie $i$ and $D_{i,j}$ is the diffusion coefficients based on the binary diffusion model of species $i$ and $j$.

The effective gas diffusivity is significantly dependent on the porosity, tortuosity and pore size for the porous GDL and CL. The binary diffusivity and Knudsen diffusivity are used, and they are described by Eqs. (11) and (12), respectively [32],

$$D_{AB} = \frac{10^{-7}T^{1.75}\sqrt{1/M_A + 1/M_B}}{P_{tot}\left(V_A^{1/3} + V_B^{1/3}\right)^2} \tag{11}$$

$$D_{Knudsen} = \frac{d_{pore}}{3}\sqrt{\frac{8RT}{\pi M}} \tag{12}$$

where $V$ is the diffusion volume, $P_{tot}$ is the total pressure of gases $A$ and $B$, $T$ the temperature, $R$ the ideal gas constant and $d_{pore}$ the mean pore diameter of the porous medium.

Finally, the effective diffusion coefficient of species $i$ in the gas mixture in the porous layers can be evaluated by combining the Knudsen and Stefan–Maxwell diffusivities in Eq. (13) [33],

$$D_{i,gas} = \frac{\varepsilon}{\tau^2\left(1/D_{Stefan-Maxwell} + 1/D_{Knudsen}\right)} \tag{13}$$

where $\varepsilon$ is the porosity, and $\tau$ the tortuosity of the porous layers.

### 2.3.3. Electrochemistry and reactions

Electrochemical reactions are assumed to occur at the interfaces between the membrane and the electrodes. The fuel cell current density $i$ is then calculated based on Ohm's Law [29],

$$i = \frac{E_{Nernst} - V - \eta}{R_e} \tag{14}$$

where $V$ and $\eta$ are the cell operating voltage and the activation overpotential, and $R_e$ is the total electric resistance of the fuel cell. The Nernst potential $E_{Nernst}$ in Eq. (14) can be described as [34],

$$E_{Nernst} = E_0 + \frac{RT}{nF}\ln\frac{X_{O_2}^{0.5}\cdot X_{H_2}}{X_{H_2O}} \tag{15}$$

where $R$ is the universal gas constant, $n$ is the number of electrons transferred, $E_0$ the theoretical potential [35] at the standard atmosphere condition (298 K, 1 bar), and is mostly 1.23 V. The superscripts in Eq. (15) refer to the stoichiometric coefficients of the hydrogen fuel cell reaction based on the PEM fuel cell reactions.

$$E_0 = -\frac{\Delta G_{rxn}}{nF} = -\frac{(\Delta H_{rxn} - T\Delta S_{rxn})}{nF} \tag{16}$$

where $\Delta G_{rxn}$ is the Gibbs free energy change, $\Delta H_{rxn}$ is the enthalpy change and $\Delta S_{rxn}$ the entropy change of reaction.

The cell activation overpotential is assumed to be composed of anodic and cathodic contributions,

$$\eta = \eta_{acti,a} + \eta_{acti,c} \tag{17}$$

where the activation overpotential $\eta_{acti,a}$ is for the anode and $\eta_{acti,c}$ for the cathode, respectively. Values of $\eta$ at both electrodes are obtained using a root finder based on Ridder's method after obtaining the numerical solutions of the Butler–Volmer equation [16],

$$i = i_0[\exp(A\eta_e) - \exp(B\eta_e)] \tag{18}$$

where



*Int. J. Energy Res.* 2017; **41**:985–1003 © 2016 John Wiley & Sons, Ltd.
DOI: 10.1002/er

$$A = \frac{2\alpha_e F}{RT} \tag{19}$$

$$B = -\frac{2(1-\alpha_e)F}{RT} \tag{20}$$

where $\alpha_e$ is the transfer coefficient and $\eta_e$ is the activation overpotential for each electrode. The local exchange current densities are given by [32],

$$i_{0,a} = \gamma_a \left(\frac{P_{H_2}}{P_0}\right)^m \exp\left(-\frac{E_{act,a}}{RT}\right) \tag{21}$$

$$i_{0,c} = \gamma_c \left(\frac{P_{O_2}}{P_0}\right)^a \left(\frac{P_{H_2O}}{P_0}\right)^b \exp\left(-\frac{E_{act,c}}{RT}\right). \tag{22}$$

The reaction orders, $a$, $b$, $m$, the pre-constant $\gamma_a$ and $\gamma_c$, and the activation energies $E_{\mathrm{act},a}$ and $E_{\mathrm{act},c}$, together with the transfer coefficients, $\alpha_e$, are listed in Table I.

#### 2.3.4. Heat transfer equations

The heat transfer is evaluated in all the regions of the selected fuel cell domain by the thermal energy equation [30],

$$\nabla\cdot\left(\rho U C_p T\right) = \nabla\cdot k\nabla T + S_T \tag{23}$$

where $S_T$ is the volumetric heat source term, $C_p$ the specific heat at constant pressure and $k$ the effective thermal conductivity corrected by the porosities of local porous materials,

$$k = k_s(1-\varepsilon) + k_g\varepsilon \tag{24}$$

where the $k_s$ and $k_g$ are the thermal conductivity of involved solid materials and gases, in the porous regions, respectively.

The source term for the energy equation is composed of the enthalpy change of the reactions and the ohmic heating. Thus the heat source term in the model can be written as [30,32],

$$S_T = \Delta H_e \frac{I}{F h_{cell}} - \frac{IV}{h_{cell}} + \frac{I^2 R_e S_{mem}^2}{h_{cell}} \tag{25}$$

where $\Delta H_e$ is the enthalpy change, $S_{mem}$ is the active surface reaction area and $h_{cell}$ is the cell height.

#### 2.3.5. GDL deformation

The GDL used in the PEM fuel cell is porous and flexible, and has physical properties being affected by deformation resulted by the compression on it. The thickness of the compressed GDL $h_{com}$ can be expressed as,

$$h_{com} = (1-\lambda)h_{initial} \tag{26}$$

where $\lambda$ is the compression ratio and $h_{initial}$ is the initial thickness of the uncompressed GDL. Considering the solid materials in the porous media, the thickness of the solid GDL $h_{solid}$ should be evaluated as [17],

$$h_{solid} = h_{initial}(1-\varepsilon_0) \tag{27}$$

where $\varepsilon_0$ is the initial porosity for the uncompressed GDL. The model is under the assumption that the change of the GDL thickness is caused by the change in the volume of pores but the solid part does not change. Thus, the porosity of the compressed GDL might be evaluated as a function of the GDL thickness [16],

$$\varepsilon_{com} = \varepsilon_0 \frac{h_{com} - h_{solid}}{h_{initial} - h_{solid}} \tag{28}$$

where the $\varepsilon_{com}$ is the porosity of the compressed GDL. In order to use Eq. (13), another physical parameter describing the porous structures is tortuosity, which is evaluated as [36],

$$\tau = 1 - 0.49\ln(\varepsilon). \tag{29}$$

### 2.4. Input parameters and boundary conditions

Table I lists the model design parameters and the input properties of related materials, kinetics and electrochemical reactions. The porosities of the GDL are varied as a function of the compression ratios caused by different assembling pressure operated on the bipolar plates. In this simplified model, a constant electric resistance is employed. The ohmic loss in the CLs and GDLs might be different under different clamping forces during assembling but this is considered. In order to investigate the effects of the GDL compression ratio on the heat transfer and mass transport processes additionally on the fuel cell performance, the simulations have been carried out for a range of compression ratios on the GDL below the land areas. It is assumed that only the porosity of the GDL below the areas exposed to the force land will change because of the compression, that is, in the GDL regions corresponding to the bipolar plate ribs. With a certain compression ratio on the GDL, the porosity of the GDL is different along the y-direction, that is, different porosity values below the channel area (middle of y-axis) and the land areas (both sides beyond the channel along the y-direction). The compression ratios of 10%, 20%, 30% and 40% of the GDL were employed. The effects of the compressed GDL on porosity, tortuosity and the source terms of Navier–Stokes equations were evaluated by equations (26) to (29). Table II shows the compressed conditions and the corresponding porosities from the compressed GDL. The cases of Base, A1, A2, A3 and A4 stand for compression ratios of 0%, 10%, 20%, 30% and 40%, respectively, caused by the clamping force below the land areas of the GDL. The corresponding porosity after compression is 0.8, 0.7, 0.6, 0.5 and 0.4, respectively. A constant porosity of 0.8 is applied for the channel area in

**Table II.** Compression cases and related porous properties of the GDL investigated. '$\lambda$' is the compression ratio, '$\varepsilon$' is the porosity and '$\tau$' is the tortuosity.

| | $\lambda$ (%)/$\varepsilon$(—)/$\tau$ | |
|---|---|---|
| Cases | Land areas | Channel area |
| Base | 0/0.8/1.109 | 0/0.8/1.109 |
| A1 | 10/0.7/1.175 | 0/0.8/1.109 |
| A2 | 20/0.6/1.250 | 0/0.8/1.109 |
| A3 | 30/0.5/1.340 | 0/0.8/1.109 |
| A4 | 40/0.4/1.449 | 0/0.8/1.109 |

**Table IV.** Results of mesh independence test.

| No. | Cell size | Average current density (A $m^{-2}$) |
|---|---|---|
| 1 | 15 600 | 5387.88 |
| 2 | 24 000 | 5394.15 |
| 3 | 40 800 | 5414.41 |
| 4 | 68 000 | 5429.29 |
| 5 | 103 200 | 5429.19 |
| 6 | 143 100 | 5429.25 |
| 7 | 189 000 | 5428.36 |

all cases. In order to evaluate the difference of compressed and uncompressed GDLs, the base case without compression on the GDL was included as well.

Before solving the partial differential equations, a set of boundary conditions for each parameter is required. The humidified gases [18] (air/water and hydrogen/water) with certain mass fractions, temperature, velocity and density are fed into the air channel inlet and fuel channel inlet, respectively. The inlet velocity is based on the desired average current density with the stoichiometric ratio 2 for the oxygen and 1.2 for the hydrogen, respectively [6]. A pressure outlet condition is prescribed at the outlets of the gas flow channels. The detailed boundary conditions applied in the computational domain can be found in Table III.

### 2.5. Grid independence test and model validation

In order to check the model performance and save computational resources, a grid independence study was performed. Seven different meshes were tested, and the average current densities obtained from these cases are shown in Table IV. The cases for the grid independence study have the same numerical settings and parameters. The result indicates that Case 4 with 68 000 cells has the minimum grid number under the requirement of numerical accuracy and stability. Therefore, the optimum mesh size of Case 4 was selected for all calculations in this study.

The predicted fuel cell V–I curve in the current numerical study is shown in Figure 4(a). A plot that considers the effect of porous media obtained by Hottinen et al. [37] was used to compare the simulation results in this study. Both have similar conditions involving the porosity change of the GDL for further investigation of the compressed GDL. The operating voltage of the predicted results shows an excellent agreement with the results from the reference. However, with increasing current density, some differences are observed between the present work and the referred one. The model investigated by Hottinen et al. [37] is two dimensional ignoring the direction along the channel, which might be the main reason of over-predicting the voltage. It is noted that a constant binary diffusion coefficient was used in the referred paper, whereas the Stefan–Maxwell model was used in the current model to obtain the diffusion coefficient based on the local temperature and species distribution. We further compared our simulations with experimental data at the operating conditions used in reference [38], as shown in Figure 4(b). Good agreement between the experimental and computed polarizations is obtained.

## 3. NUMERICAL RESULTS AND DISCUSSIONS

In this section, the numerical results of the effects of various compression ratios on the heat and mass transfer, and the electrochemical performance are presented and analyzed. At first, the effects of compression on the thermal conductivity and the associated different temperature distribution are discussed. Then, the effects of compression on the diffusion coefficients and associated mass distributions are studied. Finally, the electrochemical performance in terms of the exchange current density and the cathodic activation polarization is analyzed. In order to compare the results, the PEM fuel cell for the various cases analyzed is operated at a constant operating voltage of 0.55 V based on the potential static method.

**Table III.** Major boundary conditions. 'TB' is the top/bottom walls of the model; 'LR' is the top/bottom walls of the model.

| Parameters | TB | LR | Inlet | Outlet |
|---|---|---|---|---|
| $U$ | $\partial U/\partial z = 0$ | $\partial U/\partial y = 0$ | $U_{air/water} = 0.05\ m\ s^{-1}$<br>$U_{fuel/water} = 0.025\ m\ s^{-1}$ | $\partial U/\partial x = 0$ |
| $T$ | $\partial T/\partial z = 0$ | $\partial T/\partial y = 0$ | 353 K | $\partial T/\partial x = 0$ |
| $P$ | $\partial P/\partial z = 0$ | $\partial P/\partial y = 0$ | $\partial P/\partial x = 0$ | 2.0 atm |
| $Y_i$ | $\partial Y_i/\partial z = 0$ | $\partial Y_i/\partial y = 0$ | $Y_{air} = 0.844,\ Y_{water} = 0.156$<br>$Y_{hydrogen} = 0.406,\ Y_{water} = 0.594$ | $\partial Y_i/\partial x = 0$ |



*Int. J. Energy Res.* 2017; **41**:985–1003 © 2016 John Wiley & Sons, Ltd.
DOI: 10.1002/er

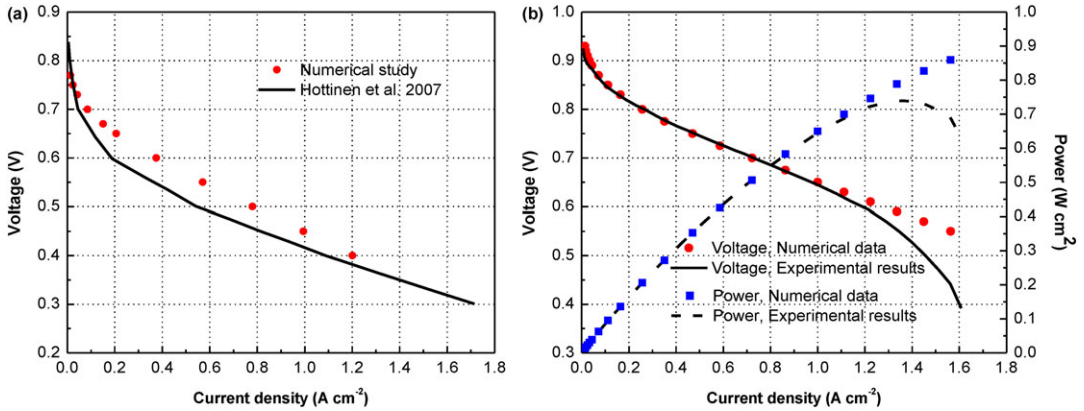


**Figure 4.** Comparison of numerical study and experimental results [37,38]. [Colour figure can be viewed at wileyonlinelibrary.com]

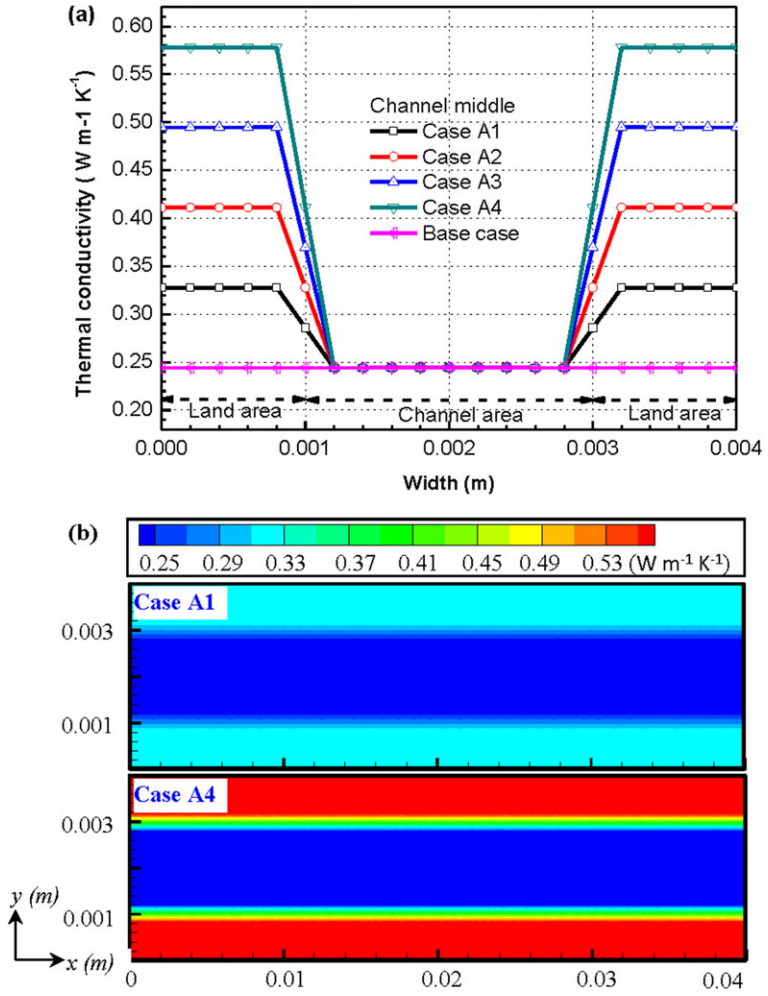


**Figure 5.** Distributions of effective thermal conductivities at GDL interface close to CL (a) at the channel inlet for different compression cases and (b) Case A1 (up) and Case A4 (below). [Colour figure can be viewed at wileyonlinelibrary.com]

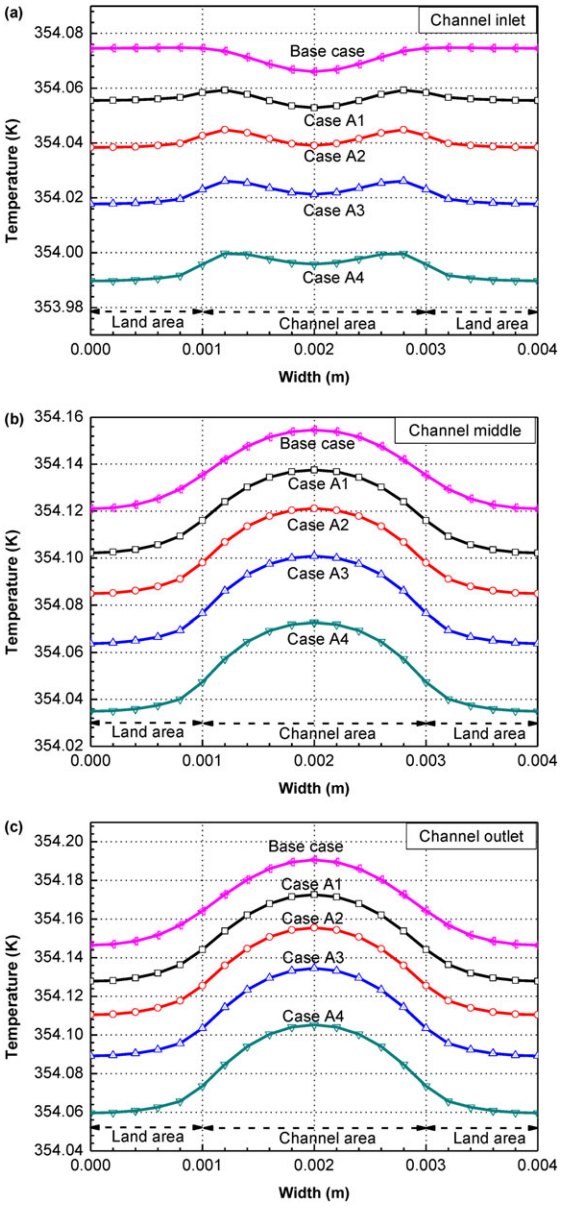


**Figure 6.** Temperature profile of GDL interface close to CL for different compression cases at different positions: (a) channel inlet, (b) channel middle and (c) channel outlet. [Colour figure can be viewed at wileyonlinelibrary.com]

### 3.1. Effect on thermal conductivity and temperature distribution

In an operating PEM fuel cell, the thermal conductivity of the different components is a key parameter to evaluate the ability of heat transfer from the reaction areas to the gas channels and bipolar plates. In most PEM fuel cell studies, the thermal conductivity of a certain component are usually regarded as uniform, that is, it is assumed that the thermal conductivity of the GDL is the same for the areas below the channel and below the ribs. According to the work of Karimi et al. [38], the effective thermal

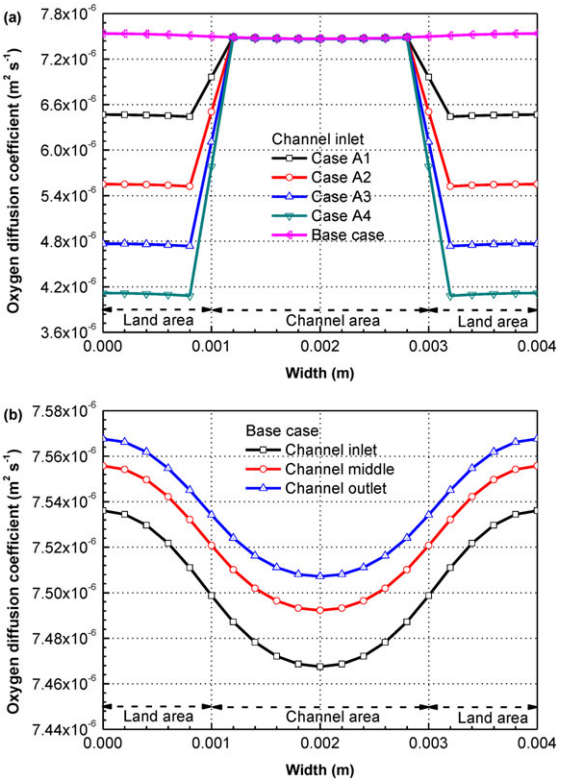


**Figure 7.** Distribution of oxygen diffusion coefficients at the interface of GDL close to CL for (a) different compression cases at channel inlet, and (b) different positions for base case along the channel. [Colour figure can be viewed at wileyonlinelibrary.com]

**Table V.** Average and standard deviation of temperature at the cathodic GDL interface close to CL and reaction interface, respectively. 'Tem' means the temperature; 'Inte.' means the interface.

| | Average Tem. (*K*) | | Standard deviation of Tem. (*K*) | |
|---|---|---|---|---|
| Case | GDL/CL Inte. | Reaction Inte. | GDL/CL Inte. | Reaction Inte. |
| Base | 354.12 | 354.13 | 0.048 | 0.047 |
| A1 | 354.11 | 354.11 | 0.046 | 0.045 |
| A2 | 354.09 | 354.09 | 0.045 | 0.043 |
| A3 | 354.07 | 354.07 | 0.043 | 0.042 |
| A4 | 354.04 | 354.04 | 0.042 | 0.041 |


*Int. J. Energy Res.* 2017; **41**:985–1003 © 2016 John Wiley & Sons, Ltd.
DOI: 10.1002/er

conductivity of the GDL through the plane is between $0.26\,W\,m^{-1}\,K^{-1}$ and $0.7\,W\,m^{-1}\,K^{-1}$ as the compression load is increased from 0.7 to 13.8 bar. In this study, the effective thermal conductivity of the GDL under compression is evaluated as a numerical function of both the thermal conductivity of solid materials and gas mixture, and the local porosity. Figure 5(a) displays the profiles of the effective thermal conductivity of the GDL close to the CL for different compression cases. It can be seen that the effective thermal conductivity below the channel region is lower than that below the rib regions. A higher compression ratio results in a higher effective thermal conductivity below the ribs. However, the base case with zero compression on the GDL results in a constant effective thermal conductivity along the cell width. From this observation, it can be concluded that the heat transfer from the GDL below the ribs is stronger than that below the channel as a consequences of a smaller porosity. The corresponding effective thermal conductivity distributions at the interface of the GDL close to the CL of Case A1 and Case A4 are shown in Figure 5(b), and it is found that the effective thermal conductivity is kept constant along the cell length while it is varying with the porosity of the GDL. This means that the porosity of the GDL is the main factor affecting the effective thermal conductivity, which agrees with the Eqn. (24).

The temperature profiles of the GDL close to the CL along the channel for different compression cases are shown in Figure 6(a), (b) and (c). It is found that, a big compression ratio on the GDL results in a lower averaged temperature at the GDL interface, which might be explained by the fact that the higher effective thermal conductivity caused by the higher compression ratio accelerates the heat transfer compared with that in Figure 5(a). In this point, the assembling pressure on the GDL is a favorable factor for the heat removal from the cell. However, the reaction effects on the average temperature cannot be neglected and will be analyzed below. The maximum temperature is located at different areas along the cell. At the channel inlet, the maximum temperature is observed at the region below the ribs for the Base case. However, the maximum temperature moves to the GDL region below the channel and rib interfaces as the compression ratio is increased from Case A1 to Case A4 at the channel inlet. A possible reason for these phenomena is that the heat transfer from the reaction sites to the gas channel via the bipolar plates becomes dominant for higher effective thermal conductivity, especially at the region far away from the channel. In addition, the maximum temperature of the GDL is in the region below the channel from the middle to the exit of the channel. This is so because most of the oxygen reduction reaction occurs in the CLs below the channels, resulting in more generated heat.

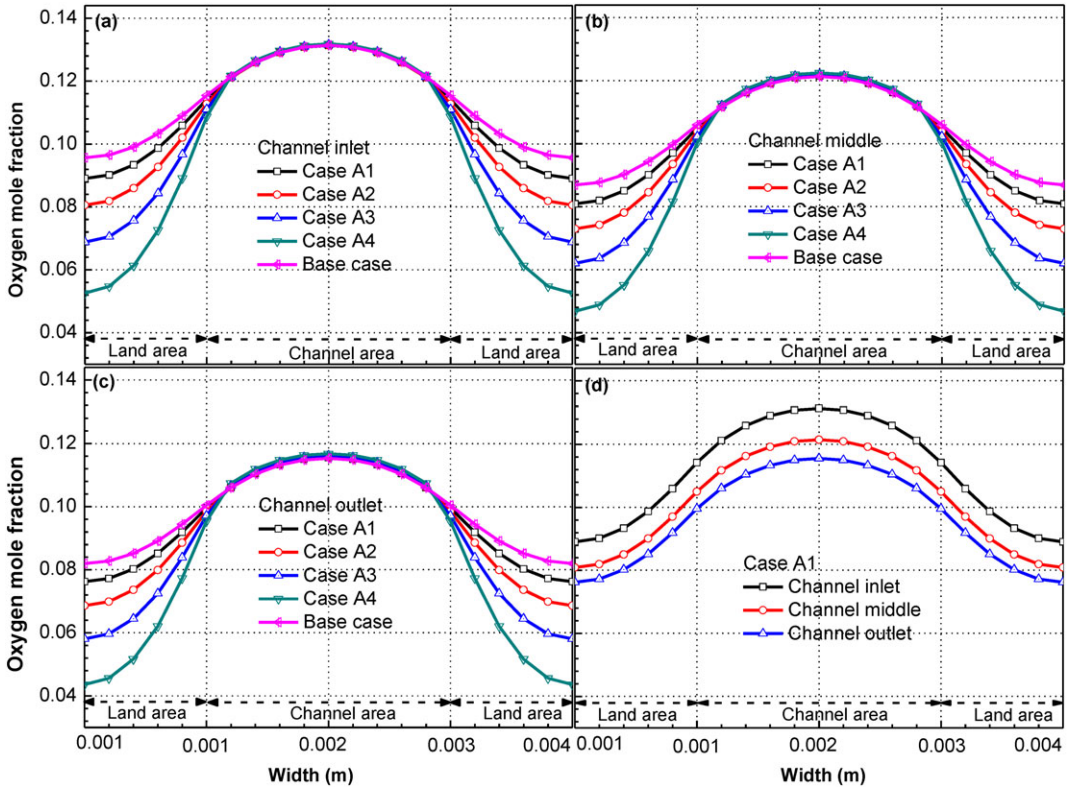


**Figure 8.** Distribution of oxygen mole fractions at the GDL interface close to CL for different compression cases at (a) channel inlet, (b) channel middle, (c) channel outlet and (d) different positions for case A1 along the channel. [Colour figure can be viewed at wileyonlinelibrary.com]

A uniform temperature is necessary for a PEM fuel cell to avoid the extreme hot spot inside the cell. Generally, the average and standard deviation of the temperature distribution can be used to predict the uniform values. It should be noted that the standard deviation is a measure to indicate the magnitude of the departure of the values from the mean temperature [39]. According to the statistical data in Table V, the average temperature at the interface of GDL close to CL and the reaction interface decreases from the Base case to Case A4. A similar tendency is observed for the standard deviation of the temperature, which varied between 0.04831 and 0.04199, 0.04718 and 0.04096, respectively. This indicates that the cell with a bigger compression of the GDL is favorable for obtaining a uniform temperature in the CLs and GDLs. As discussed in the previous paragraphs, a bigger compression of the GDL will result in a higher thermal conductivity, which might be the reason for the smaller temperature variation. It should be noted that the effects on temperature distribution are much smaller than that on mass transfer, as discussed below.

### 3.2. Effect on diffusion coefficient and mass transfer

The diffusion coefficient is important, because it determines the local reactant/product distribution. The effect of compression on the diffusion coefficient can be evaluated by Eqs (10) to (13), where this variable is a function of the porous properties, that is, porosity and tortuosity. The importance of this effect was experimentally studied by Nitta et al. [17] to determine the gas permeability of the GDL for inhomogeneous compression. It was indicated that the gas permeability decreases as a result of the

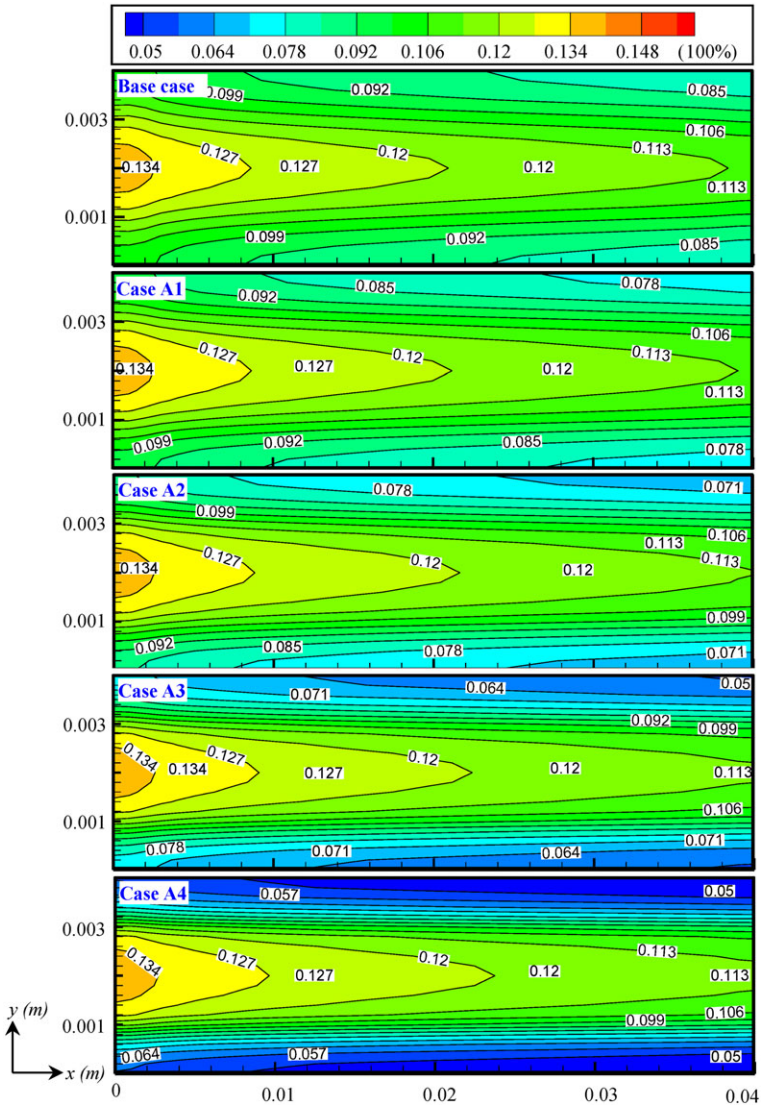


**Figure 9.** Profile of oxygen mole fractions predicted at the reaction interface from different compression cases. [Colour figure can be viewed at wileyonlinelibrary.com]


*Int. J. Energy Res.* 2017; **41**:985–1003 © 2016 John Wiley & Sons, Ltd.
DOI: 10.1002/er

reduced pore size caused by compression. The effective oxygen diffusion coefficient at the channel inlet region for the different compression cases is shown in Figure 7 (a). It is observed that the oxygen diffusion coefficient is almost constant along the width direction of the fuel cell for the uncompressed GDL. However, a quite small difference, that is, a higher oxygen diffusion coefficient, was observed in Figure 7(b), compared with those at the outlet and middle regions along the cell length direction.

Figure 7(b) indicates that the higher porosity caused by the small compression of GDL is favorable for the oxygen transfer. When the various compressions of the GDL are taken into account, the oxygen diffusion coefficients at the GDL interface close to the CL below the channels are similar but decrease as the compression ratio increases. This is caused by the decreased porosity because of the stronger clamping force. The increased tortuosity of the GDL, when the porosity decreases because of the higher compression ratio, is another possible reason for the diffusion coefficient being limited.

The diffusion coefficient within the GDL is changed by the compression, which affects the ability of mass transfer. The distributions of the oxygen mole fraction at the GDL interface close to the CL along the channel are shown in Figure 8 for different compression cases. The plots show a similar trend at the various positions along the channel, and the same positions for different compression cases. The highest oxygen concentration exists in the region below the channel, but the opposite situation appears in the region far away from the channel area. A possible reason for this is that the distance from the channel to the edge of the land areas is much longer than to that one below the channel. Additionally, the decreased diffusion coefficient limits the transfer of oxygen in the regions far away from the channel area, as discussed above.

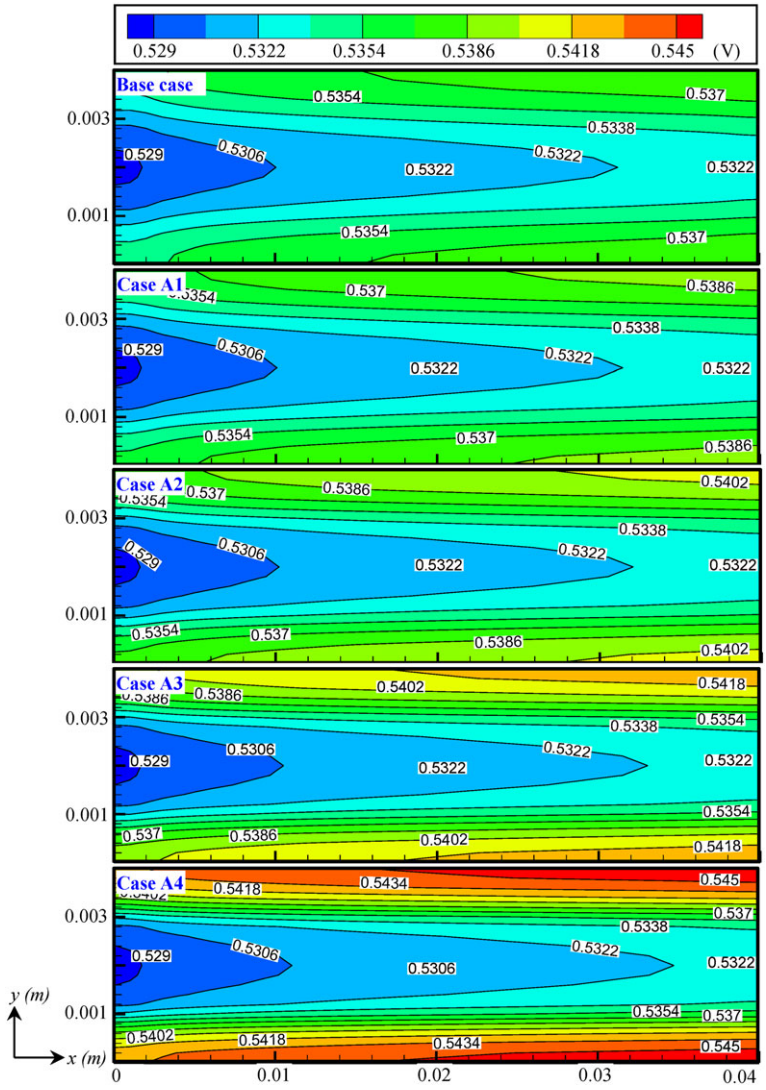


**Figure 10.** Distribution of cathode activation polarization for different compression cases. [Colour figure can be viewed at wileyonlinelibrary.com]

It is important to study the reactants distribution at the cathode reaction sites in PEM fuel cells, because they determine the local current densities, according to Eq. (33). The distributions of the oxygen mole fraction at the reaction interface for different compression cases are shown in Figure 9. There is no significant difference at the reaction interface below the channel inlet area when different compression forces are applied. However, a significant difference is observed at the both land areas. It is noted that there is about 20% difference in oxygen mole fraction at the corner of the channel inlet and that one at the channel outlet for the base case, but only 12% for the most compressed GDL in Case A4. Additionally, a nearly zero oxygen mole fraction was observed close to the outlet land area in Case A4. This indicates that a higher compression ratio results in a non-uniform oxygen concentration, especially far away from the channel areas. The compressed GDL not only affects the gas flow along the channel direction (x-direction) but also in the vertical direction of the PEM fuel cell (z-direction). This finding is reasonable as the bulk of the porous medium of the GDL may block the gas transfer in all directions. The plots in Figure 8 also support the findings in Figure 9.

### 3.3. Effect on electrochemical performance

The cathode activation polarization is the main potential loss in operating a PEM fuel cell, compared to the activation polarization in the anode because its kinetic reaction rate is several times faster than that in the cathode. Generally, the activation polarization is caused by the energy barriers, that is, activation energy between the reactants and products at certain reaction conditions. However, in a PEM fuel cell, the activation polarization is significantly

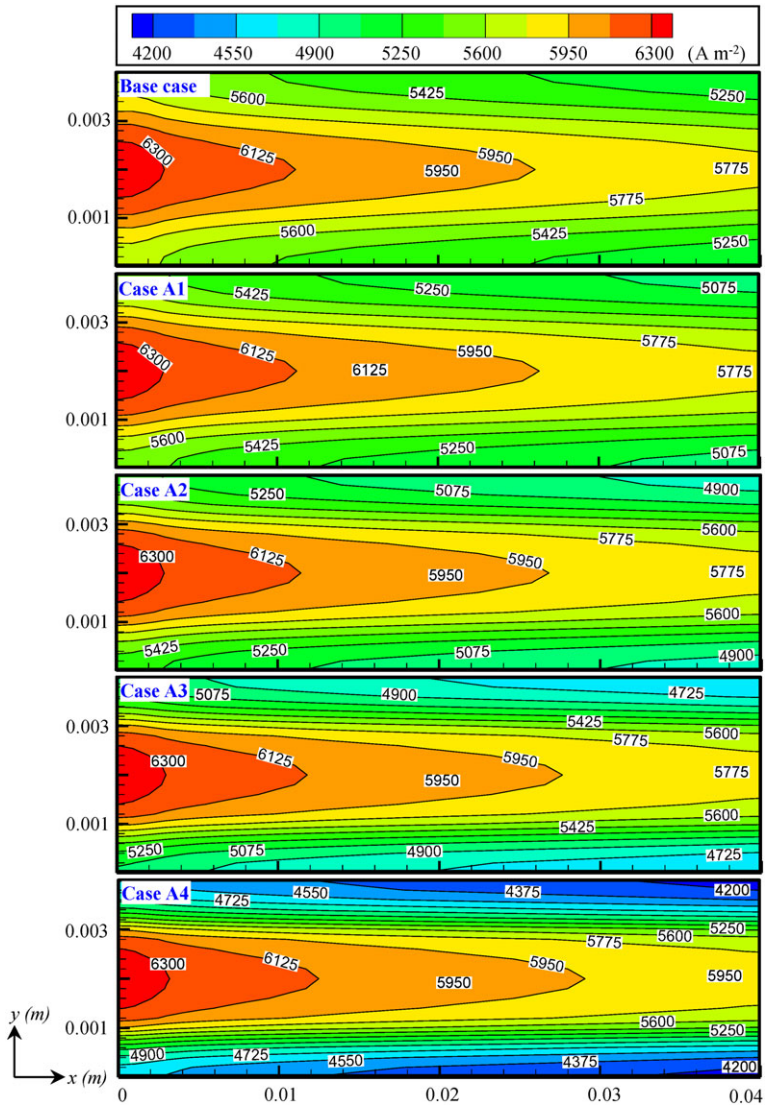


**Figure 11.** Distribution of current densities at the reaction interface for different compression cases. [Colour figure can be viewed at wileyonlinelibrary.com]


*Int. J. Energy Res.* 2017; **41**:985–1003 © 2016 John Wiley & Sons, Ltd.
DOI: 10.1002/er

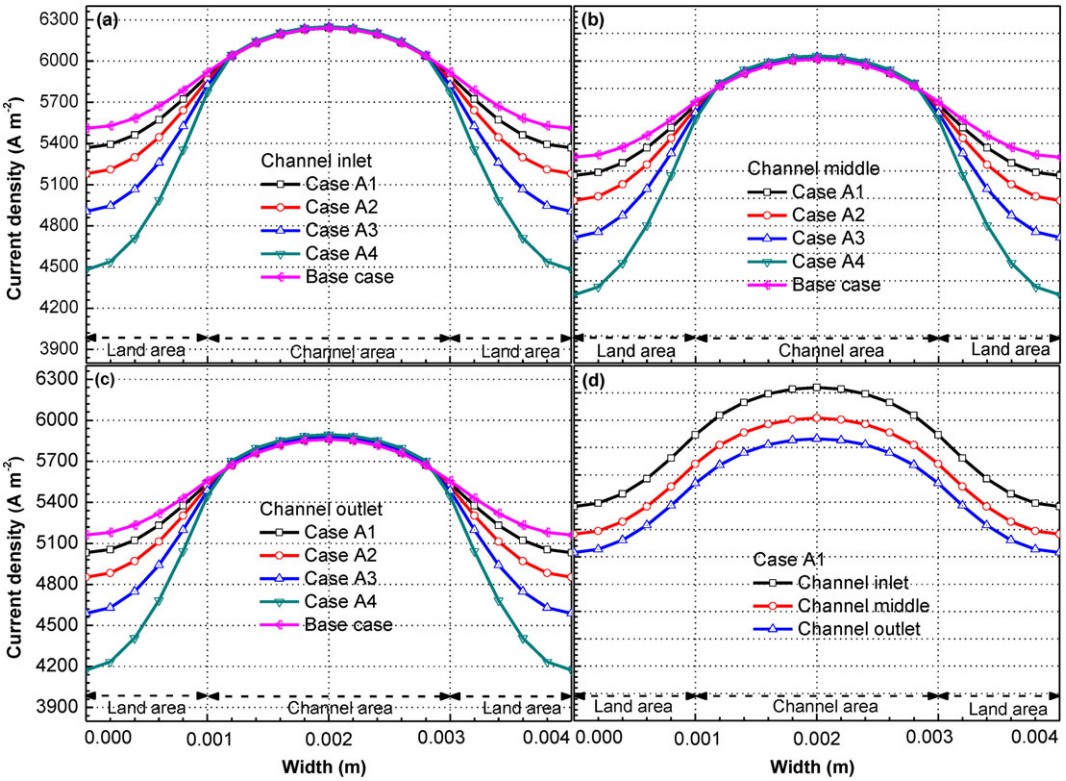


**Figure 12.** Current densities at the reaction interface of different compression cases at (a) channel inlet, (b) channel middle, (c) channel outlet and (d) different positions for case A1 along the channel. [Colour figure can be viewed at wileyonlinelibrary.com]

dependent on the local exchange current density (which is a function of the local reactant pressure, reference exchange current density, and temperature, etc.) and the average current density. Therefore, the oxygen concentration directly affects the activation loss in the cathode. It is believed that the concentration loss is minor throughout the reaction interface in this model. A comparable phenomenon might be shown in Figure 10, which shows the distribution of the cathode activation polarization at the reaction interface for different compression cases. By comparing with the oxygen concentration at the same interface in Figure 9, it is found that the higher oxygen concentration results in a lower activation loss. The reaction sites close to the channel inlet have the largest amount of fresh oxygen, which results in the lowest activation loss in this area.

The local current density at the reaction interface for the cases with different compression ratios for the cell operating voltage of 0.55 V is shown in Figure 11. As is known, the local current density distribution is related to the local oxygen concentration presented in Figure 9 and the local activation loss shown in Figure 10. The highest current density exists in the area below the channel inlet for all cases, and decreases along the channel. An extremely low current density was observed below the land area close to the channel outlet in Case A4, which is subjected to the highest compression ratio. A higher oxygen concentration gives a lower activation loss and a higher local current density, that is, more oxygen reaches the reaction sites and improves the reaction rates. The Base case with zero compression of the GDL shows the best distribution of the current density. This means that the clamping force on the PEM fuel cell increases the cell voltage loss and the non-uniformity of the local current densities.

The corresponding profiles of the local current density at the channel inlet, channel middle and channel outlet obtained from Figure 11 are shown in Figure 12. This figure is in agreement with the oxygen concentration plots

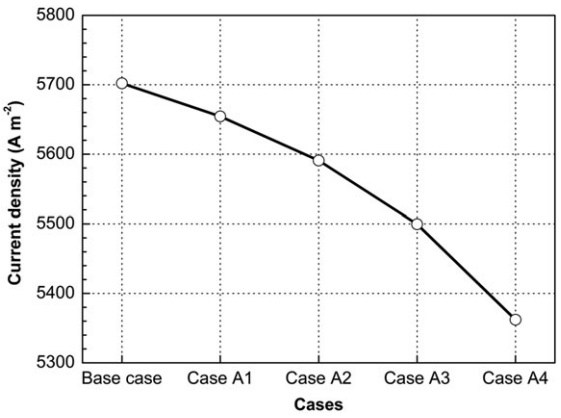


**Figure 13.** Average current densities for different compression cases.

in Figure 8, where the reaction region below the channel leads to the highest current density but it drops with the higher compression ratio below the land areas. Therefore, the oxygen concentration is one of the key factors that affect the local current density. The Base case with zero compression of the GDL shows the most uniform local current density, while the biggest difference in the local current density was observed below the land region of the GDL by 40% compression.

Another key variable from the cell modeling is the average current density, which is the output of the cell during operation, as shown in Figure 13. It shows the average current density predicted for the compression cases at 0.55 V cell voltages. The plot shows an almost linear drop from the case with 0% compression to the case with 40% compression of the GDL, that is, an average current density from 5700 A $m^{-2}$ to 5360 A $m^{-2}$. This indicates that the compression of the cell limits the cell performance. It means that the reactant diffusion term has a more important effect than the benefits of the heat transfer from compression of the GDL.

It reveals that the average temperature at the cathodic GDL interface close to CL and the reaction interface drops from base case to Case A4. On the one hand, this phenomenon might be caused by the higher effective thermal conductivity under the higher compression ratios, as shown in Figure 5(a) and Table V. On the other hand, the heat generated at the reaction sites decreases under the higher compression ratios, as shown in Figure 13. Therefore, both the effective thermal conductivity and the reaction will affect the average temperature distribution in specific cases.

## 4. CONCLUSIONS

The development of a comprehensive 3D numerical model for a PEM fuel cell has been achieved. This model accounts for the thermal and mass transfers and cell performance under various compressions on the rib/channel structure of the GDL. The direct influence caused by compression is the porosity change, that is, an inhomogeneous porosity distribution in the width direction of the channel. The model validation showed good agreement with the experimental data. The simulated results are conducted for various compression ratios on the channel land areas of the GDL, that is, 10%, 20%, 30%, 40% and 0% (for the base case). The results indicate that the lower porosity of the GDL below the land areas caused by higher compression is a positive factor for the thermal transport and contributes to obtaining a more uniform temperature. However, a depletion phenomenon is observed for the oxygen diffusion coefficient, oxygen distribution and local current density for compression conditions. These variables decrease with decreasing porosity at higher compression ratios. On the contrary, an increasing activation loss is observed for the compression cases. A higher oxygen concentration leads to a higher local current density and reaction rates. The base case with 0% compression on the GDL results in the best overall performance of the PEM fuel cell. Additionally, the change of the GDL porosity affects the mass transfer in all directions, and it has stronger impact on the oxygen transfer to the land areas in the y-direction (in plane) than to the reactions sites in the z-direction (through-plane).

In order to maximize the cell performance and ensure the gas sealing security, the clamping force on the bipolar plates should be as small as possible to prevent the porosity reduction in the GDL. Apart from the water phase change effects in the PEM fuel cell, the thickness change of the GDL caused by the intrusion into the channel may be also important, as it may affect the mass transfer in the channels. Further work in this area might be required for both geometrical deformation and water phase change. In addition, the PEM fuel cell performance is sensitive to the electron resistance. Therefore, an optimum compression ratio with the best cell performance may exist, in terms of the compression force acting on the cell. The effects of compression of the GDL on the contact resistance will be implemented in another study to replace the constant value applied in the present study.

## NOMENCLATURE

$C_p$ = specific heat at constant pressure, J $kg^{-1}$ $K^{-1}$
$d_{pore}$ = mean pore diameter of porous medium, m
$D_i$ = diffusion coefficient of species i, $m^2$ $s^{-1}$
$D_n$ = viscous resistance, $m^2$ $s^{-1}$
$E_0$ = theoretical potential, V
$E_{act}$ = activation energy, J $mol^{-1}$
$E_{Nernst}$ = Nernst potential, V
F = Faraday constant, 96 487 C $mol^{-1}$
$F_n$ = viscous inertia, $m^2$ $s^{-1}$
$\Delta G_{rxn}$ = change in Gibbs free energy, J $mol^{-1}$
$h_i$ = thickness of component i, m
$\Delta H_e$ = enthalpy change per mole electron, J $mol^{-1}e^{-1}$
$\Delta H_{rxn}$ = enthalpy change, J $mol^{-1}$
i = local current density, A $m^{-2}$
$i_0$ = local exchange current density, A $m^{-2}$
I = average current density, A $m^{-2}$
$j_i$= = mass diffusion flux of species i, kg $m^{-2}$ $s^{-1}$
k = effective thermal conductivity, W $m^{-1}$ $K^{-1}$
$M_i$ = molecular-weight of species i, kg $mol^{-1}$
n = number of electrons transferred, —
P = pressure, Pa
R = ideal gas constant, J $mol^{-1}$ $K^{-1}$
$R_e$ = electric resistance of fuel cell, $\Omega$ $m^2$
$S_i$ = source terms for partial differential equations, kg $m^{-3}$ $s^{-1}$ or J $m^{-3}$ $s^{-1}$
$S_{mem}$ = surface area of membrane, $m^2$
$\Delta S_{rxn}$ = entropy change, J $mol^{-1}$ $K^{-1}$
T = temperature, K
U = fluid velocity vector, m $s^{-1}$
V = cell voltage, V
$V_i$ = diffusion volume of species i, $m^{-3}$


*Int. J. Energy Res.* 2017; **41**:985–1003 © 2016 John Wiley & Sons, Ltd.
DOI: 10.1002/er

$X_i$ = mole fraction of species i, —
$Y_i$ = mass fraction of species i, —

$\alpha_e$ = transfer coefficient, —
$\gamma_a$ = pre-constant at anode, $A\,m^{-2}$
$\gamma_c$ = pre-constant at cathode, $A\,m^{-2}$
$\varepsilon$ = porosity of porous medium, —
$\varepsilon_{com}$ = porosity of compressed GDL, —
$\eta$ = overpotential, V
$\eta_{acti,a}$ = a anode activation overpotential, V
$\eta_{acti,c}$ = c cathode activation overpotential, V
$\eta_e$ = activation overpotential, V
$\lambda$ = compression ratio
$\mu$ = dynamic viscosity, $kg\,m^{-1}\,s^{-1}$
$\rho$ = gas mixture density, $kg\,m^{-3}$
$\tau$ = tortuosity of porous medium, —

*Subscripts*

0 = standard or ideal conditions
a = anode
acti = activation
A = gas species A
AB = binary species A and B
B = gas species B
c = cathode
cell = PEM fuel cell
com = compressed
C = gas species C
e = electron
gas = gas
i = gas species i
initial = initial condition
Knudsen = Knudsen diffusion
m = for source term in mass transfer
mem = membrane
n = for source term in momentum equation
Nernst = Nernst
p = constant pressure
pore = pores
rxn = reaction status
Stefan-Maxwell = Stefan-Maxwell diffusion
T = temperature

*Superscripts*

a = reaction order for oxygen
b = reaction order for water
m = reaction order for hydrogen

## ACKNOWLEDGEMENTS

The first author gratefully acknowledges the financial support from the China Scholarship Council (CSC).

## REFERENCES

1. Bhatt S, Gupta B, Sethi VK, Pandey M. Polymer exchange membrane (PEM) fuel cell: a review. *Int. J. Curr. Eng. Tech* 2012; **2**(1):219–226.
2. Bresciani F, Casalegno A, Varisco G, Marchesi R. Water transport into PEFC gas diffusion layer: experimental characterization of diffusion and permeation. *International Journal of Energy Research* 2014; **38**(5):602–613. doi:10.1002/er.3065.
3. Zhang L, Xia Z. Mechanisms of oxygen reduction reaction on nitrogen-doped graphene for fuel cells. *The Journal of Physical Chemistry C* 2011; **115**(22):11170–11176. doi:10.1021/jp201991j.
4. Martins LS, Gardolinski JE, Vargas JV, Ordonez JC, Amico SC, Forte MM. The experimental validation of a simplified PEMFC simulation model for design and optimization purposes. *Applied Thermal Engineering* 2009; **29**(14):3036–3048. doi:10.1016/j.applthermaleng.2009.04.002.
5. Roshandel R, Arbabi F, Moghaddam GK. Simulation of an innovative flow-field design based on a bio inspired pattern for PEM fuel cells. *Renewable Energy* 2012; **41**:86–95. doi:10.1016/j.renene.2011.10.008.
6. Obayopo SO, Bello-Ochende T, Meyer JP. Three-dimensional optimization of a fuel gas channel of a proton exchange membrane fuel cell for maximum current density. *International Journal of Energy Research* 2013; **37**(3):228–241. doi:10.1002/er.1935.
7. Williams MV, Begg E, Bonville L, Kunz HR, Fenton JM. Characterization of gas diffusion layers for PEMFC. *Journal of the Electrochemical Society* 2004; **151**(8):A1173–A1180. doi:10.1149/1.1764779.
8. Ito H, Maeda T, Nakano A, Hwang CM, Ishida M, Yokoi N, Hasegawa Y, Kato A, Yoshida T. Influence of different gas diffusion layers on the water management of polymer electrolyte unitized reversible fuel cell. *ECS Transactions* 2010; **33**(1):945–954. doi:10.1149/1.3484588.
9. Zhou P, Wu CW, Ma GJ. Influence of clamping force on the performance of PEMFCs. *Journal of Power Sources* 2007; **163**(2):874–881. doi:10.1016/j.jpowsour.2006.09.068.
10. Bazylak A, Sinton D, Liu ZS, Djilali N. Effect of compression on liquid water transport and microstructure of PEMFC gas diffusion layers. *Journal of Power Sources* 2007; **163**(2):784–792. doi:10.1016/j.jpowsour.2006.09.045.
11. Ge J, Higier A, Liu H. Effect of gas diffusion layer compression on PEM fuel cell performance. *Journal of Power Sources* 2006; **159**(2):922–927. doi:10.1016/j.jpowsour.2005.11.069.

12. Espinoza M, Andersson M, Yuan J, Sundén B. Compress effects on porosity, gas-phase tortuosity, and gas permeability in a simulated PEM gas diffusion layer. *International Journal of Energy Research* 2015; **39**(11):1528–36. doi:10.1002/er.3348.
13. Zhou P, Wu CW. Numerical study on the compression effect of gas diffusion layer on PEMFC performance. *Journal of Power Sources* 2007; **170**(1):93–100. doi:10.1016/j.jpowsour.2007.03.073.
14. Cunningham N, Lefèvre M, Lebrun G, Dodelet JP. Measuring the through-plane electrical resistivity of bipolar plates (apparatus and methods). *Journal of Power Sources* 2005; **143**(1):93–102. doi:10.1016/j.jpowsour.2004.11.062.
15. Nitta I, Himanen O, Mikkola M. Thermal conductivity and contact resistance of compressed gas diffusion layer of PEM fuel cell. *Fuel Cells* 2008; **8**(2):111–119. doi:10.1002/fuce.200700054.
16. Nitta I, Karvonen S, Himanen O, Mikkola M. Modelling the effect of inhomogeneous compression of GDL on local transport phenomena in a PEM fuel cell. *Fuel Cells* 2008; **8**(6):410–421. doi:10.1002/fuce.200700058.
17. Nitta I, Hottinen T, Himanen O, Mikkola M. Inhomogeneous compression of PEMFC gas diffusion layer: part I. Experimental. *Journal of Power Sources* 2007; **171**(1):26–36. doi:10.1016/j.jpowsour.2006.11.018.
18. Barbir F. *PEM Fuel Cells: Theory and Practice*. Academic Press: Cambridge, 2012.
19. Dicks AL. The role of carbon in fuel cells. *Journal of Power Sources* 2006; **156**(2):128–141. doi:10.1016/j.jpowsour.2006.02.054.
20. Todd B, Young JB. Thermodynamic and transport properties of gases for use in solid oxide fuel cell modelling. *Journal of Power Sources* 2002; **110**(1):186–200. doi:10.1016/S0378-7753(02)00277-X.
21. Çengel YA, Boles MA. In *Thermodynamics: An Engineering Approach*, Kanoğlu M (ed.). McGraw-Hill Education: New York, USA, 2015.
22. Zhang Z, Jia L, Wang X, Ba L. Effects of inlet humidification on PEM fuel cell dynamic behaviors. *International Journal of Energy Research* 2011; **35**(5):376–388. doi:10.1002/er.1692.
23. He G, Yamazaki Y, Abudula A. A three-dimensional analysis of the effect of anisotropic gas diffusion layer (GDL) thermal conductivity on the heat transfer and two-phase behavior in a proton exchange membrane fuel cell (PEMFC). *Journal of Power Sources* 2010; **195**(6):1551–1560. doi:10.1016/j.jpowsour.2009.09.059.
24. Khandelwal M, Mench MM. Direct measurement of through-plane thermal conductivity and contact resistance in fuel cell materials. *Journal of Power Sources* 2006; **161**(2):1106–1115. doi:10.1016/j.jpowsour.2006.06.092.
25. Sinha PK, Wang CY, Beuscher U. Effect of flow field design on the performance of elevated-temperature polymer electrolyte fuel cells. *International Journal of Energy Research* 2007; **31**(4):390–411. doi:10.1002/er.1257.
26. Chu HS, Yeh C, Chen F. Effects of porosity change of gas diffuser on performance of proton exchange membrane fuel cell. *Journal of Power Sources* 2003; **123**(1):1–9. doi:10.1016/S0378-7753(02)00605-5.
27. Uchida M, Aoyama Y, Eda N, Ohta A. Investigation of the microstructure in the catalyst layer and effects of both perfluorosulfonate ionomer and PTFE-loaded carbon on the catalyst layer of polymer electrolyte fuel cells. *Journal of the Electrochemical Society* 1995; **142**(12):4143–4149. doi:10.1149/1.2048477.
28. Nguyen PT, Berning T, Djilali N. Computational model of a PEM fuel cell with serpentine gas flow channels. *Journal of Power Sources* 2004; **130**(1):149–157. doi:10.1016/j.jpowsour.2003.12.027.
29. Min CH. Performance of a proton exchange membrane fuel cell with a stepped flow field design. *Journal of Power Sources* 2009; **186**(2):370–376. doi:10.1016/j.jpowsour.2008.10.048.
30. Yuan J, Huang Y, Sundén B, Wang WG. Analysis of parameter effects on chemical reaction coupled transport phenomena in SOFC anodes. *Heat and Mass Transfer* 2009; **45**(4):471–484. doi:10.1007/s00231-008-0449-6.
31. Di Stefano GI. *Modeling Thermal Energy Storage Systems with OpenFOAM*. 2014; http://hdl.handle.net/10589/98281.
32. Berning T, Lu DM, Djilali N. Three-dimensional computational analysis of transport phenomena in a PEM fuel cell. *Journal of Power Sources* 2002; **106**(1):284–294. doi:10.1016/S0378-7753(01)01057-6.
33. Yuan J, Sundén B. On mechanisms and models of multi-component gas diffusion in porous structures of fuel cell electrodes. *International Journal of Heat and Mass Transfer* 2014; **69**:358–374. doi:10.1016/j.ijheatmasstransfer.2013.10.032.
34. Mann RF, Amphlett JC, Hooper MA, Jensen HM, Peppley BA, Roberge PR. Development and application of a generalised steady-state electrochemical model for a PEM fuel cell. *Journal of Power Sources* 2000; **86**(1):173–180. doi:10.1016/S0378-7753(99)00484-X.
35. Borup RL, Davey JR, Garzon FH, Wood DL, Inbody MA. PEM fuel cell electrocatalyst durability

measurements. *Journal of Power Sources* 2006; **163**(1):76–81. doi:10.1016/j.jpowsour.2006.03.009.

36. Barrande M, Bouchet R, Denoyel R. Tortuosity of porous particles. *Analytical Chemistry* 2007; **79**(23):9115–9121.
37. Hottinen T, Himanen O, Karvonen S, Nitta I. Inhomogeneous compression of PEMFC gas diffusion layer: part II. Modeling the effect. *Journal of Power Sources* 2007; **171**(1):113–121. doi:10.1016/j.jpowsour.2006.10.076.
38. Wang L, Husar A, Zhou T, Liu H. A parametric study of PEM fuel cell performances. *International Journal of Hydrogen Energy* 2003; **28**(11):1263–1272. doi:10.1016/S0360-3199(02)00284-7.
39. Karimi G, Li X, Teertstra P. Measurement of through-plane effective thermal conductivity and contact resistance in PEM fuel cell diffusion media. *Electrochimica Acta* 2010; **55**(5):1619–1625. doi:10.1016/j.electacta.2009.10.035.

# Paper III

INTERNATIONAL JOURNAL OF
ENERGY RESEARCH

INTERNATIONAL JOURNAL OF ENERGY RESEARCH
*Int. J. Energy Res.* (2017)
Published online in Wiley Online Library (wileyonlinelibrary.com). DOI: 10.1002/er.3774

# Investigation of effects of non-homogenous deformation of gas diffusion layer in a PEM fuel cell

Jiatang Wang[1,*,†], Jinliang Yuan[2], Jong-Sung Yu[3] and Bengt Sundén[1]

[1]Department of Energy Sciences, Lund University, PO Box 118, Ole Römers väg 1, Lund 22100, Sweden
[2]Faculty of Maritime and Transportation, Ningbo University, Fenghua Road 818, Ningbo 315211, China
[3]Department of Energy Systems Engineering, DGIST, Daegu, 711-873, Korea

## SUMMARY

Proton exchange membrane fuel cells have been promoted due to improved breakthrough and increased commercialization. The assembly pressure put on a single cell and a fuel cell stack has important influence on the geometric deformation of the gas diffusion layers (GDLs) resulting in a change in porosity, permeability, and the resistance for heat and charge transfer in proton exchange membrane fuel cells. In this paper, both the finite element method and the finite volume method are used, respectively, to predict the GDL deformation and associated effects on the geometric parameters, porosity, mass transport property, and the cell performance. It is found that based on the isotropic Young's modulus and the finite element method, the porosity and thickness under a certain assembly pressure are non-homogeneous across the fuel cell in the in-plane direction. The variations of the porosity change and compression ratio in the cross-section plane are localized by three zones, that is, a linear porosity zone, a constant porosity zone, and a nonlinear porosity zone. The results showed that the GDL porosity and compression ratios maintain linear and nonlinear changes in the zone above the shoulders and the zone under the channel but close to the shoulder, respectively. However, a constant value is kept above the middle of the channel. The obtained non-homogeneous porosity distribution is applied together with the deformed GDL for further computational fluid dynamics analysis, in which the finite volume method is implemented. The computational fluid dynamic results reveal that a higher assembly pressure decreases the porosity, GDL thickness, gas flow channel cross-sectional areas, oxygen diffusion coefficient, oxygen concentration, and cell performance. The maximum oxygen mole fraction occurs where the maximum porosity exists. A sufficient GDL thickness is required to ensure transfer of fresh gas to the reaction sites far away from the channel. However, the reduction of porosity is a dominating factor that decreases the cell performance compared with the decreased gas channel flow area and GDL thickness in the assembly condition. Therefore, the assembly pressure should be balanced to consider both the cell performance and gas sealing security.


**KEY WORDS**

PEM fuel cells; assembly pressure; porosity; deformed GDL; transport phenomena; modeling

**Correspondence**

*Jiatang Wang, Department of Energy Sciences, Lund University, PO Box 118, Ole Römers väg 1, Lund 22100, Sweden.
†E-mail: jiatang.wang@energy.lth.se

Received 19 December 2016; Revised 11 April 2017; Accepted 11 April 2017

## 1. INTRODUCTION

A proton exchange membrane (PEM) fuel cell can convert chemical energy into electrical energy. The advantages of a PEM fuel cell are efficient energy conversion, high power density, and zero-pollutant emissions compared with a combustion engine. It has a promising potential to be used in many applications, for example, transportation, stationary power source, and communication. The interest of its wide application in these fields promotes the necessity of deep understanding of the involved processes and phenomena. It is widely known that a further breakthrough is needed to enable reduction of the cost and improve the stability before the PEM fuel cells reach real commercialization.

The porous features of the electrodes play an important role on the mass and species transport in PEM fuel cells. One of the most important components is the gas diffusion layer (GDL). It is made of carbon paper or carbon cloth, which provides a very high tensile and compressive strength. The main roles of a GDL are to distribute the reactants from the gas channels, to remove water from the reaction sites, and to transfer electrons to the bipolar plates. Other key functions of a GDL are to mechanically support the soft layers, that is, membrane and catalyst layers (CLs), and to sandwich into a membrane electrode

assembly (MEA). In the assembling process of a single cell or a stack, the GDLs, membranes, bipolar plates, and gaskets are usually clamped together by using bolts. A proper torque, also called an assembly pressure, is provided on the bolts to ensure gas sealing and to reduce the contact resistance, as demonstrated in literature [1]. However, this assembly pressure will result in deformation of the GDL. The deformation of a GDL under the channel caused by the assembly pressure was clearly observed in literature [2]. It is clear that the GDL under the ribs becomes thinner and intrudes into the gas channels. On the other hand, the GDL is deformed and the dimensions of the flow channels are reduced.

Some experimental research works have been carried out to investigate the impact of a GDL deformation caused by the assembling pressure in PEM fuel cells. Escribano et al. [3] tested the GDL deformation for different GDL materials and further studied the effects of the GDL deformation on the electric resistance. It was suggested that a lower compression is favorable for achieving high durability of the MEA. An optimum cell performance was obtained in the cell tested by Lee et al. [4] for a range of torques on the bolts in a single cell. This optimum performance was appeared because of changes in the porosity and the electrical contact resistance. To reveal the cell performance under various assembly pressures, a single PEM fuel cell test facility designed by Ge et al. [5] was employed to identify the influence of GDL compression ratios on the cell performance. The experimental results showed that there exists an optimal compression ratio for which the cell performance is maximized. In contrast, a more comprehensive experiment was designed to simultaneously measure the thickness, gas permeability, and porosity of a GDL under compression by Chang et al. [6]. They concluded that the contact resistance between the GDL and the bipolar plate is a dominating factor causing a potential loss, but not the through-plane electrical resistance of the carbon paper itself across the fuel cells. Nitta et al. [7] experimentally analyzed the contact resistance of a porous GDL under compression, and the results showed that the thermal contact resistance between the GDL and graphite decreased nonlinearly with increasing compression pressure. These experimental observations have shown that the assembly compression pressure magnitude has significant effects on the cell performance, even on other parameters like the GDL deformation, mass transfer, and contact resistance. Despite the experimental observations of the effects of assembly pressure in PEM fuel cells, only a limited number of numerical investigations have been developed in the past two decades. Computational methods might be efficient to account for the assembly effects on the mechanical behavior and mass transport in PEM fuel cells.

In the literature, some numerical models have been developed and published to analyze the effects on GDL by the assembly pressure. At the early stage, some of the results were obtained under limited conditions, for example, homogeneous compression and two-dimensional modeling by the lattice Boltzmann method [8], non-uniform porosity of the GDL without GDL deformation [9]. Bograchev et al. [10,11] numerically studied mechanical issues. They developed a two-dimensional model of the MEA to investigate the mechanical stresses generated in the fuel cell during the assembling process by ABAQUS (a commercial software for finite element analysis and computer-aided engineering) and their in-house code. The evolution of the residual deformation for various bolt torques was presented in Bograchev et al. [10]. Bograchev et al. [11], in another study, improved the model and studied the mechanical behavior of MEA with and without heating and humidification, respectively, during a fuel cell operating cycle. It was suggested that the improved model is able to predict the MEA aging issue. To predict the GDL deformation under assembly conditions and its effects on the cell performance, Zhou et al. [1,12] and Taymaz et al. [13] developed similar models to study the GDL behavior for different assembly pressures. In the study of Zhou et al. [12], it was revealed that the assembly pressure has significant effects on the PEM fuel cell performance and a high assembly pressure increases the mass transfer resistance. Taymaz et al. [13] applied a single channel model to predict the GDL deformation by ANSYS and subsequently implemented the deformed GDL to the computational fluid dynamics (CFD) model analyzed by the finite element method. The results suggested that 0.5 and 1 MPa pressure values are the optimum ones when considering the electrical properties of the fuel cell components. In another study by Zhou et al. [1], an interdigitated gas channel design was applied in a half-cell and it was suggested that there might exist a maximum power density for an optimal assembly pressure. There is no doubt that the deformed GDL caused by the assembly pressure reduces the diffusion path for the mass transport especially at high current densities. The decreased contact resistance for the thermal and electron transfer has a positive effect for increasing the cell current density under an assembly pressure. However, more research work related to the effects of assembly pressure on the mass transport and cell performance in PEM fuel cells is still needed. This is so because the deformation of a GDL by an assembly pressure is non-linear; that is, a non-linear porosity distribution occurs across the GDL in the in-plane direction. The non-linear porosity distribution had been mostly neglected or a constant porosity was widely assumed in previous studies, but it plays an important role on the transport phenomena. Salaberri et al. [14] studied a non-linear porosity distribution along the in-plane direction with the influence by the shoulder width, GDL thickness, and the fillet radius of the shoulder under various assembly pressures by a non-linear orthotropic model. In that study, they demonstrated that a varying and non-linear porosity is an important parameter. A non-linear gas permeability of the GDL in the in-plane direction was observed although a uniform pressure was maintained on the bipolar plates in an experimental test [15]. It was suggested that the non-linear gas permeability is caused by the non-linear porosity

and decreased pore diameter. Non-linear deformations of the GDL under various assembly pressures were obtained in the numerical work; however, the properties of the non-linear porosity distribution were not implemented in the CFD investigations [12,16,17]. A remarkable numerical work was presented by Shi et al. [18], who investigated water management under inhomogeneous compression coinciding with the calculated non-linear porosity. That study reported that the presence of liquid water could result in a non-uniform distribution of the porosity and permeability in the GDL. Therefore, non-linear porosity should be considered in PEM fuel cell modeling.

This work complements our previous research [19] by taking into account the geometric deformation due to the assembly pressure. In addition, the related nonlinear change of the porosity is considered. The main objective of the present work is to numerically investigate the effects of a deformed GDL, caused by the assembly pressure, on the geometric deformation, porosity, mass transfer, and cell performance. The mechanical part of the ANSYS software is applied to predict the GDL deformation for various assembly pressures. The compression ratio and porosity for various assembly pressures are determined and analyzed as a function of the position and assembly pressure, respectively. Subsequently, the deformed GDL with non-homogeneous thickness and porosity is implemented as input properties to the OPENFOAM software. The validation of the CFD model is performed by comparison of the current predictions with experimental data in the literature. The effects of the assembly pressure on the porosity, the properties of mass transport, and cell performance are analyzed comprehensively. Distributions of the local current densities and the oxygen concentration are also presented and discussed.

## 2. MODELING DESCRIPTION

The models and computational methods developed in this study include two parts, that is, the mechanical model by the finite element method in ANSYS and the CFD model by the finite volume method in OPENFOAM. The outputs from ANSYS in terms of GDL deformation are implemented into the CFD model as inputs and initial conditions for the mass transfer and cell performance analysis. To decrease the computational efforts, a single channel half-cell (i.e., one side of the cell only) model is selected for the mechanical analysis and a single channel unit-cell (i.e., both sides of the cell) model for the CFD analysis, respectively. The latter model contains all the components in a cell unit, that is, a membrane, CLs, GDLs, and bipolar plates ranging from millimeters to centimeters in size.

### 2.1. Mechanical model

The mechanical model is developed for a three-dimensional (3D) domain composed of a single channel and the electrode of a PEM fuel cell. It is assumed that the components in both the cathode and the anode of the PEM fuel cell have the same structural change behavior, and accordingly, a half-cell domain is selected as the representative one, as shown in Figure 1a. In order to allow precise calculations of the GDL deformation, unstructured meshes of the GDL, CL, and membrane have been refined to 0.02 mm, as proposed in literature [20]. In total, 49 538 elements and 97 870 nodes are included, as presented in Figure 1a.The carbon paper of GDL is made of fibers, and accordingly, there are isotropic models [13] and non-linear anisotropic models [14] to predict the GDL deformation and the transport properties presented in the literature. Large variations between isotropic and anisotropic cases could be observed [15]. This is so because different magnitudes of Young's modulus ranging from MPa to GPa were applied in the in-plane direction and through-plane direction [1,10,14,21]. The GDL is composed of isotropic and compressible carbon paper in this work, similar to TGP-H-120 carbon paper in Refs [13,22]. The classical elastic–plastic model follows the one described in Refs [10,11], and it is applied to predict the GDL deformation. The GDL behavior is divided into an elastic region and a plastic region. The tensor of deformation is presented as the sum of these [10],

$$\varepsilon_{ij} = \varepsilon_{ij}^{EL} + \varepsilon_{ij}^{PL} \tag{1}$$

where $\varepsilon EL\ ij$ is the elastic strain tensor and $\varepsilon PL\ ij$ is the plastic strain tensor.In the elastic region, the Hooke's law is employed [11],

$$\sigma_{ij} = \frac{E}{(1+v)(1-2v)}\left(v\varepsilon_{ij}^{EL} + \sum_{k}(1-2v)\varepsilon_{kk}^{EL}\delta_{ij}\right) \tag{2}$$

where $\sigma_{ij}$ is the stress tensor, $v$ is the Poisson's ratio, $E$ is the Young's modulus, and $\delta_{ij}$ is the Kronecker $\delta$-symbol. In the plastic region, the plasticity behavior is evaluated by Prandtl–Reuss theory, and the von Mises yield function is expressed as [23],

$$f(\sigma_{ij}) = \sqrt{\frac{3}{2}S_{ij}S_{ji}} - \sigma_0 \tag{3}$$

where $\sigma_0$ is the yield strength and $S_{ij}$ is the component of the deviatoric stress tensor [10],

$$S_{ij} = \sigma_{ij} - \frac{1}{3}\sigma_{kk} \tag{4}$$

when $f(\sigma_{ij}) = 0$, the yield occurs in GDL based on the von Mises yield criterion. For $f(\sigma_{ij}) < 0$, the material deforms elastically.

As suggested by Zhou et al. [1], the deformation of the CLs and membrane can be neglected as the compressive ability of the CLs and the membrane is almost 10 times less than that of the GDLs. Therefore, the deformations

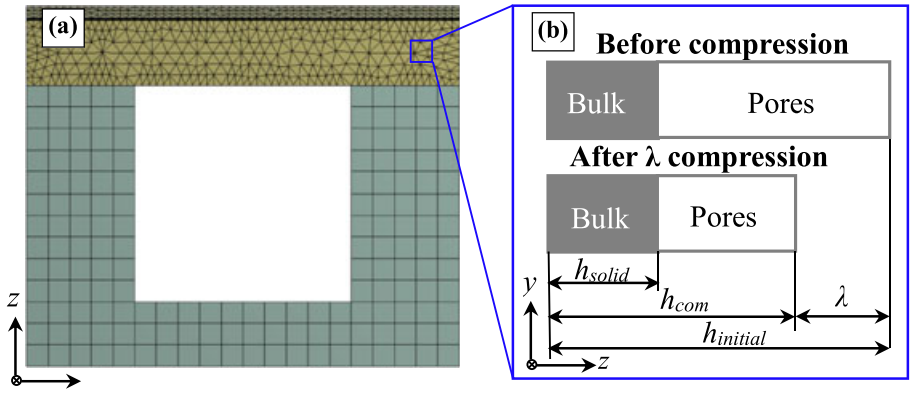


**Figure 1.** (a) A cross-sectional view of a half-cell model before deformation and (b) assumed model of deformed porous materials. [Colour figure can be viewed at wileyonlinelibrary.com]

of the bipolar plate (made of the graphite plate for which the deformation can be regarded as zero), the CLs and membrane are not considered in the current study. The dimensions of the mechanical model domain are extracted from a practical PEM fuel cell used in the reference [24], as presented in Table I. In addition, the length of the 3D cell is 0.005 m to reduce the computational time. The physical parameters of other components not listed in this table are treated as the rigid materials. During the assembling, it is assumed that a uniform pressure is applied on the top surface of the bipolar plates (in the through-plane direction in Figure 1a) and a possible localized pressure distribution around the bolts is neglected. A fixed boundary is selected in the model domain at the bottom in Figure 1a, which is the solid surface (in the through-plane direction). A horizontal displacement is given at the surrounding surfaces of the domain (in the in-plane direction). All the interfaces between the components are bonded to avoid any slip. In this model analysis, different assembly pressure conditions ranging from 0 to 3 MPa are studied.

The GDL used in the PEM fuel cell is porous and flexible and has physical properties being affected by the deformation caused by the compression on it. To describe the deformed GDL in the mechanical analysis, the thickness of the compressed GDL, $h_{com}$, is expressed as

$$h_{com} = (1 - \lambda)h_{initial} \tag{5}$$

where $\lambda$ is the compression ratio and $h_{initial}$ is the initial thickness of the uncompressed GDL. Here, it is assumed that the porous GDLs consist of the pores and the solid bulk, and only the pores under the compression by a pressure leads to a change of the GDL thickness in the through-plane direction, as illustrated in Figure 1b. The thickness of the solid materials $h_{solid}$ is then evaluated as [2]

$$h_{solid} = h_{initial}(1 - \varepsilon_0) \tag{6}$$

where $\varepsilon_0$ is the initial porosity for the uncompressed GDL. The model assumes that the change of the GDL thickness is only caused by the change in the volume of the pores but not that of the solid part. Thus, the porosity of the compressed GDL might be evaluated as a function of the GDL thickness [2],

$$\varepsilon_{com} = \varepsilon_0 \frac{h_{com} - h_{solid}}{h_{initial} - h_{solid}} \tag{7}$$

where $\varepsilon_{com}$ is the porosity of the compressed GDL. Another physical parameter describing the porous structures, tortuosity, is evaluated as [25]

$$\tau = 1 - 0.49 \ln(\varepsilon) \tag{8}$$

The results obtained from the mechanical analysis are implemented into the CFD model in terms of the deformed domains, the non-homogeneous porosity and tortuosity of the GDLs.

**Table I.** Geometric and physical parameters applied in the mechanical model.

| Parameters | Value | Reference |
|---|---|---|
| Gas channel length (for CFD model) | 0.05 m | [24] |
| Gas channel width | $1.0 \times 10^{-3}$ m | [24] |
| Gas channel height | $1.0 \times 10^{-3}$ m | [24] |
| Land area width | $0.5 \times 10^{-3}$ m | [24] |
| Thickness of bipolar plate | $0.3 \times 10^{-3}$ m | [24] |
| Thickness of GDL | $0.3 \times 10^{-3}$ m | [24] |
| Thickness of CL | $1.29 \times 10^{-5}$ m | [24] |
| Thickness of electrolyte | $1.08 \times 10^{-4}$ m | [24] |
| GDL density (carbon paper) | 400 kg $m^{-3}$ | [11] |
| GDL Young's modulus | 6.3 MPa | [22] |
| GDL Poisson's ratio | 0.09 | [22] |

## 2.2. CFD model

A complete single-channel unit-cell model is developed and applied for the CFD analysis to study the mass transport and cell performance in 3D. The CFD model

takes the outputs from the above mechanical model, including the deformed shape and the porous features of GDLs. The CFD domain for various assembly pressure conditions (i.e., 0, 1, 2, and 3 MPa) is shown in Figure 2 (here, the case for 1 MPa assembly pressure condition is illustrated as an example). The anode (fuel side) and cathode (air side) were assembled symmetrically, and each side consists of a bipolar plate, gas channel, GDL, and CL.

A number of assumptions are made in the numerical CFD model in this study. These assumptions are identical to those in our previous work [19] except the one related to the porosity change. The porosity is kept constant in the GDL above the channels but changes above the shoulders due to the compression in that work. However, the porosity varies along the cell in-plane direction both above the channels and shoulders, which is a novelty of this paper.Under these assumptions, the partial differential equations for conservation of the momentum, mass, and species transport are solved and formulated as below. The Navier–Stokes equations applied in the gas flow channel, GDL and CL, can be expressed as [19]

$$\nabla\cdot(\rho UU) = -\nabla P + \nabla\cdot\mu\nabla U + S_n \tag{9}$$

where $U$ is the fluid velocity vector, $P$ is the gas pressure, $\mu$ is the dynamic viscosity of the fluid, and $S_n$ stands for the source term. The density $\rho$ is the gas mixture density, which can be expressed as

$$\rho = \frac{P}{RT\sum_{i=1}^{N}(Y_i/M_i)} \tag{10}$$

where $Y_i$ and $M_i$ are the mass fraction and molar weight of species $i$, respectively; $T$ is the temperature, and $R$ is the ideal gas constant. A constant mixture density is applied at the cell inlet based on the inlet condition, but in the other regions, a variable density is considered by Eqn (10). The dynamic viscosity of the fluid is treated as a weighted sum of all gas species [26],

$$\mu = \sum_{i=1}^{N}\mu_i Y_i \tag{11}$$

where the localized dynamic viscosity of species $i$ for the gases, $\mu_i$, is a function of temperature and represented by a six-order polynomial [26],

$$\mu_i = \sum_{n=0}^{6} a_n \left(\frac{T}{1000}\right)^n \tag{12}$$

where the coefficients $a_n$ are unique for every species $i$ and can be found in the literature [26]. The velocity and pressure coupling for the Navier–Stokes equations is handled by employing the PISO method. To consider the effect of the porous structures, extra pressure losses occur and the source term in Eqn (9) will be non-zero in the porous layers. Equation (13) is applied in the gas flow channel, while Eqn (14) is used in the porous GDLs and CLs [27], respectively,

$$S_n = 0 \tag{13}$$

$$S_n = -(\mu D_n + 0.5\rho|U|F_n)U \tag{14}$$

In Eqn (14), the non-linear term is not considered in this study; that is, $F_n$ is set to zero. However, the pore diameter $d_{pore}$ and porosity $\varepsilon$ are involved in the first term in Eqn (14) for the fluid in the porous zones [28]:

$$D_n = \frac{150}{d_{pore}^2}\frac{(1-\varepsilon)^2}{\varepsilon^3} \tag{15}$$

The mass conservation for the gas flow can be expressed as [2]

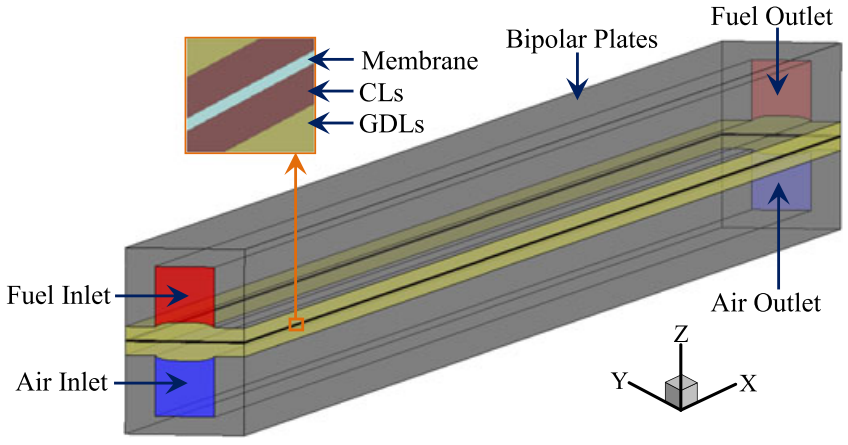


**Figure 2.** Schematic illustration of a 3D computational domain for CFD analysis for an assembly pressure condition (here, the case for a 1 MPa assembly pressure condition is illustrated as an example). [Colour figure can be viewed at wileyonlinelibrary.com]

$$\nabla\cdot(\rho U) = S_m \tag{16}$$

where the source term $S_m$ is related to the electrochemical reactions appearing at the reaction sites. It can be expressed by Eqn (17) for the cathode and by Eqn (18) for the anode [29], respectively.

$$S_{m,c} = -\frac{i}{4F}M_{O_2} + \frac{i}{2F}M_{H_2O} \tag{17}$$

$$S_{m,a} = -\frac{i}{2F}M_{H_2} \tag{18}$$

where $i$ is the local current density, $M$ is the molar weight of the involved gas species, and $F$ is the Faraday's constant (96 485 C $mol^{-1}$). The plus sign (+) is applied for the product generation and the negative sign (−) for the reactant consumption.The mass fraction of water, oxygen in the cathode, and that of hydrogen in the anode is solved by the species transport equation shown in Eqn (19) [30],

$$\nabla\cdot(\rho U Y_i) + \nabla\cdot J_i = 0 \tag{19}$$

where the mass diffusion flux is evaluated by the Fick's law [31], i.e.,

$$J_i = -\rho D_{i,gas}\nabla Y_i \tag{20}$$

where $D_{i,gas}$ is the mass diffusion coefficient of species $i$ in the involved gas mixture and $Y_i$ is the mass fraction of species $i$. It should be noted that the mass fractions of the inert species (nitrogen in the cathode and water in the anode) are not solved by Eqn (19), but they are determined from the total mass subtracted by the summation of the mass fractions of the other active species, respectively, for the anode and the cathode [32]. Due to the multi-component diffusion occurring in the cathode side, that is, oxygen, water, and nitrogen are involved, the Stefan-Maxwell model is also used to evaluate the individual diffusion coefficients in the gas mixture, as shown in Eqn (21) [27].

$$D_{Stefan-Maxwell} = D_{A,gas} = \frac{1 - X_A}{X_B/D_{AB} + X_c/D_{AC} + \ldots} \tag{21}$$

where $D_{A,gas}$ is the diffusion coefficient of the species $A$ in the mixture, $X_i$ is the molar fraction of the specie $i$, and $D_{i,j}$ is the diffusion coefficients based on the binary diffusion model of species $i$ and $j$. In the anode of the PEM fuel cells, only two species are present, and the diffusion coefficients of hydrogen and water are directly evaluated by the binary diffusion model. The binary diffusion coefficient and the Knudsen diffusion coefficient are described by Eqns (22) and (23), respectively [33],

$$D_{AB} = \frac{10^{-7}T^{1.75}\sqrt{1/M_A + 1/M_B}}{P_{tot}\left(V_A^{1/3} + V_B^{1/3}\right)^2} \tag{22}$$

$$D_{Knudsen} = \frac{d_{pore}}{3}\sqrt{\frac{8RT}{\pi M}} \tag{23}$$

where $V$ is the diffusion volume, $P_{tot}$ is the total pressure of gases $A$ and $B$, $T$ is the temperature, $R$ is the ideal gas constant, and $d_{pore}$ is the mean pore diameter of the porous medium. To account for the effects from both the small scale and porous features, the effective diffusion coefficient of the species $i$ for the gas mixture in the porous layers can be evaluated as in Eqn (24) [34],

$$D_{i,gas} = \frac{\varepsilon}{\tau^2\left(1/D_{Stefan-Maxwell} + 1/D_{Knudsen}\right)} \tag{24}$$

The electrochemical reactions are assumed to occur at the interfaces between the membrane and the CLs. The fuel cell current density $i_{cell}$ is then calculated based on Ohm's law [35],

$$i_{cell} = \frac{E_{Nernst} - V - \eta}{R_e} \tag{25}$$

where $V$ and $\eta$ are the cell operating voltage and the activation overpotential, respectively, and $R_e$ is the total electric resistance of the fuel cell. The Nernst potential $E_{Nernst}$ in Eqn (25) can be described as [35]

$$E_{Nernst} = E_0 + \frac{RT}{nF}\ln\frac{X_{O_2}^{0.5}\cdot X_{H_2}}{X_{H_2O}} \tag{26}$$

where $R$ is the universal gas constant, $n$ is the number of electrons transported, and $E_0$ is the theoretical potential [36] at standard atmosphere condition (298 K, 1 bar). $E_0$ is approximately 1.23 V,

$$E_0 = -\frac{\Delta G_{rxn}}{nF} = -\frac{(\Delta H_{rxn} - T\Delta S_{rxn})}{nF} \tag{27}$$

where $\Delta G_{rxn}$ is the Gibbs free energy change, $\Delta H_{rxn}$ is the enthalpy change, and $\Delta S_{rxn}$ is the entropy change of the reaction. The superscript in Eqn (26) refers to the stoichiometric coefficient of the hydrogen fuel cell reaction in PEM fuel cells. The cell activation overpotential is assumed to be composed of anodic and cathodic contributions,

$$\eta = \eta_{acti,a} + \eta_{acti,c} \tag{28}$$

where the activation overpotential $\eta_{acti,a}$ is for the anode and $\eta_{acti,c}$ is for the cathode, respectively. Values of $\eta$ at both electrodes are obtained by using a root finder based on the Ridder's method after obtaining numerical solutions of the Butler–Volmer equation [37],

$$i = i_0[\exp(A\eta_e) - \exp(B\eta_e)] \tag{29}$$

where

$$A = \frac{2\alpha_e F}{RT} \tag{30}$$

$$B = -\frac{2(1-\alpha_e)F}{RT} \tag{31}$$

where $\alpha_e$ is the transfer coefficient and $\eta_e$ is the activation overpotential for each electrode. The local exchange current densities are given by [35]

$$i_{0,a} = \gamma_a \left(\frac{P_{H_2}}{P_0}\right)^m \exp\left(-\frac{E_{act,a}}{RT}\right) \tag{32}$$

$$i_{0,c} = \gamma_c \left(\frac{P_{O_2}}{P_0}\right)^a \left(\frac{P_{H_2O}}{P_0}\right)^b \exp\left(-\frac{E_{act,c}}{RT}\right) \tag{33}$$

The reaction orders, $a$, $b$, and $m$; the pre-constant $\gamma_a$ and $\gamma_c$; and the activation energies $E_{\mathrm{act},a}$ and $E_{\mathrm{act},c}$, together with the transfer coefficients, $\alpha_e$, are listed in Table II.

Before solving the partial differential equations, a set of boundary conditions for all governing equations is required. The PEM fuel cell is modeled at a temperature of 353 K, and a pressure outlet condition of 3 bars is prescribed at the outlets of the gas flow channels. It is assumed that the cathode and the anode are fed with fully humidified air and hydrogen, respectively. The parameters for the humidified gases with specific mass fractions are taken from the literature [24]. The inlet velocity is based on the desired average current density with the stoichiometric ratio 2 for the oxygen and 1.2 for the hydrogen, respectively [37]. The boundary conditions for other parameters applied in the computational domain are set as zero gradients in the vertical directions of the outside surface. In this simplified model, a constant electric resistance is employed. The ohmic loss in the CLs and GDLs might be different under different assembly conditions, but this is not considered. The input properties of the related materials, kinetics, and electrochemical reactions can be found in Table II.

Control of the mesh dependence of the CFD model is necessary for judging the numerical simulations. Among the cases at various assembly pressures, the case with 3 MPa assembly pressure is the most difficult one to reach convergence, and consequently, it was selected for the grid independence tests. Several mesh numbers, that is, 26 520, 50 752, 76 183, 112 266, 159 068, 221 493, 291 042, and 381 150, were tested at 3 MPa assembly pressure, and the average current densities were monitored, as listed in Table III. The results indicate that the case with 221 493 meshes ($x \times y \times z$: 101 × 43 × 51) has the proper number of grids when considering convergence and stability. Therefore, the mesh size No. 6 was selected for the all CFD simulations under various assembly pressures.

In order to check the accuracy of the CFD simulation of the PEM fuel cell model, the simulations were compared with the experimental data from previous researchers [43] at the same operating conditions, as shown in Figure 3. Good agreement between the experimental and predicted results is obtained, in terms of the current density and the power densities in the range of the cell operating voltages higher than 0.63 V. Both the calculated and measured voltages drop fast when the current density is small, which is mainly caused by the activation losses. The voltage then

**Table II.** Input parameters and properties for the CFD model.

| Parameters and symbols | Value | Reference |
|---|---|---|
| Dynamic viscosity, $\mu$ | | |
| Air/water (initial value) | $2.03715 \times 10^{-5}$ kg m$^{-1}$ s$^{-1}$ | [26] |
| Hydrogen/water (initial value) | $1.0502 \times 10^{-5}$ kg m$^{-1}$ s$^{-1}$ | [26] |
| Density, $\rho$ | | |
| Air/water (initial value) | 0.98335 kg m$^{-3}$ | [38] |
| Hydrogen/water (initial value) | 0.1732 kg m$^{-3}$ | [38] |
| Porosity, $\varepsilon$ | | |
| CL | 0.6 | [39] |
| GDL (initial value) | 0.8 | [40] |
| Pore size, $d_{pore}$ | | |
| CL | $1 \times 10^{-6}$ m | [41] |
| GDL | $5 \times 10^{-5}$ m | [40] |
| Reaction order of $O_2$ | 0.5 | |
| Reaction order of $H_2O$ | −1 | |
| Reaction order of $H_2$ | 1 | |
| Pre-constant at cathode, $\gamma_c$ | $1.328 \times 10^{10}$ A m$^{-2}$ | [42] |
| Pre-constant at anode, $\gamma_a$ | $1.55 \times 10^{6}$ A m$^{-2}$ | [42] |
| Cathode transfer coefficient, $\alpha_c$ | 0.5 | [32] |
| Anode transfer coefficient, $\alpha_a$ | 0.5 | [19] |
| Cathode activation energy, $E_{act,c}$ | $6.6 \times 10^{4}$ J mol$^{-1}$ | [42] |
| Anode activation energy, $E_{act,a}$ | $3.46 \times 10^{4}$ J mol$^{-1}$ | [42] |
| Electric resistance, $R_e$ | $1.2 \times 10^{-5}$ Ω m$^2$ | [42] |

**Table III.** Grid independence tests for the PEM fuel cell under 3 MPa assembly pressure and the monitored average current densities.

| No. | Grids ($x \times y \times z$) | Total grid numbers | Average current density (A cm$^{-2}$) |
|---|---|---|---|
| 1 | 51 × 20 × 26 | 26 520 | 0.49033 |
| 2 | 61 × 26 × 32 | 50 752 | 0.49807 |
| 3 | 71 × 29 × 37 | 76 183 | 0.50109 |
| 4 | 81 × 33 × 42 | 112 266 | 0.50575 |
| 5 | 91 × 38 × 46 | 159 068 | 0.51101 |
| 6 | 101 × 43 × 51 | 221 493 | 0.51327 |
| 7 | 111 × 46 × 57 | 291 042 | 0.51326 |
| 8 | 121 × 50 × 63 | 381 150 | 0.51327 |

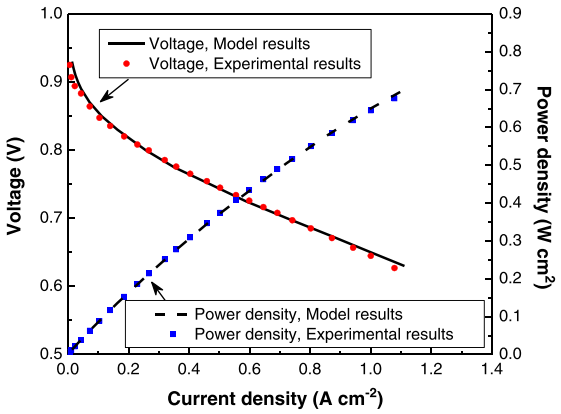


**Figure 3.** Comparison of numerical results and experimental ones [43]. [Colour figure can be viewed at wileyonlinelibrary.com]

keeps a linear decrease to the voltage 0.63 V, where the Ohmic loss is dominating. This validated model is used for the parametric studies.

## 3. NUMERICAL RESULTS AND DISCUSSION

### 3.1. Assembly pressure effects on GDL deformation

Because of the symmetric features applied in this single channel mechanical model, only the cathodic GDL deformation will be presented in this section. During the fuel cell assembly, the GDLs are clamped by the bipolar plates. Figure 4 shows the shapes of a deformed GDL for four different assembly pressures, that is, 0, 1, 2, and 3 MPa, respectively. The thickness of the GDL is kept constant along the cell width for the uncompressed case (0 MPa) but varies due to the different assembly pressures. A thinner GDL is observed above the shoulder areas as the assembly pressure is applied. This is so as the GDL above the shoulders is crushed and deformed due to the porous and flexible properties. As a result, the GDL above the channel

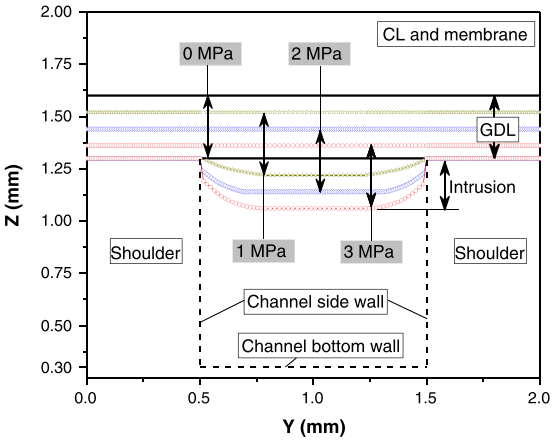


**Figure 4.** Deformed shape of the GDL in the cross-section view for different assembly pressures. [Colour figure can be viewed at wileyonlinelibrary.com]

intrudes into the channel, which leads to a reduction of the gas flow channel cross-section areas, as well as a decrease of the gas diffusion area and the porosity above the shoulder.

The porosity is one of the most important parameters characterizing the transport phenomena of the porous GDL in a PEM fuel cell. As a consequence of the assumptions for the porous materials illustrated in Figure 1b, the result of the assembly pressure loaded on the GDL is a reduction of the porosity and the thickness. The predicted porosity of the GDL along the cell in the in-plane direction is shown in Figure 5a for various assembly pressures, based on the compression ratios according to Eqn (7). The initial porosity of 0.8 was applied for the un-deformed GDL, and a constant porosity is applied in the through-plane direction. It is found that the porosity distribution of the GDL has different features in different regions. There exists a transitional region, that is, a nonlinear porosity distribution zone in the GDL region corresponding to the interface between the channel and the shoulders, a linear porosity distribution zone above the shoulders, and a constant porosity distribution zone above the middle part of the channels for the cases when an assembly pressure is applied. A similar nonlinear porosity distribution zone caused by the compression was also found in most of the available GDL models [12,18]. Unfortunately, the impact of such nonlinear porosity distributions in the GDL has not been well investigated in the literature. An assumption of a constant porosity distribution is widely used for the cell performance analyses even though the nonlinear property distribution of the GDL has been identified.

The porosity of the GDL in the constant porosity distribution zone is kept at the initial value even though the assembly pressure increases. This means that the GDL in this area is not deformed as assumed in this study. A magnification of the nonlinear porosity distribution zone, that is, a gray triangular area shown in Figure 5a, is shown in Figure 5b. As shown in Figure 5b, a sharp change

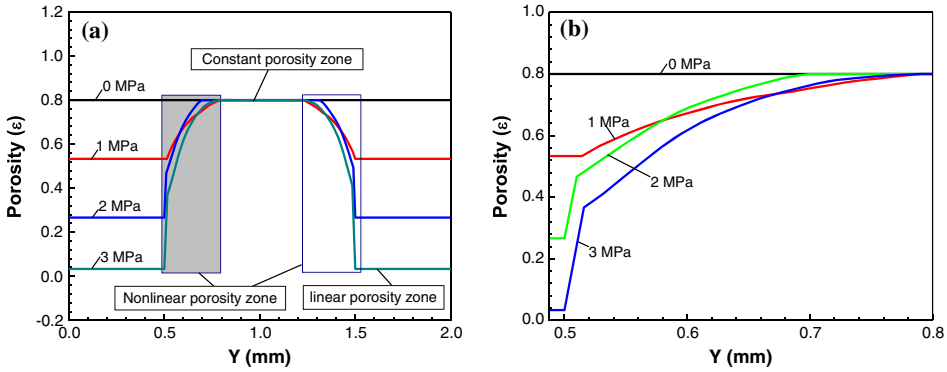


**Figure 5.** Porosity distribution in the GDL (a) in cross-section view and (b) magnification of the non-linear porosity distribution zone in gray area for different assembly pressures. [Colour figure can be viewed at wileyonlinelibrary.com]

of the porosity appears at the corner of the shoulders for the assembly pressures of 2 and 3 MPa. The porosity of the GDL is nonlinearly changed and then reaches the initial value in the area between the corner and the channel.

Figure 6 shows the compression ratios, porosities, and the corresponding fitting curves of the GDL in the nonlinear porosity distribution zone in cross-section view for different assembly pressures. The compression ratio increases with increasing assembly pressure but the porosity changes in a contradictory way in the nonlinear porosity distribution zone. The linear porosity distribution zone, that is, the GDL area above the shoulders, is studied separately. The compression ratios, porosities, and corresponding fitting curves of the GDL in that area with the specified assembly pressures are shown in Figure 7. The compression ratio and the porosity of the GDL area above the shoulders show an almost linear behavior for the specified compression pressures. This can be explained by the constant compression resistance (Young's modulus) applied in the mechanical model for the GDLs.

In the linear porosity distribution zone, approximately 0.09 and 0.16 mm of the GDL thickness reductions occur

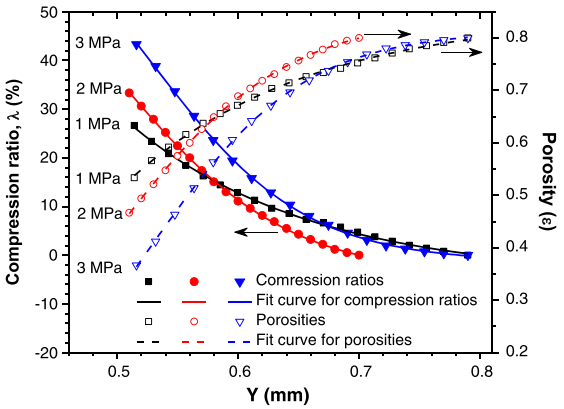


**Figure 6.** Compression ratios, porosities, and the corresponding fit curves of the GDL at the nonlinear porosity distribution zone in cross-section view for different assembly pressures. [Colour figure can be viewed at wileyonlinelibrary.com]

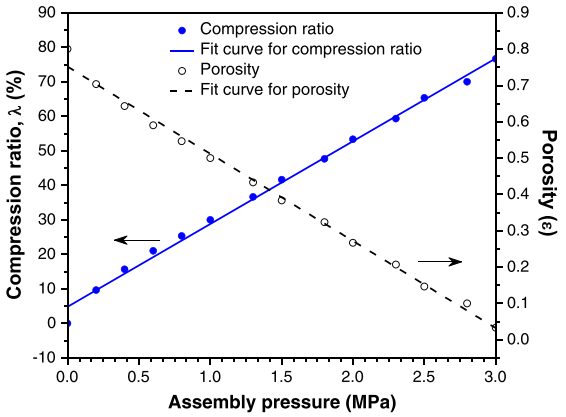


**Figure 7.** Compression ratios, porosities, and corresponding fitting curves in the GDL zone above the shoulders (i.e., linear porosity distribution zone) for different assembly pressures. [Colour figure can be viewed at wileyonlinelibrary.com]

in this single channel PEM fuel cell model for the 1 and 2 MPa assembly pressure (Figure 4), respectively. These correspond to 30% and 54% of the GDL deformed in the through-plane direction (Figure 7), respectively. As the assembly pressure increases to 3 MPa, the total thickness change increases to 0.23 mm, or 77% of the GDL was deformed. However, in terms of the GDL deformation in the nonlinear porosity distribution zone, the most significant deformation occurs in the case with the 3 MPa assembly pressure, that is, 0.13 mm (Figure 4) deformation or 43% of the GDL, appears in the through-plane direction (Figure 6). The different deformations of the GDL in the cross-section view are because of the cell structure in the PEM fuel cells, and thus, the GDL deformation is changed along the cell in the in-plane direction.

## 3.2. Assembly pressure effects on the PEM fuel cell performance

After evaluation of the mechanical behavior of the GDL for the various assembly pressures, the deformed geometry

and the predicted porosity distributions of the GDL were implemented into the CFD module. As illustrated in Figure 8, the cell performance is not sensitive to the assembly pressure at high cell voltages. The current density–power density curves change very slightly and are kept almost similar at high cell voltages. It is expected that a small amount of the reactants is consumed at the reaction sites for the lower operating conditions (i.e., higher cell voltages). A condition of 3 MPa assembly pressure may hardly ensure the gas transfer from the channel to the reaction sites via a deformed GDL. As shown in Figure 8, at the same voltage, the current densities and power densities are declining at higher assembly pressures. These cells operating at a non-zero assembly pressure show a reduced cell performance; that is, a higher assembly pressure causes a worse cell performance. This reflects that the mass transfer resistance is accumulated as the porosity decreases for large assembly pressures. A similar phenomenon has been observed in the literature [12], in which a constant porosity was applied. However, in the published literature, the reduced performance was claimed to be due to the combined effects of a reduction of the porosity, the narrowed gas flow channel cross-section areas, and the reduction of the flow path from the gas channel to the reaction sites.

A narrowed gas flow channel cross-section area decreases the amount of the gases fed into the cell when a constant gas velocity is assumed. In addition, the porosity and the thickness of the GDL decrease for increasing assembly pressure. To analyze the effects of these three factors on the cell performance in detail, the cases for different assembly pressures with various porosities are considered, as shown in Figure 9. The cases were set up at a constant cell operating voltage 0.70 V, and the obtained current densities were compared with the uncompressed case (i.e., the assembly pressure is 0 MPa). The results show that the current density decreases with an increase of the assembly pressure. The cell performance for the combination of the reduced GDL thickness and gas flow channel areas could decrease the current density by

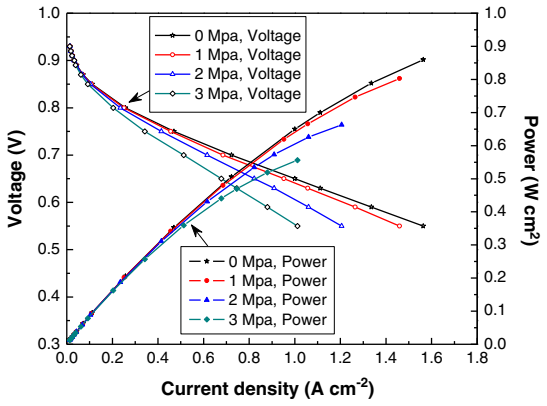


**Figure 8.** Comparison of current densities and power densities for different assembly pressures. [Colour figure can be viewed at wileyonlinelibrary.com]

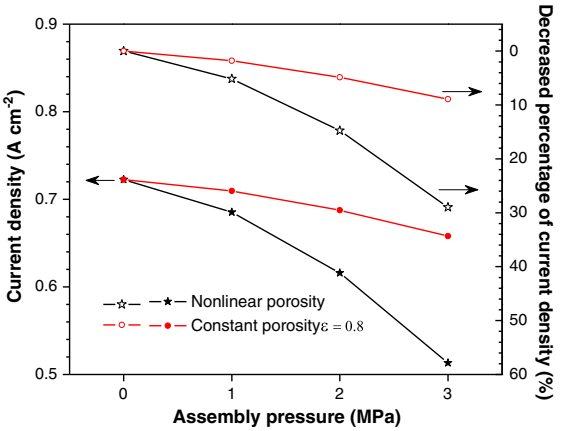


**Figure 9.** Average current densities and percentage decrease versus assembly pressures and porosities compared with the uncompressed case at cell voltage 0.70 V. [Colour figure can be viewed at wileyonlinelibrary.com]

8.9% at the 3 MPa assembly pressure. However, a significant deterioration of the current density by 29.0% appears as the decrease of the GDL porosity is further analyzed. Thus, the current density is decreased approximately 20.0% purely by the reduction of porosity at an assembly pressure of 3 MPa compared with the non-deformed cell.

Another case study for the 2 MPa assembly pressure with the initial constant porosity 0.8 but ignoring the GDL intrusion into the channels was conducted. A decreased current density by 5.0% is observed compared with the uncompressed case. Therefore, a decreased porosity plays the most significant role in reduction of the current density compared with the effects of the reduced gas flow channel areas and GDL thickness. To find out the effect of a reduced GDL thickness on the current density, the left-hand half domain at the cell middle ($x$ = 0.025 m) along the main flow direction is selected for presentation of the distribution of the cathodic oxygen mole fractions in Figure 10 for two cases. It is found that a similar distribution of oxygen mole fraction occurs in the gas channels for the compressed case in Figure 10b as for the uncompressed case in Figure 10a. However, a difference is observed in the GDL area above the shoulders (Figure 10). Especially at the zone far away from the channels, a smaller oxygen mole fraction (10.5% in Figure 10b) occurs in the compressed case with the 2 MPa assembly pressure, compared with the uncompressed case (11.5% in Figure 10a). This indicates that a reduction of the GDL thickness or a decreased diffusion area of the GDL can increase the oxygen transfer resistance from the channels to the reaction sites.

The local current densities at the reaction interface predicted for the cases with 2 MPa assembly pressure and uncompressed condition at the cell operating voltage of 0.70 V are shown in Figure 11, and the corresponding profiles at the cell middle ($x$ = 0.025 m) along the cell

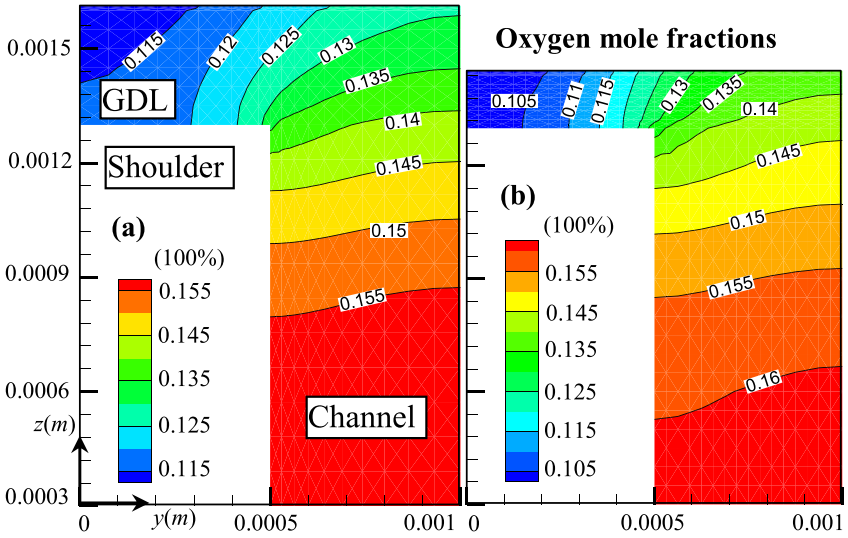


**Figure 10.** Left-hand half domain cathodic oxygen mole fraction at the cell middle ($x$ = 0.025 m) for (a) uncompressed condition (b) for 2 MPa assembly pressure, with constant porosity 0.8 and without the GDL intrusion into the channels. [Colour figure can be viewed at wileyonlinelibrary.com]

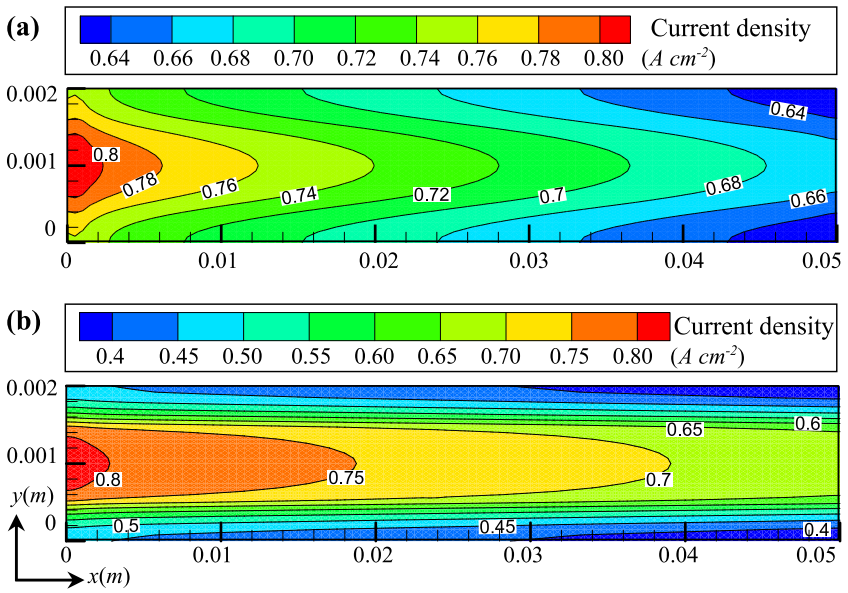


**Figure 11.** Distribution of local current densities at the reaction interface for (a) uncompressed condition and (b) 2 MPa assembly pressure at cell operating voltage of 0.70 V. [Colour figure can be viewed at wileyonlinelibrary.com]

width direction are shown in Figure 12. It is clear that the highest local current density occurs in the reaction region above the channel and at the inlet along the main flow direction. This is a result of the presence of sufficient fresh reactants (high oxygen mass fraction) in this region. A more even distribution of the local current density is observed in the case without the compression compared with the case with 2 MPa assembly pressure (Figure 12). Even though the maximum local current density above the channel (0.74 A $cm^{-2}$) is somewhat higher than that of the case without compression (0.72 A $cm^{-2}$), it is noted that the local current density for the case with 2 MPa assembly pressure is extremely low in the regions above the shoulders (Figures 11b and 12), which results in the reduction of the overall cell performance.

### 3.3. Assembly pressure effects on diffusion coefficient

Ensuring a sufficient amount of the reactants transferred from the gas channels to the reaction sites via the porous GDLs and CLs, and an efficient removal of the products

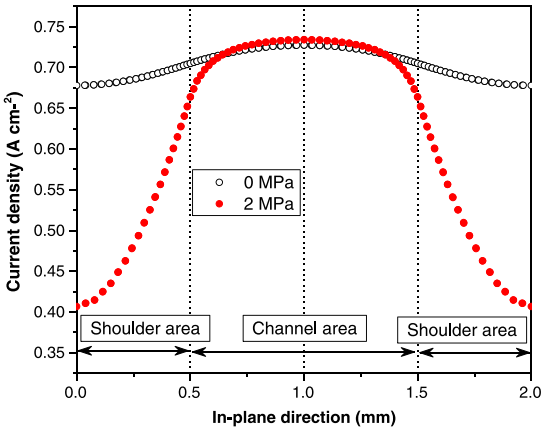


**Figure 12.** Profiles of local current densities at the reaction interface at middle cell ($x$ = 0.025 m) along the in-plane direction for uncompressed condition and 2 MPa assembly pressure at a cell operating voltage of 0.70 V. [Colour figure can be viewed at wileyonlinelibrary.com]

from the reaction sites is a pre-requirement to improve the cell performance. The diffusion coefficient is an important parameter, because it determines the local reactant/product distributions and affects the mass transfer capability. The effect of the porous properties on the diffusion coefficient is evaluated by Eqns (22) and (24), in terms of the porosity, pore size, and tortuosity. The distribution of the oxygen diffusion coefficients in the cell middle ($x$ = 0.025 m along the cell main flow direction) for the case of 2 MPa assembly pressure and another one for uncompressed condition can be found in Figure 13. It is observed that the oxygen diffusion coefficient is similar in the gas channel, however much different in the GDL. A diffusion coefficient gradient for both cases is observed. This corresponds to the shape of the GDL facing to the channels, which may be caused by the viscous resistance, as implemented in Eqns (14) and (15). On the other hand, the distribution of the oxygen diffusion coefficients agrees with that of the porosity variation along the cell in the in-plane direction as illustrated in Figure 13. In the transitional areas between the channel middle and the shoulder corners, a nonlinear and sharply changing distribution of the oxygen diffusion coefficient is observed. The uncompressed case has an almost constant oxygen diffusion coefficient in the GDL. In contrast, an approximately 10 times lower oxygen diffusion coefficient appears above the shoulders for the 2 MPa assembly pressure (Figure 13b), compared with the uncompressed case (Figure 13a). This is so because this linear porosity zone has an extremely low porosity, as shown in Figure 8. This reflects that the porosity distribution plays a significant role on the mass diffusion coefficients in the GDLs of a PEM fuel cell.

### 3.4. Assembly pressure effects on mass transfer

The distribution of the species is significant for the cell performance, which is affected by the gas flow in the channels. The distribution of the air velocity close to the inlet region ($x$ = 0.001 m) for the 2 MPa assembly pressure and the uncompressed condition can be seen in Figure 14. The results show that the gas flow areas in the gas channels decrease significantly for the 2 MPa assembly pressure due to a serious intrusion of the GDL into the gas channels as a result of the assembly pressure. In this study, a constant velocity at the inlet ($x$ = 0 m) was applied for the various cases. This reflects that the air flow fed into the cell decreases when the gas flow channel area is reduced for the 2 MPa assembly pressure. This might be one of the reasons for the reduction in the cell current density as

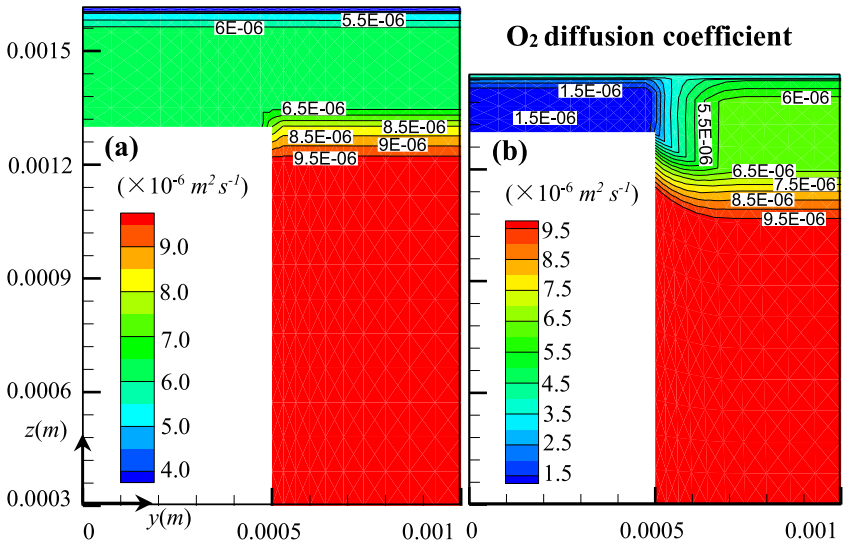


**Figure 13.** Distribution of oxygen diffusion coefficient for the left-hand half domain along the in-plane direction in the cell middle ($x$ = 0.025 m) for (a) uncompressed condition and (b) 2 MPa assembly pressure. [Colour figure can be viewed at wileyonlinelibrary.com]

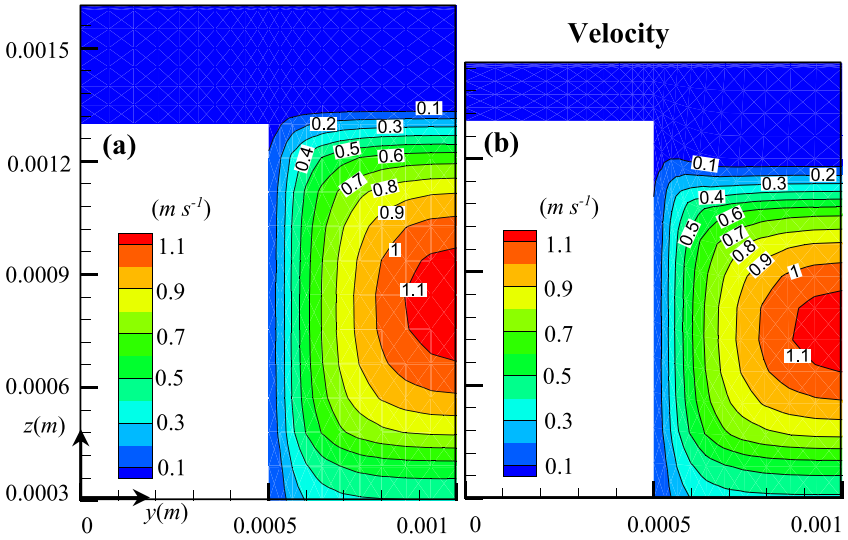


**Figure 14.** Comparison of cross-sectional air velocity distribution for the left-hand half domain at inlet region ($x$ = 0.001 m) for (a) uncompressed condition and (b) 2 *MPa* assembly pressure. [Colour figure can be viewed at wileyonlinelibrary.com]

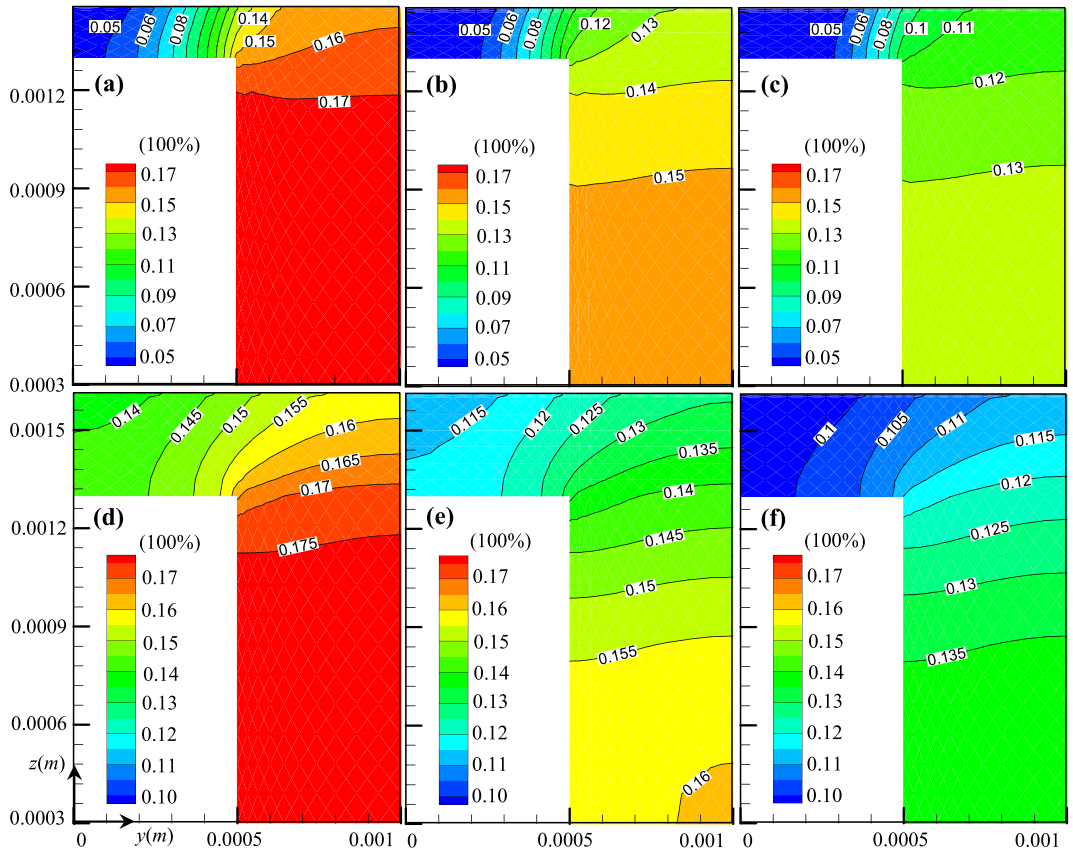


**Figure 15.** Cathodic side oxygen mole fractions for the left-hand half domain along the cell main flow direction at the (a) inlet ($x$ = 0.001 m), (b) middle ($x$ = 0.025 m), and (c) outlet ($x$ = 0.05 m) for 2 MPa assembly pressureand (d) inlet ($x$ = 0.001 m), (e) middle ($x$ = 0.025 m), and (f) outlet ($x$ = 0.05 m) for uncompressed condition. [Colour figure can be viewed at wileyonlinelibrary.com]

discussed previously (Figures 9–13). However, a constant flow fed into the cell inlet was numerically considered by Taymazet et al. [13], which showed that the cell performance is reduced as a higher assembly pressure is applied because it is believed that the mass transfer resistance is a dominating factor. In addition, the oxygen and hydrogen fed into the cell is oversupplied by the stoichiometric ratio with 2 and 1.2, respectively. The reduction of the flow at the cell inlet for the oxygen could not be a main limiting factor for the cell performance reduction. Therefore, the reduced gas flow area caused by the assembly pressure is not the dominating factor for the deterioration of the cell performance as shown in Figure 8.

It is important to study the distributions of the reactants at the cathode reaction sites in PEM fuel cells because these determine the local current densities. The cathodic oxygen mole fractions at various positions (at the inlet region, $x = 0.001$ m; at the middle, $x = 0.025$ m; and at the outlet region, $x = 0.05$ m) along the main flow direction are shown in Figure 15 for the left-hand half of the studied domain for 2 and 0 MPa assembly pressures, respectively. The results show a comparable variation at different positions along the main flow direction. For both pressure cases, the maximum oxygen mole fractions are kept similar at the channel inlet region due to a small consumption of oxygen by the reactions. With more oxygen consumption along the cell, the oxygen mole fraction is reduced in the gas channels. A more uniform distribution of the oxygen mole fraction is observed for the case with the uncompressed condition. However, a minimum mole fraction appears at the GDL area above the shoulders far away from the channels for the case of 2 MPa assembly pressure. In addition, because of the consumption of oxygen due to the electrochemical reactions, oxygen is forced to diffuse to the active sites in the CL layers through the GDLs, while the generated products and the unconsumed reactants diffuse back to the channels. The profile of the oxygen mole fractions agrees with the distribution of the oxygen diffusion coefficient (Figure 13); that is, a maximum oxygen mole fraction occurs where the maximum porosity exists for the case of 2 MPa assembly pressure.

By comparing the two conditions, it is clear that the cell performance for the 2 MPa assembly pressure is worse than that of the case with zero assembly pressure. This can be explained as the transport of oxygen is limited by the lower diffusion coefficient due to the decreased porosity, the reduced diffusion area in the GDL, and the smaller gas flow area in the channel for the 2 MPa assembly pressure.

## 4. CONCLUSIONS

In this paper, we found that the GDL above the channels intrudes into the gas channels as an assembly pressure is applied and accordingly non-homogeneous thickness and porosity along the cell in the in-plane direction appear. Three zones are identified by the mechanical model based on the porosity variations along the cell in the in-plane direction, that is, a linear porosity distribution zone, a constant porosity distribution zone, and a nonlinear porosity distribution zone. The thickness and porosity of the GDL are unchanged in the constant porosity distribution zone but vary linearly or nonlinearly in the other two distribution regions.

The predicted results from the CFD model show that a higher assembly pressure results in a reduction of the thickness and porosity of the GDL, gas flow channel area, oxygen diffusion coefficient in the porous medium, and cell performance. It is found that the reduction of the GDL porosity plays a dominating role compared with the decreased gas channel flow area and GDL thickness. An extremely low oxygen diffusion coefficient, oxygen concentration, and local current density appear in the GDL above the shoulders far away from the channels for the high assembly pressure. It is observed that a sufficiently thick GDL is favorable to ensure the gas transfer from the channel to the reaction sites in the PEM fuel cell.

The results from this investigation may provide guidance for the design and manufacturing of PEM fuel cells, by considering the effects of the assembly pressure on the non-homogeneous distribution of the thickness and porosity of the GDL. To obtain a high cell performance, the assembly pressure should be as low as possible, but gas sealing security must be ensured. However, shortcomings of this study are that the charge transfer and liquid water formation and its transport have not been considered. An optimal assembly pressure may exist because the electron conductivity is expected to be influenced by the assembly pressure. The prediction of the isotropic GDL deformation might be another limitation of this work and a non-linear anisotropic Young's modulus might be applied in future work.

### ACKNOWLEDGEMENTS

The research work was carried out at the Department of Energy Sciences, Lund University, Sweden. The first author gratefully acknowledges the financial support from China Scholarship Council.

## NOMENCLATURE

| | |
|---|---|
| $a_n$ | = coefficient for dynamic viscosity, $-$ |
| $d_{pore}$ | = mean pore diameter of electrode, $m$ |
| $D_i$ | = diffusion coefficient of species $i$, $m^2\ s^{-1}$ |
| $D_n$ | = viscous resistance, $m^2\ s^{-1}$ |
| $E_0$ | = theoretical potential, $V$ |
| $E_{act}$ | = activation energy, $J\ mol^{-1}$ |
| $E_{Nernst}$ | = Nernst potential, $V$ |
| $F$ | = Faraday constant, 96 487 $C\ mol^{-1}$ |
| $F_n$ | = viscous inertia, $m^2\ s^{-1}$ |
| $\Delta G_{rxn}$ | = change in Gibbs free energy, $J\ mol^{-1}$ |
| $\Delta H_{rxn}$ | = enthalpy change, $J\ mol^{-1}$ |

$i$ = local current density, $A\ m^{-2}$
$i_{cell}$ = average current density, $A\ m^{-2}$
$i_0$ = local exchange current density, $A\ m^{-2}$
$J_i$ = mass diffusion flux of species $i$, $kg\ m^{-2}\ s^{-1}$
$M_i$ = molecular-weight of species $i$, $kg\ mol^{-1}$
$n$ = number of electrons transferred, −
$P$ = gas pressure, $Pa$
$R$ = ideal gas constant, $J\ mol^{-1}\ K^{-1}$
$R_e$ = specific electric resistance of fuel cell, $\Omega\ m^2$
$S_i$ = source terms for partial differential equations, $kg\ m^{-3}\ s^{-1}$ or $J\ m^{-3}\ s^{-1}$
$S_{ij}$ = deviatoric stress tensor, −
$\Delta S_{rxn}$ = entropy change, $J\ mol^{-1}\ K^{-1}$
$T$ = temperature, $K$
$U$ = fluid velocity vector, $m\ s^{-1}$
$V$ = cell voltage, $V$
$V_i$ = diffusion volume of species $i$, $m^{-3}$
$X_i$ = mole fraction of species $i$, −
$Y_i$ = mass fraction of species $i$, −

*Greek letters*

$\alpha_e$ = transfer coefficient, −
$\gamma_a$ = pre-constant at anode, $A\ m^{-2}$
$\gamma_c$ = pre-constant at cathode, $A\ m^{-2}$
$\delta_{ij}$ = Kronecker delta, −
$\varepsilon$ = porosity of porous medium, −
$\varepsilon_{com}$ = porosity of compressed GDL, −
$\varepsilon EL\ ij$ = elastic strain tensor, −
$\varepsilon PL\ ij$ = plastic strain tensor, −
$E$ = Young's modulus, $MPa$
$\eta$ = overpotential, $V$
$\eta_{acti,\ a}$ = anode activation overpotential, $V$
$\eta_{acti,\ c}$ = cathode activation overpotential, $V$
$\lambda$ = compression ratio, −
$\mu$ = dynamic viscosity, $kg\ m^{-1}\ s^{-1}$
$\mu_i$ = dynamic viscosity of species $i$, $kg\ m^{-1}\ s^{-1}$
$\rho$ = gas mixture density, $kg\ m^{-3}$
$\sigma_{ij}$ = stress tensor, −
$\tau$ = tortuosity of porous medium, −
$v$ = Poisson's ratio, −

*Subscripts*

*0* = standard or ideal conditions
*a* = anode
*acti* = activation
*A* = gas species *A*
*AB* = binary species *A* and *B*
*B* = gas species *B*
*c* = cathode
*com* = compressed
*C* = gas species *C*
*e* = electron
*i* = gas species *i*
*initial* = initial condition
*Knudsen* = Knudsen diffusion
*m* = for source term in mass transfer equation
*mem* = membrane
*n* = for source term in momentum equation
*Nernst* = Nernst
*p* = constant pressure
*pore* = pores
*rxn* = reaction status
*Stefan-Maxwell* = Stefan-Maxwell diffusion

*Superscripts*

*a* = reaction order for oxygen
*b* = reaction order for water
*EL* = elastic
*m* = reaction order for hydrogen
*PL* = plastic

## REFERENCES


1. Zhou P, Wu C, Ma G. Influence of clamping force on the performance of PEMFCs. *Journal of Power Sources* 2007; **163**(2):874–881. https://doi.org/10.1016/j.jpowsour.2006.09.068
2. Nitta I, Karvonen S, Himanen O, Mikkola M. Modelling the effect of inhomogeneous compression of GDL on local transport phenomena in a PEM fuel cell. *Fuel Cells* 2008; **8**(6):410–421. https://doi.org/10.1002/fuce.200700058
3. Escribano S, Blachot JF, Etheve M, Morin A, Mosdale R. Characterization of PEMFCs gas diffusion layer properties. *Journal of Power Sources* 2006; **156**(1):8–13. https://doi.org/10.1016/j.jpowsour.2005.08.013.
4. Lee WK, Ho CH, Van Zee JW, Murthy M. The effects of compression and gas diffusion layers on the performance of a PEM fuel cell. *Journal of Power Sources* 1999; **84**(1):45–51. https://doi.org/10.1016/S0378-7753(99)00298-0
5. Ge J, Higier A, Liu H. Effect of gas diffusion layer compression on PEM fuel cell performance. *Journal of Power Sources* 2006; **159**(2):922–927. https://doi.org/10.1016/j.jpowsour.2005.11.069
6. Chang W, Hwang J, Weng F, Chan S. Effect of clamping pressure on the performance of a PEM fuel cell. *Journal of Power Sources* 2007; **166**(1):149–154. https://doi.org/10.1016/j.jpowsour.2007.01.015
7. Nitta I, Himanen O, Mikkola M. Thermal conductivity and contact resistance of compressed gas diffusion layer of PEM fuel cell. *Fuel Cells* 2008; **8**(2):111–119. https://doi.org/10.1002/fuce.200700054
8. Espinoza M, Andersson M, Yuan J, Sundén B. Compress effects on porosity, gas-phase tortuosity, and gas permeability in a simulated PEM gas

diffusion layer. *International Journal of Energy Research* 2015; **39**(11):1528–1536. https://doi.org/10.1002/er.3348

9. Chi PH, Chan SH, Weng FB, Su A, Sui PC, Djilali N. On the effects of non-uniform property distribution due to compression in the gas diffusion layer of a PEMFC. *International Journal of Hydrogen Energy* 2010; **35**(7):2936–2948. https://doi.org/10.1016/j.ijhydene.2009.05.066
10. Bograchev D, Gueguen M, Grandidier JC, Martemianov S. Stress and plastic deformation of MEA in fuel cells – stresses generated during cell assembly. *Journal of Power Sources* 2008; **180**(1):393–401. https://doi.org/10.1016/j.jpowsour.2008.02.048
11. Bograchev D, Gueguen M, Grandidier JC, Martemianov S. Stress and plastic deformation of MEA in running fuel cell. *International Journal of Hydrogen Energy* 2008; **33**(20):5703–5717. https://doi.org/10.1016/j.ijhydene.2008.06.066
12. Zhou Y, Lin G, Shih A, Hu S. Multiphysics modeling of assembly pressure effects on proton exchange membrane fuel cell performance. *Journal of Fuel Cell Science and Technology* 2009; **6**(4):041005. https://doi.org/10.1115/1.3081426
13. Taymaz I, Benli M. Numerical study of assembly pressure effect on the performance of proton exchange membrane fuel cell. *Energy* 2010; **35**(5):2134–2140. https://doi.org/10.1016/j.energy.2010.01.032
14. García-Salaberri PA, Vera M, Zaera R. Nonlinear orthotropic model of the inhomogeneous assembly compression of PEM fuel cell gas diffusion layers. *International Journal of Hydrogen Energy* 2011; **36**(18):11856–11870. https://doi.org/10.1016/j.ijhydene.2011.05.152
15. Nitta I, Hottinen T, Himanen O, Mikkola M. Inhomogeneous compression of PEMFC gas diffusion layer: part I. *Experimental. Journal of Power Sources* 2007; **171**(1):26–36. https://doi.org/10.1016/j.jpowsour.2006.11.018
16. Zhou Y, Lin G, Shih A, Hu S. Assembly pressure and membrane swelling in PEM fuel cells. *Journal of Power Sources* 2009; **192**(2):544–551. https://doi.org/10.1016/j.jpowsour.2009.01.085
17. Tanaka S, Bradfield WW, Legrand C, Malan AG. Numerical and experimental study of the effects of the electrical resistance and diffusivity under clamping pressure on the performance of a metallic gas-diffusion layer in polymer electrolyte fuel cells. *Journal of Power Sources* 2016:330273–330284. https://doi.org/10.1016/j.jpowsour.2016.08.121
18. Shi Z, Wang X, Guessous L. Effect of compression on the water management of a proton exchange membrane fuel cell with different gas diffusion layers. *Journal of Fuel Cell Science and Technology* 2010; **7**(2):021012. https://doi.org/10.1115/1.3177451
19. Wang J, Yuan J, Sundén B. Modeling of inhomogeneous compression effects of porous GDL on transport phenomena and performance in PEM fuel cells. *International Journal of Energy Research* In press 2016. https://doi.org/10.1002/er.3687.
20. Kandlikar S, Lu Z, Lin T, Cooke D, Daino M. Uneven gas diffusion layer intrusion in gas channel arrays of proton exchange membrane fuel cell and its effects on flow distribution. *Journal of Power Sources* 2009; **194**(1):328–337. https://doi.org/10.1016/j.jpowsour.2009.05.019
21. Lai Y-H, Rapaport PA, Ji C, Kumar V. Channel intrusion of gas diffusion media and the effect on fuel cell performance. *Journal of Power Sources* 2008; **184**(1):120–128. https://doi.org/10.1016/j.jpowsour.2007.12.065
22. Zhang L, Liu Y, Song H, Wang S, Zhou Y, Hu SJ. Estimation of contact resistance in proton exchange membrane fuel cells. *Journal of Power Sources* 2006; **162**(2):1165–1171. https://doi.org/10.1016/j.jpowsour.2006.07.070
23. Martemianov S, Gueguen M, Grandidier J, Bograchev D. Mechanical effects in PEM fuel cell: application to modeling of assembly procedure. *Journal of Applied Fluid Mechanics* 2009:249–254.
24. Sivertsen B, Djilali N. CFD-based modelling of proton exchange membrane fuel cells. *Journal of Power Sources* 2005; **141**(1):65–78. https://doi.org/10.1016/j.jpowsour.2004.08.054
25. Barrande M, Bouchet R, Denoyel R. Tortuosity of porous particles. *Analytical Chemistry* 2007; **79**(23):9115–9121. https://doi.org/10.1021/ac071377r
26. Todd B, Young J. Thermodynamic and transport properties of gases for use in solid oxide fuel cell modelling. *Journal of Power Sources* 2002; **110**(1):186–200. https://doi.org/10.1016/S0378-7753(02)00277-X
27. Yuan J, Huang Y, Sundén B, Wang WG. Analysis of parameter effects on chemical reaction coupled transport phenomena in SOFC anodes. *Heat and Mass Transfer* 2009; **45**(4):471–484. https://doi.org/10.1007/s00231-008-0449-6
28. Di Stefano G. Modeling thermal energy storage systems with OpenFOAM. *Doctoral Dissertation* 2014:1–94 doi:http://hdl.handle.net/10589/98281
29. Hussain M, Li X, Dincer I. Multi-component mathematical model of solid oxide fuel cell anode. *International Journal of Energy Research* 2005; **29**(12):1083–1101. https://doi.org/10.1002/er.1141

30. Su A, Chiu Y, Weng F. The impact of flow field pattern on concentration and performance in PEMFC. *International Journal of Energy Research* 2005; **29**(5):409–425. https://doi.org/10.1002/er.1059
31. Min CH. Performance of a proton exchange membrane fuel cell with a stepped flow field design. *Journal of Power Sources* 2009; **186**(2):370–376. https://doi.org/10.1016/j.jpowsour.2008.10.048
32. Ferng YM, Su A, Lu SM. Experiment and simulation investigations for effects of flow channel patterns on the PEMFC performance. *International Journal of Energy Research* 2008; **32**(1):12–23. https://doi.org/10.1002/er.1320
33. Berning T, Lu D, Djilali N. Three-dimensional computational analysis of transport phenomena in a PEM fuel cell. *Journal of Power Sources* 2002; **106**(1):284–294. https://doi.org/10.1016/S0378-7753(01)01057-6
34. Yuan J, Sundén B. On mechanisms and models of multi-component gas diffusion in porous structures of fuel cell electrodes. *International Journal of Heat and Mass Transfer* 2014; **69**:358–374. https://doi.org/10.1016/j.ijheatmasstransfer.2013.10.032
35. Akkaya AV. Electrochemical model for performance analysis of a tubular SOFC. *International Journal of Energy Research* 2007; **31**(1):79–98. https://doi.org/10.1002/er.1238
36. Borup RL, Davey JR, Garzon FH, Wood DL, Inbody MA. PEM fuel cell electrocatalyst durability measurements. *Journal of Power Sources* 2006; **163**(1):76–81. https://doi.org/10.1016/j.jpowsour.2006.03.009
37. Obayopo SO, Bello-Ochende T, Meyer JP. Three-dimensional optimisation of a fuel gas channel of a proton exchange membrane fuel cell for maximum current density. *International Journal of Energy Research* 2013; **37**(3):228–241. https://doi.org/10.1002/er.1935
38. Cengel YA, Boles MA. In *Thermodynamics: An Engineering Approach*, Kanoğlu M (ed.). Publicashed: McGraw-Hill Higher Education; New York (USA), 1994.
39. Sinha PK, Wang CY, Beuscher U. Effect of flow field design on the performance of elevated-temperature polymer electrolyte fuel cells. *International Journal of Energy Research* 2007; **31**(4):390–411. https://doi.org/10.1002/er.1257.
40. Chu HS, Yeh C, Chen F. Effects of porosity change of gas diffuser on performance of proton exchange membrane fuel cell. *Journal of Power Sources* 2003; **123**(1):1–9. https://doi.org/10.1016/S0378-7753(02)00605-5.
41. Uchida M, Aoyama Y, Eda N, Ohta A. Investigation of the microstructure in the catalyst layer and effects of both perfluorosulfonate ionomer and PTFE-loaded carbon on the catalyst layer of polymer electrolyte fuel cells. *Journal of the Electrochemical Society* 1995; **142**(12):4143–4149. https://doi.org/10.1149/1.2048477
42. Barbir F. *PEM Fuel Cells: Theory and Practice*, Elsevier (ed.). Publicashed: Academic Press; Cambridge, 2013.
43. Wang L, Husar A, Zhou T, Liu H. A parametric study of PEM fuel cell performances. *International Journal of Energy Research* 2003; **28**(11):1263–1272. https://doi.org/10.1016/S0360-3199(02)00284-7

# Paper IV

**On Electric Resistance Effects of Non-homogeneous GDL Deformation in a PEM Fuel Cell**

Jiatang Wang[1], Jinliang Yuan[2], Bengt Sundén[1,*,†]

[1]Department of Energy Sciences, Lund University, P.O. Box 118, Lund SE-221 00, Sweden

[2]Faculty of Maritime and Transportation, Ningbo University, Fenghua Road 818, Ningbo 315211, China

**Abstract**

The electric resistance is very important for the performance of a proton exchange membrane (PEM) fuel cell. However, the performance analysis is more complex as the cell operates under assembly conditions. At such conditions, the mass transfer is deteriorated but the electric conductivity is favored. In this paper, the electric resistance of a cell is evaluated by application of a recently developed method in the through-plane direction of the electrodes, together with consideration of the contact resistance between the gas diffusion layer (GDL) and bi-polar plates (BPP) for various assembly pressures. The predicted electric resistance and deformed GDL were implemented in an existing CFD code for evaluation of the PEM fuel cell performance. It is found that the electric current is distributed in a narrow area in the GDL under the shoulders and then redistributed into the BPP above the channels for all cases. The channel/rib structure promotes a non-homogeneous electric conductivity along the cell in the in-plane direction and a concentrated area of the current flow around the corner of the BPP close to the channels as the cell is subject to an assembly pressure. Additional contact areas are created between the GDL and BPP at the vertical interface when the cell operates at an assembly pressure above 2 *MPa*. Therefore, both the corner of a BPP close to the channel and the GDL region become the dominating zones, where the electric current under the middle of the channel must cross over a longer distance due to the intrusion of the GDL into the BPP. In addition, the optimized cell performance is obtained as the cell is operating below 1 *MPa* assembly pressure. The findings are useful for proper design of PEM fuel cells.

**Keywords:** PEM fuel cells; assembly pressure; electric resistance; deformed GDL; model.

**Corresponding author**

*Bengt Sundén, Department of Energy Sciences, Lund University, P.O. Box 118, Lund SE-221 00, Sweden

†E-mail: bengt.sunden@energy.lth.se

## 1. Introduction

A proton exchange membrane (PEM) fuel cell converts chemical energy into electricity. There has been accelerated interest in the development and commercialization of PEM fuel cells in recent years. Their high efficiency of energy conversion, high power density and nearly zero-pollutant emissions compared to fossil-fueled engines have made them ideal candidates for power generation for stationary and automotive applications [1]. However, at present cost, durability and stability are two significant limiting factors for widespread application of PEM fuel cells [2]. To utilize the PEM fuel cell system in an efficient way, a detailed analysis of how the involved transport phenomena are affected by various assembly and operating conditions may promote the development of effective performance.

In determining the performance, the cell potential at a certain current density is critical, as it decreases from the equilibrium value because of the irreversible potential losses (the so-called overpotentials) caused by the activation, concentration and ohmic resistances. Numerical results have demonstrated that the overpotential values decrease in the order of $\eta_{act,c} > \eta_{ohm}^{pro} > \eta_{ohm}^{el} > \eta_{act,a} > \eta_{conc,c} > \eta_{conc,a}$ (where act, ohm and conc, el, pro, c and a denote activation loss, ohmic loss, concentration loss, electrons, protons, cathodic and anodic, respectively) in a PEM fuel cell [3]. Many studies have explored the reduction of concentration and activation losses by optimizing the design [4], manufacturing [5] and materials synthesis [2]. However, it is revealed that the fuel cell operation strategies become more complex and should be adjusted when considering the assembly pressure because the ohmic loss is sensitive to the electric/ionic conductivity in the functional layers [6].

Previous studies have concentrated on investigation of ohmic resistances, including the resistance for electron transfer through electrodes (in in-plane and through-plane directions) [7, 8] and the resistance at the interfaces between components [9-11], and the one for protons in the membrane [12], as shown in Figure 1. A comparison of the electric resistance under the shoulders and channels has shown that the total electric resistance under the channels is much higher than that under the shoulders due to the channel/rib structures in a PEM fuel cell [7, 8]. The contact resistance for electrons occurring at the interface between the bi-polar plates (BPP) and gas diffusion layer (GDL) is regarded as significant because the structure and fibrous materials in the GDL [9-11]. The contact resistance is generally determined by the material properties, surface treatment [11], assembly pressure [13] and operating conditions [9]. However, an assembly pressure will reduce the contact resistance and accelerate the electron flow through the flexible layers (within the GDL and CL) but the access/removal of gases to/from the

reaction sites and proton transfer in the membrane will deteriorate, which may lead to a decreased cell performance. It is known that the GDL provides a very high tensile and compressive strength, which results in intrusion into the gas channels at assembly conditions [14]. A consequence of this is that the physical properties and performance of the GDL are changed due to the thinner GDL under the shoulders and the decreased gas flow channel areas [15]. Thus, the ohmic resistance during assembly conditions is an important property in choosing the assembly pressure and achieving acceptable cell performance.

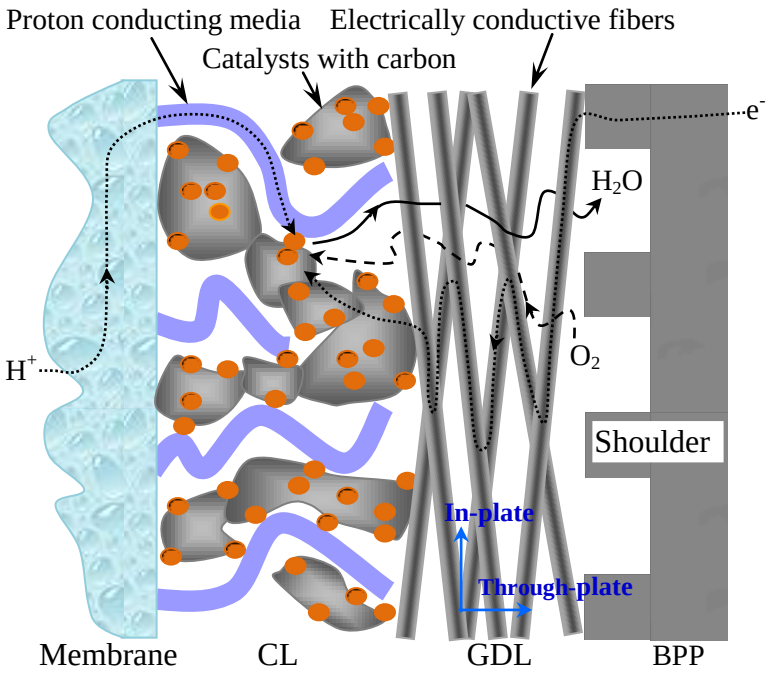


Figure 1. Transport processes in PEM cathode.

Research has been conducted earlier to investigate the influence of the assembly pressure on the electric resistance in PEM fuel cells. The electric conductivities of the GDL in the in-plane and through-plane directions have been tested under various assembly pressures. It was found that a high compression increases the GDL conductivity and decreases the contact resistances [16]. Escribano et al. [17] studied the effects of the GDL deformation on the through-plane electric resistance. In addition, a numerical and experimental study was conducted by Tanaka et al. [13] and a significant difference of the electric resistance in the through-plane direction and at the interfaces was observed when the cell was operated with various assembly pressures. Nitta et al. [18] experimentally analyzed the contact resistance of a porous GDL under compression and their results showed that the assembly pressure magnitude has significant effects on the cell performance. Chang et al. [19] concluded that the contact

resistance between the GDL and the BPP is a dominating factor in causing the Ohmic potential loss, but they did not consider the through-plane electric resistance of the carbon paper itself across the fuel cells. A relationship of the assembly pressure and the contact resistance between the GDL and BPP was presented in the literature [9]. An optimal assembly pressure was obtained by employing this relationship for the contact resistance [20]. However, the electric resistance through the deformed GDL was not explored in that study. A relationship between electric resistance and GDL and BPP, respectively, was experimentally formulated by Hamour et al. [21] when the cell was operated at assembly conditions. Some recent studies have shown a potential optimal assembly pressure for which the cell performance is maximized [22-24]. Taymaz et al. [15] suggested that 0.5 *MPa* and 1 *MPa* pressure values are optimum assembly pressures when a prescribed electric property of the fuel cell components is applied.

A balance between the electric contact resistance, through-plane electric resistance and mass transfer necessitates an optimal assembly pressure for a single cell or a fuel cell stack, particularly when considering a deformed GDL. The present study is a continuation of our previous works on the GDL deformation and its impacts on the transport processes in PEM fuel cells [25, 26]. The evaluation of the electric resistance is conducted by considering the electric contact resistance between the GDL and the BPP, and by the through-plane electric resistance assisted by a new electron transfer model implemented in an open source library of OpenFOAM. The obtained overall electric resistance of a cell is further provided as an input parameter for the PEM fuel cell performance predictions in OpenFOAM. The validation of the electric resistance model is performed by comparison of the numerical predictions with experimental data available in the literature. The effects of various assembly pressures on the electric resistances both in the through-plane direction and at the interface, as well as the transport phenomena and the cell performance, are analyzed. Finally, an optimized assembly pressure is determined with the objective to achieve the best cell performance.

## 2. Numerical Models

Both the electric resistance model and the PEM fuel cell performance model are developed for the cell configuration adopted from the mechanical model under various assembly pressures (0 *MPa*, 1 *MPa*, 2 *MPa* and 3 *MPa*), as presented in our previous work [26]. It should be noted that both configurations include the deformed shape and the porous features of GDLs, while the initial dimensions of the components before the deformation were extracted from a real PEM fuel cell presented in reference [27], and outlined in Table 1.

Table 1. Geometric and physical parameters in electric resistance model.

| Parameters | Value | Reference |
|---|---|---|
| Gas channel length | 0.05 $m$ | [27] |
| Gas channel width | $1.0\times10^{-3}m$ | [27] |
| Gas channel height | $1.0\times10^{-3}m$ | [27] |
| Land area width | $0.5\times10^{-3}m$ | [27] |
| Thickness of BPP | $0.3\times10^{-3}m$ | [27] |
| Thickness of GDL (initial) | $0.3\times10^{-3}m$ | [27] |
| Thickness of CL | $1.29\times10^{-5}m$ | [27] |
| Thickness of electrolyte | $1.08\times10^{-4}m$ | [27] |

### 2.1 Electric resistance model

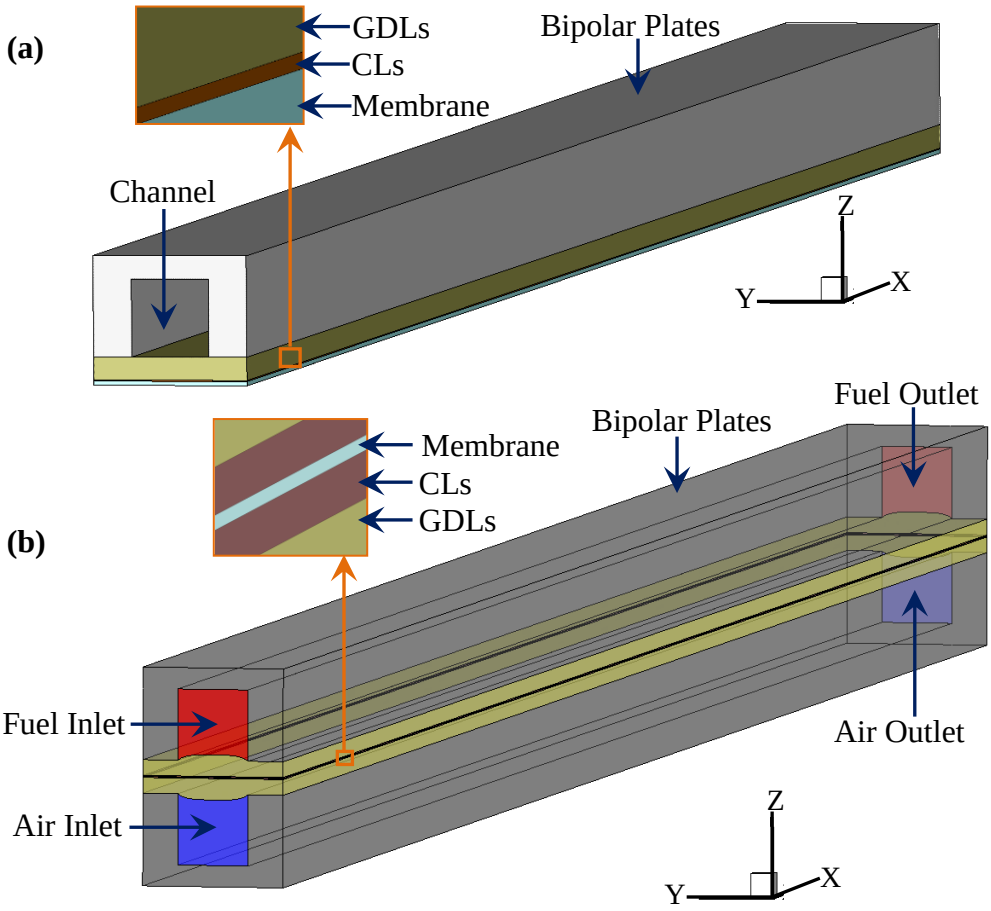


Figure 2. Schematic illustrations of a 3D computational domain for (a) electric resistance model under zero assembly pressure and (b) single channel unit-cell model (here the case under a 1$MPa$ assembly pressure is illustrated as an example).

The components in both the cathode and the anode of the cell are assumed to be symmetric around the membrane. Thus a half-cell, i.e., anodic side is selected as the representative domain for the electric resistance modeling, as shown in Figure 2a. This domain includes anodic BPP, GDL, CL and a half-sized membrane but without the gas channel.

Electric conduction in any material is the movement of electrically charged particles through a transmission medium. This movement forms an electric current in response to an electric field. The governing equation for the electron transfer through GDL, CL and BPP and the protons through the membrane can be evaluated by a Laplacian equation [28],

$$\nabla \cdot (\sigma \nabla \varphi) = 0 \tag{1}$$

where φ is electric potential. The electric/protonic conductivity σ for electrons or protons is the reciprocal of its electric/protonic resistivity,

$$\sigma = \frac{1}{\rho_e} \tag{2}$$

The electric field is the negative gradient of the electric potential,

$$E_e = -\nabla \varphi \tag{3}$$

The local current density *i* appearing in the cell components is related to the conductivity σ based on Ohm's law [29], defined as,

$$i = -\sigma \nabla \varphi \tag{4}$$

The electric resistance of the domain is predicted by a function of the average current density based on Ohm's law [29],

$$R_\Omega = \frac{\left| \varphi_{\max} - \varphi_{\min} \right|}{\bar{i}} \tag{5}$$

where $\bar{i}$ is the average current density, $\varphi_{max}$ and $\varphi_{min}$ are the maximum and minimum electric potential occurring in the domain, respectively. In order to obtain the electric conductivity of the deformed GDL, it is assumed that the porous GDLs consist of pores and a solid bulk, while only the pores contributes to a change of the GDL thickness in the through-plane direction (*z*-axis) under the compression by an assembly pressure. The electric conductivity $\sigma_{com}$ in the bulk of a GDL is related to the obtained thickness by an expression given by [11],

$$\sigma_{com} = \frac{\sigma_{initial} \cdot h_{initial}}{h_{com}} \tag{6}$$

where the compressed thickness $h_{com}$ of the bulk is expressed as,

$$h_{com} = (1-\lambda) h_{initial} \tag{7}$$

where λ is the compression ratio, as a reflection of the local deformation. Thus the electric conductivity of the compressed GDL can be evaluated by the compression ratio,

$$\sigma_{com} = \frac{\sigma_{initial}}{1-\lambda}, \ (\lambda \neq 1) \tag{8}$$

Protonic conductivity in a membrane is depending on the local temperature and water content. The correlation between these parameters has been taken into account in this model,

$$\sigma_{mem} = (0.005139\omega - 0.00326)\exp\left[1268\left(\frac{1}{303} - \frac{1}{T}\right)\right] \tag{9}$$

where $\omega$ is the water content and $T$ is the local temperature. It has been suggested that there might exit several possible ways of the ionic transfer exist in Nafion like materials [6], i.e., hydronium ions move via a vehicle mechanism at low water content ($\omega$*=2~4*), easier movement of hydronium ions at a partially hydrated membrane ($\omega$*=5~14*). Finally, both water and ions move freely in a fully hydrated membrane ($\omega$*>14*). The water content $\omega$ =10 and $T$=353 *K* were selected in this study to evaluate the protonic conductivity of a membrane to maintain a relative easy movement of protons. The other physical parameters implemented in the electric resistance model are presented in Table 2.

Table 2. Physical parameters for electric resistance model.

| Parameters | Value | Reference |
|---|---|---|
| GDL electric conductivity | 1250 $S\ m^{-1}$ | [15] |
| CL electric conductivity | 100 $S\ m^{-1}$ | [30] |
| BPP electric conductivity | $2.22\times10^{4}\ S\ m^{-1}$ | [15] |
| Water content in membrane | 10 $H_2O/SO_3H$ | [6] |

**2.2 Electric contact resistance model**

The electric contact resistance between the GDL and BPP is governed by the surface treatment and the material properties of the contacting components [9]. The assembly pressure, accordingly, leads to a decrease of the electric

contact resistance in a PEM fuel cell. The variation of the physical parameters of the GDL has been accounted for in evaluation of the electric resistance at the condition of an assembly pressure. The electric contact resistance $R_{contact}$, in the unit of $m\Omega\ cm^2$, between the GDL and BPP for electrons has been formulated in [31] as,

$$R_{contact} = 2.2163 + \frac{3.5306}{p_{contact}} \tag{10}$$

where $p_{contact}$ is the contact pressure. In a real PEM fuel cell stack or a single cell, the contact pressure is evaluated by the assembly pressure and the cell contact area [15],

$$p_{Assembly} \cdot A_{Assembly} = p_{contact} \cdot A_{contact} \tag{11}$$

where $p_{Assembly}$, $A_{Assembly}$ denote the assembly pressure and assembly area, respectively. The contact resistance can then be calculated as,

$$R_{GDL/BPP} = 2.2163 + \frac{3.5306 A_{contact}}{p_{Assembly} \cdot A_{Assembly}} \tag{12}$$

It should be noted that, in the present electric contact resistance model, the intrusion of the GDL into a gas channel is considered while the effect of the change of the contact area $A_{contact}$ between the GDL and the BPP is neglected.

**2.3 PEM fuel cell model**

A single channel unit-cell was employed to study the effects on the cell performance for various assembly pressure conditions (i.e., 0 *MPa*, 1 *MPa*, 2 *MPa* and 3 *MPa*), as shown in Figure 2b (here the case under 1 *MPa* assembly pressure condition is illustrated as an example). The domain is assembled symmetrically, consisting of BPPs, gas channels, a membrane, GDLs and CLs. The predicted value of the overall electric resistance including the through-plane resistance (by the electric resistance model) and contact resistance (by the electric contact resistance model) was provided and further implemented into this model. Correspondingly, both the bulk resistance of the components and the interfacial contact resistance between the GDL and BPP were doubled for the entire single channel unit-cell model.

For the assumptions applied in our previous research work [26], the partial differential equations for conservation of mass [14], momentum [25] and mass transport [32] are solved in the PEM fuel cell model. The equations are expressed as, respectively,

$$\nabla \cdot (\rho U) = S_m \tag{13}$$

$$\nabla \cdot (\rho UU) = -\nabla P + \nabla \cdot \mu \nabla U + S_n \tag{14}$$

$$\nabla \cdot (\rho U Y_i) + \nabla \cdot J_i = 0 \tag{15}$$

where $U$ is the fluid velocity vector, ρ is the gas mixture density, $P$ is the gas pressure, $\mu$ is the dynamic viscosity of the fluid, $Y_i$ is the mass fraction of species $i$ and $J_i$ is the mass diffusion flux. The source term, $S_m$ is related to the electrochemical reactions appearing at the reaction sites while the source term $S_n$ stands for pressure losses in the porous GDL and CL [33],

$$S_n = -(\mu D_n + 0.5\rho |U| F_n) U \tag{16}$$

where the non-linear term is not considered in the present study, i.e., $F_n$ is set to zero. However, the pore diameter $d_{pore}$ and porosity $\varepsilon$ are involved in the first right-hand term of Eq. (16) as [34],

$$D_n = \frac{150}{d_{pore}^2} \frac{(1-\varepsilon)^2}{\varepsilon^3} \tag{17}$$

The source terms $S_m$ for the mass conservation equation can be expressed by the following equations [35] for the cathode and anode, respectively,

$$S_{m,c} = -\frac{i}{4F} M_{O_2} + \frac{i}{2F} M_{H_2O} \tag{18}$$

$$S_{m,a} = -\frac{i}{2F} M_{H_2} \tag{19}$$

where $i$ is the local current density, $M$ the molar weight of the involved gas species and $F$ the Faraday's constant (96485 $C\ mol^{-1}$). The plus sign (+) is applied for the product generation and the negative sign (-) for the reactant consumption due to the electrochemical reactions.

The mass diffusion flux $J_i$ is following by Fick's law [3], i.e.,

$$J_i = -\rho D_{i,gas} \nabla Y_i \tag{20}$$

where $D_{i,gas}$ is the mass diffusion coefficient of species $i$ in the involved gas mixture, $Y_i$ is the mass fraction of species $i$. It should be noted that the mass fractions of the inert species (nitrogen in the cathode and water in the anode) are not solved by Eq. (15), but are determined from a summation of the mass fractions and subtracting the other active species, for the anode and the cathode, respectively [36]. Due to the multi-component diffusion

occurring in the cathode side, i.e., oxygen, water and nitrogen involved, the Stefan-Maxwell model is used to evaluate the individual diffusion coefficients in the gas mixture. However, in the anode of the PEM fuel cells, only two species are present, and the diffusion coefficients of hydrogen and water are directly evaluated by the binary diffusion coefficient, as provided in [25].

The electrochemical reactions are assumed to occur at the interfaces between the membrane and the CLs. The fuel cell current density $i_{cell}$ is then calculated based on Ohm's Law [37],

$$i_{cell} = \frac{E_{Nernst} - V - \eta}{R_e} \tag{21}$$

where $V$ and $\eta$ are the cell operating voltage and the activation overpotential, respectively, $R_e$ is the total electric resistance of the fuel cell. The Nernst potential $E_{Nernst}$ in Eq. (21) is described as [37],

$$E_{Nernst} = E_0 + \frac{RT}{nF} \ln \frac{X_{O_2}^{0.5} \cdot X_{H_2}}{X_{H_2O}} \tag{22}$$

where $R$ is the universal gas constant (8.314 $J\ mol^{-1}\ K^{-1}$), $n$ is the number of electrons transported and $E_0$ is the theoretical potential [38] at the standard atmosphere condition (298 $K$, 1 $bar$) which is approximately 1.23 $V$,

$$E_0 = -\frac{\Delta G_{rxn}}{nF} = -\frac{\left(\Delta H_{rxn} - T\Delta S_{rxn}\right)}{nF} \tag{23}$$

where $\Delta G_{rxn}$ is the Gibbs free energy change, $\Delta H_{rxn}$ is the enthalpy change and $\Delta S_{rxn}$ the entropy change of the reactions. The superscript in Eq. (22) refers to the stoichiometric coefficient of the hydrogen fuel cell reactions in PEM fuel cells. The cell activation overpotential is assumed to be composed of the anodic and cathodic contributions,

$$\eta = \eta_{acti,a} + \eta_{acti,c} \tag{24}$$

where the activation overpotential $\eta_{acti,a}$ is for the anode and $\eta_{acti,c}$ for the cathode, respectively. Values of $\eta$ at both electrodes are obtained using a root finder based on the Ridder's method after obtaining numerical solutions of the Butler-Volmer equation [39],

$$i = i_0\left[\exp\left(A\eta_e\right) - \exp\left(B\eta_e\right)\right] \tag{25}$$

where

$$A = \frac{2\alpha_e F}{RT} \tag{26}$$

$$B = -\frac{2(1-\alpha_e)F}{RT} \tag{27}$$

where $\alpha_e$ is the transfer coefficient and $\eta_e$ is the activation overpotential for each electrode. The local exchange current densities are given by [37],

$$i_{0,a} = \gamma_a \left( \frac{P_{H_2}}{P_0} \right)^m \exp\left( -\frac{E_{act,a}}{RT} \right) \tag{28}$$

$$i_{0,c} = \gamma_c \left( \frac{P_{O_2}}{P_0} \right)^a \left( \frac{P_{H_2O}}{P_0} \right)^b \exp\left( -\frac{E_{act,c}}{RT} \right) \tag{29}$$

where $a$, $b$ and $m$ are the reaction orders, $\gamma_a$ and $\gamma_c$ are the pre-constant, $E_{\text{act},a}$ and $E_{\text{act},c}$, are the activation energies. More detailed discussion about the PEM fuel cell modeling can be found in [26].

**2.4 Boundary conditions and initial conditions**

Before solving the partial differential equations, a set of boundary conditions (BCs) for all governing equations is required. A constant current density $i_{cell}$ = 0.7 $A\ cm^{-2}$ was applied at the membrane as the current source, which occurs at the bottom surface (membrane or electrolyte) for the Laplacian equation of the electric resistance model. The BC at the membrane is set as a gradient potential which is a function of the local conductivity [29],

$$\nabla \varphi = -\frac{i_{cell}}{\sigma} \tag{30}$$

For the BPP domain, the only variable of the interest is the electric potential. A reference potential value of zero is arbitrarily set at the top surface of the anodic BPP [29]. Finally, the BCs for the other boundaries are set as symmetry conditions.

Table 3. Inlet mass fraction (fully humidified gases) [27].

| Species | Mass fraction (%) |
|---|---|
| $O_2$, cathode | 20.885 |
| $H_2O$, cathode | 10.344 |
| $N_2$, cathode | 68.771 |
| $H_2$, anode | 37.747 |
| $H_2O$, anode | 62.253 |

The PEM fuel cell performance is modeled at a temperature of 353 *K* and a pressure of 3 *bars* is prescribed at the outlets of the gas flow channels. It is assumed that the cathode and the anode are fed with fully humidified air and hydrogen, respectively. The parameters for the humidified gases with the specific mass fractions are taken from the literature [27] as listed in Table 3. The inlet gas velocity is based on the desired average current density with the stoichiometric ratio 2 for the oxygen and 1.2 for the hydrogen, respectively [39]. The BCs for other parameters applied in the computational domain are assumed as zero gradients in the vertical directions of the outside surfaces. In this model, various electric resistances predicted in the electric resistance model combined with the contact resistance are employed for the different assembly pressures. The input properties of the related materials, kinetics and electrochemical reactions are identical to those in [26].

### 2.5 Validation of the electric resistance model

Validation is important to ensure the accuracy of a numerical model. The further developed OpenFOAM code with the electric resistance model to evaluate the electric resistance was validated by two different geometrical cuboids. The dimension of one cuboid is 1 *cm*×1 *cm*×2 *cm* (Cuboid A) while the other is 2 *cm*×2 *cm*×1 *cm* (Cuboid B). Constant potential values of 0 *V* and 1 *V* were set as BCs at the top of the BPP and the bottom of the membrane, respectively. The remaining BCs are set as mentioned in the above section. The theoretical prediction is based on both Pouillet's law and Ohm's law,

$$R_{\Omega} = \frac{l}{\bar{\sigma} A} \tag{31}$$

$$i = \frac{\Delta \varphi}{R_{\Omega}} \tag{32}$$

where $l$ and $A$ denote the length and cross-sectional area of the conductor, respectively, $\bar{\sigma}$ is the average electric conductivity and $R_{\Omega}$ is in the unit of Ω here. Δφ is the maximum potential difference between the membrane and BPP (Here 1 *V* was applied for the theoretical prediction). The validation is conducted by comparing the predictions obtained by the above two equations and the numerical results.

## 3. Results and Discussions

### 3.1 Model validation results

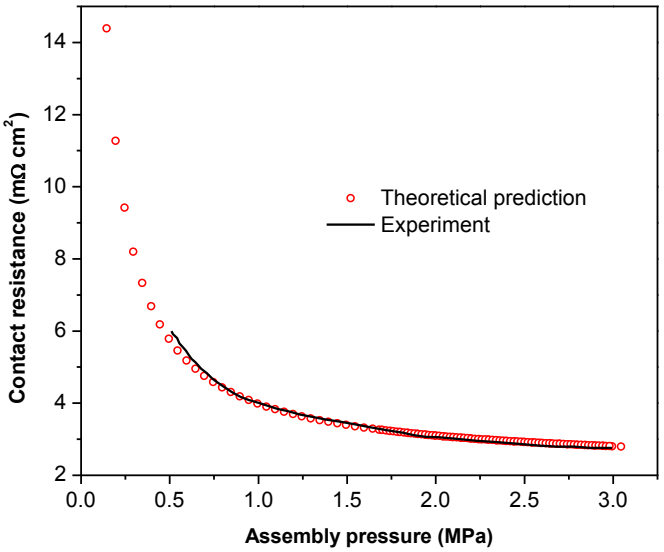


Figure 3. Comparison of theoretical and experimental contact resistances [11] between GDL and BPP.

A comparison of the electric contact resistance by the predictions and the experimental results is presented in Figure 3. It is found that the contact resistance measured by Mishra et al. [11] can be fitted by Eq. (12) with a pretty good accuracy. The assembly pressure decreases the contact resistance, which supports the fact that there is a better contact between the GDL and BPP as the assembly pressure increases. The contact resistance decreases sharply with the assembly pressure at pressures below 1 *MPa*. However, above 1.0 *MPa* there is still a slight decrease in resistance with increasing pressure. But there is no significant change of the contact resistance at higher assembly pressures. This is so because the maximum contact is reached at a certain pressure between the GDL and BPP.

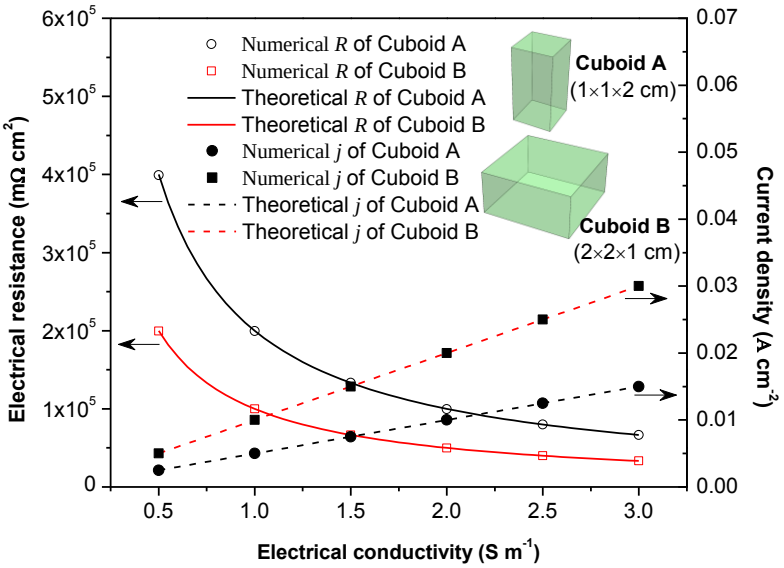


Figure 4. Comparison of electric resistance and current density v.s. electric conductivity.

The theoretically and numerically predicted electric resistance and current density as function of the electric conductivity are shown in Figure 4. It is clear that relatively accurate electric conductivity and current density are obtained by the electric resistance model for the various tested bulk electric conductivities. It is found that the electric resistance inversely decreases with increasing electric conductivity, but the current density keeps a linear increase with increasing electric conductivity.

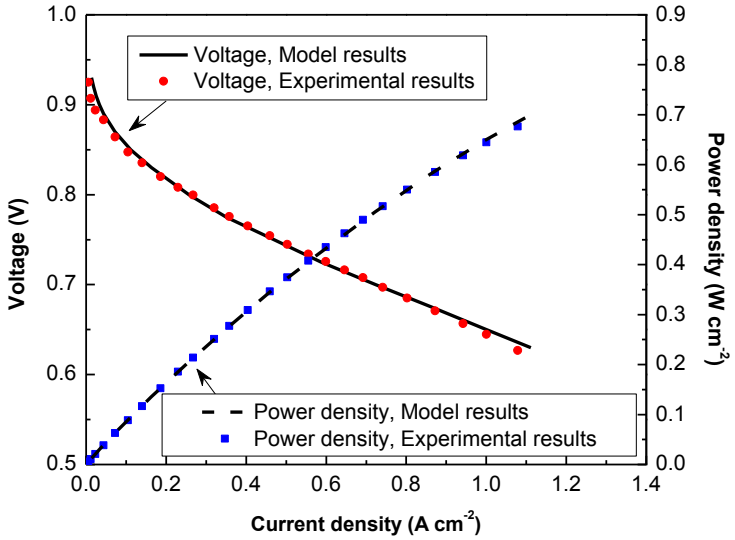


Figure 5. Comparison of cell electrochemical performance [40].

A contact resistance of 14.3 $m\Omega\ cm^2$ was applied for the case of zero assembly pressure (The constant resistance value was taken from reference [11] and [20]). After obtaining the through-plane electric resistance of a cell and the contact resistance between GDL and BPP, the overall cell resistance including the two main factors was applied to the PEM fuel cell model. To reveal the accuracy of the CFD simulations of the PEM fuel cell model, the simulations shown in Figure 5 were compared with experimental data from reference [40] at the same operating conditions (in which the assembly pressure is zero). Good agreement between the experimental and predicted results was obtained, in terms of the current density and the power densities for the cell operating voltages higher than 0.63 V. Both the calculated and measured voltages drop sharply when the current density is small, mainly caused by the activation losses. The voltage then decrease linearly until 0.63 V, where the Ohmic loss becomes dominating. This validated model is then used for the further parametric studies.

### 3.2 Assembly pressure effects on GDL electric conductivity

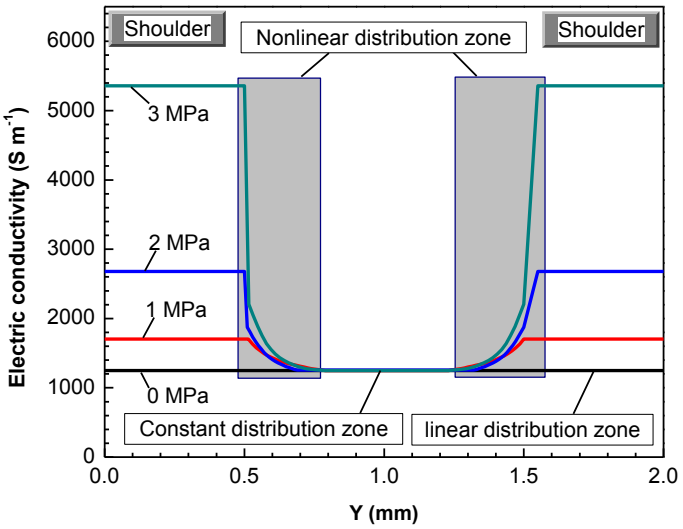


Figure 6. Cross-sectional distribution of electric conductivity in the GDL for different assembly pressures.

The electric conductivity is one of the most important parameters characterizing the transport of electrons in a PEM fuel cell. During fuel cell assembly processing, GDLs are usually clamped by the BPPs. The result of the assembly pressure is deformation of the GDL and then a reduction of the electric conductivity in the through-plane direction, as shown in Figure 6. It is found that the electric conductivity distribution of the GDL has different features in different regions along the cell width direction. There exist non-homogeneous features, i.e., a nonlinear distribution zone in the GDL region corresponding to the corner between the channel and the shoulders (as shown in both the grey areas in Figure 6), a linear distribution zone under the shoulders and a constant distribution zone under the middle part of the channels for the cases when an assembly pressure is applied. As a result of a higher assembly pressure, the electric conductivity of the GDL decreases sharply in the linear distribution zone which is caused by a dramatic compression by the assembly pressure, as shown in our previous work [26].

To identify the effects of the geometry change of the components on the electric conductivity, a comparison of the volume-weighted average electric conductivity in the fuel zone (including porous GDL and CL) and the entire half-cell under different assembly pressures is shown in Figure 7. It is revealed that a higher assembly pressure results in a high electric conductivity for both studied domains. This agrees well with the evidence shown in Figure 6 that the assembly pressure improves the electric conductivity in the GDL. This means that in the interest of obtaining high electric conductivity of a cell, a higher assembly pressure is favorable.

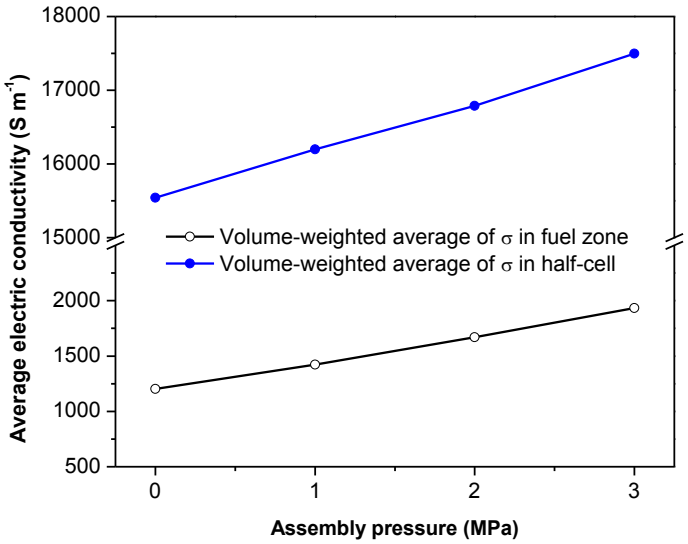


Figure 7. Volume-weighted average of electric conductivity in fuel zone (including GDL and CL) and entire half-cell for different assembly pressures.

### 3.3 Assembly pressure effects on cell electric resistance

It is meaningful to examine the cell resistance due to the bulk resistance (in the through-plane direction) and the contact resistance. The bulk resistances of a cell as well as the contact resistances between the GDL and BPP are presented in Figure 8 as function of the assembly pressure. Generally, the contact resistance between GDL and BPP is quite small compared with the bulk resistance predicted by this model. However, a contradictory result was obtained by Vikram et al. [41], which shows that the contact resistance plays a dominating role in the cell electric resistance. A possible reason might be that a larger ratio of shoulder/channel was applied by Vikram et al. As shown in Figure 8, the bulk resistance of the cell decreases with increasing assembly pressure. A similar tendency is observed for both the contact resistance and the sum of the two resistances (i.e., overall resistance of a cell). The bulk resistance through the cell contributes as much as 76 percent of the total cell resistance at the assembly pressure of 0 *MPa* but 92.7 percent at the higher assembly pressure of 3 *MPa*. Figure 8 shows the significance of the bulk resistance of the cell for varying assembly pressure.

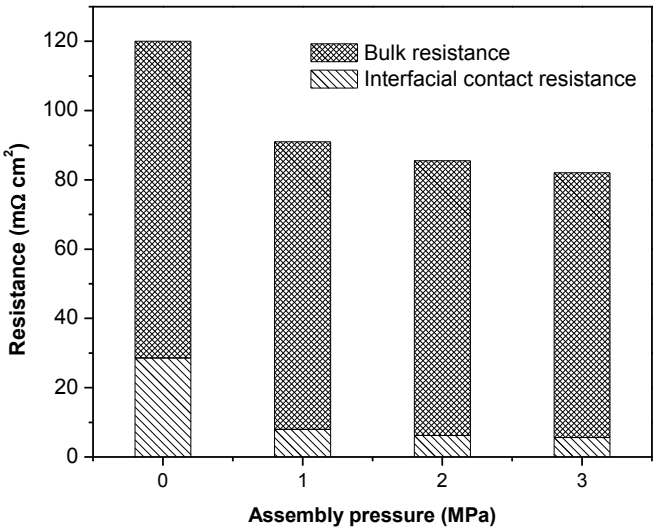


Figure 8. Variation of the bulk resistance and total interfacial contact resistance between GDL and BPP for different assembly pressures.

### 3.4 Assembly pressure effects on electric field

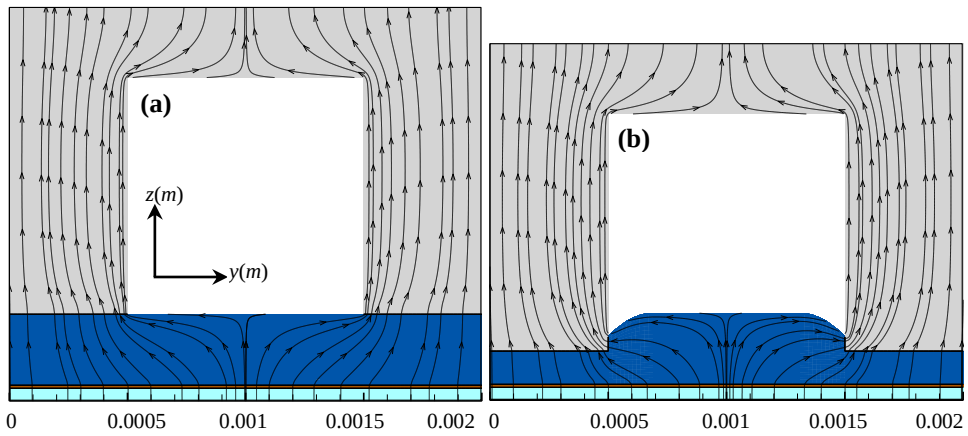


Figure 9. Streamlines of electric field transfer through membrane and anodic cell at the cell middle (x=0.025 *m*) for (a) uncompressed condition (b) 2 *MPa* assembly pressure.

In the present study, the electric field in the fuel cell is caused by electric charges/current flow from the reaction sites to the external circuit. In general, this electric field in the cell is also called the electrostatic field, which does not change with time because charges/currents are stationary when a fuel cell is operating at steady state. The corresponding streamlines are presented in Figure 9 for the electric field through the membrane and the anodic side at the cell middle (x=0.025 *m* along the cell main flow direction) for the case of 2 *MPa* assembly pressure, and

another one for uncompressed condition. The lines and arrows illustrate the current flow direction which starts from the current source, i.e., membrane interface, to the lower potential zone, i.e., the top surface of BPP. Only a portion of the BPP makes contact (the other portion is open for access of reactant gases and removal of products), while the GDL bridges the channels and redistributes the electric current. As found, the current below the channel flows across with a longer distance from the middle of the GDL to the BPP's shoulders. In other words, the electric field is redistributed and becomes more uniform from the shoulders to the top of BPP. It is noted that the electric field at the BPP's corner close to the channel is significantly concentrated, especially for the case with 2 *MPa* assembly pressure. The reason is that a greater contact area was created at the corner, i.e., a tiny contact area in the vertical interface of BPP is generated by the intrusion of the GDL into the channel as a result of the assembly pressure. As a consequence, additional electric current flows from the intrusion of the GDL below the channel to BPP's shoulders along the cell width direction.

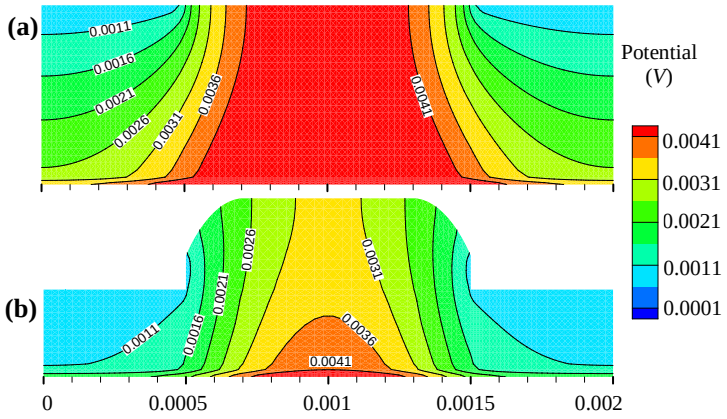


Figure 10. Local potential distribution in anodic GDL and CL at the cell middle (x=0.025 *m*) for (a) uncompressed condition (b) 2 *MPa* assembly pressure.

The local potential distribution in the anodic GDL and CL, and BPP at the cell middle (x=0.025 *m*) for the case of 2 *MPa* assembly pressure and another one for the uncompressed condition are presented in Figure 10 and Figure 11, respectively. For both cases, the maximum potential appears in the porous electrode below the channel region in Figure 10. In contrast, the minimum value occurs in the GDL below the shoulders. However, the region of the minimum value is significantly larger but that for the maximum value is significantly smaller for the case of 2 *MPa* assembly pressure, compared with those for the uncompressed condition. This means that the electric current favors flowing in the GDL below the channel area even though this case has a much improved electric conductivity of the

GDL below the shoulders (see Figure 6) when the cell is operated at 2 *MPa* assembly pressure. The direct reflection of this favor is shown in Figure 11, i.e., the case with 2 *MPa* assembly pressure shows a slightly higher potential at the BPP's corner close to the channels. As shown in Figure 11, in the corner the highest potential appears which agrees well with the concentrated electric field shown in Figure 9.

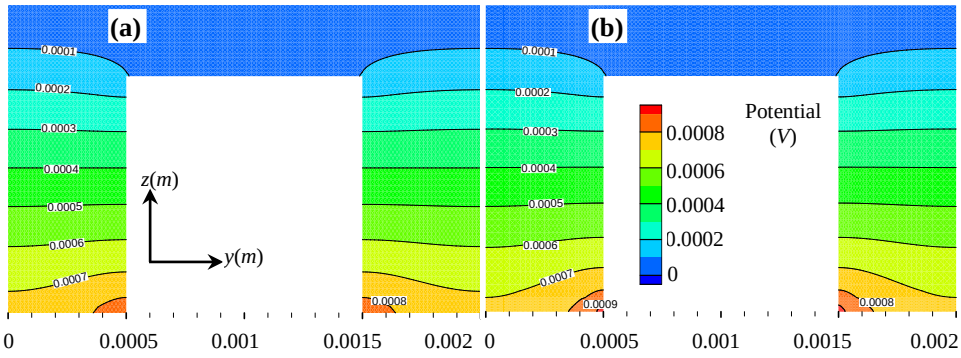


Figure 11. Local potential profile in anodic BPP at the cell middle (x=0.025 *m*) for (a) uncompressed condition (b) 2 *MPa* assembly pressure.

### 3.5 Assembly pressure effects on local current density

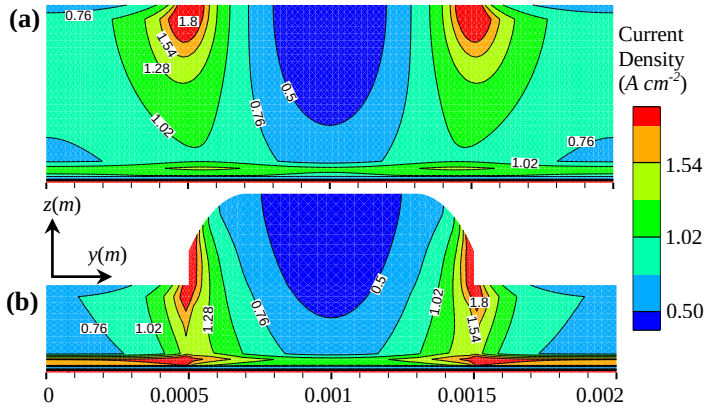


Figure 12. Current density distribution in anodic GDL and CL at the cell middle (x=0.025 *m*) for (a) uncompressed condition (b) 2 *MPa* assembly pressure.

The local current density is predicted and presented in Figure 12 and Figure 13 for the anodic GDL and CL, as well as BPP at the cell middle (x=0.025 *m*) for the case of 2 *MPa* assembly pressure and uncompressed condition, respectively. It is clear that the highest current density occurs in the GDL around the corner of BPP close to the

channel. The difference between the two assembly conditions is that the case with 2 *MPa* assembly pressure has an additional vertical interface (connecting the GDL and BPP) having the maximum current density. However, the maximum value for the latter case is below the BPP's corner. This means that this larger connecting area of the case at 2 *MPa* assembly pressure is favorable in passing through electrons. This finding can be observed in Figure 13c and Figure 13d, which are the magnifications of the bottom shoulders of the BPP (blue rectangular areas) shown in Figure 13a and Figure 13b, respectively. The profile of the maximum current densities varies for different conditions. The maximum current density shows a longer distribution area from the BPP's corner to the channel in the cell width direction for the case with zero assembly pressure. This appears mainly along the vertical direction close to the interface for the other case. This is so because the electric current more easily flows upward from the GDL to the BBP's shoulder around the corner for the case with zero assembly pressure. However, the current needs to flow along the horizontal direction from the intrusion of the GDL below the channel to the vertical interface between the GDL and BPP.

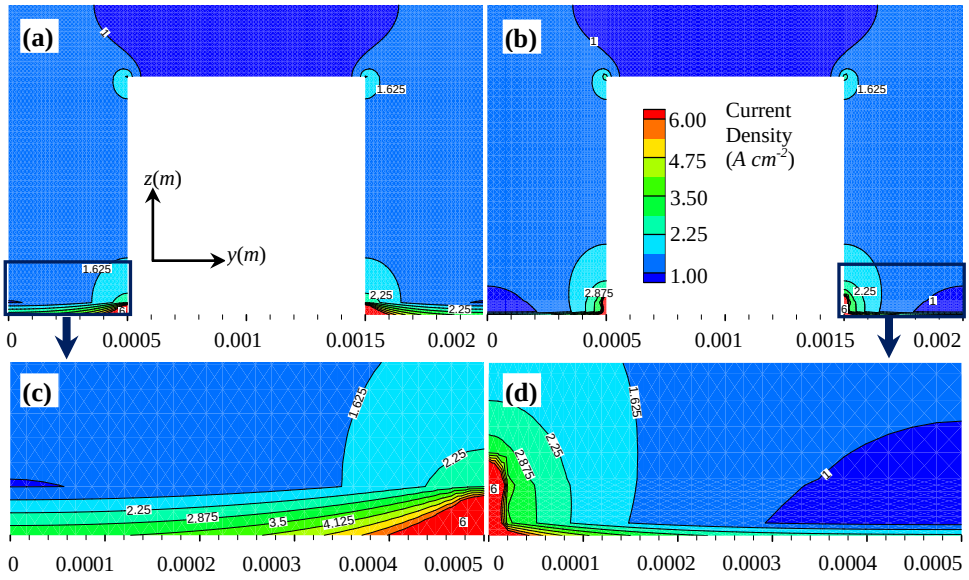


Figure 13. Current density distribution in anodic BPP at the cell middle (x=0.025 *m*) for (a) uncompressed condition (b) 2 *MPa* assembly pressure, and (c) and (d) magnification of blue rectangular area shown in (a) and (b), respectively.

### 3.6 Assembly pressure effects on cell performance

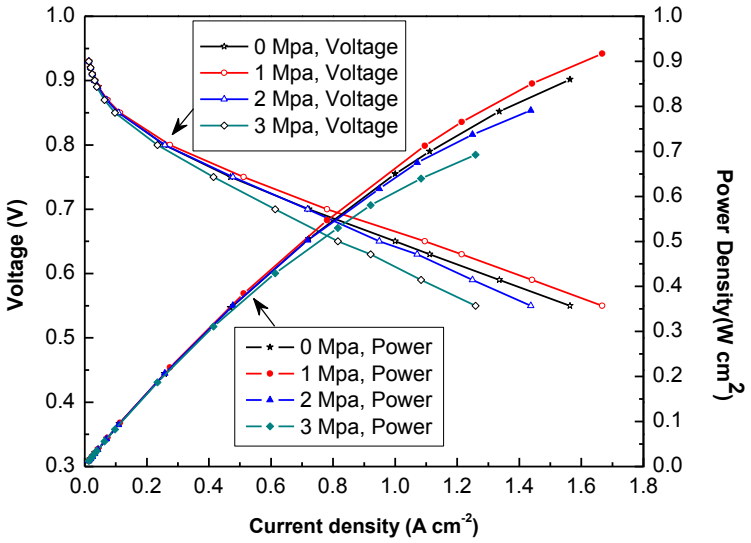


Figure 14. Comparison of voltage and power densities v.s. current density for different assembly pressures.

After evaluation of the electric performance of the half-cell domain for the various assembly pressures, the obtained cell resistances were implemented in the previously developed PEM fuel cell module, as presented in [26]. As illustrated in Figure 14, the cell performance is not sensitive to the assembly pressure at high cell voltages, i.e., the current density-power density curves are kept almost without change. It is expected that a small amount of the reactants is consumed at the reaction sites at higher cell voltages. On the other hand, the cell operating at 1 *MPa* assembly pressure shows the best cell performance compared with the other cases at lower cell voltages. Then the cell performance becomes worse with increasing the assembly pressure. A similar phenomenon has been observed in the study [20], in which a constant cell resistance was applied and 0.3 *MPa* was identified as the optimized assembly pressure. However, the results of our previous research [26] show that the cells operating under a non-zero assembly pressure have a reduced cell performance, i.e., a higher assembly pressure causes a worse cell performance due to the reduced porosity of the deformed GDL and the narrowed cross-sectional areas of the gas flow channel. This is because the mass transfer resistance is accumulated as the porosity decreases. An improved electric conductivity may overcome the deterioration by the mass transfer resistance when the cell is operating at a proper assembly pressure.

## 4. Conclusions

In the present study, an electric transport process model was developed and validated in OpenFOAM to predict the through-plane electric resistance of a PEM fuel cell. The GDL below the channels intrudes into the gas channels as an assembly pressure was applied and accordingly a non-homogeneous electric conductivity along the cell in-plane direction appeared. Our results suggest that a higher assembly pressure results in a decreased cell resistance. However, 1 *MPa* assembly pressure is an optimized assembly condition when both the contact resistance between GDL and BPP, and the electric resistance in the through-plane of the cell are considered. It is found that the through-plane resistance plays a dominating role compared with the contact resistance in a cell. A GDL below the channel is favorable for higher potentials even though the case has an improved electric conductivity of the GDL below the shoulders for assembly pressure conditions. The BPP's corner close to the channel becomes a concentrated area for the electric field and the current, because the additional contact interface created by the intrusion of the GDL into the channel. Furthermore, a longer transfer distance is also found for the electron transfer when an intrusion appears and this also suggests that the contact interface is the only path way for electron transfer through from GDL to BPP. To obtain the optimized cell performance, the assembly pressure should be considered properly to ensure the gas sealing security and lower electric resistance. The results from this investigation may provide guidance for the design and manufacturing of PEM fuel cells.

**Acknowledgments**

The research work was carried out at the Department of Energy Sciences, Lund University, Sweden. The first author gratefully acknowledges the financial support from China Scholarship Council (CSC).

**References**

[1] Pathapati P, Xue X, Tang J. A new dynamic model for predicting transient phenomena in a PEM fuel cell system. Renewable Energy. 2005;30:1-22.

[2] Wang J, Li S, Zhu G, Zhao W, Chen R, Pan M. Novel non-noble metal electrocatalysts synthesized by heat-treatment of iron terpyridine complexes for the oxygen reduction reaction. Journal of Power Sources. 2013;240:381-9.

[3] Min CH. Performance of a proton exchange membrane fuel cell with a stepped flow field design. Journal of Power Sources. 2009;186:370-6.

[4] Sinha PK, Wang CY, Beuscher U. Effect of flow field design on the performance of elevated-temperature polymer electrolyte fuel cells. International Journal of Energy Research. 2007;31:390-411.

[5] Mehta V, Cooper JS. Review and analysis of PEM fuel cell design and manufacturing. Journal of Power Sources. 2003;114:32-53.

[6] Barbir F. PEM Fuel Cells: Theory and Practice. Cambridge: Academic Press; 2013.

[7] Higier A, Liu H. Effects of the difference in electrical resistance under the land and channel in a PEM fuel cell. International Journal of Hydrogen Energy. 2011;36:1664-70.

[8] Higier A, Liu H. Direct measurement of current density under the land and channel in a PEM fuel cell with serpentine flow fields. Journal of Power Sources. 2009;193:639-48.

[9] Zhou Y, Lin G, Shih A, Hu S. A micro-scale model for predicting contact resistance between bipolar plate and gas diffusion layer in PEM fuel cells. Journal of Power Sources. 2007;163:777-83.

[10] Wu Z, Zhou Y, Lin G, Wang S, Hu SJ. An improved model for predicting electrical contact resistance between bipolar plate and gas diffusion layer in proton exchange membrane fuel cells. Journal of Power Sources. 2008;182:265-9.

[11] Mishra V, Yang F, Pitchumani R. Measurement and prediction of electrical contact resistance between gas diffusion layers and bipolar plate for applications to PEM fuel cells. Journal of Fuel Cell Science and Technology (Transactions of the ASME). 2004;1:2-9.

[12] Bautista-Rodríguez CM, Rosas-Paleta A, Rivera-Márquez JA, Solorza-Feria O. Study of electrical resistance on the surface of Nafion 115® membrane used as electrolyte in PEMFC technology part ii: surface response methodology. International Journal of Electrochemical Science. 2009;4:60-76.

[13] Tanaka S, Bradfield WW, Legrand C, Malan AG. Numerical and experimental study of the effects of the electrical resistance and diffusivity under clamping pressure on the performance of a metallic gas-diffusion layer in polymer electrolyte fuel cells. Journal of Power Sources. 2016;330:273-84.

[14] Nitta I, Karvonen S, Himanen O, Mikkola M. Modelling the effect of inhomogeneous compression of GDL on local transport phenomena in a PEM fuel cell. Fuel Cells. 2008;8:410-21.

[15] Taymaz I, Benli M. Numerical study of assembly pressure effect on the performance of proton exchange membrane fuel cell. Energy. 2010;35:2134-40.

[16] Nitta I, Hottinen T, Himanen O, Mikkola M. Inhomogeneous compression of PEMFC gas diffusion layer: part I. Experimental. Journal of Power Sources. 2007;171:26-36.

[17] Escribano S, Blachot JF, Etheve M, Morin A, Mosdale R. Characterization of PEMFCs gas diffusion layers properties. Journal of Power Sources. 2006;156:8-13.

[18] Nitta I, Himanen O, Mikkola M. Thermal conductivity and contact resistance of compressed gas diffusion layer of PEM fuel cell. Fuel Cells. 2008;8:111-9.

[19] Chang W, Hwang J, Weng F, Chan S. Effect of clamping pressure on the performance of a PEM fuel cell. Journal of Power Sources. 2007;166:149-54.

[20] Zhou Y, Lin G, Shih A, Hu S. Multiphysics modeling of assembly pressure effects on proton exchange membrane fuel cell performance. Journal of Fuel Cell Science and Technology. 2009;6:041005-12.

[21] Hamour M, Grandidier J, Ouibrahim A, Martemianov S. Electrical conductivity of PEMFC under loading. Journal of Power Sources. 2015;289:160-7.

[22] Zhou P, Wu C, Ma G. Influence of clamping force on the performance of PEMFCs. Journal of Power Sources. 2007;163:874-81.

[23] Lee WK, Ho CH, Van Zee JW, Murthy M. The effects of compression and gas diffusion layers on the performance of a PEM fuel cell. Journal of Power Sources. 1999;84:45-51.

[24] Ge J, Higier A, Liu H. Effect of gas diffusion layer compression on PEM fuel cell performance. Journal of Power Sources. 2006;159:922-7.

[25] Wang J, Yuan J, Sundén B. Modeling of inhomogeneous compression effects of porous GDL on transport phenomena and performance in PEM fuel cells. International Journal of Energy Research. 2016;41:985–1003.

[26] Wang J, Yuan J, Yu J-S, Sundén B. Investigation of effects of non-homogenous deformation of gas diffusion layer in a PEM fuel cell. International Journal of Energy Research. In press, 2017.

[27] Sivertsen B, Djilali N. CFD-based modelling of proton exchange membrane fuel cells. Journal of Power Sources. 2005;141:65-78.

[28] Yang WJ, Kang SJ, Kim YB. Numerical investigation on the performance of proton exchange membrane fuel cells with channel position variation. International Journal of Energy Research. 2012;36:1051-64.

[29] Berning T, Lu D, Djilali N. Three-dimensional computational analysis of transport phenomena in a PEM fuel cell. Journal of Power Sources. 2002;106:284-94.

[30] Zhou Y, Lin G, Shih A, Hu S. Assembly pressure and membrane swelling in PEM fuel cells. Journal of Power Sources. 2009;192:544-51.

[31] Zhang L, Liu Y, Song H, Wang S, Zhou Y, Hu SJ. Estimation of contact resistance in proton exchange membrane fuel cells. Journal of Power Sources. 2006;162:1165-71.

[32] Su A, Chiu Y, Weng F. The impact of flow field pattern on concentration and performance in PEMFC. International Journal of Energy Research. 2005;29:409-25.

[33] Yuan J, Huang Y, Sundén B, Wang WG. Analysis of parameter effects on chemical reaction coupled transport phenomena in SOFC anodes. Heat and Mass Transfer. 2009;45:471-84.

[34] Di Stefano G. Modeling thermal energy storage systems with OpenFOAM. Doctoral Dissertation. 2014:1-94.

[35] Hussain M, Li X, Dincer I. Multi‐component mathematical model of solid oxide fuel cell anode. International Journal of Energy Research. 2005;29:1083-101.

[36] Ferng YM, Su A, Lu SM. Experiment and simulation investigations for effects of flow channel patterns on the PEMFC performance. International Journal of Energy Research. 2008;32:12-23.

[37] Akkaya AV. Electrochemical model for performance analysis of a tubular SOFC. International Journal of Energy Research. 2007;31:79-98.

[38] Borup RL, Davey JR, Garzon FH, Wood DL, Inbody MA. PEM fuel cell electrocatalyst durability measurements. Journal of Power Sources. 2006;163:76-81.

[39] Obayopo SO, Bello-Ochende T, Meyer JP. Three‐dimensional optimisation of a fuel gas channel of a proton exchange membrane fuel cell for maximum current density. International Journal of Energy Research. 2013;37:228-41.

[40] Wang L, Husar A, Zhou T, Liu H. A parametric study of PEM fuel cell performances. International Journal of Energy Research. 2003;28:1263-72.

[41] Vikram A, Chowdhury PR, Phillips RK, Hoorfar M. Measurement of effective bulk and contact resistance of gas diffusion layer under inhomogeneous compression-Part I: Electrical conductivity. Journal of Power Sources. 2016;320:274-85.

# Paper V

**Proceedings of EFC2017**
**European Fuel Cell Technology & Applications Conference - Piero Lunghi Conference**
**December 12-15, 2017, Naples, Italy**

# EFC17035

# ELECTRIC TRANSPORT PROCESS FOR THE BULK OF A PEM FUEL CELL

Jiatang Wang*, Jinliang Yuan**, and Bengt Sundén*
*Department of Energy Sciences, Lund University, P.O. Box 118,
Lund SE-221 00, (*Sweden*)
**Faculty of Maritime and Transportation, Ningbo University,
Fenghua Road 818, Ningbo 315211, (*China*)

***Abstract* - Performance of a proton exchange membrane (PEM) fuel cell is very sensitive to its electric resistance appearing in its functional components. In this paper, the electric resistance as well as related parameters of a cell is evaluated by a recently developed numerical method in the through-plane direction of the electrodes. The results show that the channel/rib structure leads to non-homogeneous electric field and current flow, especially within the region around the corner of bi-polar plates (BPP) close to the channel. In addition, the current below the channel flows across with a longer distance from the middle of the gas diffusion layer (GDL) to the BPP's shoulders. Finally, the electric resistance is predicted with 99.4 $m\Omega\ cm^2$ of the bulk of an entire cell for the studied case condition.**

***Index Terms* –electric resistance, electrode, numerical method, PEM fuel cell.**

## I. INTRODUCTION

Electric resistance plays an important role for the performance of a proton exchange membrane (PEM) fuel cell [1]. It is known that a smaller ohmic loss resulting from a small electric resistance favors a better cell performance. The effort on decreasing the electric resistance is of interest to optimize the cell performance.

Previous research works have been concentrated on investigating ohmic resistances caused by electron transfer through electrodes (in through-plane direction) [2]. A comparison of the electric resistance under the shoulders and channels has shown that the total electric resistance under the channels is much higher than that under the shoulders caused by the channel/rib structures in a PEM fuel cell [3]. In the present study, the evaluation of the electric resistance and electric transport process are conducted by a newly developed electron transfer model implemented in an open source library of OpenFOAM. The distribution of the electric field and current density are presented and analyzed.

## II. NUMERICAL DESCRIPTION

A half-cell, i.e., the anodic side is selected as the representative domain for the electric resistance modeling, as shown in Fig. 1.

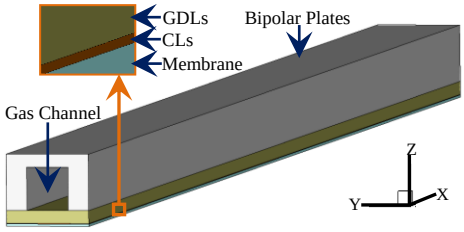


**Fig. 1. Schematic illustrations of the electric resistance model.**

The governing equation for the electron transfer through the entire domain can be evaluated by a Laplacian equation [4],

$$\nabla \cdot (\sigma \nabla \varphi) = 0 \tag{1}$$

where φ is electric potential and σ is electric/protonic conductivity. Then the electric field, local current density and electric resistance of the domain can be obtained by the following equations [5], respectively,

$$E_e = -\nabla \varphi \tag{2}$$

$$j = -\sigma \nabla \varphi \tag{3}$$

$$R_\Omega = \frac{|\varphi_{\max} - \varphi_{\min}|}{\bar{j}} \tag{4}$$

where $\bar{j}$ is the average current density, $\varphi_{max}$ and $\varphi_{min}$ are the maximum and minimum electric potential occurring in the

domain, respectively. A constant current density $i$ = 0.7 $A\ cm^{-2}$ was applied at the membrane as the current source for the Laplacian equation. The missing parameters of this model can be found in [6].

## III. Results and Discussions

The local current density is predicted and presented in Fig. 2 for the domain at the cell middle (x=0.025 *m*). It is clear that the highest current density occurs in the GDL below the corner of the BPP close to the channel. This highest value can be clearly observed in Fig. 2c, which is a magnification of the bottom shoulders of the BPP (blue rectangular areas) in Fig. 2b. It is found that the maximum current density appears in a larger distribution area at the bottom of the BPP close to the channel. This is so because the electric current flows upward more easily from the GDL to the BPP's shoulder around the corner.

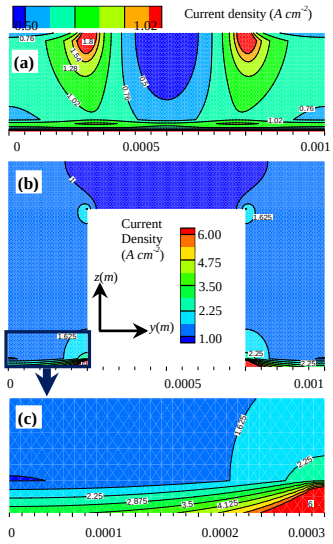


**Fig. 2. Current density distribution at the cell middle in (a) anodic GDL and CL, (b) anodic BPP and (c) magnification of blue rectangular area shown in (b).**

The streamlines of the electric field are presented in Fig. 3 at the cell middle (x=0.025 *m*). The lines and arrows illustrate the current flow direction which starts from the current source (generated at the membrane interface) to the lower potential zone appearing at the top surface of BPP. Only a portion of the BPP makes contact and the other portion is open for access of reactant gases and removal of products, while the GDL bridges the channels and redistributes the electric current. As shown, the current below the channel flows across with a longer distance from the middle of the GDL to the BPP's shoulders. In other words, the electric field is redistributed and becomes more uniform from the shoulders to the top of BPP. It is noted that the electric field at the BPP's corner close to the channel is significantly concentrated. In addition, the electric resistance of an entire cell was predicted as 99.4 $m\Omega\ cm^2$ based on this model.

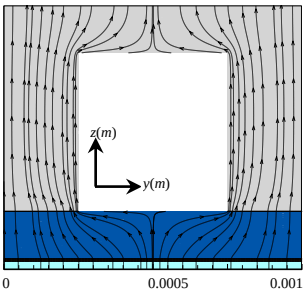


**Fig. 3. Streamlines of electric field transfer through membrane and anodic cell at the cell middle.**

## IV. Conclusion

In the present study, an electric transport process model was developed in OpenFOAM to predict the through-plane electric properties of a PEM fuel cell. The predicted results show that the BPP's corner close to the channel becomes a concentrated area for the electric field and current, because of the channel/rib structure. Furthermore, the current below the channel flows a longer distance to the shoulders compared with the one below the shoulders. Finally, the electric resistance is predicted as 99.4 $m\Omega\ cm^2$ of the bulk of an entire cell based on this model.


## Acknowledgment

The research work was carried out at the Department of Energy Sciences, Lund University, Sweden. The first author gratefully acknowledges the financial support from China Scholarship Council (CSC).


## References


[1] Barbir, F., PEM Fuel Cells: Theory and Practice, Cambridge, Academic Press, 2013.

[2] Higier, A., Liu, H., Effects of the difference in electrical resistance under the land and channel in a PEM fuel cell, International Journal of Hydrogen Energy, Volume 36, 2011, Pages 1664-1670.

[3] Higier, A., Liu, H., Direct measurement of current density under the land and channel in a PEM fuel cell with serpentine flow fields, Journal of Power Sources, Volume 193, 2009, Pages 639-648.

[4] Yang, W.J., Kang, S.J., Kim, Y.B., Numerical investigation on the performance of proton exchange membrane fuel cells with channel position variation, International Journal of Energy Research, Volume 36, 2012, Pages 1051-1064.

[5] Berning, T., Lu, D., Djilali, N., Three-dimensional computational analysis of transport phenomena in a PEM fuel cell, Journal of Power Sources, Volume 106, 2002, Pages 284-294.

[6] Wang, J., GDL Deformation and its Effects on Electric resistance and Transport Phenomena in a PEM Fuel Cell [Doctoral Dissertation], Sweden: Lund University, 2017.

# Notes